PROJECTION DOMAIN COMPRESSION OF IMAGE INFORMATION

by

JOHN OLUTAYO IBIKUNLE

A thesis submitted for the degree of
Doctor of Philosophy in the Faculty of Engineering,
University of London.

Department of Electrical Engineering,
Imperial College of Science and Technology,
University of London,
London.

April 1987

ABSTRACT

This thesis investigates and develops projection domain compression (PDC) of image information. Two forms of PDC are defined. The first involves the compression of projected information that essentially corresponds to an *unknown* image distribution. The potential applications of this PDC form in tomographic processing environments are discussed. The object of the second PDC form is to reduce the dimensionality of the image data compression problem. It operates by first projecting *known* image information, defined on an N–dimensional hyperplane, onto an admissibly small number of $(N-1)$–dimensional hyperplanes (projections) and then compresses the projected information on an intra–plane basis.

Information transformation properties and stochastic properties of the projection mapping of 2–D image information are respectively examined for two important forms of projection geometry. Under idealized conditions, an optimistic theoretical result of information preservation in the projection domain is obtained. The associated stochastic results indicate that the projection mappings are whitening transformations when applied to wide sense stationary image fields.

Various compression procedures that exploit the frequency structure of projected information, derived through angle–radius (AR) based projection mapping, are proposed. Intra–projection and inter– projection coding, based on the radial and angular frequency properties, respectively, are described. In computer simulations of these schemes, for projection data acquired from typical pictures, compression ratios of the order of 10 are realized with acceptable image reconstructions. Mismatched quantization can however produce severe artifacts in the reconstructions. An algorithm, based on the peculiar bow–tie shape of the 2–D AR frequency band region of projected information, is also developed. Compression ratios of the order of 11 are achieved.

The use of vector quantization (VQ) for PDC is also studied. Good performance of VQ based PDC is achieved by controlling the memory between vectors derived

from the projection data. Two adaptive VQ based procedures are proposed and implemented. Good image reconstructions can be achieved for compression ratios of the order of 16.

Projection based block coding (PBBC) of known image information is examined in its non adaptive and adaptive forms. Good pictorial results are obtained at bit rates in the range 1.0–2.0 bits/pixel. Inexact reconstruction, however, limits the performance of such schemes in comparison to that of orthogonal mapping based image coding schemes. Extensive quantitative experiments are conducted to study this reconstruction distortion as a function of image correlation, image area and the number of projections acquired from Gauss–Markov image fields. The experimentation culminates in the derivation of a projection allocation algorithm that systematically determines the number of projections to be generated from an image or sub–image in order that the average reconstruction distortion is minimized over an image ensemble of arbitrary dimensions. Performance tests of the algorithm are presented.

A rate–distortion analysis for establishing the performance bounds of PDC is presented. The derived bounds reflect the fact that distortion is produced by the compression and reconstruction procedures in PDC. The incorporation of the stochastic properties of projection mappings into the analysis yields a specific bound for intra– projection compression. This bound is computed and compared with practical performance levels. A variation of the bound which is designed to be representative of tomographic imaging procedures, in which there exist considerable uncertainty in the projection generation, is also discussed.

Within the framework of the analysis, the performance of intra—projection compression, in the presence of high level channel noise, is observed. A means of controlling this noise especially as it affects the image reconstruction stage is discussed.

To my father, TUNDE IBIKUNLE

ACKNOWLEDGMENTS

I wish to acknowledge Dr. R.A. King for his supervision, keen insight and guidance in the course of this work.

Many thanks are due to Dr. A.S. Kwabwe for his interest in the work; in the course of our several conversations, he raised many specific questions some of which I have addressed in this thesis. I am also grateful for the various stimulating discourses I had with other members of Dr. King's research group. Their warm friendship is also deeply appreciated.

I would wish to thank Dr. M. Goldberg of the Electrical Engineering Department, Ottawa University, Canada, for drawing my attention to important references that have been of considerable benefit to this work.

I am thankful to Ola Fakolujo who found the time to help out a great deal in the preparation of photographic prints. I am very much indebted to Ade Osinubi whom has not only helped in the preparation of some of the diagrams and typescript but has been a marvellous friend; his encouragement has been invaluable.

I express my gratitude to my father for his wholehearted encouragement and financial support. There are many friends and colleagues, too many to mention here, who have expressed sincere interest and concern about myself and my work. I am deeply grateful to you all.

My heartfelt thanks are due to my fiancée Adetokunbo Olujohungbe for her invaluable love, devotion and support throughout the course of this work.

Finally, I wish to thank God for His mercies and blessings all the way along.

TABLE OF CONTENTS

		Page
ABSTRACT		2
DEDICATION		4
ACKNOWLEDGEMENTS		5
TABLE OF CONTENTS		6
IMPORTANT NOTATION		13
CHAPTER 1	INTRODUCTION	19
1.1	Applications of Data Compression in Image Processing	19
1.2	The Data Compression Problem	19
1.3	The Concept of Projection Domain Compression	21
1.3.1	Projections	21
1.3.2	Generalized Concept of PDC	22
1.4	Mode 1 PDC and Potential Applications	24
1.4.1	Possible Architectures for Tomographic Systems with Mode 1 PDC	26
1.4.1.1	Multi–projection Generation Single Reconstruction System	26
1.4.1.2	Single Projection Generation Multi–Reconstruction System	28
1.4.1.3	Multi–Projection Generation Multi–Reconstruction System	28
1.5	Mode 2 PDC: Image Compression Potential	28
1.6	Previous Work on Projection Based Compression	30
1.7	Scope of Thesis	31
1.8	Outline of Thesis	33

CHAPTER 2	BACKGROUND FOR PROJECTION DOMAIN COMPRESSION	36
2.1	Introduction	36
PART A:	Reconstruction from the Projection Domain	37
2.2	The Radon Transform	37
2.3	Reconstruction Techniques	40
2.3.1	Transform Methods	40
2.3.1.1	Convolution Backprojection	40
2.3.1.1.1	Discrete Convolution Functions	43
2.3.1.1.2	Interpolation Approaches	45
2.3.1.2	Fourier Inversion	45
2.3.1.3	Other Transform Methods	48
2.3.2	Finite Series Expansion Reconstruction Methods (FSER)	49
2.3.2.1	Algebraic Reconstruction Techniques	50
2.3.2.2	Non–iterative Series Expansion	51
2.3.3	FSER versus Transform Methods	52
2.3.4	Reconstruction Considerations for PDC	53
2.4	Discrete Modelling of the Radon Transform	53
2.4.1	The Slope–Intercept Discrete Radon Transform (SI- DRT)	54
2.4.2	The Angle–Radius DRT and its Implementation	56
PART B:	Information Theoretic and Stochastic Appraisals for the Projection Domain	62
2.5	Information Preservation Considerations in the Projection Domain	62
2.5.1	Discussion	65
2.6	Stochastic Characterization of the Projection Domain	66
2.6.1	Cross–correlation Property	67
2.6.2	Auto–correlation Properties	68
2.6.3	Discussion	70

2.6.4	Summary of Stochastic Properties of the SI–Radon Transform	70
2.7	Some Empirical Results of Auto–correlation Measures of Projection Data	71
PART C:	Data Compression Techniques in a Projection Domain Environment	77
2.8	Data Compression for a Mode 1 PDC System	78
2.8.1	Predictive Compression	78
2.8.2	Linear Transform based Techniques	78
2.8.3	Hybrid Techniques	80
2.8.4	Quantization	80
2.8.5	Performance Considerations	81
2.8.5.1	Fidelity Measures	81
2.8.5.2	Determining the Compression Level	82
2.9	Data Compression for a Mode 2 PDC System	82
2.10	Summary and Conclusions	83
CHAPTER 3	COMPRESSION BASED ON THE FREQUENCY STRUCTURE OF PROJECTED INFORMATION	85
3.1	Introduction	85
3.2	Intra-projection Coding (INTRAP):- PDC based on Radial Frequency	86
3.2.1	A Cosine Projection–Slice Theorem	87
3.2.2	Implementation of Cosine Transform based INTRAP	88
3.2.3	Simulation Approach, Results and Discussion	91
3.2.3.1	Bit Allocation	91
3.2.3.2	Quantization Artifacts in INTRAP and Associated Controls	92
3.2.3.2.1	Augmenting INTRAP by Projection Interpolation	92
3.2.3.2.2	Matched Quantization	94

3.3	Inter-projection Coding (INTERP):- PDC based on Angular Frequency Structure	98
3.3.1	Simulation Results and Discussion	101
3.4	Comparisons of INTRAP and INTERP with 2-D DCT Coding of Projection Data	104
3.5	The 2-D AR Frequency Structure of the Projection Domain	104
3.5.1	Theoretical Background	104
3.5.2	Implications of 2-D Frequency Structure for PDC	107
3.5.2.1	Band-shape Effects on INTRAP and INTERP	107
3.5.2.2	Sampling Effects of the Band-shape	107
3.5.3	A 'Bow-tie' Algorithm for PDC	110
3.5.4	Simulation Procedure, Results and Discussion	112
3.5.4.1	Spectral Shapening	112
3.5.4.2	Encoding Algorithm	114
3.5.4.3	Results	118
3.6	Summary	122
CHAPTER 4	PROJECTION DOMAIN COMPRESSION USING VECTOR QUANTIZATION	124
4.1	Introduction	124
4.2	Survey of Image based VQ	125
4.2.1	Spatial Domain VQ	126
4.2.2	Transform Domain based VQ	128
4.3	VQ in a Projection Domain Environment	130
4.3.1	Main features of VQ	131
4.3.1.1	Definition and Design	131
4.3.1.2	Distortion Considerations	135
4.3.1.3	Bit Rate Considerations	136
4.3.1.4	Vector Formation from Projection Domain Data	136

4.3.2	Direct VQ in the Projection Domain	140
4.3.3	Enhanced VQ for PDC	142
4.3.3.1	Simulation Details and Results	146
4.3.4	Adaptive Enhanced VQ: A Zonal VQ Variation	151
4.3.5	Large Shape Adaptation based VQ for PDC	157
4.3.5.1	Simulation, Results and Discussion	159
4.4	Summary	168
CHAPTER 5	SOME DEVELOPMENTS FOR MODE 2 PDC	170
5.1	Introduction	170
5.2	'In–place' Fourier based Simulation for PDC	171
5.3	Projection Based Block Coding (PBBC) of Images	174
5.3.1	Description and Implementation	174
5.3.2	Comparison of PBBC with 2–D Fourier Transform Coding	177
5.3.3	Adaptive PBBC	180
5.4	Relationships of Reconstruction Error with Image Correlation, Image Area and the Number of Projections: A Quantitative Study	182
5.4.1	Introduction	182
5.4.2	Description and Results of Quantitative Experiments	183
5.4.2.1	Random Picture Generation	183
5.4.2.2	Reconstruction Error as a Function of Image Correlation and the Number of Projections	184
5.4.2.3	Interaction of Reconstruction Error with Encoding Distortion	186
5.4.2.4	Reconstruction Error as a Function of Image Correlation, Image Area and the Number of Projections	188
5.5	A Projection Allocation Algorithm for Minimal Reconstruction Distortion	191

5.5.1	Introduction	191
5.5.2	A Parametric Formula for Reconstruction Distortion as a Function of the Number of Projections	191
5.5.3	Statement of the Projection Allocation Problem	194
5.5.4	Potential Applications for Projection Allocation	194
5.5.5	Development of the Allocation Formula	195
5.5.6	Some Performance Tests of the Algorithm	197
5.6	A Lower Bound of Reconstruction Distortion	202
5.7	Summary and Conclusions	203
CHAPTER 6	A RATE–DISTORTION THEORETIC ANALYSIS FOR PDC	205
6.1	Introduction	205
6.2	Fundamentals of Rate–distortion Theory	206
6.3	The Generalized PDC Model	209
6.3.1	Equivalent Compression Scheme	212
6.3.2	Problem Statement	214
6.4	Fidelity Criterion	215
6.5	An Upper Bound of the Rate–Distortion Function for PDC	218
6.5.1	Discussion	222
6.6	A Rate–Distortion Bound for Intra–projection Compression	224
6.7	A Representative Compression Bound for Uncertain Projection Generation	228
6.8	Evaluation of Bounds	229
6.8.1	Introduction	229
6.8.2	Comparisons of Intra–projection Compression Bounds based on Equivalent Markov and Sample Statistics	230

6.9	Comparison of Theoretical Bounds with Sub–optimal Compression	234
6.9.1	Sub–optimal Intra–projection Compression	234
6.9.2	Sub–optimal 2–D Radial and Angular Compression	236
6.10	Controlling Reconstruction Distortion	238
6.11	Performance of Intra–projection Compression in the Presence of Channel Noise	243
6.12	Summary	247
	CONCLUSIONS	249
APPENDIX I	THE ONE–PROJECTION THEOREM FOR THE SLOPE–INTERCEPT RADON TRANSFORM	258
APPENDIX II	STOCHASTIC PROPERTIES OF THE SLOPE–INTERCEPT RADON TRANSFORM	261
APPENDIX III	INFORMATION RATE OF GAUSSIAN RANDOM VARIABLES	266
APPENDIX IV	RELATIONSHIP BETWEEN THE SI–RT AND AR–RT	268
	REFERENCES	271

IMPORTANT NOTATION

NOTE:-

Only what is considered to be important notation for the thesis is listed here. Some symbols, not included here, have been employed just for convenience at their time of use.

PDC	— Projection Domain Compression.
$\mathbf{x}$	— A column vector that defines a hyperplane in the image domain.
$\mathbf{x}^T$	— Transpose of $\mathbf{x}$.
$\mathbf{t}$	— Defines a hyperplane in the projection domain.
$\Re^N$	— N–dimensional real Euclidean space.
$f(\mathbf{x})$	— Image function defined over the hyperplane $\mathbf{x}$.
$P(t_p;\mathbf{t})$	— Projection function defined on a hyperplane $\mathbf{t}$; the orientation of the projection path is determined by the parameter t_p.
CAT or CT	— Computer aided tomography.
MPGSR	— Multi-projection generation single reconstruction system.
SPGMR	— Single projection generation multi–reconstruction system.
MPGMR	— Multi-projection generation multi–reconstruction system.
AR–RT	— Angle–Radius Radon transform.
AR–DRT	— Angle–Radius Discrete Radon Transform.
SI–RT	— Slope–Intercept Radon Transform.
SI–DRT	— Slope–Intercept Discrete Radon Transform.
θ, t	— Angular and radial parameters of the AR–RT.
$P(\theta, t)$	— A projection domain function acquired from the AR–RT.
$P_\delta(\theta, t)$	— Corresponds to $P(\theta, t)$ when the image function is an impulse function.
$\Delta\theta, \Delta t$	— Sampling intervals in the angular and radial

parameters of the AR–RT.

$\widetilde{P}(\theta,t)$ — Projection domain function acquired from a modified AR–RT.

q,τ — Slope and intercept parameters of the SI–RT.

$P(q,\tau)$ — Projection domain function corresponding to the SI–RT.

$\widetilde{P}(q,\tau)$ — Projection domain function corresponding to the modified SI–RT.

$\Delta q, \Delta\tau$ — Sampling intervals in the slope and intercept parameters of the SI–RT.

$P(\theta,\omega)$ — Radial based Fourier transform of $P(\theta,t)$.

$P(\omega_\theta,\omega_t)$ — 2–D angle–radius Fourier transform of $P(\theta,t)$.

$P_\delta(\omega_\theta,\omega_t)$ — 2–D angle–radius Fourier transform of $P_\delta(\theta,t)$.

$P(q,\omega)$ — Intercept based Fourier transform of $P(q,\tau)$.

$|\omega|$ — Radial frequency response of ideal inverse Radon transform.

B_t — Radial bandwidth of $P(\omega_\theta,\omega_t)$.

B_θ — Angular bandwidth of $P(\omega_\theta,\omega_t)$.

CBP — Convolution backprojection.

FSER — Finite series expansion reconstruction.

RAM–LAK — Ramachandran and Lakshminarayanan.

$\mathbf{P}$ — A matrix or sequence of projection samples.

$\mathbf{P}_i$ — The i^{th} row vector of the matrix $\mathbf{P}$ and corresponds to the i^{th} projection in the projection domain.

$\widehat{\mathbf{P}}$ — A matrix or sequence of encoded projection samples.

$\widehat{\mathbf{P}}_i$ — A compressed/encoded version of $\mathbf{P}_i$.

$\widehat{\mathbf{P}}_v$ — A virtual projection domain matrix.

$\mathbf{F}$ — A matrix of image samples.

$\widehat{\mathbf{F}}$ — A matrix of encoded image samples.

$\mathbf{f}$ — A vector or sequence of image samples.

$\widehat{\mathbf{f}}$ — A vector or sequence of encoded image samples.

$r_f(x_1, y_1; x_2, y_2)$ — Auto–correlation function of an image function $f(x, y)$.

$r_P(\theta_1, \theta_2; t_1, t_2)$ — Auto–correlation function of $P(\theta, t)$.

$r_P(q_1, q_2; \tau_1, \tau_2)$ — Auto–correlation function of $P(q, \tau)$.

$r_{fP}(x, y, \theta, t)$ — Cross–correlation function between $f(x, y)$ and $P(\theta, t)$.

$r_{fP}(x, t, q, \tau)$ — Cross–correlation function between $f(x, t)$ and $P(q, \tau)$; $f(x, t)$ may be a space–time or space–space dependent function.

WSS — Wide sense stationary.

$R_\theta(m)$ — Average inter–projection sample auto–correlation function.

$R_t(m)$ — Average intra–projection sample auto–correlation function.

M_t — No. of radial coefficients per projection.

M_θ — No. of projections within the matrix $\mathbf{P}$.

ρ_θ^m - Equivalent first order Markov inter– projection correlation.

ρ_t^m — Equivalent first order Markov intra–projection correlation.

$\Phi_P(\omega_1, \omega_2)$ — Power spectral density function of projected information.

$\Phi_f(\omega_1, \omega_2)$ — Power spectral density function of image information.

$\Phi_P(\theta_i, \omega_2)$ — Power spectral density function of the projection generated, on angle θ_i, through the AR–RT or AR–DRT.

$\Phi_P(q, \omega)$ — Power spectral density function of projected information generated along slope q, through the SI–RT.

$\Phi_{P\hat{P}}(\omega_1, \omega_2)$ — Cross-power spectrum between original and compressed projected information.

bits/ps — bits/projected sample.

B_Q — Quantizer bit rate (bits/pixel) in a mode 2 PDC system.

B_Q' — Final bit rate of encoding, using a finite number of projections in a mode 2 PDC system.

MSE, NMSE — Mean squared error and normalized MSE.

NMSE(P) — The NMSE of distortion between $\mathbf{P}$ and $\hat{\mathbf{P}}$.

NMSE(F) — The NMSE of distortion between the image reconstruction from $\hat{\mathbf{P}}$ and the image reconstruction from $\mathbf{P}$.

NMSE(I) — The NMSE of distortion due to projection interpolation.

INTRAP — Intra–projection compression.

INTERP — Inter–projection compression.

$I(\mathbf{P}_i, \mathbf{P}_{i+2})$ — Projection interpolation operation between $\mathbf{P}_i$ and $\mathbf{P}_{i+2}$.

$BWT(.)$ — Spectral shapening operator for bow–tie algorithm.

$E_c(.)$ — Special encoding operation within the bow–tie algorithm.

$S_e\{\mathbf{A}\}$ — Set of elements in a matrix or vector $\mathbf{A}$.
The elements are not necessarily ordered as in $\mathbf{A}$.

VQ — Vector quantization.

PVQ — Predictive vector quantization.

FSVQ — Finite–state vector quantization.

M/S–VQ — Mean–shape vector quantization.

G/S–VQ — Gain–shape vector quantization.

ZVQ — Zonal vector quantization.

$Q(\mathbf{v})$ — Vector quantizer or mapping of the vector $\mathbf{v}$.

$d\{\mathbf{v}, Q(\mathbf{v})\}$ — Distortion per vector of vector quantization.

$R_k^M(Q(\mathbf{v}))$ — Associated rate of vector quantization for a codebook of dimensions (M, k).

LBG - Linde, Buzo and Gray.

VF1, VF2 & VF3 Inter–projection, intra–projection and square block vector formation procedures.

PDC–VQ — Vector quantization applied directly in the projection domain.

PDC–HT–VQ — Enhanced VQ of projection data via constrained pre–processing by Hadamard transformations.

PDC–CT–VQ — Enhanced VQ of projection data via constrained pre–processing by Cosine transformations.

MVQ — Multi–stage vector quantization.

IT,OT — In–training and Out–of–training.

PBBC	—	Projection based block coding.
$\mathbb{IE}$	—	An Image ensemble.
$\mathbf{F}_i$	—	The i^{th} image wihin the image ensemble $\mathbb{IE}$.
$G(\rho_1, \rho_2, A)$	—	Parametric constant for projection allocation; parameters are the one–step row and column Gauss–Markov correlations (ρ_1, ρ_2) and the image area A.
$M(\Theta)$	—	A set of projection allocations over an image ensemble.
$D(\Theta)$	—	A set of average MSEs over an image ensemble.
$M_\theta^{(N)}$	—	Total number of projections to be allocated to an ensemble of N image fields.
Σ	—	Set of energy values associated with an image ensemble.
$\Sigma^{1/2}$	—	Set of image rms values associated with an image ensemble.
M_{θ_i}	—	The number of projections to be acquired from the i^{th} image within an image ensemble.
$D_L(\rho_1, \rho_2, A)$	—	Lower bound of reconstruction distortion for a given correlation level ρ_1, ρ_2 and area A.
$D_L(A)$	—	Lower bound of reconstruction distortion for a given area A.
$M_J(\mathbf{P}, \widehat{\mathbf{P}})$	—	Mutual information between vector sequences $\{\mathbf{P}\}$ and $\{\widehat{\mathbf{P}}\}$ when the vectors belong to J–dimensional vector space.
$R_J(D)$	—	J–block rate–distortion function.
$M(P, \widehat{P})$	—	Mutual information between the sequences $\mathbf{P} = \{P(k,l)\}$ and $\widehat{\mathbf{P}} = \{\widehat{P}(k,l)\}$.
$R(D_{T\alpha})$	—	Parametric rate–(total) distortion function.
$R(D_{C\alpha})$	—	Parametric rate–(compression) distortion function.
$D_{T\alpha}$	—	Parametric total MSE due to compression and reconstruction.
$D_{C\alpha}$	—	Parametric MSE due to compression or encoding.
D_I	—	Distortion due to reconstruction.
D_{Imin}	—	Minimum reconstruction distortion.

$C^*(\theta_i, \omega_2)$	— Angle–dependent compression filter that processes projections independently (the asterisk denotes the 'complex conjugate').
$S^*(\theta_i, \omega_2)$	— Angle–dependent blurring filter at reconstruction stage.
$W(\theta_i, \omega_2)$	— Angle–dependent Wiener filter for minimizing D_I.
E[.]	— Ensemble average operator.
$\mathrm{Var}(\mathbf{P}_i)$	— Variance computed over samples of $\mathbf{P}_i$.
$\mathrm{Tr}[\mathbf{A}]$	— The trace of a matrix $\mathbf{A}$.
Re[.], Im[.]	— Real or imaginary part of argument.
$\mathrm{col}[\mathbf{A}]_i$	— The i^{th} column of matrix $\mathbf{A}$.
$\mathrm{diag}[\mathbf{A}]$	— The diagonal of matrix $\mathbf{A}$.
$\mathbf{I}$	— Identity matrix.
$\mathbf{I}_{dc}$	— Singular diagonal matrix whose diagonal elements are all unity, but one, which is identically zero.

CHAPTER ONE

INTRODUCTION

1.1 Applications of Data Compression in Image Processing

Data compression is an important factor in various and diverse image processing applications which include digital television, teleconferencing, remote sensing via satellite, signal transmission via aircraft, radar, sonar and fascimile and image archiving in biomedical applications [1,2,3]. The associated data rates of information generated in these applications reach enormous proportions and some form of fidelity constrained information control, for transmission or storage purposes, is required through data compression. Statistical dependency or redundancy within image data effectively dictates the level of compression for a given fidelity requirement.

Many techniques have evolved over the years for image data compression. These have included predictive systems [1] which exploit the predictability within an image, transform domain techniques [1] which map the image information into another domain more suitable for data compression and are primarily based on packing a maximum amount of image information into a minimum number of samples and hybrid schemes [4] which combine predictive and transform based compression procedures. These schemes are reviewed in the context of their application to projection domain information (to be subsequently defined) of images in chapter two. It is instructive at this stage to consider a formal appraisal of the general signal data compression problem.

1.2 The Data Compression Problem

In digital signal processing, a set $S = \{s_1, s_2, \dots, s_K\}$ of signal samples is typically associated with a corresponding set $B = \{b_1, b_2, \dots, b_K\}$ of information carrying units where each b_i is the number of units required to represent each s_i subject to a fidelity (quality) constraint. The signal representation at the source generation point is expected to be of high quality and on average a large number of information units are needed to meet this requirement. When the elements of S are to be conveyed to a reception point, through a transmission or storage medium (i.e. channel) with a limited information carrying capacity C, a means must be found of reducing the average information rate (information units/ signal sample) of the source signal set before transmission or storage. This corresponds to the data compression or source coding problem.

The objective of a data compressor is therefore to find another set of information carrying units $\widehat{B} = \left\{\widehat{b}_1, \widehat{b}_2, \dots, \widehat{b}_M\right\}$ that would correspond to a sample set $\widehat{S} = \{\widehat{s}_1, \widehat{s}_2, \dots, \widehat{s}_K\}$ where the average information rates $\widehat{b}_{av}$ and b_{av} derived from sets $\widehat{B}$ and B, respectively, are such that

$$\widehat{b}_{av} = \frac{1}{M}\sum_{i=1}^{M}\widehat{b}_i < b_{av} = \frac{1}{K}\sum_{i=1}^{K} b_i \tag{1.1}$$

and M is not necessarily equal to K. Moreover, the set $\widehat{S}$ is required to be an adequate representation of S within the limits of a pre–specified fidelity level.

It is sufficient to convey the elements of S to the reception point through a channel of capacity C (information units/sample) at a rate such that

$$\widehat{b}_{av} \leq C \tag{1.2}$$

An indicator of the amount of compression is the compression ratio CR:

$$CR = b_{av}/\widehat{b}_{av} \tag{1.3}$$

The information rate in an image processing environment is measured in bits /picture element. The information rate is strictly related to the entropy $H(S)$ of the image signal set $S = \{s_1, s_2, \ldots, s_K\}$ which, for a sequence of discrete amplitude (quantized) samples, is

$$H(S) = -\sum_{i=1}^{L} P(s_i) \log_2 P(s_i) \tag{1.4}$$

where $P(s_i)$ is the probability that s_i will be quantized to one discrete amplitude level from a set of $L = 2^{b_{av}}$ possible levels and b_{av} is the pre–determined fixed binary word length (no. of bits) for encoding each level. For adequate spatial resolution, the image size K is typically large (of the order of 10^5) and in non–fascimile based applications $b_{av} > 1$. Therefore, the computation of $H(S)$ is tedious and the average data rate b_{av} is more conveniently employed as a measure of the average information rate although b_{av} is normally larger than $H(S)$.

1.3 The Concept of Projection Domain Compression

The focus of this work is on the development of projection domain compression (PDC) of image information. 'Image information', here, includes both pictorial and non–pictorial data and in general refers to any N–dimensional function that can be reconstructed from its $(N-1)$–dimensional projections. It is informative to consider the definition of the projection process before outlining the generalized concept of PDC and the motivation for its development.

1.3.1 Projections

A projection is essentially a mapping of an N–dimensional function to an $(N-1)$–dimensional function and is obtained by integrating the N–dimensional function over a particular direction in the image hyperplane.

Specifically, let $f(\mathbf{x})$, $\mathbf{x}^T = (x_1, x_2, \ldots, x_N) \in \Re^N$, be a function in N–dimensional real Euclidean space $\Re^N$ and suppose $f(\mathbf{x})$ is only non–zero within a subspace $\mathcal{V} \subset \Re^N$ such that $f(\mathbf{x}) = 0$, $\mathbf{x} \notin \mathcal{V}$. Then a projection $P(t_p; \mathbf{t})$, $\mathbf{t}^T = (t_1, t_2, \ldots t_{p-1}, t_{p+1}, \ldots t_N) \in \Re^{N-1}$, of $f(\mathbf{x})$ in a direction specified by t_p, over a subspace $\mathcal{V}$, is the mapping $\mathcal{P}f$

$$\mathcal{P}f : \Re^N \rightarrow \Re^{N-1} \tag{1.5}$$

where the orientation of the projection process may be obtained by the orthogonal transformation A of co-ordinates in $\Re^N$. This transformation is given as [5]:

$$\widehat{\mathbf{t}} = A\mathbf{x} \tag{1.6}$$

where $\widehat{\mathbf{t}}^T = (t_1, t_2, \ldots, t_{p-1}, t_p, t_{p+1}, \ldots t_N) \in \Re^N$. Several geometries of the projection mapping are available [6,7]. However, a widely used form involves $f(\mathbf{x})$ being projected on to the hyperplane $\mathbf{t}$ such that $t_p\mathbf{e}_p$ is perpendicular to $\mathbf{t}$ where $\mathbf{e}_p$ is an $(N-1)$–dimensional vector whose p_{th} element is 1 and others are identically zero. Under these conditions, the mapping of (1.5) may be explicitly written as

$$P(t_p; \mathbf{t}) = \int_{\mathcal{V}} f(A^T\widehat{\mathbf{t}})\, dt_p \tag{1.7}$$

The collection of such mappings over different co-ordinate transformations A in $\Re^N$ constitutes the projection domain information of $f(\mathbf{x})$. Fig. 1.1 depicts the geometry of the projection operation of (1.7) for the case $N = 2$. The form of A is also shown to be a function of angular displacement between $\widehat{\mathbf{t}}$ and $\mathbf{x}$.

1.3.2 Generalized Concept of PDC

The generalized concept of PDC may be established by the respective definitions of its two related but distinct forms which have been named as **mode 1 PDC** and **mode 2 PDC**, respectively.

A mode 1 PDC system is one in which information available in a number M of $(N-1)$–dimensional projection spaces is compressed by exploiting the redundancy within and/or between the spaces prior to a reconstruction of the corresponding N–dimensional function from the M projection spaces.

Mode 2 PDC may be conceived of as a scheme in which image information within N–dimensional space is projected on to a number, M,of $(N-1)$–dimensional projection spaces to enable $(N-1)$–dimensional compression techniques to be applied to the spaces. Compression may however be effected on an inter–space basis if redundancy permits. A compressed version of the image information is reconstructed from the M compressed $(N-1)$–dimensional projections.

The implications of these definitions are that mode 1 PDC systems would be relevant to applications in which information is *originally* available in projected form and apriori knowledge of the image information is not necessarily available while mode 2 PDC systems would be configured to compress *given* image information by transformation to the projection domain.

It is important to note that there is an intrinsic problem of reconstruction from projected information. This is an inexact inversion problem that evolves when the respective hyperplanes $\mathbf{t}$ and $\mathbf{x}$ on which $P(t_p;\mathbf{t})$ and $f(\mathbf{x})$ are defined, are only specified at discrete locations in $\Re^{N-1}$ and $\Re^{N}$, respectively and when only a finite number of projections are available. This problem, outlined in chapter two, therefore adds a further fidelity constraint on the projection domain compressor as the reconstruction process itself produces distortion. Some motivating factors for the development of PDC are duly outlined.

1. The projection mapping is intrinsically an integration one and may therefore be viewed as a low pass filtering operation in the image domain, which may in turn lead to substantial redundancy in the projection domain. The high redundancy may permit considerable compression.
2. The mapping, by definition and in respect of mode 2 PDC in particular, effectively allows a reduction of dimensionality of the compression problem. Clearly, more gains of compression are realized from the use of fewer projections.
3. Several analytical relationships exist between projection domain information and image domain data; they may serve as useful structures for the development of PDC schemes.
4. The theory and implementation of image reconstruction from projections has been well developed and therefore PDC may be suitably incorporated into tomographic applications which employ such background.
5. The possibility of dual application of PDC to tomographic and image processing environments is an attractive feature of PDC. Potential applications and further implications for mode 1 and 2 PDC are discussed in the following sections.

1.4 Mode 1 PDC and Potential Applications

Mode 1 PDC is viable for applications in which information is intrinsically generated in the projection domain prior to a non–trivial image reconstruction. Some of these applications which may be generally classified as tomographic ones, include medical diagnostic imaging [8], radio astronomy [9], geophysical prospecting [10] and non–destructive testing [11]. These techniques all employ, in varied forms, the well developed computer aided tomography (CAT or CT) as a tool of reconstruction of some image distribution function. CAT is essentially a practical implementation, based on digital computational procedures of theoretical formulae, for inverting the projection mapping (equation 1.7). The major benefit of CT (and hence projection domain data generation and processing) is the ability to view internal structure of a 3–D body on a cross-sectional plane (of any orientation in the body) in image form, without invasive examination of the body. However, the type of this image form differs for various applications and ranges from the spatial distribution of tissue structure in medical imaging [8] to brightness and electron density distributions in radio astronomy [12].

It is known that the data generated in these tomographic applications reaches tremendous levels [1,8] and therefore PDC will serve as an effective procedure for controlling the data in a transmission or storage process before image reconstruction at some reception or retrieval point. The block diagram of fig. 1.2 shows a general set–up for the mode 1 PDC system. In most tomographic applications, the projection generation and reconstruction procedures are physically located on the same site. In this instance, the additional expense of the compressor could be limited to the cost of special purpose hardware (for carrying out the compression functions) and would therefore not substantially increase the overall costs of the tomographic hardware whose scanning technology (projection generation) is generally sophisticated [8] and would most probably account for a greater part of the costs.

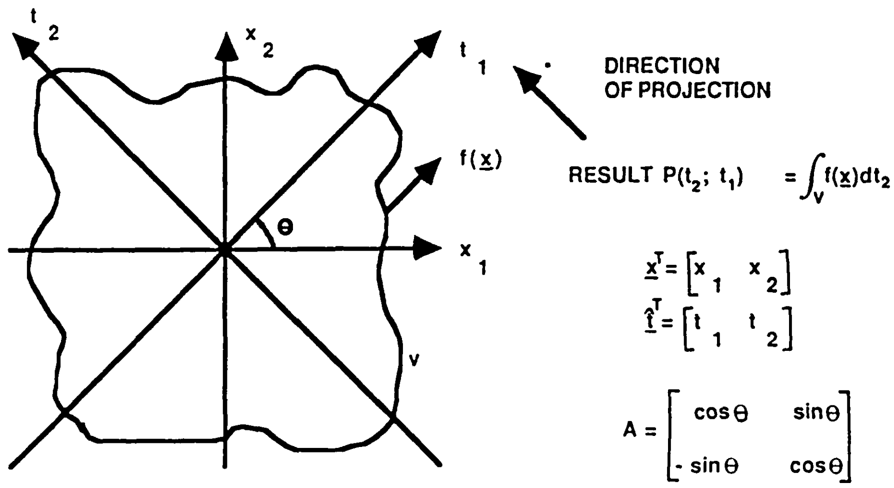

FIG. 1.1 A CO-ORDINATE GEOMETRY FOR PROJECTING $f(\underline{x})$ in R^2 ONTO R.

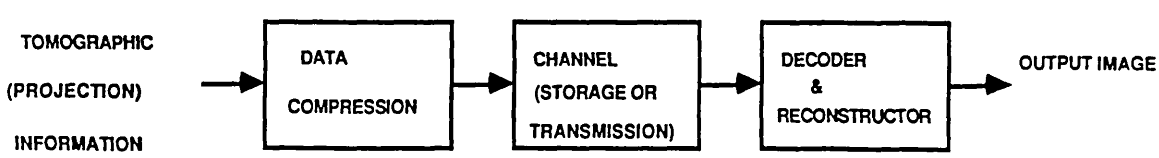

FIG 1.2: BASIC BLOCK DIAGRAM FOR MODE 1 PDC.

An on–site system which includes projection generation, compression and reconstruction facilities is particularly relevant when the reconstructions are not required to be instantaneous (i.e. there is no time constraint between tomographic information generation and reconstruction). This is often the specification in medical diagnostic imaging when a biologist or physician needs to mathematically section a large volume of projected information (possibly corresponding to a volume of a vital anatomical organ) in order to explore a biological process or make possible clinical diagnosis from the reconstructions of the section. This inadvertently requires some efficient form of storage, through data compression, which is definitely practicable for a state of the art projection system such as the dynamic spatial reconstructor (DSR) at Mayo clinic [8], which is known to generate up to 112 2–D projections every 60ms for cardiac or respiratory organ observations.

The versatility of the basic tomographic system, coupled with efficient compression, may be considerably enhanced if the site of reconstruction differs from that of projection generation. Depending on the costs, various types of tomographic system architectures are tenable. We consider a few.

1.4.1 Possible Architectures for Tomographic Systems with Mode 1 PDC

1.4.1.1 Multi–Projection Generation Single Reconstruction System (MPSGR)

A possible configuration of this structure is shown in fig. 1.3a. Here, scanning machines at various data sites may share the resource of a common reconstructor (usually a high speed computer) via a remote link. Image reconstructions of projections (that have been suitably compressed before transmission or storage at the generation sites) may be buffered and transmitted via an image coder back to the reconstruction sites. This architecture is advantageous when the technological or economic resources for projection generation outweigh those of the computational

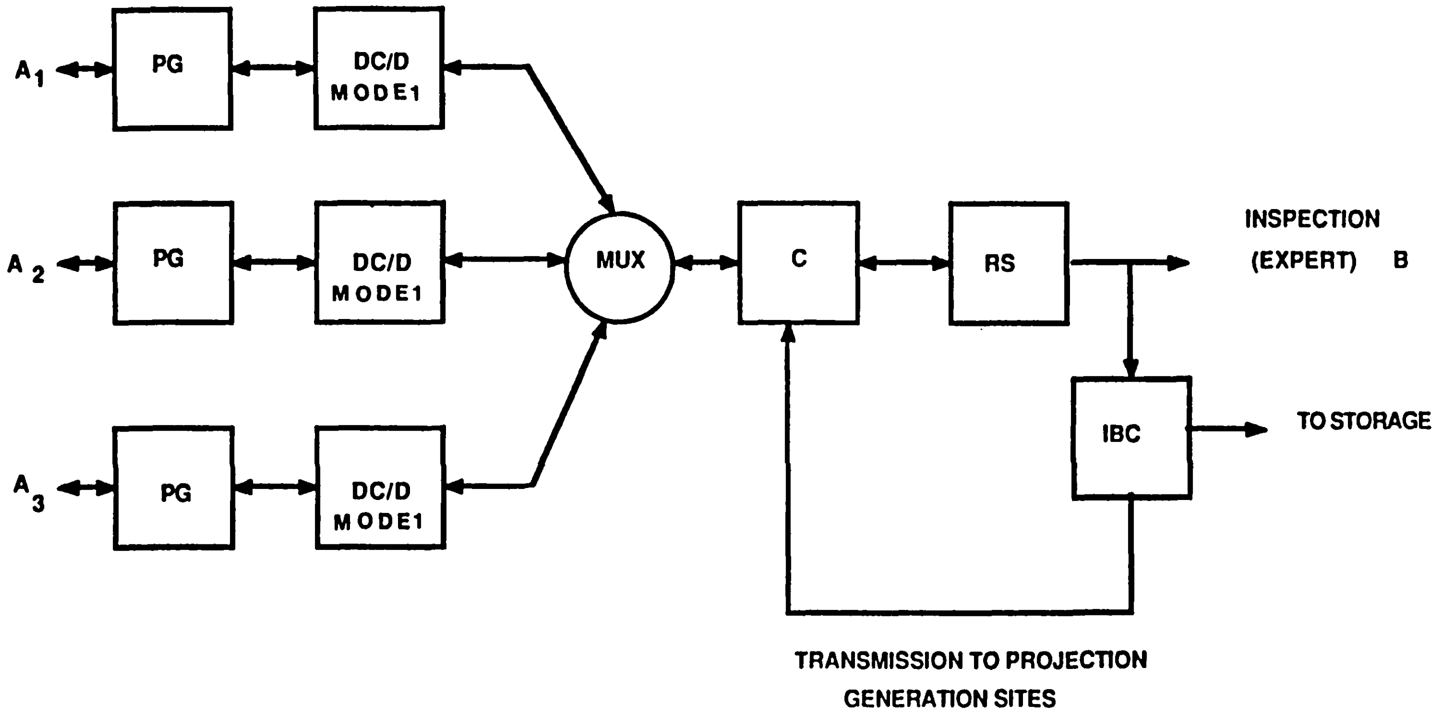

PG - PROJECTION GENERATION SITE
DC/D - DATA COMPRESSOR (FORWARD PATH)
DECODER (REVERSE PATH)
MUX - MULTIPLEXER
C - CHANNEL
RS - RECONSTRUCTION SITE
IBC - IMAGE BUFFER AND COMPRESSOR

FIG 1.3a POSSIBLE ARCHITECTURE FOR MULTI-PROJECTION GENERATOR SINGLE RECONSTRUCTOR SYSTEM facilities for reconstruction. Moreover, an expert interpreter (e.g. specialist physician, geologist or astronomer) situated at B (in fig 1.3a) may offer worthwhile advice on the reconstructed imagery to fellow workers at the data gathering sites (at A).

Depending on the application (medical, geophysical, astronomical etc), the system may be part of a local area network (LAN) or a wider area network (WAN).

1.4.1.2 Single Projection Generation Multi–Reconstruction System (SPGMR)

It appears that with the current advancement of VLSI design [13], the SPGMR (fig. 1.3b) is a more realistic architecture than the MPSGR as most of the reconstruction facilities (the computer and image display systems) would be electronic rather than the larger and more expensive mechanical structures required in state of the art scanning systems [8]. Compression of the projections is still of importance for onward transmission through the bandwidth limited links. The development of data communications between computers may also provide a means of rapid dissemination of reconstructed information, between users at various reconstruction sites, about a subject (e.g. anatomical feature, geophysical area or astronomical body) scanned at A.

1.4.1.3 Multi–Projection Generation Multi–Reconstruction System (MPGMR)

An MPGMR system obviously offers the potential for more flexibility and applicability than the MPGSR and SPGMR schemes, respectively, however the complexity and expense would clearly increase.

1.5 Mode 2 PDC : Image Compression Potential

A mode 2 PDC system, shown in fig. 1.4, operates as typical image compressor. The objective of the system is to compress an image subject to an image based fidelity criterion. The advantages of a mode 2 system will largely depend on how few the number of projections can be to sufficiently represent an image within some

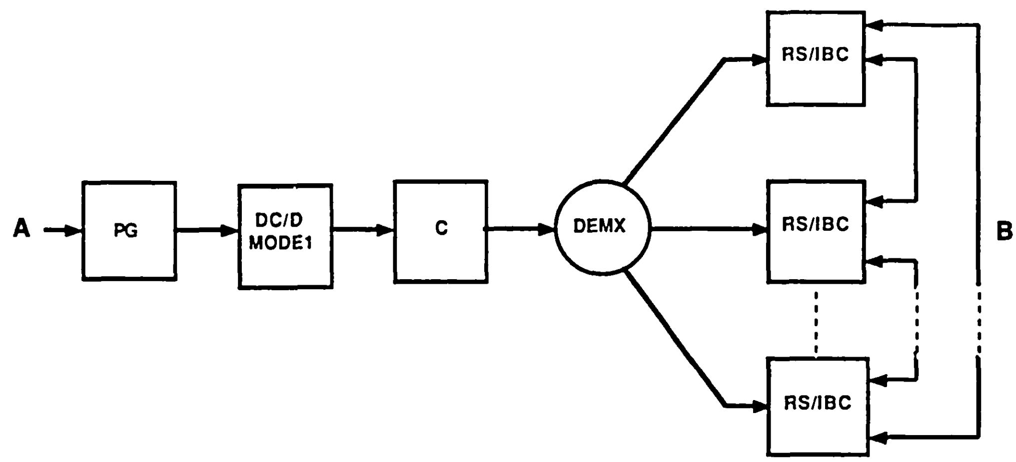

DEMX - DEMULTIPLEXER

FIG 1.3b POSSIBLE ARCHITECTURE FOR SINGLE PROJECTION GENERATOR
MULTI-RECONSTRUCTOR SYSTEM

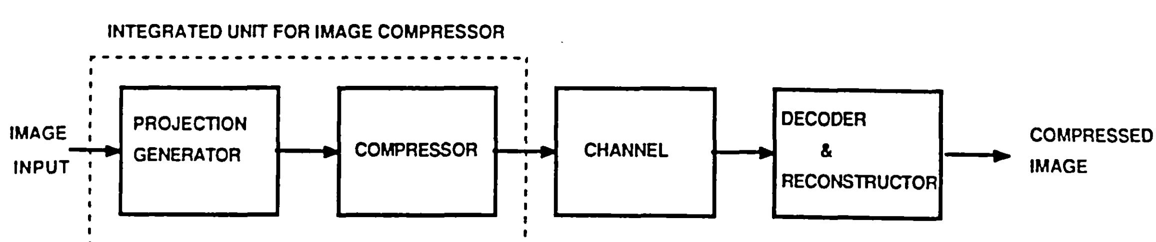

FIG. 1.4 BASIC MODE 2 PDC SYSTEM

acceptable quality of reconstruction. A means of systematically determining the number of projections per image field is discussed in chapter five.

Of importance to the mode 2 system, is the requirement for a fast means of projection generation; such a procedure, described by Fraser et al [14], involves a simulation of a simple optical arrangement that exploits a key Fourier domain relationship between the projected data and its corresponding image form; this relationship may also be employed in the reconstruction procedure.

1.6 Previous Work on Projection Based Compression

Although the explicit definitions of mode 1 and 2 PDC given in the preceding section are unique to this study, there have been a few workers who have conducted some data compression experiments in the projection domain. Jain and Jain [15] have implemented a 3–D transform coding procedure for compresssing a set of 2–D projections of a dog's thorax. According to our definitions, this corresponds to a mode 1 PDC application. They report high compression ratios of the order of 16 and 200 which are reasonable values on account of the exceptional redundancy observed from the projection images (corresponding to X–ray pictures) and the relatively low detail in the final reconstructions.

A first time application of the powerful vector quantization (VQ) technique for compression of projections [16], derived from a head and shoulder image, offers a limiting compression ratio of about 8, however a circular distortion effect was quite noticeable at this compression level. Subsequent improvements based on VQ processing are reported in chapter four.

From a brief examination of the subjective effects of varying the number of projections, the number of samples per projection and the number of bits per sample, respectively, on the visual quality of an image, Mersereau [17] suggested that the principles of tomography may be employed for picture compression as images of reasonable quality could be reconstructed from a relatively small number of projections. In effect, this was a basis for applying PDC in a mode 2 environment.

Using a Fourier based approach for projection generation, Fraser et al [14] also observed that reasonable picture compression is obtained by using a few projections (of the order of 100) in compressing various pictures, each having 256×256 picture elements. The limiting bit rate is 1.1 bits/pixel. Although they use a digital computer simulation, they emphasize that the projection generation process may be carried out by an incoherent optical system. The compression (quantization) is done in the Fourier space of projection data which theoretically corresponds to the Fourier domain of the original image. They argue that a simple re–arrangement of optical components can facilitate an optical reconstruction process.

Although the subject of this thesis is data compression, it is worthwhile noting that the projection domain has been successfully employed for other applications such as written numeral recognition [18], line detection in the presence of high level additive and multiplicative noise [19], motion detection [20] and motion estimation [21] respectively.

1.7 Scope of Thesis

This thesis wishes to examine the efficacy, on an experimental and theoretical basis, of projection domain compression of image information with respect to tomographic data processing and image data processing, respectively. In accordance with this objective, various compression procedures have been developed, of which most are designed to exploit fundamental analytical relationships between projected information and the corresponding image domain data. This is thought to be the expedient approach for mode 1 PDC, in particular, as the image domain distribution is not necessarily known to the compressor. Moreover, the theoretical relationships also serve as a basis for determining fast turnaround of projection generation and image reconstruction procedures which is crucial to mode 2 PDC.

Inexact reconstruction is a problem encountered in any of the PDC modes. However, for mode 1 processing, this difficulty is reasonably viewed to be *intrinsic* to the tomographic application and is not actually under the control of the compressor. Therefore, the best procedure for the mode 1 compressor is to acknowledge the distortion that results from reconstruction and offer as much compression as possible for a total fidelity constraint conditioned on the total distortion produced by compression and reconstruction. A rate–distortion theoretic analysis is presented in the thesis which attempts to optimize the mode 1 compression process, in terms of achieving the highest compression level for the combined compression and reconstruction distortion constraint.

The reconstruction process is considered to be an integral part of the mode 2 system. The number of projections is therefore a vital parameter for the mode 2 design. The thesis presents a framework for minimizing the level of reconstruction error, based on a systematic choice of the number of projections for a given compression level.

Theoretical appraisals in this work have included entropy transformation and stochastic analyses, respectively, of projected information, derived from random image fields under idealized projection procedures; the results are essentially limiting descriptions of what can be obtained in practice. Two forms of geometries for projection generation have been considered in the theoretical discussions. One of them corresponds to the geometry of fig. 1.1 and we refer to it as the angle–radius (AR) geometry for projection mapping. The AR geometry, also known as the 'parallel–beam' geometry [22], is widely employed in medical imaging. The second form is a slope–intercept (SI) geometry which is of considerable importance in geophysical applications [10].

In the main, the channel (see figs 1.2–3) has been considered noiseless, however in a brief study, the effects of additive white noise on image reconstructions, introduced into an optimized mode 1 PDC system, are observed. A procedure for controlling the effects is outlined.

In this thesis, PDC is only studied for a projection mapping from 2–D image planes to 1-D projections and moreover, the images are pictorial in nature and can be visually interpreted according to natural scenes and objects. In all the experimental implementations, the AR–geometry has been assumed.

1.8 Outline of Thesis

Chapter two presents relevant background to PDC. Image reconstruction (from the projection domain) theory is outlined and the two classes of transform and finite-series methods of reconstruction are reviewed especially with respect to the support of PDC. Discrete modelling of the projection process is described, based on a slope–intercept Radon transform (SI–RT) and an angle–radius Radon transform (AR–RT) respectively. These projection kernels (in their discrete and continuous forms) have been used to study the respective entropy transformation properties and stochastic properties of the projection domain. Empirical measures of auto–correlation of projection data derived from the angle–radius *discrete* Radon transform (AR–DRT) are duly observed as an indication of the available redundancy within the data. Finally, classical data compression techniques are briefly reviewed in the context of their applicability within the PDC systems.

The development of data compression schemes that effectively exploit the frequency structure of projected information, especially as it relates to the frequency space of the corresponding image domain information is the subject of chapter three. These schemes include 1–D intra–projection and inter–projection compression algorithms that exploit the radial and angular frequency variations, respectively; the sensitivity of image reconstructions to mismatched quantization is also studied within the 1–D procedures. A brief comparison of these schemes with 2–D block transform compression of projection data precedes a more detailed appraisal of the 2–D frequency structure of the projection domain. This leads to the development of a so called *bow-tie* algorithm for PDC that relies on systematic shapening of the 2–D frequency space of a given projection domain.

Chapter four is concerned with the application of vector quantization (VQ) to projected information in various forms. A comprehensive review of this powerful technique, as applied to image data compression and its fundamental principles, are respectively presented. Effects of vector formation from projection data, as manifested in reconstructed pictures, are observed. A vector formation scheme that windows projection samples on an inter–projection basis enables an enhanced form of VQ processing of projection data. This procedure simultaneously improves the basic VQ design process and exploits the frequency structure of projection data. Two adaptive forms of the enhanced system are described where one is dependent on the spatial and/or energy distribution of radial frequency coefficients of projection data and the second is designed to adapt, via a multi–stage gain–shape VQ processor, to projection data derived from more than one image.

The work of chapters three and four is presented in the context of mode 1 PDC.

The fifth chapter discusses some interesting developments for mode 2 processing for which the corresponding PDC system operates as an image compressor. The Fourier based scheme of [14] is employed for simulating the projection generation and reconstruction. Projection based block coding (PBBC) of images is examined and compared with conventional Fourier transform coding. An adaptive PBBC scheme which varies the number of projections acquired from each image sub–block as a function of sub-block a.c. energy is also described.

Novel quantitative experiments for studying the error of image reconstruction from projections as a function of the number of projections generated, image auto–correlation and image size, severally and jointly, for Gauss–Markov image data, are reported. On the basis of empirical results of the experimentation, an algorithm for systematically determining the number of projections required in a mode 2 PDC system for minimization of an average error of reconstruction, is derived. A lower bound of such distortion is presented and several performance tests of the algorithm are carried out.

A rate–distortion analysis for PDC is presented in chapter six. The object is to minimize the bit rate (maximize the compression ratio) subject to constraints of compression distortion and an intrinsic reconstruction distortion (the latter not being under the control of the compressor). Lower rate–distortion bounds are derived for a generalized PDC processor and an intra–projection processor, respectively. These results are accordingly compared with practical compression levels of some of the algorithms discussed in chapter three. A variation of the intra–projection compression bound that is suitable for tomographic applications in which there is considerable uncertainty of obtaining a projection at a particular angle, is also discussed. A joint optimization procedure in which the bit rate and the intrinsic reconstruction error are minimized subject to the constraint of compression distortion, is briefly described. A demonstration of the algorithm is shown when the reconstruction distortion is assumed to include additive white Gaussian channel noise.

Conclusions and suggestions for further work are presented in chapter seven.

Appendix I contains a unique proof of a new one projection theorem for the slope–intercept Radon transform. The main result shows a condition under which a discrete–space image can be exactly reconstructed from a finite number of projections. This is instigated by the discussion of entropy analysis in chapter two.

Appendix II contains a proof of a new slope–intercept based projection theorem for random fields and proofs of associated properties of projected information, acquired by the slope–intercept Radon transform.

Appendix III outlines the background of the information rate of Gaussian random variables; this is of importance to the rate–distortion theoretic development of chapter six.

Appendix IV briefly examines the relationship between the SI- and AR-based projection geometries for $\Re^2$ space.

CHAPTER TWO

BACKGROUND FOR PROJECTION DOMAIN COMPRESSION

2.1 Introduction

The reconstructor is a crucial feature of the projection domain compressor whatever the mode of operation and therefore the relevant background of the theory of reconstruction from an image function is introduced in Part A of the chapter. The two distinct classes of reconstruction algorithms, namely, transform and finite series methods are reviewed particularly with respect to their advantages and disadvantages in section 2.3

Section 2.4, in Part A, discusses the discrete modelling of the Radon transform which is instrumental in generating projected information. Although the Radon kernel used in this thesis assumes an angular–radial parametric form which has profound applications in medical imaging and radio astronomy, another important kernel form, dependent on intercept and slope descriptors [23], is also described. This latter representation is useful in geophysical inversion applications and has a simple discrete space formulation which serves as a guide for the description of the discrete AR–RT.

As the focus of this work is on compression, due attention is also given to the stochastic modelling of the projection domain in Part B. First, a theoretical study of the information transformation from the image domain to the projection domain, based on the two types of discrete Radon transforms, is reported in section 2.5. Then the stochastic properties of the projection domain, derived from the AR–RT kernel, are discussed in accordance with the not well known stochastic theorems of Jain and Ansari [24] in section 2.6. However, independent proofs of the results are provided here in view of their importance and the rather formal presentation of [24]. Moreover, unique results of stochastic characterization for the SI–RT are summarized.

The results of empirical evaluation of the auto–correlation structure of projection domain data acquired from typical image functions and more random types of imagery are discussed in section 2.7.

Finally, a brief overview of compression strategies that may support PDC is given in Part C (sections 2.8 and 2.9).

PART A: Reconstruction from the Projection Domain

2.2 The Radon transform

A projection domain function $P(\theta, t)$ may be generated from an image domain function $f(x, y)$ by the angle–radius based Radon transform (AR–RT), defined as

$$P(\theta,t) = \int\int_{I} f(x,y)\,\delta(x\cos\theta + y\sin\theta - t)dx\,dy \tag{2.1}$$

which is a line integration of $f(x, y)$, forced by the dirac delta function $\delta(.)$ across the $x - y$ plane within a region I (see fig. 2.1). The radial parameter t is not the familiar polar co–ordinate radius but a perpendicular distance from the origin and in general $P(\theta_1, 0) \neq P(\theta_2, 0)$ for $\theta_1 \neq \theta_2$.

The function $f(x, y)$ may be exactly retrieved from the inversion formula of Radon [6], specified as

$$f(x,y) = \int_0^{\pi} H\left(\frac{\partial P(\theta,t)}{\partial t}\right)d\theta \tag{2.2a}$$

with the Hilbert transform

$$H(h(\theta,t)) = -\frac{1}{\pi}\int_a^b \frac{h(\theta,s)}{t-s}ds \tag{2.2b}$$

for $t \in [a, b]$. A full derivation of (2.2a) is found in [25] and shall not be reproduced here, however, the basis of the inversion formula is considered shortly.

A more suitable form of (2.2), especially from the viewpoint of computer implementation, is

$$f(x,y) = \int_0^{\pi} \int_{-\infty}^{\infty} |\omega| P(\theta,\omega) \exp(-\jmath\omega t) d\omega\, d\theta \tag{2.3a}$$

with

$$P(\theta,\omega) = \int_a^b P(\theta,t) \exp(-\jmath\omega t) dt \tag{2.3b}$$

This formula carries out the Hilbert transformation and the differentiation in (2.2a) in the Fourier domain, respectively, and avoids potential numerical instability due to the partial differentiation. The foundation of (2.3a) (and hence 2.2a) lies in the special form of a *generalized projection theorem* [26] which is summarized by

$$\int_a^b P(\theta,t)\, \alpha(t)\, dt = \int\int_I f(x,y) \alpha(x\cos\theta + y\sin\theta) dx\, dy \tag{2.4}.$$

The theorem states that a 2–D operation $\alpha(.)$ in the image domain is equivalent to the 1–D radial application of $\alpha(.)$ in the projection domain on an angle θ.

When $\alpha(t) = \exp(-\jmath\omega t)$, equation (2.4) becomes

$$\int_a^b P(\theta,t) \exp(-\jmath\omega t) dt = \int\int_I f(x,y)\ \exp(-\jmath\omega(x\cos\theta + y\sin\theta))\, dx\, dy \tag{2.5a}$$

or

$$P(\theta,\omega) = F(\omega_x,\omega_y) \tag{2.5b}$$

where $\omega_x = \omega\cos\theta$, $\omega_y = \omega\sin\theta$. The above relation, otherwise known as the *projection-slice theorem*, claims that the Fourier transform of a projection with respect to the radial variable is equivalent to an *angular slice* of the 2–D Fourier transform $F(\omega_x,\omega_y)$ of the image function from which the projection is generated. This correspondence is shown geometrically in fig 2.2.

The bearing of (2.5) on (2.3) is implicit as $f(x,y)$ is effectively obtained by (continuous) addition or backprojection, over θ, of the angular slices of the 2–D transform of $f(x,y)$.

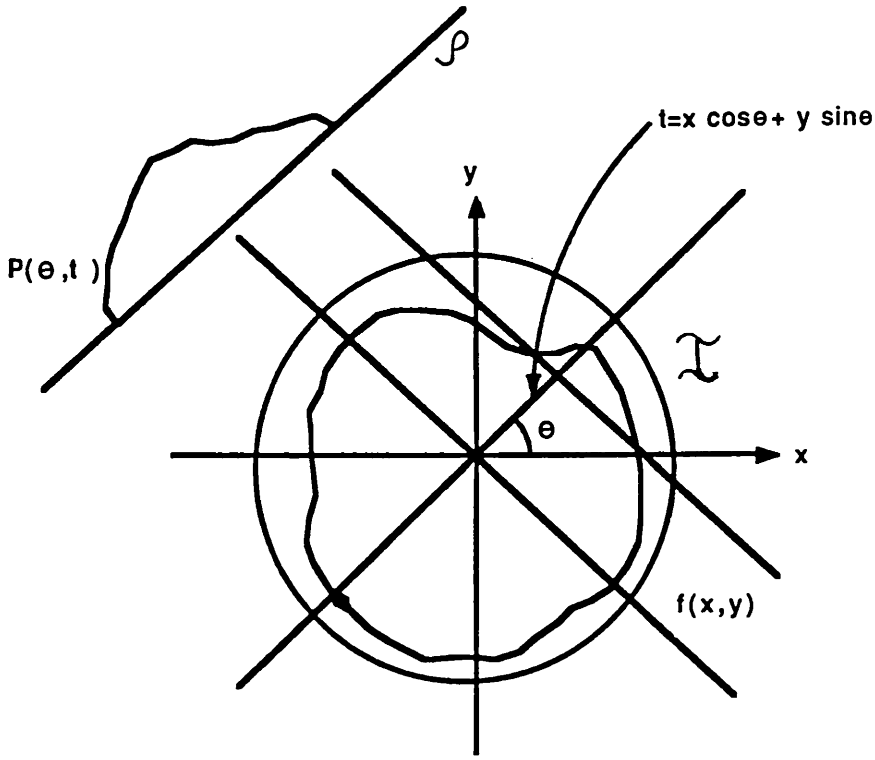

FIG. 2.1 GEOMETRY FOR GENERATING A PROJECTION P(θ,t) FROM f(x,y) ON ANGLE θ. $\mathcal{P}$ AND $\mathcal{I}$ ARE THE RESPECTIVE DOMAINS OF P(θ,t) AND f(x,y).

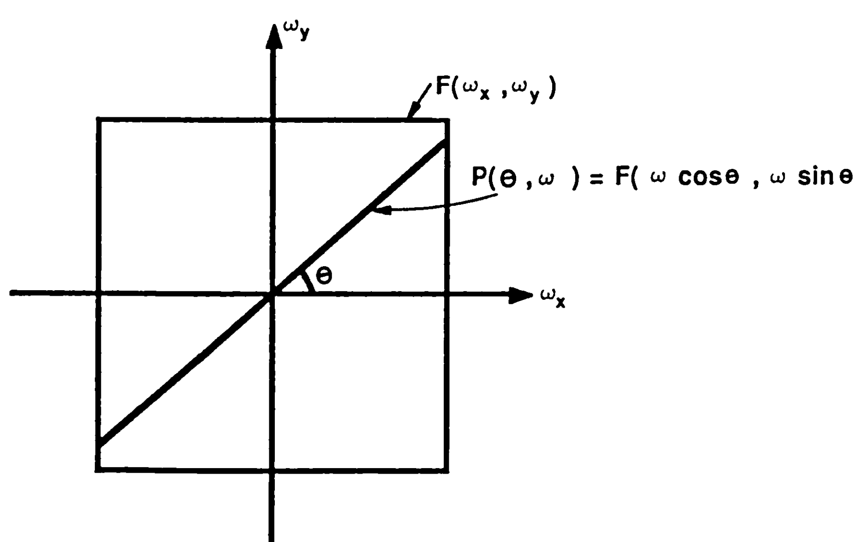

FIG. 2.2 THE PROJECTION-SLICE THEOREM GEOMETRY : THE RADIAL FOURIER TRANSFORM $P(\theta, \omega)$ OF $P(\theta, t)$ IS A SLICE OF THE TWO DIMENSIONAL FOURIER PLANE $F(\omega_x, \omega_y)$ OF f(x,y) ON ANGLE θ .

2.3 Reconstruction Techniques

An image function $f(x, y)$ may be unambiguously determined if the corresponding projection domain function $P(\theta, t)$ is known for a continuum of parameter values in the respective ranges $\theta \in [0, \pi)$ and $t \in [a, b]$ ($[a, b]$ is the radial interval bounding the region in I in which $f(x, y)$ is defined). This is evident from the projection–slice theorem as the Fourier space of $f(x, y)$ is completely specified if an infinite number of transformed projections are available. However, for practical applications $P(\theta, t)$ is only known for a discrete and finite number of values of t and θ.

Other problems associated with discretization tend to be dependent on the technique of reconstruction. The algorithms for image reconstruction from projection data may be classified into two distinct categories of *transform methods* [26] and *finite series* methods [27]. The schemes of the first category exploit analytical forms and variations of the general reconstruction formula (2.3) where the angular radial variables are discretized solely for computational purposes. The second set of strategies formulate the reconstruction problem, from the onset, as a discrete–space one and in general, a system of algebraic–linear equations, constrained by various optimization criteria, have to be solved to obtain an approximate image function.

The projection domain compression algorithms, developed in this thesis, have favoured the use of transform methods due to their relative amenability to software, hardware and faster implementation in comparison to finite series techniques, as the latter methods are predominantly iterative in nature. Therefore, while the finite series aproach is briefly discussed, more emphasis is placed on the transform approach.

2.3.1 Transform Methods

2.3.1.1 Convolution Backprojection (CBP)

Convolution backprojection is a transform method that is a direct implementation of the Radon inversion formula (2.3) which is decomposable into the Fourier domain operation for projection filtering by $|\omega|$ and the backprojection step, respectively.

The backprojection associates a point (x, y) within the region I with all convolved projection samples $Q(\theta, t) = H(\partial P(\theta, t)/\partial t)$ where all the $P(\theta, t)$ had contributions from the point in the forward Radon transformation of (2.1). In particular, for a given line integral location $t' = x \cos\theta' + y \sin\theta'$, all associated points (x, y) have identical backprojection values from the filtered projection sample $Q(\theta', t')$.

Discrete execution of (2.3) necessarily requires an adequately sampled structure for each projection. The adequacy of sampling is theoretically ensured by imposing Nyquist constraints on the radial sampling interval Δt such that $\Delta t < \pi/B_t$ where B_t is the band–limitation on the radial frequency ω. The problem with this approach is that the band–limitation corrupts the reconstruction since $f(x, y)$ (and hence $P(\theta, t)$ is a spatially limited function and therefore cannot also be band–limited [28]. A typical modification of (2.3), in view of the preceding argument, is [26]:

$$f_B(x, y) = \int_0^{\pi} \int_{-\pi/B_t}^{\pi/B_t} H_B(\omega) \exp(\jmath\omega(x \cos\theta + y \sin\theta))P(\theta, \omega)d\omega\, d\theta, \quad (2.6a)$$

where $H_B(\omega)$ is a band-limiting window such that

$$H_B(\omega) = 0, \qquad |\omega| > \frac{\pi}{B_t} \qquad (2.6b).$$

This is an indication that CBP can do no better than produce a band–limited version of $f(x, y)$ that is, $f_B(x, y)$. The band–limiting function also serves a useful purpose in windowing potential wideband noise which would be inadvertently amplified by $|\omega|$ in the reconstruction process. The choice of $H_B(\omega)$ is of importance to the performance of CBP as different windows clearly lead to different convolution functions $H_B(\omega)\,|\omega|$ for the reconstruction. Various types of window functions will be considered shortly.

The discretization of the angular parameter in the projection domain is normally carried out by uniform sampling over the complete angular range $[0, \pi)$ in I. Therefore, in specifying the desired number of projections to be used in reconstruction as M_θ, the angular sampling interval is $\Delta\theta = \pi/M_\theta$.

In most applications, the plane in I is sampled for computational purposes and (2.6) is accordingly reformulated as follows [25,26]:

$$f_B(m\Delta x, n\Delta y) = \Delta\theta \sum_{k=0}^{M_\theta - 1} \widehat{Q}(k\Delta\theta, t') \tag{2.7a}$$

for $t' = m\Delta x \cos k\Delta\theta + n \sin k\Delta\theta$, $0 \leq k \leq M_\theta - 1$, $M_- \leq m \leq M_+$ and $N_- \leq n \leq N_+$ where in general

$$\begin{aligned} J_+ &= \frac{(J-1)}{2} \\ J_- &= -\frac{(J-1)}{2} \end{aligned} \tag{2.7b}$$

when J is odd and

$$\begin{aligned} J_+ &= \frac{J}{2} - 1 \\ J_- &= -\frac{J}{2} \end{aligned} \tag{2.7c}$$

when J is even, J being an integer. The function $\widehat{Q}(k\Delta\theta, t')$ is obtained in a two–step process of convolution:

$$Q(k\Delta\theta, l\Delta t) = \Delta t \sum_{l'=L_-}^{L_+} P(k\Delta, l'\Delta t)\, h((l-l')\Delta t) \tag{2.7d},$$

for $0 \leq k \leq M_\theta - 1$ and $L_- \leq l \leq L_+$, and interpolation

$$\widehat{Q}(k\Delta\theta, t') = \Delta t \sum_{l=L_-}^{L_+} Q(k\Delta\theta, l\Delta t)\, I(t' - l\Delta t) \tag{2.7e}$$

where $h(l)$ is a spatial domain discrete–space representation of the Fourier domain kernel $H_B(\omega)\,|\omega|$ and $I(t')$ is a data independent interpolation function that provides the backprojection in (2.7a) with interpolated values, at t' in the radial specification, that would otherwise correspond to line integrations passing through the sample locations $(x, y) = (m\Delta x, n\Delta y)$ in I. It is interesting to note that the trapezoidal approximation of (2.7a) to the backprojection integral in (2.6) is an optimal quadrature procedure when the projection domain is sampled on a uniform basis in the angular parameter [25].

2.3.1.1.1 Discrete Convolution Functions

Several discrete convolution functions have been proposed in the literature [25,29,30, 31]. Most of these functions can be obtained, indirectly, by modelling a Fourier domain function $D_g(\omega)$ as a replicated version of $D_h(\omega) = H_B(\omega)\,|\omega|$, that is

$$D_g(\omega) = \frac{1}{\Delta t}\sum_{m=-\infty}^{\infty} D_h(\omega + \frac{2\pi m}{\Delta t}) \qquad (2.8).$$

The periodicity of $D_g(\omega)$ (with period $2\pi/\Delta t$) permits a Fourier series representation of the form:

$$D_g(\omega) = \sum_{l=-\infty}^{\infty} h(l)\exp(-\jmath l\Delta t\omega) \qquad (2.9)$$

and therefore coefficients of the series which correspond to the required convolution function samples are:

$$h(l) = \frac{\Delta t}{2\pi}\int_{-\frac{\pi}{\Delta t}}^{\frac{\pi}{\Delta t}} D_g(\omega)\,\exp(\jmath l\Delta t\omega)\,d\omega \qquad (2.10).$$

Alternatively, band-limiting $D_g(\omega)$ to $|\omega| \le B_t = \pi/\Delta t$ and sampling the inverse transform of the band-limited $D_g(\omega)$ would also yield the function $h(l)$.

Some interesting forms of $h(l)$ and the equivalent Fourier domain functions for normalized frequency $\omega' = \omega/2\Delta\pi$ are listed in table 2.1. The first convolution function corresponds to the so called Shepp–Logan filter [29] and a close examination of its frequency domain form, indicates that it is effectively a low pass filter attenuating frequency contributions near $\omega' = 1/2\Delta t$. The filter proposed by Bracewell and Riddle [30] is a band-limiting one which removes the frequencies between $C/2\Delta t$ and $1/2\Delta t$, where C is the proportion of spectrum passed by the filter. Incidentally, this convoluting function is the same as that employed by Ramachandran and Lakshminarayanan [31] for $C = 1$; this filter shall be referred to as the RAM–LAK filter for convenience. The third filter which may be obtained by a convolution of the respective spatial domain representations of $|\omega'|$ and the generalized Hamming window, has been used by Chesler and Riederer [32]. Interestingly, the three point running average structure of the Hamming window has been used for minimizing

	Discrete Convolution Function	Frequency Domain Form
Used/Proposed by:	$h(l)$	$D_h(\omega') = \lvert\omega'\rvert H_I(\omega')$
Shepp & Logan [29]	$\frac{2}{\pi^2 \Delta t(1-4l^2)}$	$\lvert\omega'\rvert \operatorname{sinc}(\omega'\Delta t)\operatorname{rect}(\omega'\Delta t)$
Bracewell & Riddle [30]	$\frac{C^2}{4\Delta t}[2\operatorname{sinc}(Cl) - \operatorname{sinc}^2(\frac{Cl}{2})]$ $0 \le C \le 1$	$\lvert\omega'\rvert \operatorname{rect}(\frac{\omega'\Delta t}{C})$ $0 \le C \le 1$
Chesler & Riederer [32]	$A(l) * H_\alpha(l)$ $A(l) = \operatorname{sinc}^2(\frac{l}{2})$ $H_\alpha(l) = \begin{matrix} \alpha, & l = 0 \\ \frac{1-\alpha}{2}, & \lvert l\rvert = 1 \\ 0, & \text{otherwise} \end{matrix}$ $0 \le \alpha \le 1$	$\lvert\omega'\rvert [\alpha + (1-\alpha)\cos(\omega'\Delta t)]$ $\cdot \operatorname{rect}(\omega'\Delta t))$ $0 \le \alpha \le 1$

$$\operatorname{sinc}(x) = \frac{\sin x}{x} \qquad \operatorname{rect}(x) = \begin{cases} 1, & \lvert x\rvert \le \frac{1}{2} \\ 0, & \lvert x\rvert \ge \frac{1}{2} \end{cases}$$

Table 2.1 Some typical discrete convolution functions that are used in the CBP algorithm the effect of additive white noise in projections for any filter and interpolation combination.

2.3.1.1.2 Interpolation Approaches

Band-limited or sinc interpolation is the most effective form of generating projection samples at required radial locations for the discrete backprojection of (2.7) when the radial parameter has been sampled under Nyquist constraints. However, Lagrange interpolation is preferred [25] due to its relative ease of implementation. Also, in the limit of a large number of pivot points (pre-interpolation samples), it is known to approach sinc interpolation. In accordance with the notation used hitherto, an l^{th} order Lagrange basis function for interpolation in (2.7) may be written as [33, pg33]:

$$I(t') = L_l(t') = \frac{1}{\Delta t} \prod_{m=M_-}^{M^+} \frac{(t' - m\Delta t)}{(l - m)} \tag{2.11}$$

for $0 \leq l \leq m$ and where

$$I(t')|_{t'=m\Delta t} = L_l(m\Delta t) = \delta_{lm} = \begin{cases} 1 & l = m \\ 0 & l \neq m \end{cases} \tag{2.12}$$

is valid. Of note, are one and two point Lagrange interpolators which respectively result in the well known zeroth order and linear interpolation methods [25].

2.3.1.2 Fourier Inversion

Fourier inversion is an important transform method of reconstruction, based on the projection slice theorem (2.5). This inversion is implicit, as the theorem effectively stipulates that the Fourier space of the image domain may be generated from the Fourier transforms of the projections of the image. For discrete–space processing, an image is generated by an inverse 2–D discrete Fourier transform (DFT) of its Fourier domain. The image DFT coefficients are located at points on a cartesian grid, however, the discrete frequency space of the associated projection data is specified by points on a polar grid (see fig. 2.3a). Therefore, the major problem of the Fourier inversion approach is one of interpolation from the known polar co–ordinate samples to the unknown cartesian points. This is depicted in fig. 2.3b.

Sophisticated interpolation methods may be employed, however, computational expense typically limits the approaches to one or two point Lagrange interpolation [5]. The 2–D planar processing actually requires the 1–D linear interpolation formula to be applied twice in succession, hence, a bilinear interpolation of four points is performed for a cartesian point $(X, Y) = (\omega \cos\theta, \omega \sin\theta)$, as seen in fig. 2.3b, from $P(\theta_k, l\Delta\omega)$, $P(\theta_k, (l+1)\omega)$, $P(\theta_{k+1}, l\Delta\omega)$ and $P(\theta_{k+1}(l+1)\Delta\omega)$ for $\theta_k \leq \theta \leq \theta_{k+1}$ and $l\Delta\omega \leq \omega \leq (l+1)\Delta\omega$ for some integer l.

The polar grid sampling represents an inefficient use of the Fourier domain of the image as samples near the origin are more densely packed than those in the outer radial regions. Consequently, the error of interpolation increases for points further away from the origin.

Mersereau and Oppenheim [5] have proposed a polar expansion scheme and a concentric squares representation, respectively, of 1–D frequency transformed projections for improving the Fourier inversion. The first procedure increases the number of Fourier slices (hence projections) by band–limited (sinc) interpolation prior to bilinear interpolation from polar to cartesian co–ordinates. The second scheme relies on sampling projections such that the overall distribution of their Fourier points may describe a concentric squares formation rather than the concentric circles representation of fig. 2.3a. Interpolation from the concentric squares raster to the desired cartesian locations may be accomplished by 1–D horizontal or vertical schemes rather than a radial and angular approach required by the polar grid. In addition, corresponding Fourier coefficients on each projection are not separated by large circular distances in outer radial positions, but by straight lines. Improvements of the concentric squares formulation may be obtained by a concentric squares expansion in a similar manner to polar expansion [5].

A modified polar grid representation of the Fourier coefficients is also described by Lewitt [26]. In an effort to improve the polar sampling, coefficients are offset on

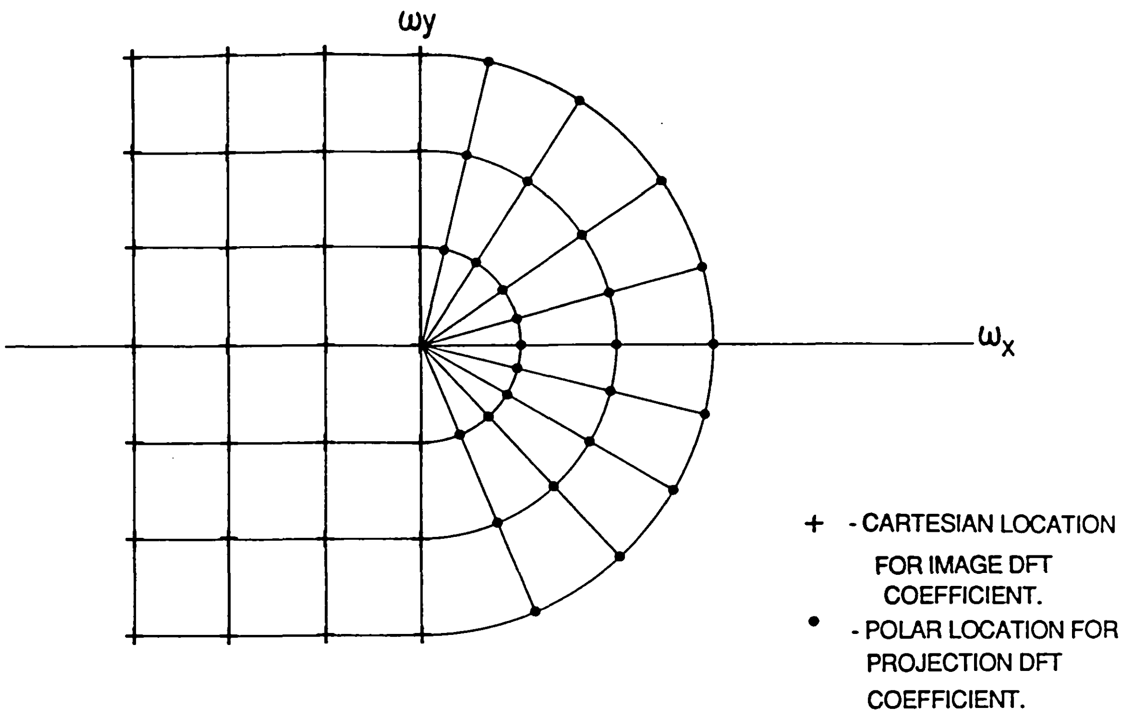

FIG. 2.3a HALF - PLANES OF CARTESIAN AND POLAR GRIDS, DEPICTING THE LOCATIONS OF THE DISCRETE FOURIER SPACE COEFFICIENTS OF THE IMAGE 2-D DFT AND THE PROJECTION 1-D DFTS.

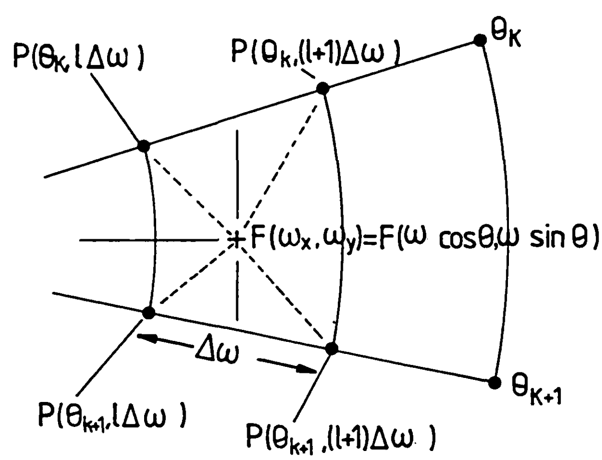

FIG. 2.3b GEOMETRY FOR INTERPOLATION IN THE FOURIER SPACE FROM FOUR LOCATIONS OF PROJECTION DFT COEFFICIENTS TO A DESIRED CARTESIAN LOCATION $(\omega_x, \omega_y) = (\omega \cos\theta, \omega \sin\theta)$; $l\Delta\omega < \omega < (l+1)\Delta\omega$ AND $\theta_k < \theta_k < \theta_{k+1}$.

alternate Fourier slices to produce a pattern in which the average distance between Fourier samples is considerably reduced, compared to the separation between their polar locations as shown in fig 2.3a. This improves the interpolation to cartesian locations.

In comparison to CBP, it appears that Fourier inversion is inferior and less dominant in applications that require reconstruction from the projection domain. The relative simplicity of CBP and its potential of producing good reconstructions are factors that account for its prolific use [22,26,27]. Nevertheless, the Fourier method potentially involves less computation for reconstruction than CBP due to the availability of fast Fourier transformations.

The effects of interpolation error are more severe for Fourier inversion than CBP [26]. This is more so when the Fourier domain is quite oscillatory in character, when local smoothing or interpolation produces sharp fluctuations in the domain which will be translated into spurious and possibly aliased (depending on how undersampled the Fourier domain is) features in the image domain. Inexact interpolation in CBP algorithms is manifested in the image domain both as additional smoothing and spurious effects due to piecewise lower order interpolation, although the smoothing may be considered to be an integral part of the reconstruction process since the windows used in the convolution kernels are effectively smoothing filters. The spurious effects are also controllable by the choice of window, as discussed earlier.

2.3.1.3 Other Transform Methods

Some other reconstruction techniques that may be classified as transform methods, since they depend on explicit analytical representation prior to discretization, are the Rho–filtered Layergram method [25,26] and reconstruction by using *annular* harmonics and polynomial fits to projections, respectively [22].

The Rho–filtered layergram (RHL) approach is also based on the Fourier projection slice theorem and its operations are similar to those of CBP, however, they are applied in reverse order. That is, the backprojection is followed by 2–D spatial filtering. The RHL operations are, however, better implemented by optical processors rather than digital computers, as in order to avoid aliasing in the reconstructed picture, the dimensions of the intermediate arrays must be much larger than the dimensions of the final picture. Moreover, the 2–D spatial image filtering is clearly more difficult to implement than the 1–D radial filtering of CBP in the projection domain.

The respective annular harmonics and polynomial fitting methods essentially depend on computing coefficients of infinite expansions and using the expansions to synthesize reconstructions of the final image [26] and are similar to the non–iterative finite series expansion schemes to be discussed in the next section.

2.3.2 Finite Series Expansion Reconstruction Methods (FSER)

FSER is generally characterized as finding a vector solution $\mathbf{X}$ to the approximate relation

$$\mathbf{Y} \simeq R\mathbf{X} \tag{2.13}$$

where R is some transformation soon to be described [6,22,27] and $\mathbf{Y}$ is a measurement vector. The vector $\mathbf{X} = [x_1, x_2, \ldots, x_J]^T$ may be considered to be an image vector whose samples are distributed on a square grid format over a continuous space image function $f(r, \phi)$ (defined with respect to polar co–ordinates).

The image vector samples or pixels, together with a set of basis pictures $B = [b_1(r,\phi), b_2(r,\phi), \ldots, b_J(r,\phi)]^T$, may define a so called $n \times n$ digitization $\hat{f}(r,\phi)$ of $f(r,\phi)$ for $J = n^2$, which is expressed as

$$\hat{f}(r,\phi) = B^T\mathbf{X} \qquad (2.14).$$

Each member R_i of a set $\{R_1, R_2, \ldots, R_I\}$ of linear and continuous functionals is considered to operate on (2.14) in the fashion

$$R_i\hat{f} = R_iB^T\mathbf{X} \tag{2.15}$$

where the continuity condition on R_i requires that [7,22]:

$$y_i = R_i f \simeq R_i \hat{f} \tag{2.16}$$

for $Y = [y_1, y_2, \ldots, y_I]^T$. The measurement vector may be viewed as a projection, derived from $f(r, \phi)$ by a corresponding projection matrix transformation R. The elements of R are seen to be $R_i b_j$ for $i \in [1, I]$, $j \in [1, I]$ by comparing (2.16) with (2.13) and (2.14), respectively.

Therefore, in summary, the FSER is a discrete reconstruction process that estimates an unknown vector $\mathbf{X}$ from a known data vector $\mathbf{Y}$ where the elements of $\mathbf{X}$ are related to a continuous image function $\hat{f}(r, \phi)$ that is a desirably close approximation to the exact image function $f(r, \phi)$. The distinguishing aspect between FSER and transform methods is that there is a discretization from the onset rather than discretization of explicit inversion formulae as is the case for transform methods.

Numerous approaches have been reported in the literature [22,27] for solving the system of linear equations based on different forms of basis functions $\{b_1, b_2, \ldots, b_J\}$ and solution concepts. A solution concept involves setting up optimization criteria or tolerance conditions on the system of equations. Its importance lies in the need to address the problems of ill–posedness of (2.13) when it is not uniquely solvable due to the sparsity of R or (2.13) being under or over determined. Moreover, if the continuity condition is violated, in which case a close approximation of $\hat{f}(r, \phi)$ to $f(r, \phi)$ is not guaranteed [7,22,27], some regularization of the equations is required, using the solution concept.

2.3.2.1 Algebraic Reconstruction Techniques (ART)

Algebraic reconstruction techniques (ART) [6,22,27] are methods in which successive iteration values $\mathbf{X}^{(k)}$ of $\mathbf{X}$ are to be obtained till the convergence to an $\mathbf{X}^*$, a reliable estimate of $\mathbf{X}$ within the limits of a given tolerance, is realized. These schemes are discussed at length in [27].

More effective variations of the basic ART formulation are developed by introducing entropy or quadratic optimization, separately or collectively constrained by (2.13). The entropy method seeks to conditionally maximize the apriori information [34,35] available about the object to be reconstructed and is useful for reconstructions from projections that are available within a limited sub–range of angles [27]. Quadratic optimization procedures include minimum variance, least squares and Bayesian estimation of the required vector $\mathbf{X}$ [22]. Rockmore and Macovski [36,37] describe, in companion papers, a maximum likelihood (minimum variance) approach to FSER using an arbitrary basis set. Their algorithm exploits the stochastic nature of projection data using the knowledge of the probability density (pdf) of the measurement of the $\mathbf{Y}$ vector. In CAT applications, this pdf is typically characterized as Poisson as a result of photon noise being registered at the detector.

2.3.2.2 Non–iterative Series Expansion

Non–iterative series expansion methods may be applied for solving (2.13) when the system of equations can be simplified by appropriate choices of the basis pictures $\{b_1, b_2, \ldots, b_J\}$. A corollary of estimating $\mathbf{X}$ from (2.13) is providing a minimum norm solution of

$$R^T R\mathbf{X} = R^T \mathbf{Y} \tag{2.17}$$

where $||\mathbf{Y} - R\mathbf{X}||^2$ is the norm. The goal of non–iterative procedures is to permit $R^T R$ to assume a simple structure such as block diagonality and to also effect a careful choice of basis vectors, for the inversion of $R^T R$. Suitable basis functions dependent on annular harmonic and polynomial decompositions, respectively, are comprehensively described in [22].

Some interesting non–iterative variations of FSER modelling are respectively considered by Davidson and Grunbaum [38] and Wood and Morf [39]. With the aim of deriving *angle dependent* reconstruction filters prior to backprojection, the first co–authors have posed the problem in a minimum norm form of (2.7). Using finite Gegenbauer polynomial decompositions of the reconstruction filters, they have secured a block diagonal reduction of $R^T R$ that in turn facilitates the solution. The second pair of workers have developed an efficient minimum variance estimation of $\mathbf{X}$ by exploiting the respective block–circulant structures of the covariance matrix of $\mathbf{Y}$ and $R^T R$.

2.3.3 FSER versus Transform Methods

As a rule, transform methods are faster image reconstructors than series–expansion methods since the most effective forms of the latter tend to be iterative and exhibit slow convergence. Moreover, the CBP techniques, in particular, are known to give very good reconstructions, compared to FSER, when substantial projection domain information is available. However, the main advantage of FSER is its inherent amenability to different applications and conditions of reconstruction.

Some non–standard situations of reconstruction are exemplified by the restricted view problems that arise in medical imaging when dosage levels or intervening bone structure limits the number of projections to very few or to be within a small angular sub–range of $[0, \pi)$ [40,41,42]. The problem may be further complicated, as obstructing structure may cause the generation of truncated or hollow projections [43,44]. Hitherto, reconstruction from the projection domain has been considered in the context of parallel beam (AR–based) projection geometry of fig. 1.1 and although CBP has been satisfactorily modified to accommodate divergent or fan beam geometries, more complex geometries and envisaged applications of tomographic reconstruction [45] may necessitate a more flexible reconstruction approach such as FSER.

It must be emphasized, however, that CBP remains the dominant technique for computerized reconstruction from the projection domain [25] and even when incomplete projections (truncated and/or hollow) are available, projection completion methods are developed to 'fill–out' the projections before CBP [43,44]. Analytical continuation is also employed before CBP to estimate the projections over the complete angular interval $[0, \pi)$ when constraints on the angular range of projection prevail [46].

2.3.4 Reconstruction Considerations for PDC

Although, in principle, PDC cannot be dissociated from the constraints (e.g. incompleteness of projections or projection angle range) of the application in which it is being utilized, we wish to assume, throughout the thesis, that we have a standard projection domain. That is, the projections have been obtained over the whole range $[0, \pi)$ and truncation or hollowness of projections are respectively non–existent. Therefore, in the light of the discussion of section 2.3.4, CBP has been employed as the reconstructor for a mode 1 configuration. Furthermore, the Shepp–Logan filter has been dominantly employed as the convoluting filter along with a two point Lagrange interpolator, on the basis of the results of an extensive reconstruction performance study of Rowland [25]. He has evaluated the performance of CBP using ten different filters respectively combined with six different Lagrange interpolators. On the basis of measures of spatial resolution and radial oscillations produced by the respective reconstructions, he observed that the RAM-LAK, Shepp–Logan and generalized Hamming ($\alpha = 0.54$) filters, each combined with a two point Lagrange interpolator gave the three best reconstructions. However from his results, it is seen that the Shepp–Logan filter, corresponding to a low–pass sinc filter, offers the best compromise between good spatial resolution and low radial oscillations.

For mode 2 processing, discussed in chapter five, we have used an 'in–place' Fourier inversion approach [14] as it offers us the flexibility of fast implementation of compression models, experimented with, in that chapter.

2.4 Discrete Modelling of the Radon Transform

The discrete form of the inverse Radon transform has been discussed in some detail in section 2.3. However, in generating the projection domain from a discretized image domain, problems of implementing the corresponding discrete Radon transform (DRT) evolve. At this stage it is informative in this section and of benefit to the succeeding one on entropy analysis (in Part B of the chapter), to briefly study a DRT that is characterized by slope and intercept variables as opposed to angular and radial specifications. This alternative representation gives substantial insight into how an angle–radius based DRT (AR–DRT) and a modified implementation of it can be described.

2.4.1 The Slope–Intercept Discrete Radon Transform

The slope–intercept Radon transform (SI–RT) is predominantly used in geophysical inversion [10] where the object is to reconstruct some 2–D space–time function (or seismic section) of a horizontally layered geophysical medium from a plane wave decomposition (projection) of the wavefields that propagate through the medium. The decomposition is often used to estimate the speed or angle at which a plane wave propagates through the geophysical structure [23]. The continuous SI–RT [10] of a seismic section $f(x,t)$ may be written as

$$P(q,\tau) = \int\int_S f(x,t)\,\delta(xq - t + \tau)\,dx\,dt \tag{2.18}$$

with q and τ being slope and intercept parameters, respectively, of the projection domain of $f(x,t)$ bounded in a region S. Equation (2.18) represents the line integration, over the space-time $(x - t)$ plane along the line $t = qx + \tau$, of $f(x,t)$. This operation is shown, diagramatically, in fig. 2.4; the slope parameter q is seen to have units of inverse velocity, otherwise referred to as slowness [23].

The inversion of $P(q,\tau)$, to yield $f(x,t)$, is obtained through a similar procedure as the case of the angle–radius Radon transform (AR–RT) in (2.1); the inversion formula is expressed as:

$$f(x,t) = \int_{-\infty}^{\infty} H\left(\frac{\partial P(q,\tau)}{\partial \tau}\right) dq \tag{2.19}$$

and $H(.)$ is again the Hilbert transformation defined in (2.2b).

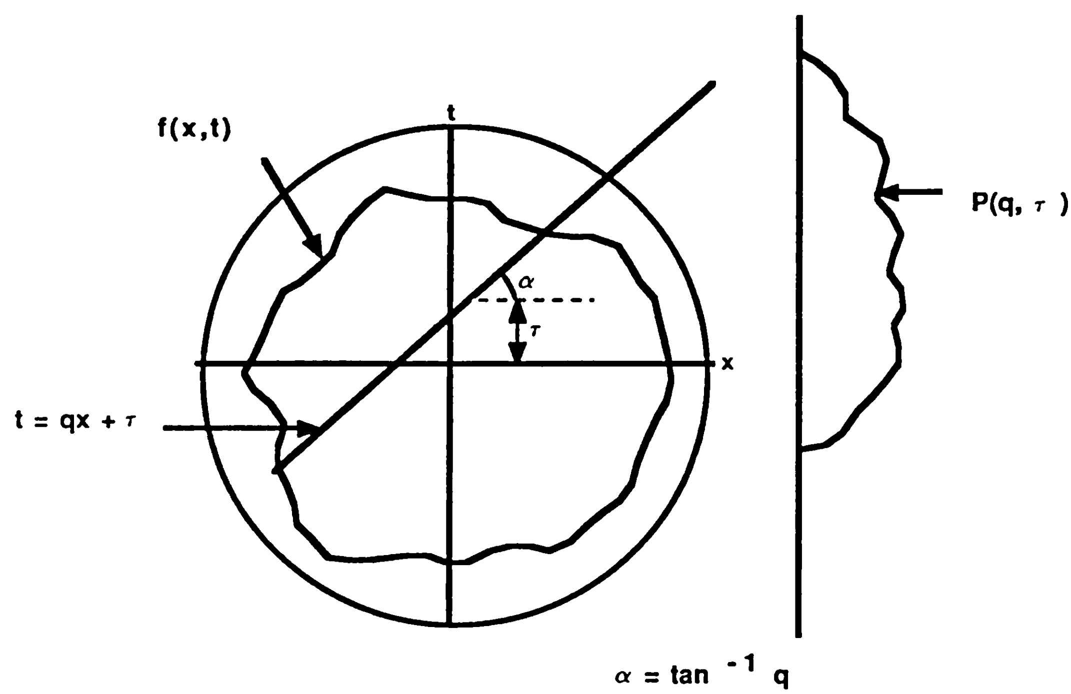

Fig. 2.4 Geometry for implementing the slope-intercept Radon transform over a plane f(x,t). For a given slope q, a projection $P(q, \tau)$ is generated by taking line integrals (each line having intercept τ) over f(x,t).

A discrete equivalent of (2.18) is [23]:

$$P(k\Delta q, l\Delta\tau) = \Delta x \Delta t \sum_m \sum_n f(m\Delta x, n\Delta t)\, \delta(m\Delta x . k\Delta q - n\Delta t + l\Delta\tau) \qquad (2.20)$$

where k, l, m and n are all integers and Δq and $\Delta\tau$ are the sampling increments of the slope and intercept, respectively. In this case, the forcing function $\delta(.)$ is the unit impulse function. The discrete rectangularly sampled space–time function is depicted in fig. 2.5. The figure highlights the problem of discretization of the Radon transform. The solid lines of integration, otherwise referred to as synchronous lines [23], pass through samples that are present at the proper time delay (n) for all detecting locations (m). The dashed line represents a typical non–synchronous integration line. The synchronous lines may not be sufficiently packed to permit effective reconstruction of the function or measurements of the speed of propagation through the medium $f(x, t)$. Consequently, non–synchronous lines must be converted into synchronous ones by interpolating from original samples to the non–synchronous delays. Scheibner and Parks [23] focus on this problem for the SI–DRT.

2.4.2 Angle–Radius DRT and its Implementation

The synchronous SI–DRT of (2.20) suggests a similar definition for an angle–radius DRT (AR–DRT). We write such a DRT as:

$$\begin{aligned} P(k\Delta\theta, l\Delta t) = \sum_m \sum_n & f(m\Delta x, n\Delta y) \\ & \cdot \delta(m\Delta x \cos k\Delta\theta + n\Delta y \sin k\Delta\theta - l\Delta t) \end{aligned} \qquad (2.21)$$

and k, l, m and n are integers. Again the image function $f(x, y)$ has been rectangularly sampled at integer multiples of Δx, Δy and $\Delta\theta$ and Δt are the respective angular and radial sampling intervals of the DRT. As seen in fig. 2.6, the level of synchronization of line integration is low.

In order to simulate the AR–DRT, in practice, full synchronization of integration is required for all $\theta_k = k\Delta\theta$, $\theta_k \in [0, \pi)$. To do this, we 'overlay' $f(m, n)$ with

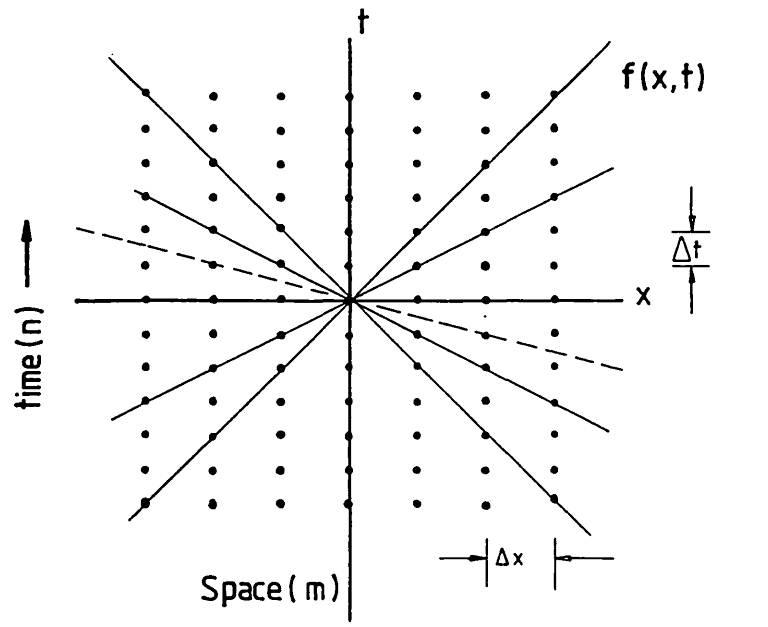

FIG. 2.5 GEOMETRY FOR IMPLEMENTING THE SI-DRT OVER A SAMPLED (SPACE-TIME) FUNCTION

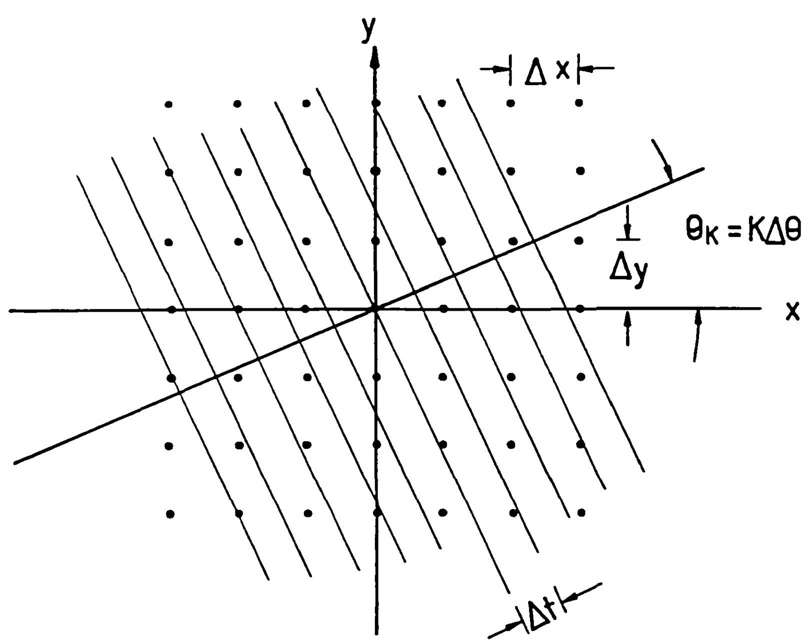

FIG. 2.6 GEOMETRY FOR IMPLEMENTING THE AR-DRT OVER A SAMPLED FUNCTION.

a circularly limited function $f_c(x, y)$ (where this function contains $f(m, n)$; see fig. 2.7). On the basis of the general definition of the projection process in chapter one, a projection at θ_k is generated within a co–ordinate system $t - s$ that is rotated by θ_k with respect to the $x - y$ cartesian co–ordinate system. A fixed sampling interval Δt along the t co–ordinate (which also corresponds to the radial parameter of the AR Radon transform) specifies the location of integration lines. A similar sampling interval Δs along each line of integration, parallel to the s co-ordinate, locates integration points along the line. This sampling interval may be made proportional to the length L_l of the l^{th} line of integration by fixing the number of points per line. However, this number is preferably chosen such that the maximum sampling interval (corresponding to the longest integration line) does not exceed the size of the smallest feature to be resolved in the reconstruction. The smallest feature size also controls the choice of Δt.

The integration of $f_c(x, y)$, along the integration lines, may be written as;

$$P(k, l) = \sum_j f_c(x_{jkl}, y_{jkl}) \tag{2.22}$$

with

$$x_{jkl} = l\Delta t \cos\theta_k - j\Delta s \sin\theta_k \tag{2.23}$$

$$y_{jkl} = l\Delta t \sin\theta_k + j\Delta s \cos\theta_k \tag{2.24}$$

where j, k and l are integers and x_{jkl} and y_{jkl} specify a point within the $t - s$ co–ordinate system relative to the $x - y$ co–ordinate system. When (x_{jkl}, y_{jkl}) does not coincide with image points $f_c(x, y)$, $x = m\Delta x$, $y = n\Delta y$ (i.e. non–synchronous integration points) bilinear interpolation from the four surrounding image points of $f(m, n)$ is effected to estimate $f_c(x_{jkl}, y_{jkl})$. Also, integration points that fall without the area of $f(m, n)$ are set to zero or some constant value such as the spatial mean of the image. The uniform level is preferred so as not to produce other statistical variations in the projections that are not originally available in $f(m, n)$. Various rotations of this integration procedure produce different projections of $f(m, n)$.

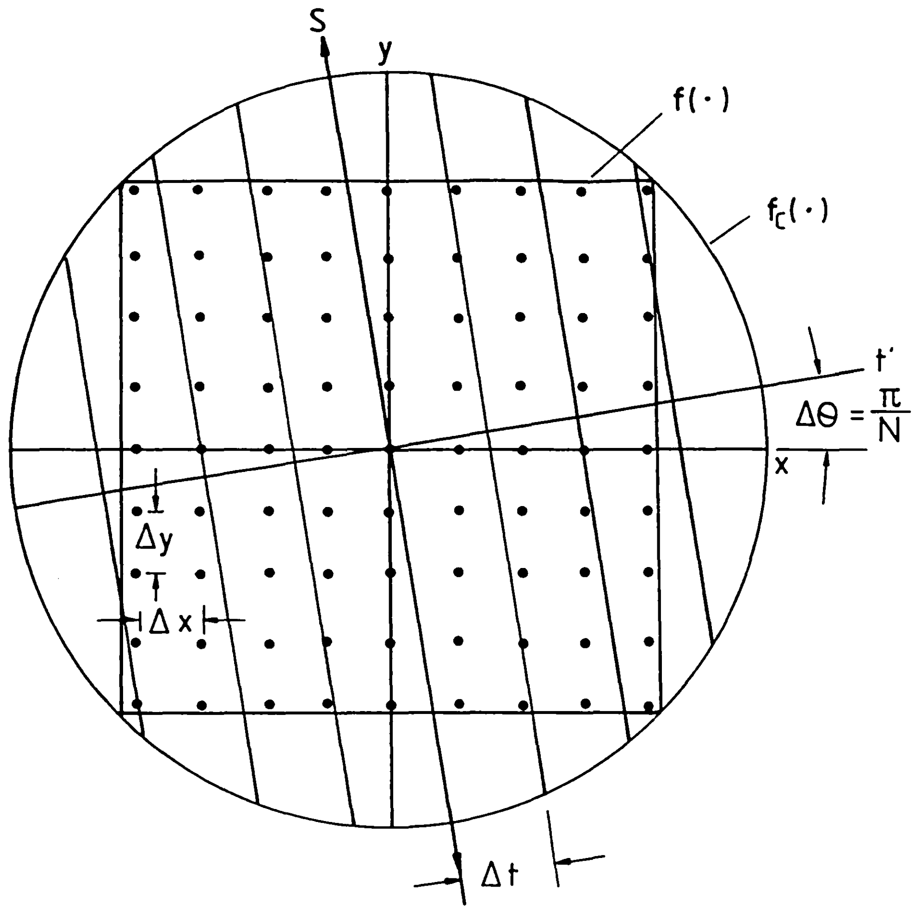

FIG. 2.7a GEOMETRY FOR SIMULATING THE AR - DRT ON AN N X N IMAGE PLANE f(.)

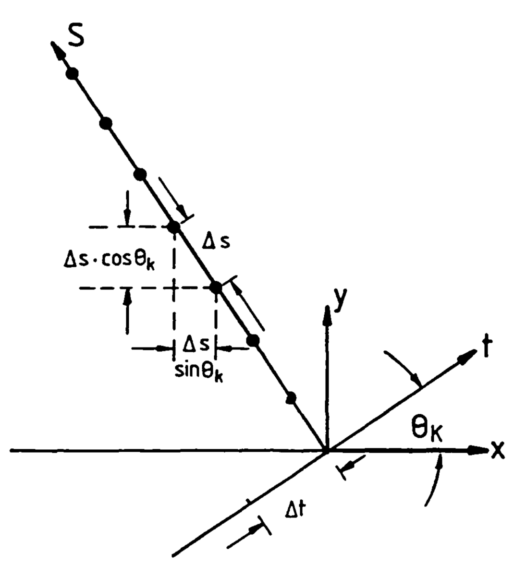

FIG. 2.7b SELECTION OF INTEGRATION POINTS ALONG A LINE FOR A GIVEN ORIENTATION θ_k .

Fig. 2.8 Reconstruction of MAN from 128 projections

Fig. 2.9 Reconstruction of BOY from 128 projections

Fig. 2.10 Reconstruction of BOX from 128 projections

Fig. 2.11 Reconstruction of BOY from 256 projections

Fig. 2.12 Original MAN image

Fig. 2.13 Original BOY image.

Fig. 2.14 Original BOX image

Figs. 2.8—11 are examples of CBP based reconstruction of images (128×128pixels in dimension) that had been projected using the implementation just described. Figs. 2.12–14 are the original images from which the projections were acquired. The radial resolution was set at $\Delta t = 1.414$ for all cases. Points of integration were located at intervals $\Delta s \leq \Delta t = 1.414$; the intervals were proportional to the lengths of the integration lines. The images of fig. 2.8—10 are reconstructions from 128 projections in each case. Fig. 2.11 is a reconstruction from 256 projections. In all cases, the Shepp-Logan filter was used. The overall structural detail in the images is recognizable, however, smaller features in the reconstructions may be detectable by increasing the resolution of projection, particularly in the radial parameter. That is, choosing smaller values of Δt.

For the development of mode 1 PDC, we have restricted the tomographic data to 128 radial samples per projection over 128 projections for $\Delta t = 1.414$ and $\Delta\theta = \pi/128$. The adherence to the specified radial sampling interval effectively enables the performance of mode 1 compression algorithms to be evaluated in the presence of limited projection data (in the sense of low radial resolution).

PART B: Information Theoretic and Stochastic Appraisals for the Projection Domain

2.5 Information Preservation Considerations in the Projection Domain

It has been mentioned earlier that exact reconstruction of the continuous–space $f(x,y)$ is possible when $P(\theta,t)$ is defined for a continuum of angles within the range $[0,\pi)$ and when t is defined throughout the diameter of projection. In other words, under these conditions, the projection domain preserves the image domain in projected form. We also wish to theoretically determine, using the DRT basis functions (the SI–DRT and AR–DRT, respectively) if information (or entropy) can be preserved for discrete–space processing. Entropy preservation, would justify to some extent, the efficacy of data compression of projected data. Similar theoretical considerations have been investigated by Andrews [47] for frequency domain compression.

We examine the entropy transformation in SI–DRT in detail and quote the results of the AR–DRT as the analysis is the similar. The integers k, l, m, n of (2.20) are assumed to belong to the interval $[0, N-1]$, where N is some integer greater than unity. Ordering the discrete space function values $\{f(m,n)\}$ for $0 \leq m, n \leq N-1$ and $\{P(k,l)\}$, for $0 \leq k, l \leq N-1$ into vectors $\mathbf{f}$ and $\mathbf{P}$, respectively, enables equation (2.20) to be written as

$$\mathbf{P} = D\mathbf{f} \tag{2.25}$$

where D is the SI–DRT matrix and the vectors $\mathbf{f}$ and $\mathbf{P}$ are such that $\mathbf{f}^T = [f(0,0), f(0,1), \ldots, f(N-1, N-1)]$ and $\mathbf{P}^T = [P(0,0), P(0,1), \ldots, P(N-1, N-1)]$ respectively.

These vectors are each assumed to have continuous amplitude components. Therefore the corresponding differential entropy measure for such a vector $\mathbf{\Gamma}$ is

$$H_e(\mathbf{\Gamma}) = -\int \beta(\mathbf{\Gamma}) \log \beta(\mathbf{\Gamma})\, d\mathbf{\Gamma} \tag{2.26}$$

where $\beta(\mathbf{\Gamma})$ is the joint probability density function (pdf) of elements within the N^2–dimensional vector $\mathbf{\Gamma}$.

The linear transformation D of (2.25) permits the respective entropies of $\mathbf{f}$ and $\mathbf{P}$ to be related by the correspondence [48]:

$$H_e(\mathbf{P}) = H_e(\mathbf{f}) + \mathrm{E}[-\log J(\mathbf{f}/\mathbf{P})] \tag{2.27}$$

and $(J(\mathbf{f}/\mathbf{P}))^{-1} = J(\mathbf{P}/\mathbf{f})$ is the Jacobian of the transformation, equivalent to $|D|$ the determinant of the DRT matrix D; E[.] is an ensemble average operator.

We modify the SI–DRT basis function $\delta(m\Delta x k\Delta q - n\Delta t + l\Delta\tau)$ by multiplying it by a scaling factor a such that $a = (\Delta x \Delta t)^{-1}$; as will be seen, this permits an orthonormality condition on the SI–DRT. Employing this scaled basis function in the SI–DRT formula of (2.20), the elements d_{kmln} of D may be written as

$$d_{kmln} = \frac{\partial P(k\Delta q, l\Delta\tau)}{\partial f(m\Delta x, n\Delta t)} = \delta(m\Delta x k\Delta q - n\Delta t + l\Delta\tau) \tag{2.28}$$

for $0 \leq k, l, m, n \leq N-1$. Consequently, elements γ_{rsuv} of $D^T D$ that result from the inner product of the rs^{th} row of D^T and the uv^{th} column of D are:

$$\gamma_{rsuv} = \sum_{k=0}^{N-1}\sum_{l=0}^{N-1} \delta(r\Delta x k\Delta q - s\Delta t + l\Delta\tau)\,\delta(u\Delta x k\Delta q - v\Delta t + l\Delta\tau) \tag{2.29}$$

for $0 \leq r, s, u, v \leq N-1$. By definition of the impulse basis function, it is apparent that

$$\gamma_{rsuv} = \begin{cases} 1 & \text{for } (r-u)\Delta x\Delta q + (v-s)\Delta t = 0 \\ 0 & \text{otherwise.} \end{cases} \tag{2.30}$$

The non–zero values of γ_{rsuv} occur when $r = u$ and $v = s$ for $0 \leq k, l \leq N-1$ and therefore, $D^T D$ is an $N^2 \times N^2$ identity matrix which in turn indicates that D, under the modified basis format, is an orthogonal matrix. The Jacobian of the transformation of (2.25) is therefore explicitly valued as

$$J(\mathbf{P}/\mathbf{f}) = (J(\mathbf{f}/\mathbf{P}))^{-1} = |D| = 1 \qquad (2.31);$$

substituting (2.31) in (2.25) permits

$$H_e(\mathbf{P}) = H_e(\mathbf{f}) \qquad (2.32).$$

This result and the associated analysis state that in generating N^2 samples of projected information from an equal number of samples of image data, using a scaled impulse basis structure for the SI–DRT, image domain information is preserved.

A similar result may be obtained for the AR–DRT using the same analytical approach; in this case the elements of $D^T D$ are

$$\gamma_{rsuv} = \begin{cases} 1 & \text{for } (r-u)\Delta x\cos\theta_k + (v-s)\Delta y\sin\theta_k = 0 \\ 0 & \text{otherwise.} \end{cases} \qquad (2.33).$$

2.5.1 Discussion

A corollary of the entropy correspondence is that it is possible to develop image data compression schemes for bandwidth reduction or storage minimization that would perform as efficiently in the projection domain. Shannon's first theorem [49] for noiseless coding justifies such an inference as it claims that the entropy of an information source is the lower bound of its compression at an arbitrarily small distortion level.

However, the orthogonality of D also implies that the image vector $\mathbf{f}$ may be retrieved without ambiguity. This appears to be impracticable in the light of the review of section 2.2 which highlighted the problems of inexact reconstruction. It may be argued that the information preservation result is an optimistic one that can only be obtained by employing an idealized basis function—the impulse function. In CT applications, the impulse functions would require the source X–rays to have infinitesimal beam–widths. However, in order that they have finite power, the widths must also be finite [50].

A theoretical result put forward by Mersereau and Oppenheim [5], has similar implications to (2.32). They show that a band–limited sampled image function may be uniquely reconstructed from its AR–based projection domain that contains a *finite* number of projections. They cautiously point out, however, that the principles for exact reconstruction * do not lead to practical reconstruction algorithms.

Summarizing, it would appear that the proven conditions of (2.30) and (2.33) are at best, ideal criteria relating the projection domain to the image domain and they do not specify how the entropy can be preserved in practice, as is the case for related theoretical results in [5]. These considerations may therefore question the viability of PDC. For mode 1 processing, where image information is originally available in the projection domain, this question is not important as the object is to efficiently compress the available projection data such that the final picture is

* For completeness, a similar but unique proof of exact image reconstruction from the SI–RT is presented in Appendix II.

not overtly distorted as a result of compression [1]. The implications for mode 2 processing are however more far reaching due to the latent reconstruction error in a mode 2 system. Other discrete space transformation procedures that can yield orthogonality in practice would always be at an advantage. Nevertheless, if the reconstruction error is small or controllable through a pre–determination of parameters (e.g. the number of projections, to be employed) mode 2 PDC may still be a feasible approach. These considerations are pursued experimentally and theoretically in chapter 5.

2.6 Stochastic Characterization of the Projection Domain

In several studies, projection domain stochastic analysis has been limited to introducing random disturbances in the domain that is fundamentally characterized as deterministic and estimating the resultant distortion produced in the corresponding image domain reconstruction. In some cases the approach has been to develop minimum error reconstruction algorithms or estimate feature or object locations from the noisy projection information [6,25,36,37,51]. The noise based stochastic modelling, in the main, focuses on combating the irregularities and statistical uncertainties that are typically encountered in generating projections under mode 1 applications; photon measurement noise is a prevalent phenomenon in CT [6,36,37].

However, it is expedient for compression purposes, to assume from the outset that the projection domain information is a random output generated by Radon transformation of stochastic image data. Intuitively, these considerations enable a potential compressor to adapt to the statistics available within the projection domain, in accordance with the randomized nature of its corresponding image space. This latent stochastic nature implicitly served as the basis of the previous information theoretic analysis. Jain and Ansari [24] have formally presented somewhat not well known theorems, describing the stochastics of projections of random imagery. However, they do not rigorously develop them. In particular, they define a projection slice theorem that relates the power spectrum of a projection with the power spectrum of the image from which it is derived. The importance of the theorem and its relevance to PDC deserves a more comprehensive treatment and in this section, cross–correlation properties between a continuous space random image function $f(x, y)$ and the corresponding projection domain function $P(\theta, t)$ and the auto–correlation characteristics of $P(\theta, t)$ are fully analysed. The power spectrum theorem is also examined on the basis of the derived results.

2.6.1 Cross-correlation Property

Let $f(x, y)$ be a wide sense stationary (WSS) random zero mean image field. Therefore, its auto–correlation function $r_f(x_1, y_1; x_2, y_2)$, x_1, y_1, x_2, y_2 being spatial parameters of $f(x, y)$, is

$$\begin{aligned} r_f(x_1, y_1, x_2, y_2) &= \mathrm{E}[f(x_1, y_1)f(x_2, y_2)] \\ &= \mathrm{E}[f(x_1, y_1)f(x_1 + \tau_1, y_1 + \tau_2)] \\ &= r_f(\tau_1, \tau_2) \end{aligned} \tag{2.34}$$

with $\tau_1 = |x_1 - x_2|$,$\tau_2 = |y_1 - y_2|$. The operator E[.] is again an ensemble average operator.

The cross–correlation $r_{fP}(x, y; \theta, t)$ between the image domain function and its projection domain may be obtained as follows:

$$r_{fP}(x, y; \theta, t) = \mathrm{E}[f(x, y)P(\theta, t)] \qquad (2.35).$$

Using the formal definition of the AR–Radon transform of (2.1) in (2.35) we have

$$r_{fP}(x, y; \theta, t) = \int\!\!\int_I \mathrm{E}[f(x, y)f(u, v)]\delta(u\cos\theta + v\sin\theta - t)\, du\, dv \qquad (2.36).$$

Setting spatial lags $\tau_1 = |u - x|$, $\tau_2 = |v - y|$ in (2.35) yields

$$\begin{aligned} r_{fP}(x, y; \theta, t) = \int\!\!\int_I & r_f(\tau_1, \tau_2)\delta(\tau_1\cos\theta + \tau_2\sin\theta \\ & + x\cos\theta + y\sin\theta - t)\, d\tau_1\, d\tau_2 \end{aligned} \tag{2.37}$$

which indicates that the cross-correlation between the image and the projection domain is a Radon transformation of the auto- correlation of the image plane; this relationship may be summarized as

$$r_{fP}(x,y;\theta,t) = \hat{\phi}(\theta, x\cos\theta + y\sin\theta - t) \tag{2.38}$$

where $\hat{\phi}(.)$ is a function defined in the projection domain, whose image function is $r_f(\tau_1,\tau_2)$. The salient feature of (2.38) is that a cross–correlation of the random fields $f(x,y)$ and $P(\theta,t)$ remains constant along integration paths, specified by (θ,t), over the image plane. Thus, all points $(x,y) \in I$ on a particular integration line have the same cross-correlation with the corresponding projection sample that results from their integration. This is intuitively satisfactory, as the backprojection of $P(\theta,t)$ is equal for all points (x,y) that correspond to (θ,t) in the equation $x\cos\theta + y\sin\theta = t$. From the viewpoint of PDC , the cross-correlation property suggests that any distortion produced at $P(\theta,t)$ will also be equivalently distributed over corresponding integration points.

2.6.2 Auto-correlation Properties

The auto-correlation function $r_P(\theta_1,t_1;\theta_2,t_2)$ for any pair of angle and radial components at (θ_1,t_1) and (θ_2,t_2) is

$$r_P(\theta_1,t_1;\theta_2,t_2) = \mathrm{E}[P(\theta_1,t_1)P(\theta_2,t_2)] \tag{2.39}$$

and on using the standard Radon transform (2.1) again, we obtain

$$r_P(\theta_1,t_1;\theta_2,t_2) = \int\int_I r_{fP}(x,y;\theta_2,t_2)\,\delta(x\cos\theta_1 + y\sin\theta_1 - t_1)\,dx\,dy \qquad (2.40).$$

Therefore, in projecting the cross–correlation function of (2.38), the auto–correlation function may be derived.

To explicitly characterize $r_P(\theta_1,t_1;\theta_2,t_2)$, equation (2.40) and the Fourier transform relationship between $\hat{\phi}(\theta_2, x\cos\theta_2 + y\sin\theta_2 - t_2)$ (from equation (2.38)) and a function $\hat{\Phi}(\theta_2,\omega)$ are employed. Accordingly, for

$$\hat{\phi}(\theta_2,s) = \frac{1}{2\pi}\int_{-\infty}^{\infty} \hat{\Phi}(\theta_2,\omega)\,e^{\jmath\omega s}\,d\omega \tag{2.41}$$

(where $s = x\cos\theta_2 + y\sin\theta_2 - t_2$), equation (2.40) may be written as

$$r_P(\theta_1,t_1;\theta_2,t_2) = \iint_I \left[\frac{1}{2\pi}\int_{-\infty}^{\infty} \hat{\Phi}(\theta_2,\omega)\, e^{\jmath\omega s}\, d\omega\right] \delta(x\cos\theta_1 + y\sin\theta_1 - t_1)\, dx\, dy \qquad (2.42).$$

Interchanging integrals and using the identity $\delta(z) = |\alpha|\,\delta(\alpha z)$ for the dirac delta function [52,pg 57] we have

$$r_P(\theta_1,t_1;\theta_2,t_2) = \left[\frac{1}{2\pi}\int_{-\infty}^{\infty}\int_{-\infty}^{\infty} \hat{\Phi}(\theta_2,\omega)e^{(-\jmath\omega t_2)}d\omega\right]\iint_I e^{\jmath\omega(x\cos\theta_2+y\sin\theta_2)} \cdot \frac{|\omega|}{\omega^2}\,\delta(\omega(x\cos\theta_1 + y\sin\theta_1 - t_1))\, d\omega x\, d\omega y \qquad (2.43)$$

$$= \frac{1}{2\pi}\int_{-\infty}^{\infty} \frac{\hat{\Phi}(\theta_2,\omega)}{|\omega|} e^{\jmath\omega(t_1-t_2)}\delta(\theta_1 - \theta_2)\, d\omega$$

$$= \delta(\theta_1 - \theta_2)\Psi(\theta_2, t_1 - t_2) \qquad (2.44);$$

it is clear that $\Psi(\theta_2, t_1 - t_2)$ is the inverse (radial based) Fourier transform of $\hat{\Phi}(\theta_2,\omega)/|\omega|$. Hence, according to (2.44), the major attribute of the auto–correlation function of the projection domain information $P(\theta,t)$ of a WSS image function $f(x,y)$ is that $P(\theta,t)$ is WSS in the radial parameter and uncorrelated in its angular variable. The corollary of this is that the Radon transform is a whitening transformation in θ for stationary random image fields.

A projection slice theorem for random fields is defined in [24]; it is based on a similar analysis for cross–correlation and auto–correlation as developed here for a modified Radon transform structure. This modified transform generates a projection $\widetilde{P}(\theta,t)$ on angle θ whose radial Fourier transform $\widetilde{P}(\theta,\omega)$ is associated with $P(\theta,\omega)$, the corresponding radial Fourier transform of $P(\theta,t)$, by

$$\widetilde{P}(\theta,\omega) = |\omega|^{1/2}\, P(\theta,\omega) \qquad (2.45).$$

The theorem states that the power spectral density function (sdf) $\widetilde{\Phi}(\theta,\omega)$ of $\widetilde{P}(\theta,t)$ is an angular slice of the 2–D sdf $\Phi_f(\omega_1,\omega_2)$ of the image field $f(x,y)$, that is

$$\widetilde{\Phi}(\theta,\omega) = \Phi_f(\omega_1,\omega_2)\big|_{\substack{\omega_1=\omega\cos\theta \\ \omega_2=\omega\sin\theta}} \qquad (2.46).$$

Moreover, the sdf $\Phi(\theta,\omega)$ of $P(\theta,t)$ (which, by definition, is the Fourier transform of $r_P(\theta_1,t_1;\theta_2,t_2)$) is such that

$$\Phi(\theta,\omega)=\frac{\widetilde{\Phi}(\theta,\omega)}{|\omega|} \tag{2.47}$$

2.6.3 Discussion

Significantly, when it is known that an image field is WSS then a projection domain compressor may simply encode the projections in an independent manner. This approach is studied experimentally in chapter three and analytically in chapter six, in a rate–distortion analysis of PDC.

The projection slice theorem for random fields effectively offers a technique for estimating the power sdf of the image field from the sdfs of the image projections. This important stochastic relationship has been used to model angle–dependent image reconstruction filters for controlling high level noise [24]. Interestingly , our rate–distortion analysis for mode 1 PDC suggests the use of such filters.

2.6.4 Summary of Stochastic Properties of the SI–Radon transform

Due to the analytical similarity of the SI–RT (2.18) with the AR–RT (2.1), the foregoing analysis for the projection domain derived from the latter transform may be similarly applied for obtaining stochastic results of SI projected information. Therefore, the following unique results are formally stated here; the corresponding proofs are briefly outlined in Appendix II.

1. **Cross–Correlation:** The cross–correlation $r_{fP}(x,t;q,\tau)$ of a WSS space–time or space–space random image field $f(x,t)$ with its SI–RT may be written as

$$r_{fP}(x,t;q,\tau)=\hat{\phi}(q,xq-t+\tau) \tag{2.48}$$

   which implies that the cross–correlation of all points $f(x,t)$ integrated over the line $t=qx+\tau$ have a constant cross–correlation with their integration $P(q,\tau)$. Also, $\hat{\phi}(q,xq-t+\tau)$ is a projection domain function whose image field is the auto–correlation function of $f(x,t)$.

2. **Auto–correlation:** The auto–correlation $r_P(q_1, \tau_1; q_2, \tau_2)$ of $P(q, \tau)$, the projection domain function of the WSS $f(x,t)$, is such that

$$r_P(q_1, \tau_1; q_2, \tau_2) = \delta(q_1 - q_2)\Psi(q_1, \tau_1 - \tau_2) \tag{2.49}$$

where $\Psi(.)$ is a projection domain function of the cross–correlation of (2.48). This result indicates that the SI Radon transform is a whitening transform in its slope parameter and is stationary in its intercept component. A theorem based on these results may be stated as follows.

Theorem. *SI Projection Theorem for Random Image Fields. The power spectral density $\widetilde{\Phi}(q, \omega)$ of a modified SI based projection $\widetilde{P}(q, \tau)$, on a slope q, is equivalent to the 2–D power spectrum $\Phi_f(\omega_1, \omega_2)$ of a stationary random image field $f(x,t)$ evaluated on the line $\omega_1 = q\omega$. Formally,*

$$\widetilde{\Phi}(q, \omega) = \Phi_f(\omega_1, \omega_2)|_{\substack{\omega_1 = q\omega \\ \omega_2 = \omega}} \tag{2.50}$$

where the 1–D intercept based Fourier transform $\widetilde{P}(q, \omega)$ of $\widetilde{P}(q, \tau)$ corresponds to

$$\widetilde{P}(q, \omega) = |\omega|^{1/2} P(q, \omega) \tag{2.51}$$

and $P(q, \omega)$ is the corresponding transform of $P(q, \tau)$ — the projection of $f(x,t)$ on slope q. The power spectrum $\Phi(q, \omega)$ of $P(q, \tau)$ is estimated from (2.48) by the frequency dependent weighting:

$$\Phi(q, \omega) = \frac{\widetilde{\Phi}(q, \omega)}{|\omega|} \tag{2.52}.$$

The proof is found in Appendix II.

2.7 Some Empirical Results of Auto–correlation Measures of Projection Data

Figs. 2.15–17 are results of auto–correlation measures obtained from projected information of the MAN and BOY images (see figs. 2.12–13) and the phase plane of the MAN image, respectively. The latter is an example of a random image field.

From a sequence $\{P(k,l)\}$ of projection samples , for $0 \leq k \leq M_\theta - 1$ and $0 \leq l \leq M_t - 1$ where M_θ and M_t are the number of projections and the number of radial samples per projection, respectively, an average *intra-projection* or radial sample correlation $R_t(m)$ and an average *inter-projection* or angular sample correlation $R_\theta(m)$ are respectively computed. The sample radial correlation is

$$R_t(m) = \frac{1}{M_\theta} \sum_{k=0}^{M_\theta - 1} \alpha_k^{-1} \sum_{n=0}^{M_t - 1 - m} \widetilde{P}(k,n)\widetilde{P}(k,n+m) \tag{2.53}$$

for $m = 0, 1, \ldots, M_\theta - 1$ where

$$\widetilde{P}(k,l) = P(k,l) - \frac{1}{M_t} \sum_{n=0}^{M_t - 1} P(k,n) \tag{2.54}$$

for all k and

$$\alpha_k = \sum_{n=0}^{M_t - 1} [\widetilde{P}(k,n)]^2 \qquad (2.55).$$

The angular correlation $R_\theta(m)$ can be similarly expressed just by computing the correlation over the angular index of the projected information and interchanging M_θ and M_t in the expressions of (2.53–55) accordingly. The functions $R_t(m)$ and $R_\theta(m)$ satisfy $-1 \leq R_t(m), R_\theta(m) \leq 1$.

The equivalent first order Markov auto-correlation functions ρ_t^m and ρ_θ^m of $R_t(m)$ and $R_\theta(m)$ were also respectively computed for comparison with the true second order statistics of projection data. The respective Markov correlations are estimated as

$$\rho_t^m = \frac{1}{M_\theta} \sum_{k=0}^{M_\theta - 1} \left\{ \alpha_k^{-1} \sum_{n=0}^{M_t - 1} \widetilde{P}(k,n)\widetilde{P}(k,n+1) \right\}^m \tag{2.56}$$

for $m = 0, 1, \ldots, M_\theta - 1$ and

$$\rho_\theta^m = \frac{1}{M_t} \sum_{l=0}^{M_t - 1} \left\{ \alpha_l^{-1} \sum_{n=0}^{M_\theta - 1} \widetilde{P}(n,l)\widetilde{P}(n+1,l) \right\}^m \tag{2.57}$$

for $m = 0, 1, \ldots, M_t - 1$.

These measurements were evaluated for $M_t = M_\theta = 128$. From the results, it is observable that there exists considerable inter–projection and intra-projection correlation over short to medium correlation lags in projected data of typical imagery. The curves corresponding to sample auto–correlation functions indicate that the inter–projection correlation falls off more rapidly than the intra–projection correlation. It is interesting to see that the angular correlation drops to a negative correlation and then rises after a few lags to a small positive value. This characteristic may be explained by observing typical amplitude profiles of projected samples (of the MAN image) over different angles, for specified radial locations; fig 2.18 portrays these profiles for radial locations corresponding to $l = 32$ and $l = 64$ respectively. The profiles appear to vary in an oscillatory manner over the range $0 \leq k \leq 127$ (which is equivalent to $0 \leq \theta < \pi$) such that samples are both positively and negatively correlated over large separations.

Fig. 2.19 shows typical projection profiles for projections indexed at $k = 32$ and $k = 64$ (approximately corresponding to $\theta = \pi/4$ and $\theta = \pi/2$ respectively). The amplitudes are slowly varying over the projections except at the tail regions where a rapid fall to zero is registered. These regions correspond to the spatial limits of the image plane, within the diameter of the projection circle (see fig. 2.7), for a given projection angle. The negative intra–projection correlation may be accounted for by the correlation between samples in the amplitude rise region of the profiles, with those in the amplitude roll–off region.

The equivalent Markov auto–correlation curves reveal the difference in auto–correlation with true sample correlation when the projected information is approximated by first order Markov processes. This approximation is used in chapter six to determine the effect of Markov modelling of the data on the evaluation of rate–distortion measures for PDC.

Expectedly, the statistics of the projected phase plane indicate that projecting a statistically independent random field would not produce much correlation in the projection domain.

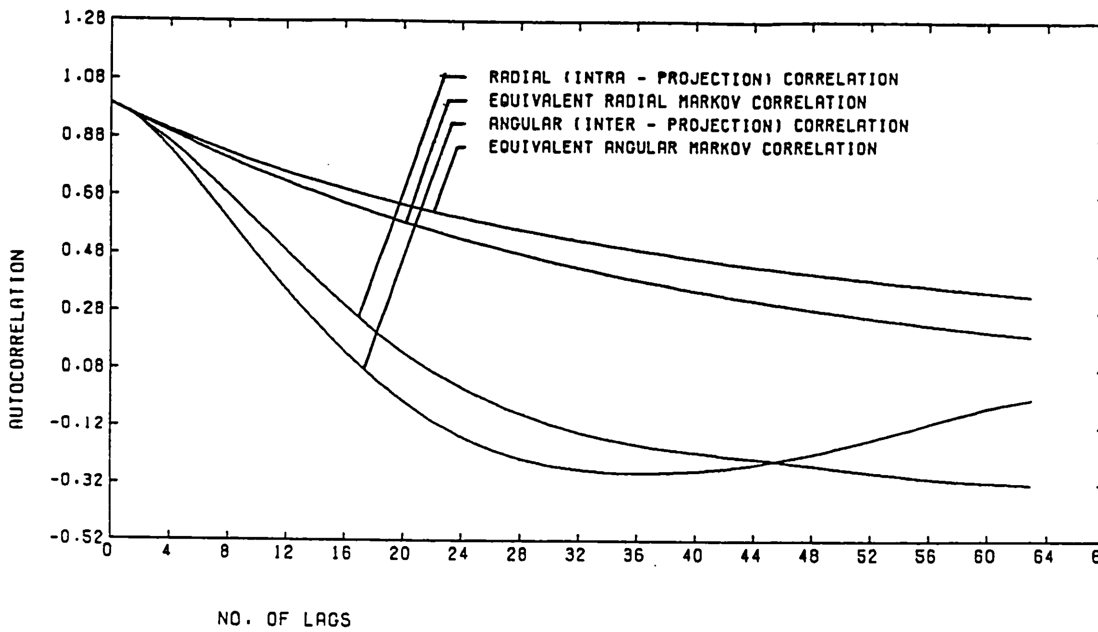

FIG. 2.15 RADIAL AND ANGULAR CORRELATION OF PROJECTED 'MAN'

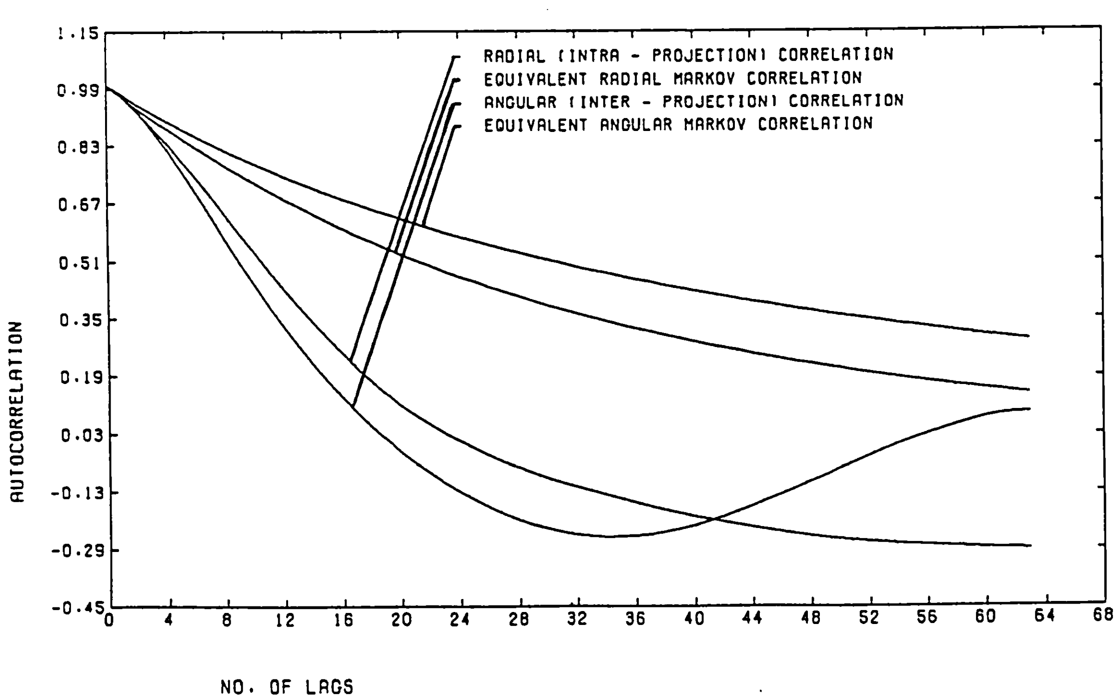

FIG. 2.16 RADIAL AND ANGULAR CORRELATION OF PROJECTED 'BOY'

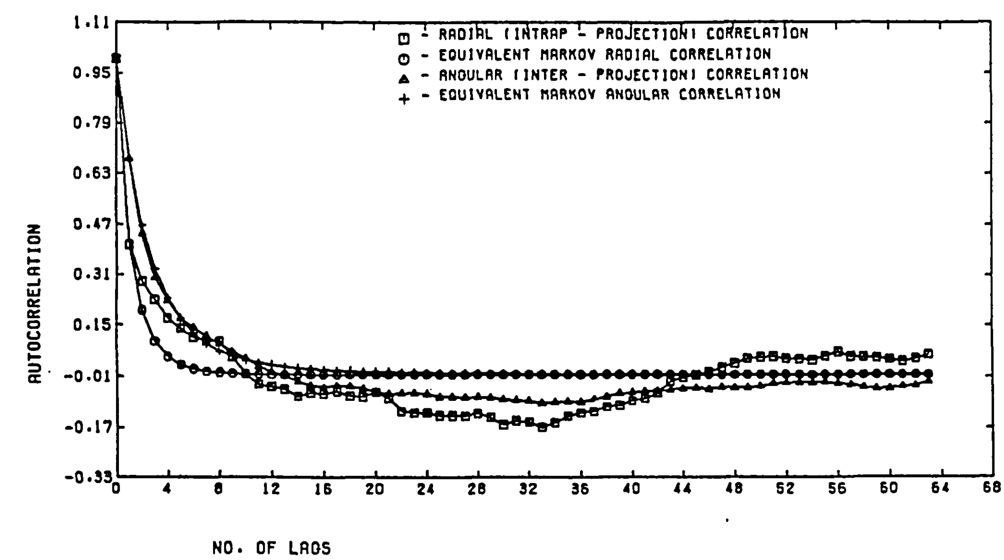

FIG. 2.17 RADIAL AND ANGULAR CORRELATION OF PROJECTED PHASE PLANE

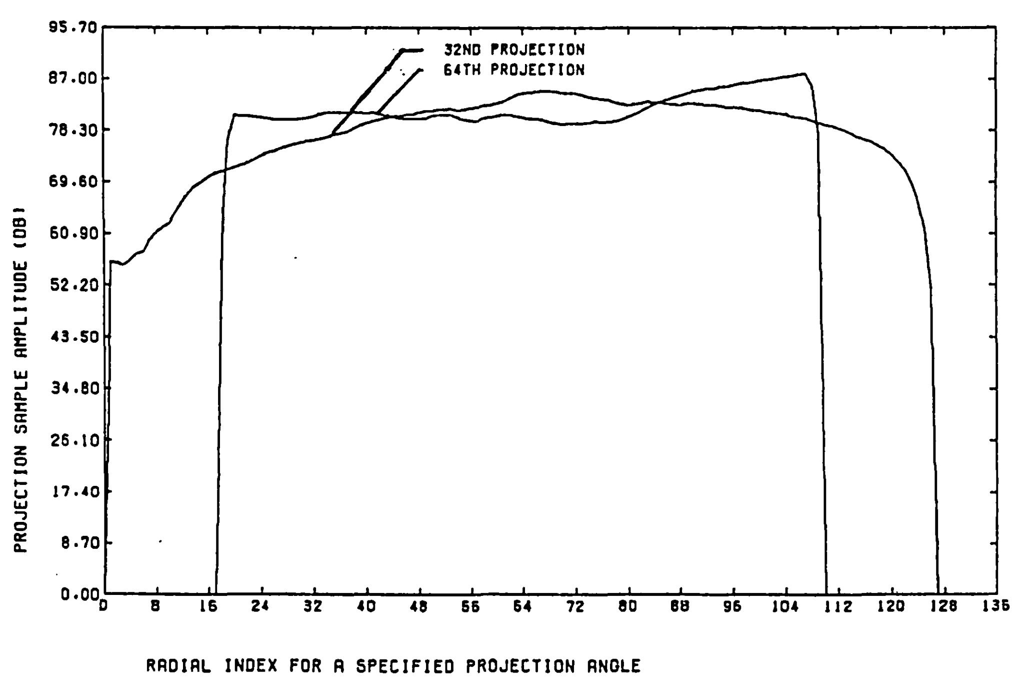

FIG. 2.18 TYPICAL PROFILES OF RADIAL INFORMATION FOR SPECIFIED ANGLES

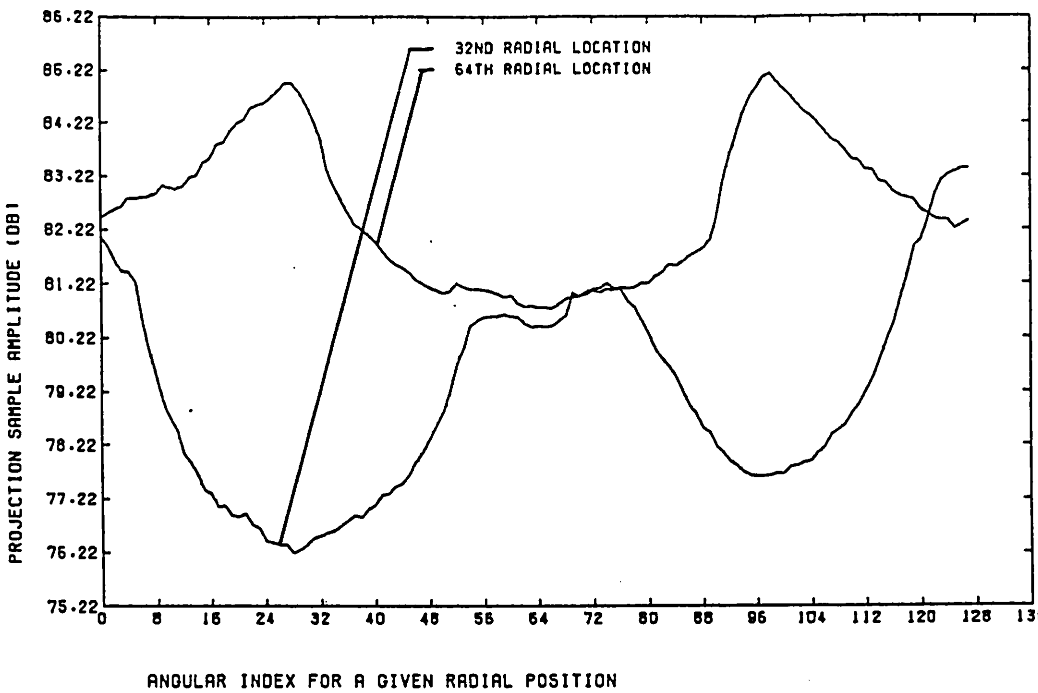

FIG. 2.19 TYPICAL PROFILES OF ANGULAR INFORMATION FOR SPECIFIED RADIAL LOCATIONS

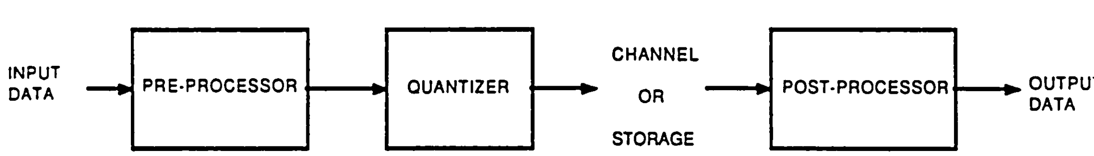

FIG. 2.20 GENERAL REPRESENTATION OF A DATA COMPRESSOR

It is difficult to empirically verify the theoretical results of section 2.5.2 partially due to the use of the idealized dirac delta function in the analytical discussion. Nevertheless, the stochastic results serve as a theoretical basis for studying the performance of compression schemes that are based on intra–projection processing; this is duly considered in a simulation scheme in chapter three and in the development of associated rate–distortion performance bounds in chapter six.

In many respects, from a compression view–point, the high inter– and intra–projection correlation over small to medium spans of samples is encouraging and in subsequent chapters the discussion focuses on how to exploit such correlation.

PART C: Data Compression Techniques in a Projection Domain Environment

Given the constraints of reconstruction from and high correlation of projection data, the data compressor must be able to produce considerable but controlled compression of the data whether it is to serve a mode 1 or mode 2 system. A data compressor may be generally represented as a three component system as shown in fig. 2.20, that is, a cascade of a pre–processor of input information and a quantizer linked through a channel or storage device to a post–processor which outputs a compressed version of the input data. This part of the chapter outlines possible approaches for the choice of the data compressor components (excluding what is considered to be a noiseless channel or storage device) for mode 1 PDC , against the background of the distinct classes of predictive, transform and hybrid [1] data compression techniques. Relevant factors affecting the development of components for the data compressor in a mode 2 environment are also discussed. Associated performance measures of the compression level and accompanying distortion are respectively described.

2.8 Data Compression for a Mode 1 PDC System

2.8.1 Predictive Compression

High correlation or predictability of projected data may encourage the use of predictive compression schemes. The pre-processor of these well known systems may be associated with a predictor, which by effective estimation of the input information, enables a prediction error sequence (whose samples exhibit little cross–correlation) to be passed on to a memoryless quantizer for onward transmission or storage. The post–processor usually operates by using the same prediction filter coefficients to reconstruct a compressed version of the pre–processor input from the transmitted or stored error (prediction error) information. The gains of predictive compression are realized when the energy content of the error sample sequence is considerably smaller than the input data such that substantially fewer bits are required to represent the error signal than the original input information. The relatively simple implementation of predictive systems and the low storage requirements would be of importance to a PDC configuration especially if the time between scanning for tomographic data and image reconstruction is required to be very limited. However the performance of predictive systems, for the purposes of high compression, is limited as they are known to produce localized degradations in the data; in a projection domain environment these degradations may in turn enhance the error of image reconstruction. Moreover, channel or storage errors are known to propagate extensively through predictive systems.

2.8.2 Linear Transform Based Techniques

A principle motivation for the use of these techniques is the generalized projection theorem, earlier discussed in PART A (section 2.1), which directly relates a linear transform of a projection to the same transformation of the image field. The pre–processor in a transform based compressor is chosen to be a linear and invertible transformation (the inverse transform corresponds to the post-processor) which attempts to map most of the energy of the input data into a minimum band of transformed input information; this procedure enables the discarding of several coefficients that have a low energy content. It is also beneficial that the transform produces a transformed sequence with sufficiently low correlation , to support subsequent zero–order memory quantization. An additional requirement is that a transform kernel have a fast computational algorithm which is invaluable to a fast turnaround of tomographic processing.

Most transformations may be categorized as sinusoidal or frequency transforms such as the Fourier, Cosine and Sine transforms or sequency transforms, examples of which are the Walsh–Hadamard, Haar and Slant transforms [53,54,55]. Any transform compression technique that is potentially based on the projection theorem must use a sinusoidal transform for AR based projection data, as the sequency transform kernels do not possess trigonometric parameters. The intra–projection compression approach, presented in the following chapter, is based on a special form of the generalized projection theorem known as the *Cosine projection-slice theorem.*

In the experimentation of [1,15], a set of projection images (2–D projections of 3–D structure) were block transform coded in a manner synonymous with block transform coding of images. A similar approach is briefly considered in chapter three for 2–D block transform coding of projection data. A more sophisticated 2–D Fourier transform based compression approach is also studied. It is based on the peculiar shape of the joint angle–radius frequency response of projection information that is acquired from projecting an image field containing an impulse or collection of impulses.

In general, transform techniques offer the potential of much higher compression than predictive systems [1]. Moreover, the inverse transform enables the facility of redistributing the errors accrued by quantization or channel/storage degradations over the compressed data, rather than the objectionable localization of such distortion that obtains in predictive systems. The deterministic forms of many transforms often make them more amenable to the changes in input data statistics than is the case for predictive methods which are best suitably optimized to the input data or otherwise effectively adapted over statistical variations. Memory requirements, delays for pre–transform data acquisition and the number of operations (logical or arithmetical), however, make the transform approaches more complex. Nevertheless, efficient design of custom–built hardware [56] for carrying out transform functions may offset these limitations.

Most importantly, the applications of transform systems in PDC (mode 1) enable us to exploit the wide ranging implications of the projection theorem— the most important of these, being the relation of frequency structure of projected information with the equivalent structure of the corresponding image field, as is discussed in the next chapter.

2.8.3 Hybrid Techniques

The pre–processor for the hybrid compression approach would be a combination of the predictive and transform pre–processors [4]. The motivation for this approach is to combine the attractive features of the predictive and transform systems. Typically, transformations are applied to reduce correlations between input data samples and prediction follows to remove the remaining redundancy in the transformed data before quantization. Although not strictly a predictive based hybrid approach, we consider the use of transforms for decorrelating projected information and vector quantization for reducing residual correlation, in chapter four.

2.8.4 Quantization

The effects of quantization are important to PDC especially in view of the intrinsic distortion of image reconstruction. A major problem encountered with quantization is the mismatch of the statistics of the data (pre-processed or not) with the quantizer format. The effects of this phenomenon in reconstructed imagery are briefly investigated for intra–projection and inter-projection compression procedures in chapter three.

Chapter four focuses on the application of the powerful vector quantization (VQ) technique to projection data. VQ is a procedure by which samples of the quantizer input are windowed in groups (vectors) of k samples such that quantization is carried out in $\Re^k$ space rather than the scalar quantization in $\Re$ space. A vector of samples is quantized as a signal point in $\Re^k$ by being mapped into one of a pre–determined number of partitions or subspaces of $\Re^k$. The signal point corresponding to the centre of gravity of each partition is known as the *codeword* or representative vector of the partition. The grouping of samples into vectors is implemented on the basis of their spatial and/or temporal correlation or proximity. VQ is a practical procedure for approaching the lower bounds of compression performance [57] and may therefore be suitably applied for PDC.

2.8.5 Performance Considerations

2.8.5.1 Fidelity Measures

The fidelity of a data compressor may be assessed by evaluating the distortion in the compressed data relative to the input information. The output of the data compressor of mode 1 configured PDC is strictly projected information, however, the corresponding image reconstruction is usually the more acceptable form in which the data is interpreted. Therefore, to objectively assess the fidelity of mode 1 PDC for given projection information, the distortion of compressed projection data relative to the input data and the distortion of the reconstructed image (from compressed projection data) with respect to the image associated with the original projection data are respectively computed. The distortion measure used in the subsequent chapters has been the well known normalized mean squared error (NMSE) [58,pg182]. Given the peculiar reconstruction process involved in PDC, some other measures such as the full–width at half maximum (FWHM) and mean secondary overshoot (MSO) [25] may also be employed. The FWHM has been used to measure the resolution of reconstructed imagery and the MSO, the level of radial oscillations in the reconstructions. For simplicity and analytical convenience, the NMSE has been adhered to in this thesis.

2.8.5.2 Determining the Compression Level

The compression ratio associated with data compression has been expressed in equation (1.2) in chapter one. The determination of the average number b_{av} of bits to represent the data source of projections without apriori knowledge of the corresponding image field is not trivial, as the (projected) data is initially available in continuous amplitude form. A reasonable procedure for estimating b_{av} is to allocate bits to quantize the input projection samples and measure the resulting distortion with reference to the original projection samples. If the distortion is below an acceptable level, then the associated average number of allocated bits would correspond to b_{av}. In carrying out this procedure for projection data generated by the procedure described in section 2.4.2, 10 bits/sample is found to be adequate for achieving insignificant distortion for projection data of typical imagery. It is important to note, however, that the units of b_{av} are *bits /projected sample* in mode 1 processing rather than bits/pixel. This is reasonable since the input information to the mode 1 based compression scheme is projection data.

2.9 Data Compression for a Mode 2 PDC system.

The mode 2 PDC system operates as a true image coder and must therefore be configured to produce an output image that is a compressed but acceptable representation of the input image. In the context of the general three component data compression structure of fig. 2.20, the pre–processor for the mode 2 system includes the projection generation procedure, which in turn implies that the number of projections is an important parameter of mode 2 compression *. Preferably, the pre–processor should have an in–built mechanism for specifying the number of projections required to satisfy a fidelity criterion of image reconstruction, when fed with an input image. This problem is extensively studied in chapter five.

---

* By definition, the number of projections is not as important to mode 1 PDC, as it is determined by the tomographic application.

Invariably, any of the compression techniques for the mode 1 systems may be used in a mode 2 configuration, once the projections have been generated. A relatively fast turnaround Fourier based algorithm for simulating mode 2 PDC is described in [14] and briefly outlined in chapter five. This algorithm is used to investigate the feasibility of projection based block coding of images in the same chapter. The block coding technique operates in a similar manner to block transform coding with the added facility of varying the projections acquired per image sub–block.

The post–processor would also include the reconstructor whatever the actual data compression procedure is.

Evaluating the distortion of the output image of the mode 2 system relative to the input picture, completely specifies the performance as the intermediate distortion between the original and compressed projection data is not important, as in mode 1 based processing.

If the quantizer within the mode 2 system operates, on average, at B_Q bits/pixel and if M_θ projections are used for encoding an $N_1 \times N_2$ dimensioned image field, the final average bit rate is

$$B'_Q = M_\theta \frac{B_Q}{N_1 N_2} \text{bits/pixel} \tag{2.57}$$

and if the original image is quantized at b_{av} bits/pixel then the compression ratio CR is

$$CR = \frac{b_{av}}{B'_Q} \quad (2.58).$$

2.10 Summary and Conclusions

The distinctive methods of transform and finite series expansion image reconstruction have been reviewed in this chapter. The benefits of acceleration and dependability of the convolution backprojection technique, along with its dominant use in existing practical tomographic applications, enable it to be the more viable reconstruction approach in mode 1 PDC.

Discrete representation of the Radon transform (the projection domain generator) has also been discussed for the respective slope–intercept and angle–radius parametric forms of the transform. The model used in this thesis for simulating the projection generation on an angular basis has been described and some pictorial examples of reconstruction are shown.

Information theoretic and stochastic analyses of the projection domain are respectively reported. The former analysis expresses an optimistic result of entropy preservation, on discrete Radon transformation of a discrete-space image function. The limitations of the result lie in the difficulty of realizing exact reconstruction of the spatially discrete image , in practice, despite theoretical possibilities as proven in [5] for the AR–Radon transform (AR–RT) and in Appendix I for the SI–RT.

The stochastic analysis for the AR–RT has been based on the formal representations in [24]. For the AR–RT, the main result is that the projections are uncorrelated in the angle parameter and wide sense stationary (WSS) in the radial parameter. New stochastic results have been formally summarized for the SI–RT and proven in Appendix II. The SI–RT is a whitening process in the slope variable and WSS in the intercept parameter. The results, for both parametric forms of projection generation, are based on conditions of wide sense stationarity of the image field and the use of the dirac aperture function.

Empirical estimation of auto–correlation structure of both angular and radial projection information, derived from typical pictures, indicate that substantial intra–projection (radial) and inter–projection (angular) correlation exists over short to medium radial and angular spans when using the described procedure for projection generation simulation.

An overview of data compression procedures that may support PDC on a mode 1 and 2 basis, respectively, is included. The performance measures, in respect of the fidelity and level of data compression, are outlined for the respective PDC modes.

CHAPTER THREE

COMPRESSION BASED ON THE FREQUENCY STRUCURE

OF PROJECTED INFORMATION

3.1 Introduction

The frequency structure of projected information is well defined with respect to the corresponding image Fourier domain, by the projection slice theorem, introduced in the preceding chapter. This structure may be readily exploited for compression purposes, particularly on the basis of the energy distribution of Fourier information which typically rolls off with increased frequency and the representation of N-dimensional image frequency space in the form of a number of $(N-1)$-dimensional subspaces.

While the projection slice theorem expresses a simple projection–image frequency relationship that is based on the radial parameter of the projection domain, a *similar* correspondence for angular frequency is not easy to obtain. However, the periodic nature of projected data along the angular parameter implies that the corresponding inter–projection frequency domain is essentially discrete. The angular frequency space may be viable for effecting an inter–projection compression scheme to exploit the high auto–correlation (as observed in chapter two) that is obtainable on an angular basis.

This chapter commences with a study of 1–D intra–projection and inter–projection compression schemes, based on the corresponding radial and angular frequency transforms, respectively. The effects of mismatched quantization on the different compression procedures are observed with respect to artifacts produced in reconstructed imagery. Procedures for improved encoding are suggested and implemented.

In viewing the collection of projections generated from a 2–D image plane as a 2–D matrix of data, a typical 2–D block transform coding procedure is implemented for comparisons with the 1–D schemes. Such a 2–D approach naturally stimulates a study of the intrinsic properties of the 2–D frequency plane of projected information; section 3.5 discusses the associated theory of the angle-radius frequency structure of a projection domain and a robust compression algorithm that takes advantage of the structure.

It is important to emphasize that the PDC approach of this chapter is directed towards mode 1 applications where the objective is to compress given projection data, subject to fidelity criteria in the image domain and relative to an image space generated from an uncompressed projection domain.

3.2 Intra–projection Coding (INTRAP):- PDC based on Radial Frequency

Intra–projection compression (INTRAP) is principally motivated by the radial frequency relationship of projection data with the frequency domain of the associated image information. However, a stochastic element also suggests the viable use of INTRAP. The AR–based projection slice theorem for random fields (see equation 2.46) indicates that a WSS image field $f(x,y)$ is translated, on Radon transformation, into a series of uncorrelated WSS projections. This theoretical whitening effect therefore implies that the projections may be encoded or compressed in an uncorrelated manner. This assertion is however not true for typical non–stationary image information. Nevertheless, it is worthwhile investigating the independent projection space processing under WSS assumptions, in the knowledge that compression performance can be improved if inter–projection correlation is also exploited. Such stochastic issues along with associated optimal compression structures are considered in more detail in chapter six.

With respect to the radial frequency structure, INTRAP may be specified by the projection slice theorem (equation 2.5). A tenable INTRAP scheme is to have a collection of radial Fourier transforms of projections at each angle θ and encode them independently. However, since a high quality transform performance (in terms of compaction of energy within the transforms and the production of a substantially decorrelated sequence per transform) is desirable for exploiting the assumed WSS statistics of the projections $P(\theta, t)$, a different form of radial frequency correspondence is considered.

3.2.1. A Cosine Projection Slice Theorem

From the generalized projection theorem (equation 2.4), it is true that

$$\int_a^b P(\theta,t)\, v_m(t)\, dt = \int\int_I f(x,y)\, v_m(x\cos\theta + y\sin\theta)\, dx\, dy \tag{3.1}$$

where $v_m(t)$ may belong to a family $\{v_0(t), v_1(t), \dots\}$ of orthogonal functions such that

$$\int_a^b v_i(t)\, v_j^*(t)\, w(t)\, dt = h_j\, \delta_{ij} \tag{3.2}$$

is valid with respect to the weight function $w(t)$ in the interval $[a, b]$. The parameter δ_{ij} is the Kronecker delta function, that is

$$\delta_{ij} = \begin{cases} 0 & i \neq j \\ 1 & i = j \end{cases} \tag{3.3}$$

and

$$h_j = \int_a^b w(t)\ |v_j(t)|^2\ dt \tag{3.4}.$$

If the integral $\int_a^b P^2(\theta,t)\, w(t)\, dt$ exists and is finite in a Lebesgue sense then a generalized Fourier series representation is possible. Hence

$$P(\theta,t) = w(t) \sum_{i=0}^{\infty} P_{\theta,i}\, v_i(t) \tag{3.5}$$

and also, from (3.1), we may write

$$f(x,y) = w(x\cos\theta + y\sin\theta) \sum_{i=0}^{\infty} f_{\theta,i} v_i(x\cos\theta + y\sin\theta) \tag{3.6}.$$

It follows that the respective series coefficients $P_{\theta,m}$ and $f_{\theta,i}$ are such that

$$P_{\theta,m} = f_{\theta,m} = \int_a^b P(\theta,t)\, v_m^*(t)\, dt \tag{3.7}$$

$$= \iint_I f(x,y)\, v_m^*(x\cos\theta + y\sin\theta)\, dx\, dy \tag{3.8}.$$

If we choose $v_m(t) = \exp(-\jmath\omega_o t)$, $w(t) = 1$ and set $\omega_o = 2\pi(b-a)$ then it can easily be shown that the orthogonality condition of (3.2) is satisfied when $h_j = b - a$ and we have a *discrete frequency* form of the Fourier projection slice theorem. For compression purposes, a more appropriate choice of $v_m(t)$ is $v_m(t) = C_m(t) = \cos(m\cos^{-1} t)$; $C_m(t)$ is the m^{th} order Chebyschev polynomial of the first kind and is orthogonal on the interval $[-1,1]$ with weight $w(t) = (1-t^2)^{-1/2}$ [59]. Specifically,

$$\int_{-1}^{1} C_m(t)\, C_n(t)(1-t^2)^{-1/2}\, dt = \begin{cases} \pi, & m = n = 0 \\ \frac{\pi}{2}, & m = n \neq 0 \end{cases} \tag{3.9}$$

and according to (3.8)

$$P_{\theta,m} = f_{\theta,m} = \int_{-1}^{1} P(\theta,t)\, \cos(m\cos^{-1} t)\, dt \tag{3.10}$$

$$= \iint_I f(x,y)\, \cos(m\cos^{-1}(x\cos\theta + y\sin\theta))\, dx\, dy \tag{3.11}.$$

This correspondence may be regarded as the *generalized Cosine projection slice theorem* and states that the Cosine transformation on projection $P(\theta,t)$ is equivalent to the 2–D Cosine transformation of the image function $f(x,y)$, on the projection orientation θ. This relationship effectively serves as a basis for Cosine radial frequency based INTRAP; the near optimal performance of the deterministic Cosine transform is well known with respect to the optimal statistical Karhunen –Loéve transform (KLT) which offers the minimum mean squared error of transform coding for Gauss–Markov data.

3.2.2 Implementation of Cosine transform based INTRAP

Since a discrete space implementation of INTRAP is required, discrete orthogonality properties of the Chebyschev polynomial must be specified. Such properties may be related to the zeroes t_r of $C_m(t) = \cos(m\cos^{-1} t)$, by [59]

$$\sum_{r=0}^{m-1} C_k(t_r)\, C_l(t_r) = \begin{cases} m, & k = l = 0 \\ \frac{m}{2}, & k = l \neq 0 \\ 0, & k \neq l \end{cases} \tag{3.12}$$

for $k + l < 2m$ and $t_r = \cos[(2r+1)\pi/2m]$ for $r = 0, 1, \ldots, m-1$.

Therefore, for a given set $\mathbf{P}$ of projections $\mathbf{P}_i$, $\mathbf{P} = [\mathbf{P}_0|\mathbf{P}_1|\ldots|\mathbf{P}_{M_\theta-1}]^T$, $\mathbf{P}_i = [P(i,0), P(i,1), \ldots, P(i, M_t-1)]^T$ ($\mathbf{P}$ may be viewed as an $M_\theta \times M_t$ matrix, of projection samples $P(m,n)$, whose i^{th} row vector corresponds to a projection $\mathbf{P}_i$) the discrete Cosine transform (DCT) on each $\mathbf{P}_i$ may be expressed as [59]

$$\begin{aligned} Q_P(i,0) &= \frac{1}{M_t} \sum_{r=0}^{M_t-1} P(i,r) \\ Q_P(i,k) &= \frac{2}{M_t} \sum_{r=0}^{M_t-1} P(i,r) \cos\frac{(2r+1)k\pi}{2M_t} \quad k = 1, 2, \ldots, M_t - 1 \end{aligned} \tag{3.13}$$

The matrix format for the DCT is normally defined [60] as

$$\mathbf{T}_c = \left[\frac{\sqrt{2}}{M_t} \quad k = 0, r = 1, 2 \ldots, M_t{-}1 \;\middle|\; \frac{2}{M_t} \cos\frac{(2r+1)k\pi}{2M_t} \quad k, r = 1, 2 \ldots, M_t{-}1 \right]^T \tag{3.14}$$

where k and r respectively index the rows and columns of $\mathbf{T}_c$. The $\sqrt{2}$ factor permits the orthogonality constraint $\mathbf{T}_c\,\mathbf{T}_c^T = \mathbf{I}$, where $\mathbf{I}$ is an $M_t \times M_t$ identity matrix. These DCTs, over different projections, may be specified by the matrix operation

$$\mathbf{P}\,\mathbf{T}_c^T = [\,\mathbf{T}_c\mathbf{P}_0\,|\,\mathbf{T}_c\mathbf{P}_1\,|\,\cdots\,|\,\mathbf{T}_c\mathbf{P}_{M_\theta-1}\,]^T \tag{3.15}$$

and therefore, the generalized processor of fig. 3.1 suffices for the implementation of INTRAP. The bit allocation and quantization steps are outlined shortly. The Hilbert transform $H(\widehat{\mathbf{P}}_i)$ of each compressed projection $\widehat{\mathbf{P}}_i$ and the summation (i.e. backprojection) over all $H(\widehat{\mathbf{P}}_i)$ produces the reconstructed image matrix $\widehat{\mathbf{F}}$ from the compressed projection domain $\widehat{\mathbf{P}}$.

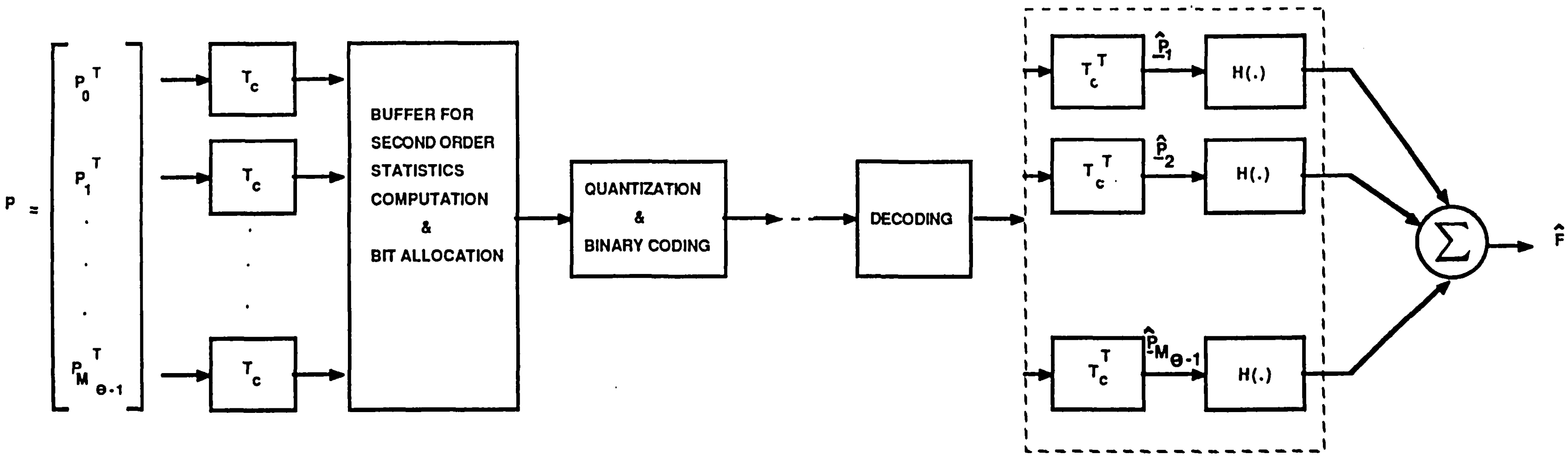

FIG. 3.1 GENERALIZED STRUCTURE FOR INTRA-PROJECTION COMPRESSION.

It is important to mention that a small saving in the overall bit rate (bits/projected sample (bits/ps)) for compressing the information $\mathbf{PT}_c^T$, results from a 'd.c.' condition on (3.11) which ensures that

$$\begin{aligned} P_{\theta,0} = f_{\theta,0} &= \int_{-1}^{1} P(\theta,t)dt \\ &= \int\int_{I} f(x,y)\, dx\, dy \end{aligned} \qquad (3.16).$$

This translates , in practice, to

$$Q_P(i,0) \approx Q_P(j,0) \qquad i \neq j \qquad (3.17)$$

for discrete–space processing. Therefore, one d.c. coefficient suffices in the specification of $\mathbf{PT}_c^T$.

3.2.3 Simulation Approach, Results and Discussion

Projection domain matrices of 128×128 dimensions are generated from image information using the modified AR–DRT procedure discussed in the previous chapter. Bit Allocation and quantization are carried out within the framework of the INTRAP processor (fig. 3.1) to code the discrete cosine transformed projection data.

3.2.3.1 Bit Allocation

The bit allocation formula of Wintz and Kurtenbach [61] is employed for the assignment of bits b_k to the k^{th} transformed sample within the vector $\mathbf{T}_c\mathbf{P}_i$. Sample variances σ_k are computed for the k^{th} sample within a transformed projection $\mathbf{T}_c\mathbf{P}_i$. Hence, the bit assignment is given as

$$b_k = B + 2.0\left(\log_{10} {\sigma_k}^2 - \frac{1}{M_t} \sum_{l=0}^{M_t-1} \log_{10} \sigma_l^2 \right) \qquad (3.18)$$

for $k = 0, 1, \ldots, M_t - 1$. The parameter B is the average bit rate specified for coding a projection, that is, $BM_t = \sum_{k=0}^{M_t-1} b_k$.

3.2.3.2 Quantization Artifacts in INTRAP and Associated Controls

The effects of mismatched quantization on the INTRAP scheme are observed for straightforward uniform quantization of the elements of $\mathbf{PT}_c^T$ according to the bit assignment of (3.18). It is worthwhile viewing the associated distortion artifacts that would result in reconstructed imagery. Some results of this approach are shown for average bit allocations of $B = 2.0, 3.0, 3.5$ and 4.0 bits/projected sample, respectively, in figs 3.2a–d for the MAN image. The strong circular oscillations at the lower bit rates are most unacceptable. These rates are relative to 10 bits/ps for representing original projection data.

3.2.3.2.1 Augmenting INTRAP by Projection Interpolation

One way of circumventing this distortion problem, at the lower bit rates, is to simply encode alternate projections at higher bit rates and interpolate for missing projections at the reception or retrieval point of the INTRAP scheme. Such an approach, reported by Acharaya et al [62], uses Kalman estimators to supply reconstruction algorithms with extra (estimated) projections for time varying reconstructions of heart movements.

In our case, a simple linear interpolation on the circular path between projections is used to approximate projected information which is not stored or transmitted. The circular path actually refers to one over a cylindrical surface as the parameters (θ, t) of the AR–RT describe a 'line' on a surface of a half–infinite cylinder [25] as seen in fig 3.3a. The prevalent auto–correlation over short spans between projections evidently buttresses the interpolation based INTRAP scheme. This linear interpolation $I(\widehat{\mathbf{P}}_k, \widehat{\mathbf{P}}_{k+1})$ on a circular path $\Delta\beta$ (see fig 3.3a; cylinder has unit radius) between compressed projections $\widehat{\mathbf{P}}_k$ (on angle θ_k) and $\widehat{\mathbf{P}}_{k+2}$ (on θ_{k+2}) for an approximate projection $\widehat{\mathbf{P}}'_{k+1}$ (at θ_{k+1}) may be described by

$$\widehat{P}'(\theta_{k+1}, l\Delta t) = I(\widehat{\mathbf{P}}_k, \widehat{\mathbf{P}}_{k+1}) = \frac{1}{\Delta\beta} \cdot [\widehat{P}(\theta_{k+2}, l\Delta t)(\theta_{k+2} - \theta_{k+1}) + \widehat{P}(\theta_k, l\Delta t)(\theta_{k+1} - \theta_k)] \tag{3.19}$$

Fig. 3.2a INTRAP (Mismatched Quantization)
2.0 bits/ps (MAN)

Fig. 3.2b INTRAP (Mismatched Ouantization)
3.0 bits/ps (MAN)

Fig. 3.2cINTRAP (Mismatched Quantization)
3.5 bits/ps (MAN)

Fig. 3.2d INTRAP (Mismatched Quantization)
4.0 bits/ps (MAN)

where $l = 0, 1, \ldots, M_t - 1$, $\theta_m = m\pi / M_\theta$, $m = 0, 1, \ldots, M_\theta - 1$, $\Delta\beta = \theta_{k+2} - \theta_k$ and Δt is the radial sampling interval between integration lines of the modified AR–DRT. The values $\widehat{P}'(\theta_m, l\Delta t)$ and $\widehat{P}(\theta_m, l\Delta t)$ for $l = 0, 1, \ldots, M_t - 1$ are essentially components of the vectors $\widehat{\mathbf{P}}'_m$ and $\widehat{\mathbf{P}}_m$ respectively. Fig. 3.3b depicts the interpolator that would be required in the generalized processor of fig. 3.1, precisely at the output of the inverse frequency transform modules and at the input of the reconstruction filters (i.e. the Hibert transformations). A non–trivial element of the interpolation is the preservation of end projections i.e. $\widehat{\mathbf{P}}_0, \widehat{\mathbf{P}}_1$ or $\widehat{\mathbf{P}}_{M_\theta - 2}, \widehat{\mathbf{P}}_{M_\theta - 1}$, if an even number of projections are required at the reconstruction point since the operator $I(\widehat{\mathbf{P}}_k, \widehat{\mathbf{P}}_{k+2})$ only generates an odd number of projections for an input set of M_θ projections.

Figs. 3.4a and 3.4b are results of intra–projection compression of projection data of the MAN image for bit rates of approximately 2.0 bits/ps and 1.75 bits/ps. Half of the 128 projections derived per image are encoded at 4.0 bit/ps and 3.5 bits/ps, respectively, with the other half regenerated by interpolation at the receiver. The distortion is still slightly visible at the lower rate.

3.2.3.2.2 Matched Quantization

The interpolation in conjunction with uniform quantization offer a facility of obtaining acceptable reconstructions at lower bit rates, however, the overall bit rate is still relatively high and the interpolation introduces more complexity into the INTRAP scheme. Therefore, distribution dependent Max quantization [63] is required to improve the performance. Empirical measures (see figs. 3.5a–b) of the distributions of the respective radial (Cosine) frequency transformed projection information, associated with the MAN and BOX images, clearly indicate that the spread of values are non–uniform.

Detailed simulations [64] have indicated that the Laplacian distribution is largely representative of Cosine transformed coefficients of most types of imagery. A confirmatory test, shows the Laplacian Max quantizer to have a 1dB advantage

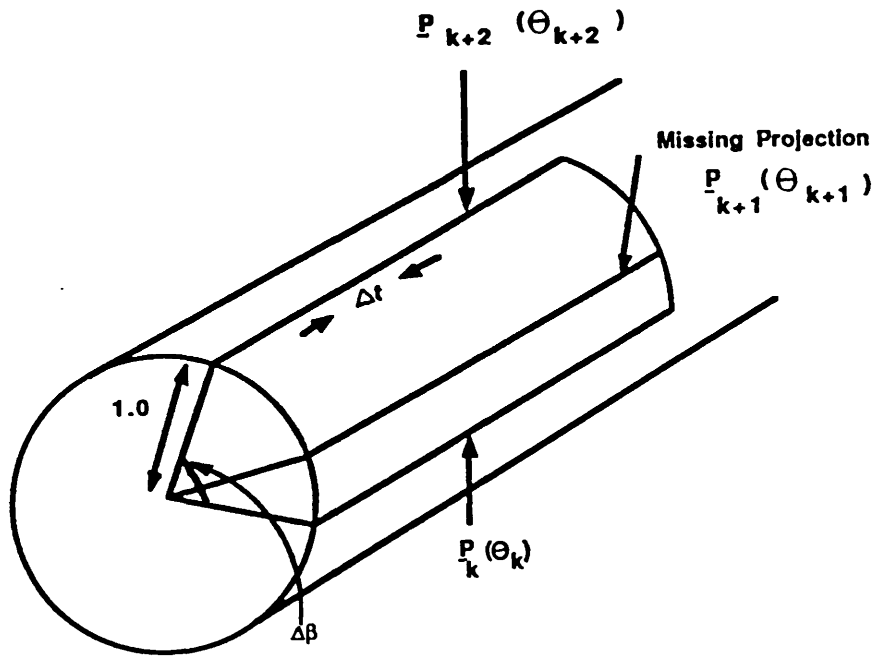

FIG. 3.3a. GEOMETRY FOR INTERPOLATING FOR P_k FROM P_{k+1} AND P_{k+2} OVER THE CIRCULAR DISTANCE $\Delta\beta$ ON THE HALF-INFINITE CYLINDER SPACE OF THE PROJECTION DOMAIN.

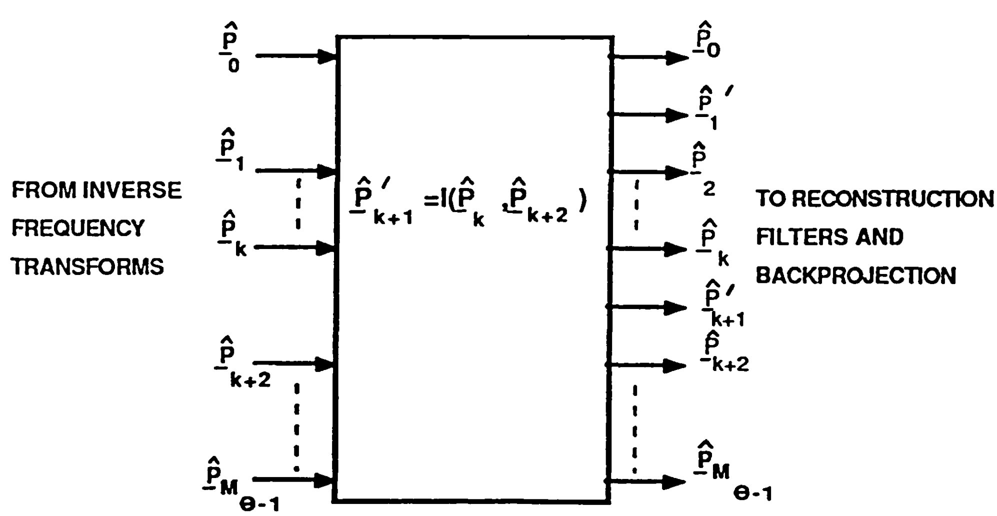

FIG. 3.3b EXTRA PROCESSING FOR INTERPOLATION AT RECEIVER/RETRIVAL POINT

Fig. 3.4a Augmented INTRAP
(Projection Interpolation) 2.0 bits/ps
(MAN)

Fig. 3.4b Augmented INTRAP
(Projection Interpolation) 1.75 bits/ps
(MAN)

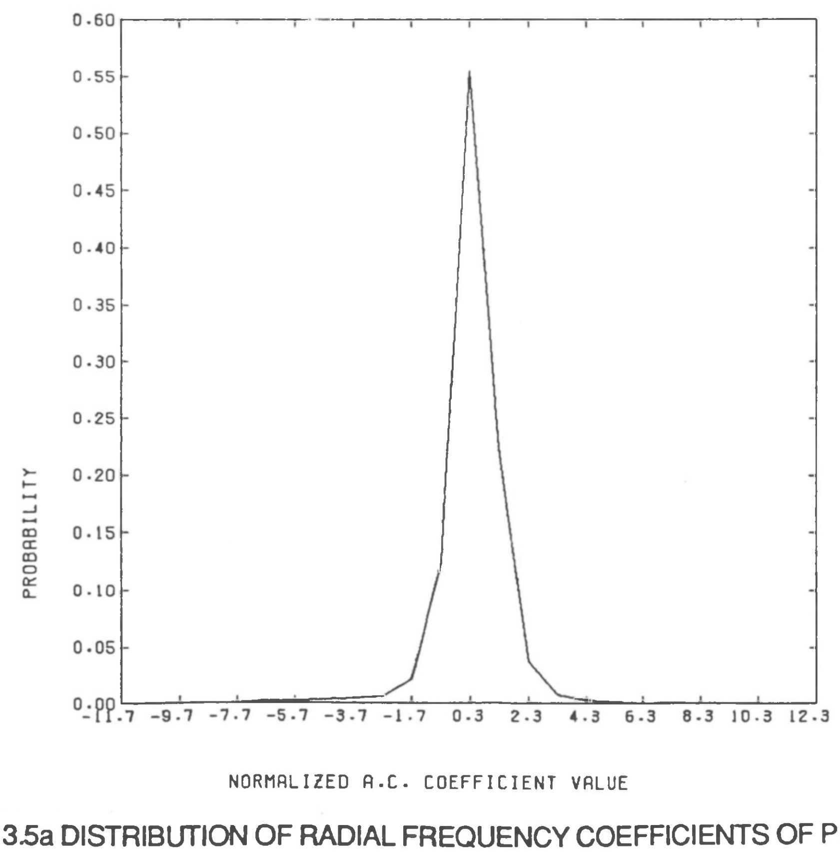

FIG. 3.5a DISTRIBUTION OF RADIAL FREQUENCY COEFFICIENTS OF PROJECTED 'MAN'

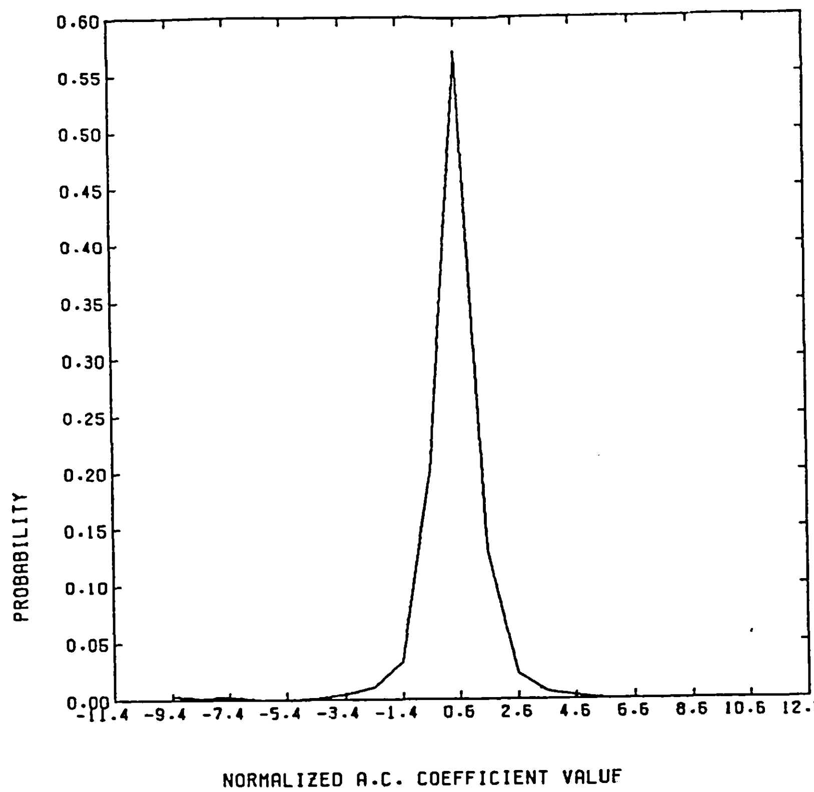

FIG. 3.5b DISTRIBUTION OF RADIAL FREQUENCY COEFFICIENTS OF PROJECTED 'BOX'

System	Bit Rate bits/ps *	NMSE(P) 10^{-4}	NMSE(F) 10^{-3}
INTRAP	1.5	2.786	6.659
	2.0	2.021	4.844
	2.5	1.760	2.713
	3.0	0.975	1.895
	4.0	0.484	0.813
INTERP	1.0	2.579	7.459
	1.5	1.116	3.019
	2.0	0.736	1.545
	2.5	0.485	0.895

* (bits/projected sample)

Table 3.1 : Simulation Results of the INTRAP and INTERP schemes applied to Projected MAN data

of less distortion over a Gaussian quantizer and 1.2dB over the uniform quantizer for the INTRAP scheme.

Comprehensive objective results based on Laplacian quantization for the MAN image, are found in table 3.1. The numerical distortion measure NMSE(P) is associated with the distortion due to encoding of the projection domain data and NMSE(F) evaluates the distortion of the image reconstructed from the encoded projection data $\widehat{\mathbf{P}}$, relative to the image reconstruction from original data $\mathbf{P}$. Some pictorial results are shown in figs 3.6a–c for the MAN image and in figs. 3.6d and 3.6f, for the BOY and BOX images, respectively.

Clearly, the interpolation process can enable further reduction in bit rate with little additional distortion; results of interpolation combined with appropriately matched quantization are shown in figs. 3.7a–c at 1.0 bit/ps. Although there is no exceptional degradation in these reconstructions, the relative blur of feature detail is noticeable. Table 3.2 shows the corresponding distortion levels produced by this last procedure.

3.3 Inter–projection Coding (INTERP):- PDC based on Angular Frequency Structure

An inter–projection compressor (INTERP) would largely depend on the angular properties of projected information. The geometry for generating $P(\theta, t)$ (cf. fig 2.1) indicates that it is *definitely* periodic with period 2π and *essentially* periodic with period π. More generally

$$P(\theta + k\pi, (-1)^k t) = P(\theta, t) \tag{3.20}$$

The above condition defines a Mõbius strip property [65,pg 440] of the projection domain function $P(\theta, t)$ where the strip is connected at 0 and π. The periodicity over 2π allows the Fourier representation

$$P(\theta, t) = \sum_{k=-\infty}^{\infty} P_{k,t}\, e^{\jmath k\theta} \tag{3.21}$$

Fig. 3.6a INTRAP (Matched Quantization)
2.0 bits/ps (MAN)

Fig. 3.6b INTRAP (Matched Quantization)
2.5 bits/ps (MAN)

Fig. 3.6c INTRAP (Matched Quantization)
3.0 bits/ps (MAN)

Fig. 3.6d INTRAP (Matched Quantization)
2.0 bits/ps (BOY)

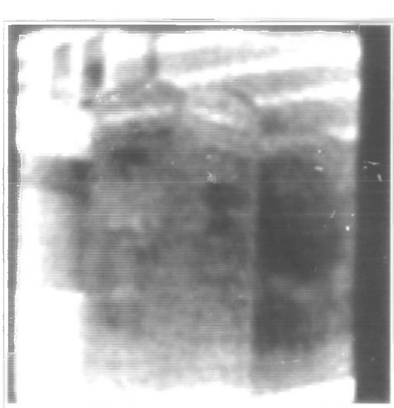

Fig. 3.6e INTRAP (Matched Quantization)
2.0 bits/ps (BOX)

Fig. 3.7a INTRAP (Matched Quantization/Projection Interpolation), 1.0 bits/ps (MAN)

Fig. 3.7b INTRAP (Matched Quantization/Projection Interpolation) 1.0 bits/ps. , (BOY).

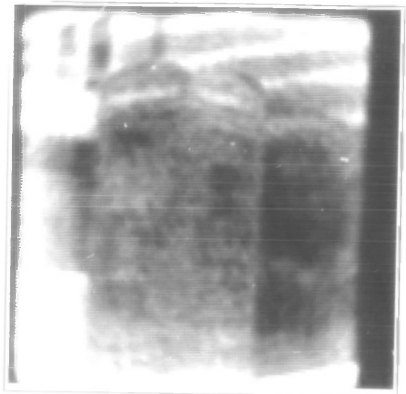

Fig. 3.7c INTRAP (Matched Quantization/Projection Interpolation), 1.0 bits/ps. , (BOX).

Image	NMSE(P) 10^{-4}	NMSE(I)* 10^{-5}	NMSE(F) 10^{-3}
MAN	2.021	0.65	6.027
BOY	1.597	7.77	23.813
BOX	2.806	11.07	13.412

* (NMSE distortion due to interpolation)

Table 3.2 : Distortion Results of Augmented INTRAP (with appropriate quantization) at 1.0bit/ps.

with

$$P_{k,t} = \frac{1}{2\pi} \int_0^{2\pi} P(\theta, t)\, e^{-jk\theta}\, d\theta \tag{3.22}$$

and therefore, $P(\theta, t)$ has a discrete spectrum in θ at each radial position t. The number of significant coefficients $P_{k,t}$ depends upon the angular smoothness (or correlation) of $P(\theta, t)$. At this stage, the focus is to exploit the angular correlation for a given radial point t, independently of all other radial points. That is, INTERP is the angular equivalent of INTRAP.

The WSS considerations of the previous section would deem the INTERP process unnecessary especially if the image signal statistics (and therefore, statistics of its projection domain) were Gaussian, as $P(\theta, t)$ would be necessarily independent in the angular specification. Nevertheless, as earlier empirical measures have shown, substantial correlation prevails for most types of imagery.

Here, the same INTRAP processor structure is used for implementing INTERP; the matrix $\mathbf{P}$ of projections is simply transposed at the input of fig. 3.1 i.e. the matrix $\mathbf{T}_c\mathbf{P}$ is processed by the encoder rather than $\mathbf{P}\mathbf{T}_c$.

3.3.1 Simulation Results and Discussion

The mismatched uniform quantization produces a rather streaky effect, radiating from the image centre as is observed in figs 3.8a–b. The overall image structure is not as severely distorted as the results from INTRAP under the same conditions.

Introducing Max quantization (for the Laplacian distribution) again improves the pictorial appearance, as seen in figs. 3.8c–e. Objective results of the INTERP scheme , in table 3.1, show that, at 2.0 bits/ps, its performance is of the order of 4dB better than the INTRAP scheme. The reasons for such improved compression may be attributed to the angular–radial frequency spectral shape. This interesting spectral structure is examined in section 3.5.

Fig. 3.8a INTERP (Mismatched Ouantization)
1.5 bits/ps (MAN)

Fig. 3.8b INTERP (Mismatched Quantization)
2.0 bits/ps (MAN)

Fig. 3.8c INTERP (Matched Quantization)
1.0 bits/ps (MAN)

Fig. 3.8d INTERP (Matched Quantization)
1.5 bits/ps (MAN)

Fig. 3.8e INTERP (Matched Quantization)
2.0 bits/ps (MAN)

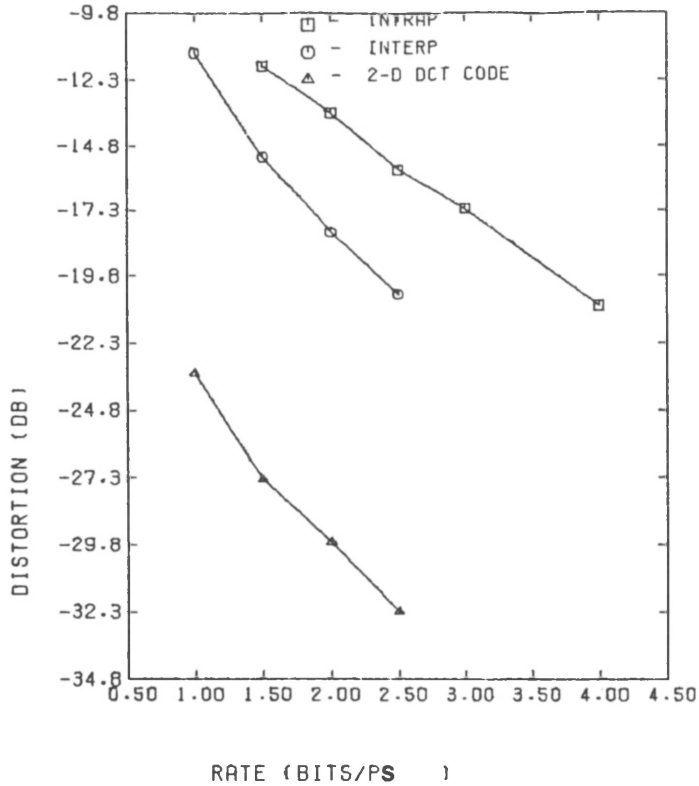

FIG. 3.9 DISTORTION-RATE COMPARISON OF 2-D DCT, INTERP AND INTRAP BASED PROCESSING OF PROJECTED 'MAN' DATA

Fig. 3.10a 2-D DCT (16 x 16), 1.0 bit/ps (MAN)

Fig. 3.10b 2-D DCT (16 x 16), 1.5 bits/ps (MAN)

3.4 Comparisons of INTRAP and INTERP with 2–D DCT Coding of Projection Data

A graphical distortion–rate comparison , in fig. 3.9, of the INTRAP and INTERP processors with 2–D DCT block coding of the projection matrix of the MAN image confirms the expected result that a 2–D approach that exploits the intra–projection and inter–projection based correlations, would improve the performance. The 2–D block coding procedure is similar, in principle, to the 3–D block transform coding experimentation of Jain and Jain [15] for 2–D projected data. Figs 3.10a–b are some corresponding picture results of the block code for the MAN image.

3.5 The 2–D AR Frequency Structure of the Projection Domain

The quality of the 2–D block coding approach motivates a study of the intrinsic 2–D frequency structure of projected information and a possible application of the structure within a PDC framework. Accordingly, this section introduces the not well known theory of the band–regional shape of the 2–D AR–RT. Various implications of the theory are discussed in accordance with PDC and a compression algorithm that exploits the band shape is discussed in section 3.5.3.

The theoretical background is based on an approach of Rattey and Lindgren, outlined in [66]; they have considered the sampling constraints, of a continuous–space projection domain, based on the 2–D AR spectral characteristics and have applied such conditions to tomographic image reconstructions from limited projection data [67].

3.5.1 Theoretical Background

If $f(x,y)$ in I is solely described by an impulse $\delta(x-x_o, y-y_o)$ at a polar co-ordinate location (r_o,ϕ_o) with respect to the origin, where $x_o = r_o\cos\phi_o$, $y_o = r_o\sin\phi_o$, then according to equation (2.1), the AR–RT of $f(x,y)$ is

$$\begin{aligned} P_\delta(\theta,t) &= \int_{-\infty}^{\infty}\int_{-\infty}^{\infty} \delta(x-x_o, y-y_o)\delta(t-(x\cos\theta + y\sin\theta))\,dx\,dy \\ &= \delta(t-(x_o\cos\theta + y_o\sin\theta)) \qquad (3.23a) \end{aligned}$$

or equivalently

$$P_\delta(\theta,t) = \delta(t - r_o \cos(\theta - \phi_o)) \tag{3.23b}$$

where $\phi_o = \tan^{-1} y_o/x_o$. The unbounded spatial limits of $f(x,y)$ effectively invoke a band–limitation [28] on the frequency space of $P_\delta(\theta,t)$. In addition, (3.23b) indicates that the projection domain of an impulse is completley described by a sinusoidal line mass (see fig. 3, [66]).

Expressing an arbitrary $f(x,y)$ in terms of a *collection* of impulses, implies that

$$f(x,y) = \int_{-\infty}^{\infty}\int_{-\infty}^{\infty} f(x_o,y_o)\,\delta(x-x_o,y-y_o)\,dx_o\,dy_o \tag{3.24}$$

and the corresponding Radon transform

$$\begin{aligned} P(\theta,t) &= \int_{-\infty}^{\infty}\int_{-\infty}^{\infty} f(x_o,y_o)\,\delta(t-(x_o\cos\theta + y_o\sin\theta))\,dx_o\,dy_o \\ &= \int_{0}^{\infty}\int_{0}^{2\pi} f(r_o\cos\phi_o, r_o\sin\phi_o)\,|r_o|\,\delta(t - r_o\cos(\theta-\phi_o))\,dr_o\,d\phi_o \end{aligned} \tag{3.25}$$

is a weighted continuous sum of line masses.

Since $P_\delta(\theta,t)$ (in (3.23b)) is effectively the point spread function of the Radon transform, by superposition, its Fourier structure adequately describes the Fourier domain of $P(\theta,t)$ associated with an arbitrary $f(x,y)$. Evaluating the Fourier transform $P_\delta(\omega_\theta,\omega_t)$ of $P_\delta(\theta,t)$, yields

$$\begin{aligned} P_\delta(\omega_\theta,\omega_t) &= \int_{0}^{2\pi}\int_{0}^{\infty} \delta(t - r_o\cos(\theta-\phi_o))\,e^{-\jmath\omega_\theta\theta}\,e^{-\jmath\omega_t t}\,d\theta\,dt \\ &= \int_{0}^{2\pi} e^{-\jmath\omega_t r_o\cos(\theta-\phi_o)}\,e^{-\jmath\omega_\theta\theta}\,d\theta \end{aligned} \tag{3.26}$$

When the periodic complex exponential $\exp(-\jmath\omega_t r_o\cos(\theta-\phi_o))$ is re–expressed as $\exp(-\jmath\omega_t r_o\sin((\theta-\phi_o)-\pi/2))$, a Fourier series representation results:

$$e^{\jmath\omega_t r_o\sin((\theta-\phi_o)-\pi/2)} = \sum_{m=-\infty}^{\infty} J(m,\omega_t r_o)\,e^{\jmath m((\theta-\phi_o)-\pi/2)} \tag{3.27}$$

where an m^{th} order Bessel function $J(m,\omega_t r_o)$ of the first kind is defined with respect to the periodic angular parameter θ :

$$J(m,\omega_t r_o\sin\theta) = \frac{1}{2\pi}\int_{-\pi}^{\pi} e^{\jmath(\omega_t r_o\sin\theta - m\theta)}\,d\theta \tag{3.28}$$

Using (3.27) in (3.26) gives

$$P_\delta(\omega_\theta,\omega_t) = \sum_{m=-\infty}^{\infty} 2\pi J(m,\omega_t r_o \sin\theta) e^{-\jmath(\phi_o+\pi/2)} \cdot \delta(\omega_\theta - m) \qquad (3.29).$$

Essentially, the real valued function $J(m,\omega_t r_o \sin\theta)$ defines a discrete angular spectrum for $P_\delta(\theta,t)$ of bandwidth B_δ which may be explicitly specified by invoking the well known Carson's rule of Frequency Modulation (FM) theory [52] for sinusoidal waveforms. In particular, an intermediate bandwidth for $P(\theta,t)$ may be written as

$$B_\delta = 2(1+|\omega_t r_o|) \qquad (3.30).$$

Wideband and narrowband [50] frequency structures of projected information may be approximately band–limited to

$$B_\delta = 2\ |\omega_t r_o| \qquad (3.31a)$$

and

$$B_\delta = 2 \qquad (3.31b)$$

respectively.

If the image function $f(x,y)$ is bounded within a region I by a circle of radius R_f, then by the superposition relation of (3.24) and the generalized bandwidth of (3.30), it follows that the 2–D AR Fourier structure $P(\omega_\theta,\omega_t)$ of $P(\theta,t)$ may be completely specified as

$$P(\omega_\theta,\omega_t) = \int_0^{2\pi}\int_0^{\infty} f(r_o\cos\phi_o, r_o\sin\phi_o)\, P_\delta(\omega_\theta,\omega_t)\ |r_o|\ dr_o\, d\phi_o \qquad (3.32a)$$

when

$$m = |\omega_\theta| \leq \frac{B_\theta}{2} = |\omega_t R_f| + 1 \qquad (3.32b)$$

where

$$P_\delta(\omega_\theta,\omega_t) = \sum_{m=-B_\delta/2}^{B_\delta/2} 2\pi\, J(m,\omega_t r_o)\, e^{-\jmath m(\phi_o+\pi/2)} \cdot \delta(\omega_\theta - m) \qquad (3.32c)$$

and for $m > B_\theta/2$, $P(\omega_\theta, \omega_t)$ is effectively zero. The corresponding band–region of $P(\omega_\theta, \omega_t)$ is illustrated in fig. 3.11a and is seen to have a bow–tie shape when band–limited to B_t in the radial frequency.

3.5.2 Implications of 2–D Frequency Structure for PDC

It is instructive to briefly examine some relevant implications of the well defined Fourier structure of (3.32), with respect to PDC.

3.5.2.1 Band–shape Effects on INTRAP and INTERP

The bow–tie shape may effectively explain the limitations of the 1–D intra–projection compression approach relative to the inter–projection system, as the spectral spread in the radial frequency co–ordinate is considerably emphasized over the angular frequency content by a factor equivalent to the radius R_f of projection. Thus, distortion effects may also be more predominant in the radial frequency based system INTRAP.

The distortion from INTRAP and INTERP as implemented in the previous sections, is primarily due to the quantization and bit allocation processes. For INTRAP, the latter procedure, at low bit rates, implicitly distorts the band–shape of fig. 3.11a by setting many bits to null i.e. discarding several coefficients. This effect is clearly less destructive for INTERP. Inefficient quantization contributes to the production of artifacts for both configurations. However, the structural deformation in reconstructed imagery assosciated with INTRAPis the more unacceptable.

3.5.2.2 Sampling Effects of the Band-shape

Fig. 3.11a strictly portrays the basedband region of the Fourier structure of continuous space projection domain information $P(\theta, t)$. The bow–tie shape is replicated in the non–aliased fashion of fig. 3.11b when $P(\theta, t)$ is adequately sampled (in the Nyquist sense) in a rectangular format. That is

$$P(k\Delta\theta, l\Delta t) = \sum_{m=-\infty}^{\infty} \sum_{n=-\infty}^{\infty} P(\theta, t)\delta(\theta - m\Delta\theta, t - n\Delta t) \tag{3.33}$$

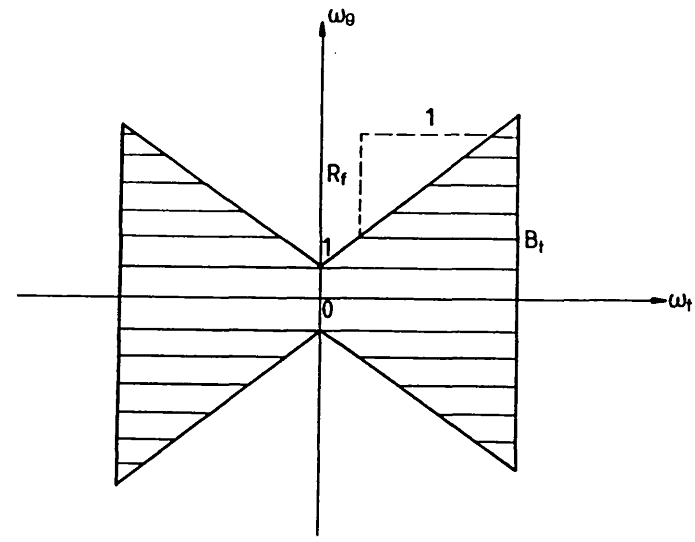

FIG. 3.11a 2-D (BASEBAND) FOURIER STRUCTURE OF P(θ,t).

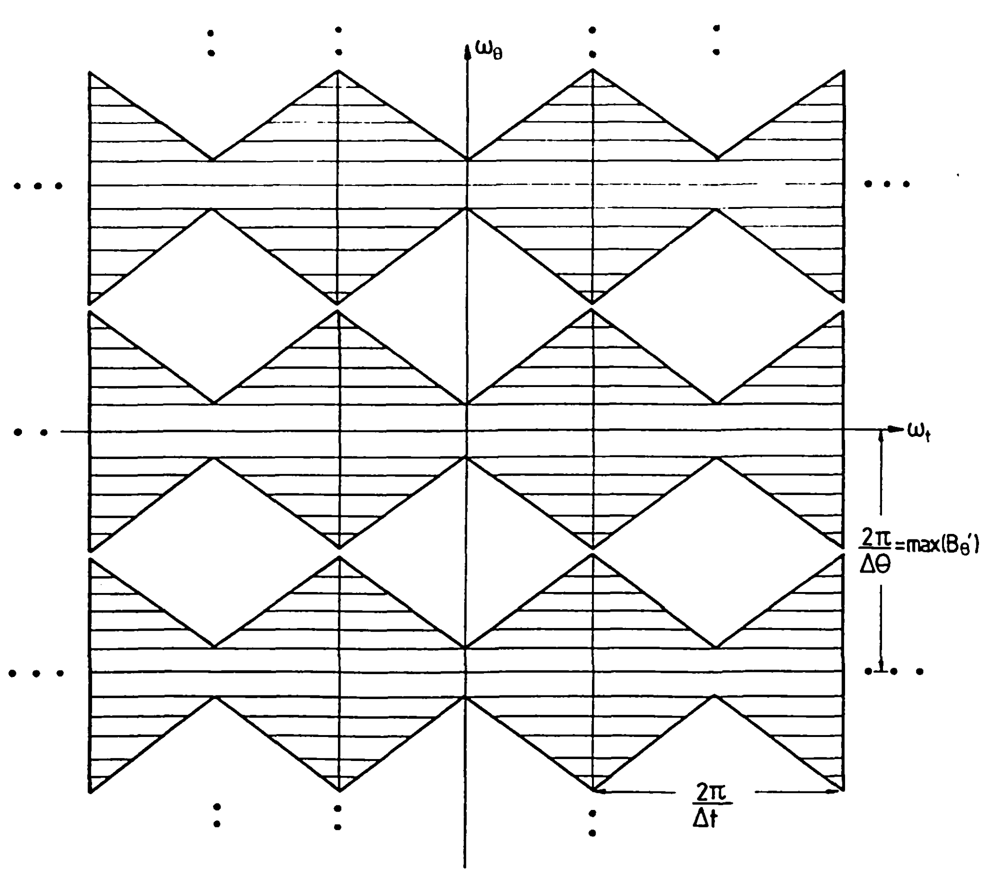

FIG. 3.11b 2-D FOURIER STRUCTURE OF RECTANGULARLY SAMPLED P(θ,t).

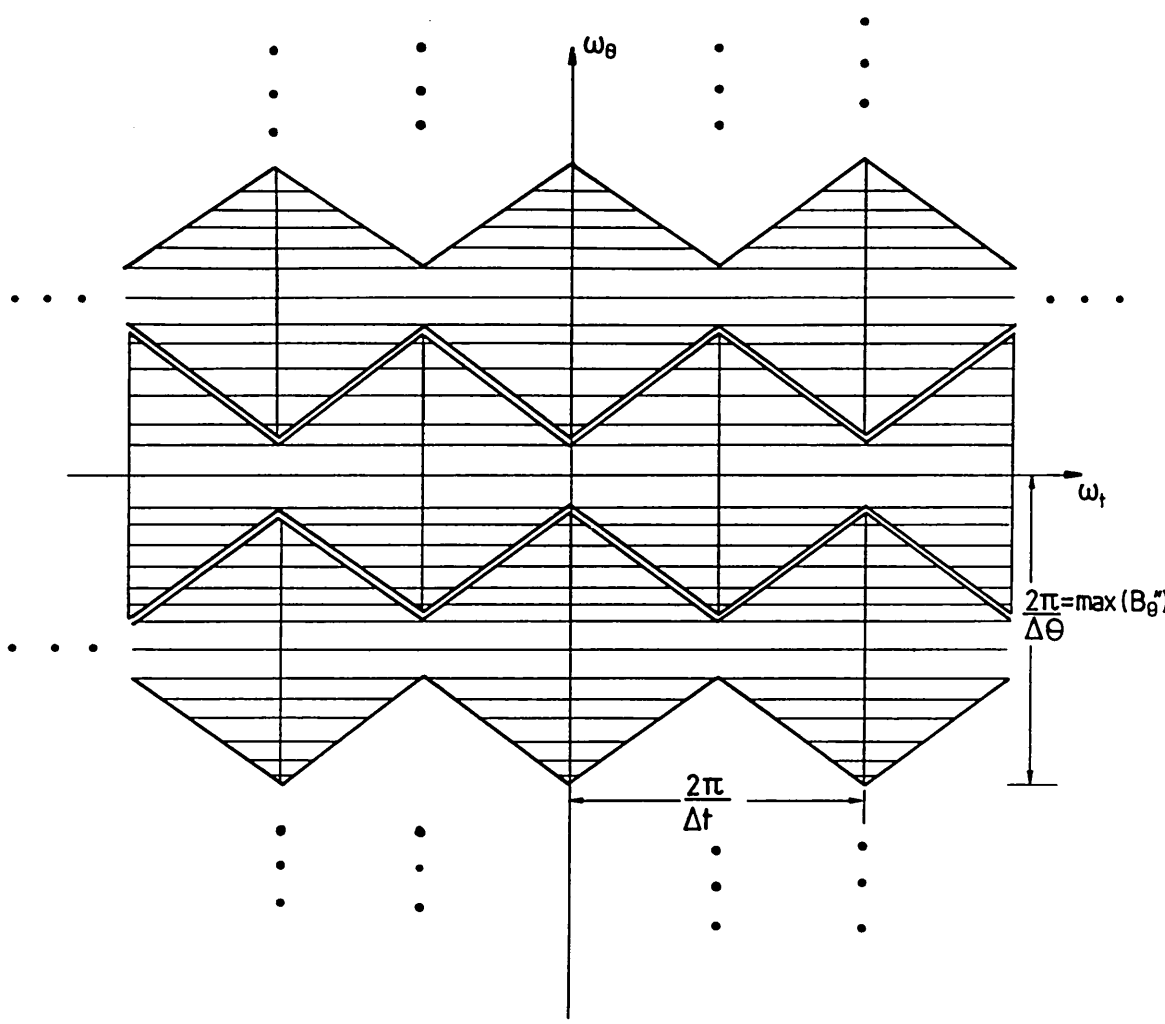

FIG. 3.11c FOURIER STRUCTURE OF HEXAGONALLY SAMPLED P(θ,t).

for $\Delta t < 2\pi/B_t, \Delta\theta < 2\pi/B'_\theta, B'_\theta = 2(1 + |B_t R_f|)$.

It has been pointed out [66] that when $P(\theta, t)$ is sampled hexagonally i.e. [68]

$$P(k'\Delta\theta, l'\Delta t) = \sum_{k=-\infty}^{\infty} \sum_{l=-\infty}^{\infty} P(\theta, t)\delta(\theta - \frac{2k-l}{2}\Delta\theta, t - l\Delta t) \qquad (3.34)$$

with $\Delta t < 2\pi/B_t, \Delta\theta < 2\pi/B''_\theta, B''_\theta > B'_\theta$, the ω_θ– ω_t frequency plane is more efficiently utilized, as seen in fig 3.11c; it is observable that a horizontal spectral shift in the ω_θ–ω_t plane , by $\pi/\Delta t$, yields a periodically extended hexagonal shaped band–region about the baseband. The corresponding spatial domain (of the shifted spectrum) sample arrangement is known to have a 13.4 percent reduction of the mean sampling density relative to rectangular sampling [66]. The Möbius strip property (see equation (3.20)) of $P(\theta, t)$ can further decrease the sampling requirements to nearly 50 percent below rectangular sampling [66] for the projection domain.

The benefits of efficient sampling procedures to compression are obvious, however, accompanying implementation problems arise. Although Mersereau [68] has presented several hexagonal sampling based linear algorithms (e.g. DFT, digital filter designs) of rectangular array processing, the fact remains that many algorithms and hardware systems are configured as a sequence of 1–D row (column) processors, cascaded by another set of column (row) implementations. Rectangular sampling is effectively a straightforward extension of the row–column 1–D procedures and is predominantly adhered to.

While the gains of hexagonal sampling are not incorporated into the algorithm to be described in the next section, the intrinsic bow–tie shape of the frequency domain of $P(\theta, t)$ provides the basic support for the compression procedure.

3.5.3 A 'Bow-tie' Algorithm for PDC

The continuous–space Fourier transform of $P(\theta, t)$, explicitly defined in (3.31), immediately suggests a controlled band–limiting procedure on the discrete Fourier space generated from the (discrete) projection domain $\mathbf{P} = [\mathbf{P}_0|\mathbf{P}_1|\ldots|\mathbf{P}_{M_\theta-1}]^T$. Specifically, if the DFT matrix $\mathbf{T}_f$ is such that

$$\mathbf{T}_f = \left[(-1)^n \exp(-\jmath\frac{2\pi mn}{N}) \quad m,n = 0,1,\ldots,N-1\right] \tag{3.35}$$

and also if it is assumed, for convenience, that $N = M_\theta = M_t$ i.e. $\mathbf{P}$ is a square matrix, then a centered 2–D DFT spectrum of $\mathbf{P}$ is generated from the transformation

$$\mathbf{Q} = \mathbf{T}_f\,\mathbf{P}\,\mathbf{T}_f^T \qquad (3.36).$$

Since rectangular array processing is assumed, $\mathbf{Q}$ is equivalently obtained from the 2–D z transform; its elements are:

$$Q(z_1', z_2') = \sum_{k=0}^{N-1}\Big[\sum_{l=0}^{N-1} P(k,l)(-1)^{l+k} z_2^{-l}\Big]\, z_1^{-k} \tag{3.37}$$

where $z_1^{-k} = e^{-\jmath\omega_\theta k\Delta\theta}, z_2^{-l} = e^{-\jmath\omega_t l\Delta t}$ and $z_1' = z_1 e^{-\jmath\pi} = e^{-\jmath\omega_\theta'\Delta\theta}$, $z_2' = z_2 e^{-\jmath\pi} = e^{-\jmath\omega_t'\Delta t}$; $P(k,l)$ are the elements of $\mathbf{P}$, obtained under the assumption of Nyquist sampling of $P(\theta,t)$. The z kernels (z_1', z_2') are related to (3.36) via the relations

$$\omega_\theta' = \frac{2\pi}{N\Delta\theta}(m_1 + \frac{N}{2}) = m_1'\Delta\omega_\theta \qquad \begin{array}{l} m_1' \in [0, N-1] \\ m_1 \in [\frac{-N}{2}, \frac{N}{2} - 1] \end{array} \tag{3.38a}$$

and

$$\omega_t' = \frac{2\pi}{N\Delta t}(m_2 + \frac{N}{2}) = m_2'\Delta\omega_t \qquad \begin{array}{l} m_2' \in [0, N-1] \\ m_2 \in [\frac{-N}{2}, \frac{N}{2} - 1] \end{array} \tag{3.38b}$$

respectively where $\Delta\omega_\theta = \frac{2\pi}{N\Delta\theta}$ and $\Delta\omega_t = \frac{2\pi}{N\Delta t}$ are the angular and radial frequency sampling intervals of the discrete transformation of equation (3.36). The integer variables (m_1', m_2') effectively index the locations of Fourier samples in the matrix $\mathbf{Q}$ and (m_1, m_2) index the locations of the samples in discrete Fourier space.

Utilizing (3.38) in the bandwidth constraint of (3.32), permits the following condition on $Q(z_1', z_2')$:

$$Q(m_1', m_2') = 0, \qquad \text{for} \qquad m_1' > \left(\frac{2\pi}{N\Delta\theta}\right)^{-1}\Big\{\Big[R_f \cdot \frac{2\pi m_2'}{N\Delta t}\Big] + 1\Big\} \tag{3.39}$$

where in this case [.] implies the nearest integer to the argument.

Therefore, a simple procedure for compressing given projection data in $\mathbf{P}$ evolves, which commences with the transformation of (3.36) followed by a systematic discarding of coefficients or spectral shapening, according to (3.39). Denoting the latter operation on $\mathbf{Q}$ as $BWT(\mathbf{Q})$ which yields a modified matrix $\mathbf{Q}_{BW}$ and a subsequent encoding operation by $E_c(\mathbf{Q}_{BW})$ which results in the output $\widehat{\mathbf{Q}}_{BW}$, a compressed version of $\mathbf{P}$ is obtained from

$$\widehat{\mathbf{P}} = \mathrm{Re}\left\{ \mathbf{T}_f \widehat{\mathbf{Q}}^*_{BW} \mathbf{T}_f^T \right\} \tag{3.40}$$

where $\widehat{\mathbf{Q}}^*_{BW}$ is the complex conjugate of the output of $E_c(\mathbf{Q}_{BW})$.

The aggregate of these steps is called the *bow–tie algorithm* where the bow–tie clearly refers to the spectral shapening, according to the baseband region of fig. 3.11a.

3.5.4 Simulation Procedure, Results and Discussion

The basic procedures of the bow–tie algorithm are depicted in fig. 3.12. The respective spectral shapening and encoding operations $BWT(.)$ and $E_c(.)$ are the more important steps and therefore, their respective configurations are comprehensively discussed.

3.5.4.1 Spectral Shapening

The model of fig. 2.7 is used to generate the discrete space projected information in $\mathbf{P}$ and as such, the angular and radial sampling intervals $\Delta\theta$ and Δt are well defined. Therefore, $BWT(.)$ may readily be implemented.

From a 128×128 projection matrix $\mathbf{P}$, a corresponding Fourier space is generated using (3.35). Applying $BWT(.)$ to $\mathbf{Q}$ for $\Delta\theta = \pi/128$ and $\Delta t = 1.414$, enables about 5K of the 16K Fourier coefficients to be methodically dispensed with. Table 3.3 contains the numerical distortion results of this operation in the respective projection and image domains (the encoder $E_c(.)$ is bypassed). An immediate comparison of table 3.3 with tables 3.1 and 3.2 reveals the apparently disturbing fact

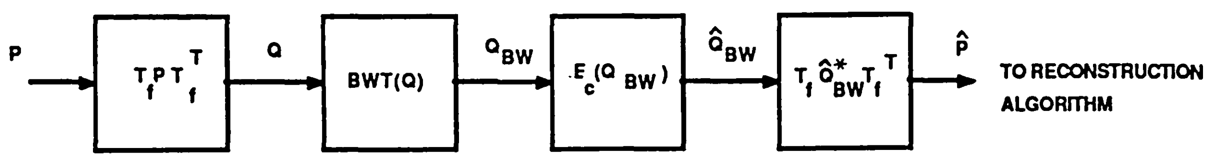

FIG. 3.12 BASIC PROCEDURES FOR BOW-TIE AGORITHM FOR PDC.

Image	NMSE(P) 10^{-2}	NMSE(F) 10^{-3}
MAN	0.143	1.385
BOY	0.135	0.574
BOX	0.333	2.46

Table 3.3 : Quantitative Distortion Results due to the Bow–tie structure based Spectral Shapening

that the distortion NMSE(P), produced in the projection domain, is substantially higher from the spectral shapening output. The estimated distortion is about 8dB more than that obtained from the INTRAP processor at 2.0bits/ps in the projection domain of the MAN image and up to 11dB for the same comparison for the BOX image. On the other hand, the pattern of high distortion that results from $BWT(.)$ is limited if not reversed in the image domain; in particular, the NMSE(F) for INTRAP at 2.0bits/ps is 3.3dB more than the associated distortion from $BWT(.)$ for the MAN image.

The pictures of figs. 3.13a–c are relatively good results obtained from the bow–tie algorithm processor, without encoding. While the distortion solely produced by $BWT(.)$ does not introduce severe artifacts in the image domain, the encoder $E_c(.)$ must be robust enough to produce very little additional distortion in the projection domain, at reasonable levels of compression. Such an algorithm is described in the next sub–section. The good quality image reconstructions that result from $BWT(.)$, as compared to those from original projection information (see figs. 2.8–10), effectively justify the bow–tie frequency structure.

3.5.4.2 Encoding Algorithm

Given the objectives of minimal distortion encoding, the scheme of fig. 3.14 is proposed. The spectrally shapened 128×128 information in $\mathbf{Q}_{BW}$ is first buffered and then partitioned (in frequency space) into r concentric regions $H_1, H_2, \ldots, H_r$. The partitioning enables the encoder to take the magnitude–wise bunching of spectral coefficients within various frequency bands into consideration. If the elements of $\mathbf{Q}_{BW}$ are denoted as $Q_{BW}(m_1', m_2')$ then first $E_c(.)$ computes the log–magnitude $\Psi(m_1', m_2') = \log_e |Q_{BW}(m_1', m_2')|$ and the phase $\Gamma(m_1', m_2\prime)$ of these elements. A further simple regional normalization operation $\alpha_i(.)$ for the magnitude and a global one $\beta(.)$ for the phase are respectively given as

$$\psi_i(m_1', m_2') = \alpha_i(\Psi(m_1', m_2')) = \Psi_i(m_1', m_2')\left\{\max_{\Psi_i \in S_e\{H_i\}} [\Psi_i(m_1', m_2')]\right\}^{-1} \quad (3.41)$$

Fig. 3.13a Bow-tie Algorithm (Without Coding)
(MAN)

Fig. 3.13b Bow-tie Algorithm (Without Coding)
(BOY)

Fig. 3.13c Bow-tie Algorithm (Without Coding)
(BOX)

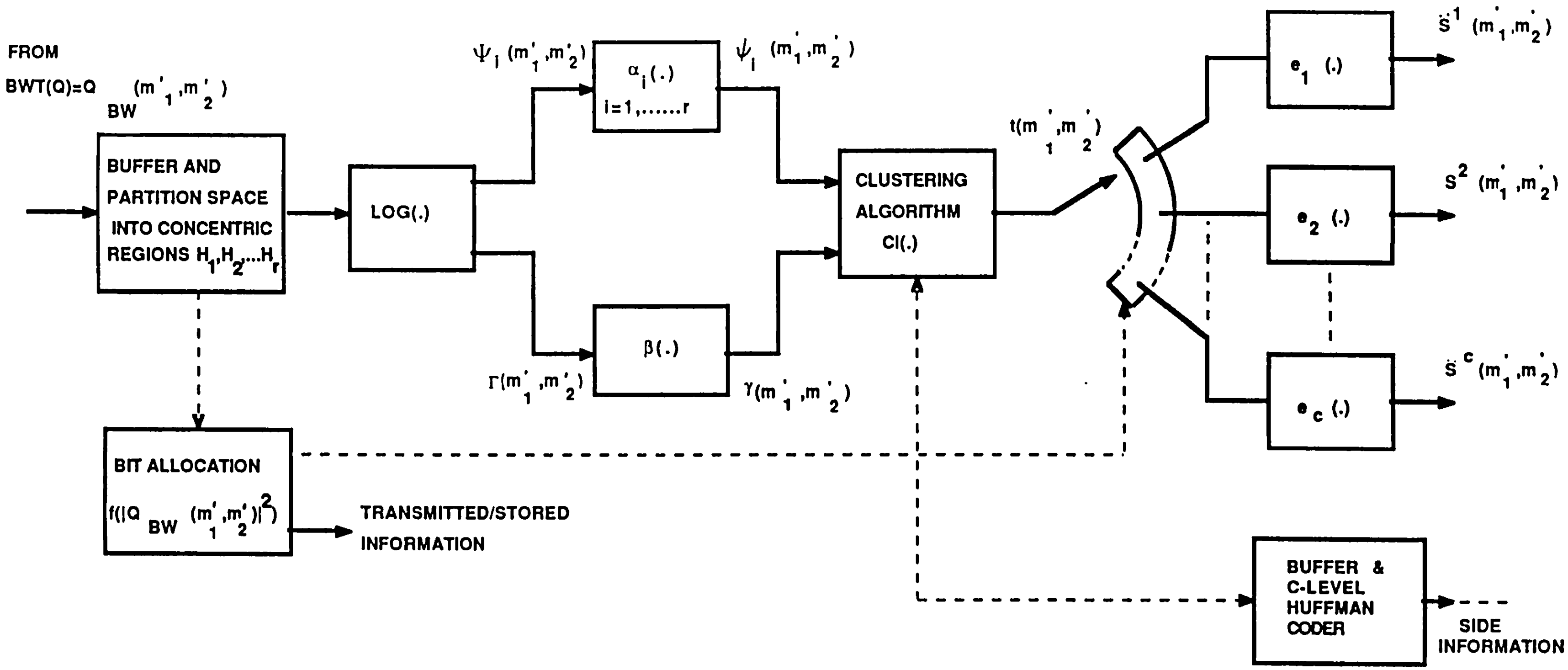

FIG. 3.14 ENCODING SYSTEM $E_c(Q_{BW})$ SUPPORTING BOW-TIE ALGORITHM FOR PDC.

for $i = 1, 2, \ldots, r$ and

$$\gamma(m_1', m_2') = \beta(\Gamma(m_1', m_2')) = \frac{\Gamma(m_1', m_2')}{\pi} \tag{3.42}$$

where $S_e\{H_i\}$ denotes the set of elements of $\mathbf{Q}_{BW}$ that belong to the frequency partition H_i. Therefore, $-1.0 \leq \psi_i(m_1', m_2'), \gamma(m_1', m_2') \leq 1.0$ (although strictly, $0 < \psi_i(m_1', m_2') \leq 1.0$) for $i = 1, 2, \ldots, r$.

The clustering algorithm $Cl(.)$, which discriminates between $\psi_i(m_1', m_2')$ and $\gamma(m_1', m_2')$ only on the basis of their respective points of entry (see fig. 3.14) into the algorithm, simply maps an input into the appropriate j^{th} partition (of c available ones) of the real line $\Re$ in the interval $[-1.0, 1.0]$. In essence, for any input $t(m_1', m_2')$ into $Cl(.)$ the output is the same sample but with an identifier for specifying the partition. In particular, the output $s^j(m_1', m_2')$ is such that

$$s^j(m_1', m_2') = Cl(t(m_1', m_2')) \tag{3.43}$$

if and only if

$$-1.0 + 2c^{-1}(j-1) \leq t(m_1', m_2') \leq 1.0 + 2c^{-1}j$$

A c–level Huffman coder tracks the clustering algorithm which in turn enables a decoder to identify a received sample with respect to the j^{th} partition.

The clustering operator $Cl(.)$ also switches on an encoder $e_j(.)$ if an input to $Cl(.)$ is assosciated with the j^{th} partition. That input is encoded by uniform quantization *within the bounds* of the j^{th} partition. The enabled encoder is synchronized with a bit assignment generator that is conditioned on the spectral coefficient energy $|Q(m_1', m_2')|^2$, (it is clear that after spectral shapening, the remaining bits are assigned to $\mathbf{Q}_{BW}$, as depicted in fig. 3.14) as a first approximation to the second order statistics of the coefficients. The bit allocation is split between the magnitude and the phase for uniform quantization at the point (m_1', m_2') where it is assumed that $\Psi(m_1', m_2')$ and $\Gamma(m_1', m_2\prime)$ are encoded one after (before) the other.

In summary, the encoding process involves an initial segmentation of the (transformed) signal space of $Q_{BW}(m_1', m_2')$ on the real line $\Re$, followed by quantization within the initial partitions. On the whole, the added distortion that is introduced into the bow–tie algorithm by $E_c(.)$ may be guaranteed to be small due to the controlled signal partitioning. However, the overhead required for tracking the partitioning process , through Huffman coding, increases the overall bit rate.

Nevertheless, the very nature of the 2–D AR Frequency structure of projected information still allows substantial compression by the bow-tie algorithm. Conjugate symmetry properties readily indicate that approximately half the ω_θ–ω_t plane is redundant i.e

$$P(\omega_\theta, \omega_t) = P^*(-\omega_\theta, -\omega_t) \qquad (3.44).$$

Moreover, on the basis of the Bessel function property

$$J(m, \omega_t r_o) = (-1)^m J(-m, \omega_t r_o)$$

[52], we may write the 2–D AR spectrum of (3.32) as

$$P(-\omega_\theta, \omega_t) = (-1)^m P^*(\omega_\theta, \omega_t) \qquad (3.45).$$

Therefore, $P(\omega_\theta, \omega_t)$ may be completely defined on a quarter–plane (strictly a quarter of a bow–tie) of the ω_θ–ω_t frequency plane; the high redundancy clearly lowers the required bit rates considerably.

3.5.4.3 Results

The numerical results from the bow–tie algorithm are summarized in tables 3.4 for the MAN,BOY and BOX image information, respectively. A four level Huffman coder is used to track the clustering algorithm. To control the magnitude bunching in the spectral content, sixty concentric frequency regions are found to be adequate. The average number of bits for encoding the spectrally modified data $\mathbf{Q}_{BW}$ is B_{BW} and B_H is the average bit rate for tracking the clustering process. The total average number of bits used in the coding process is B_T.

A comparison of table 3.4 with 3.3 verifies the low distortion produced by the algorithm $E_c(.)$ in the projection domain. Some corresponding picture results are

Image*	B_{BW}	B_H	$B_T = B_{BW} + B_H$	NMSE(P) 10^{-3}	NMSE(F) 10^{-3}
MAN	0.802	0.436	1.238	1.445	2.045
	0.732		1.168	1.450	2.170
	0.518		0.954	1.493	3.430
	0.451		0.887	1.511	4.110
BOY	0.737	0.457	1.194	0.150	2.240
	0.623		1.078	0.160	3.300
	0.448		0.905	0.187	5.990
BOX	0.760	0.440	1.196	3.333	3.337
	0.624		1.064	3.335	3.934
	0.425		0.865	3.426	5.631

* (reconstructed image)

Table 3.4 Quantitative Results from Bow–tie Algorithm

Fig. 3.15a Bow-tie Algorithm (MAN) , 0.95 bits/ps

Fig. 3.15b Bow-tie Algorithm (MAN) , 1.16 bits/ps.

Fig. 3.15c Bow-tie Algorithm (BOY) , 0.91 bits/ps.

Fig. 3.15d Bow-tie Algorithm (BOY) , 1.16 bits/ps.

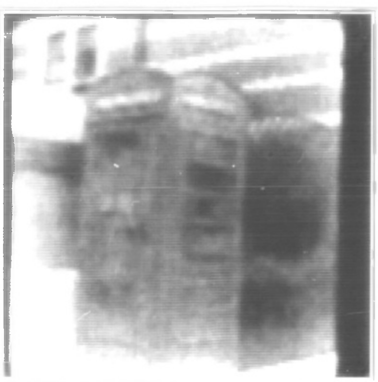

Fig. 3.15e Bow-tie Algorithm (BOX) , 0.87 bits/ps.

Fig. 3.15f Bow-tie Algorithm (BOX) , 1.19 bits/ps.

Fig. 3.16a Bow-tie Algorithm (Without Clustering)
(MAN)

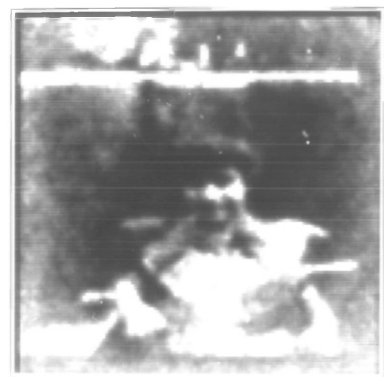

Fig. 3.16b Bow-tie Algorithm (Without Clustering)
(BOY)

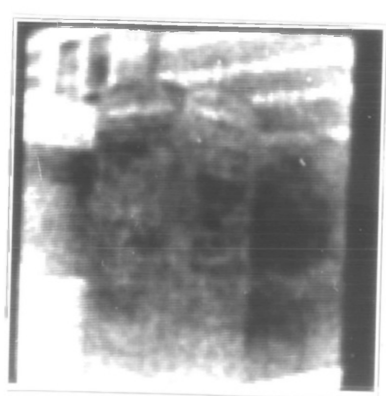

Fig. 3.16c Bow-tie Algorithm (Without Clustering)
(BOX)

shown in figs. 3.15a–f. The quality of performance is relatively impressive compared to that of the INTRAP and INTERP schemes respectively.

Figs. 3.16a–c are results of the bow–tie algorithm when the clustering $Cl(.)$ is bypassed in the encoding algorithm $E_c(.)$. A rather cloudy effect is noticeable in the reconstructed imagery. This reaffirms the need for robust encoding after spectral shapening by $BWT(.)$.

3.6. Summary

The focus of this chapter has been on exploiting the frequency structure of projected information for compression under a mode 1 status. Such structure has been considered theoretically in one and two dimensional forms for PDC.

A Cosine projection theorem has been discussed and used as a basis for implementing a Cosine transform based intra–projection compressor (INTRAP) that exploits the radial correlation of projection data. Associated effects of quantizer mismatch for this system have been first offset by introducing receiver interpolation for alternate projections and subsequent distribution–dependent Max quantization.

The INTRAP scheme has also been utilized in the form of an inter–projection codec INTERP for reduction of angular redundancy; in general better results are achieved for INTERP than INTRAP for a given projection domain.

The even better quality obtained from 2–D block transform coding of projection data, has inspired a detailed consideration of the 2–D AR frequency structure of the projection domain. This structure may be described by a bow–tie shaped band–region. A complete expression for this Fourier spectrum is provided. The effects of the band—shape have been considered in accordance with the performance of the INTRAP and INTERP schemes and the possible coding gains that might result from a more efficient sampling structure (that results from the bow–tie shape) for tomographic or projection information.

A novel approach, supported by the peculiar band–shape, has led to the development of a compression scheme called the bow–tie algorithm. Essentially, the algorithm shapens the discrete Fourier spectrum of given projection data, into a bow–tie form and uses an elaborate encoding algorithm for producing minimal distortion. Although the projection domain distortion levels that result from the bow–tie algorithm appear to be rather high, no visible artifacts appear in the image reconstructions at relatively high compression levels (compared to the INTRAP and INTERP schemes).

CHAPTER FOUR

PROJECTION DOMAIN COMPRESSION USING VECTOR QUANTIZATION

4.1 Introduction

In the previous chapter, compression structures that relied on the frequency structure of projected information were studied. While the pre–quantization processor ensured an exploitation of the frequency domain properties of projection data, the quantizer itself was a scalar system. In this chapter, we wish to continue the discussion of PDC, with the emphasis on developing a framework for the application of vector quantization (VQ) in the projection domain.

Over the years, VQ has emerged as a powerful data compression technique [69]. While the method has firm theoretical support in information theory [57, pg 66], the novel developments of design algorithms [70,71,72] for VQ have ensured its relative practicability for low–bit rate compression. The individual sample encoding approach of scalar quantization implicitly assumes a zero–order memory input sequence of data samples. This limits the performance (with respect to redundancy removal) of even distribution dependent optimal (in a minimum MSE sense) quantizers [63] when substantial inter–sample memory prevails. On the one hand, VQ with its effective block–sample coding strategy, enhances the efficiency of quantization by exploiting the correlation between samples of a block or vector. However, it is also interesting to note that from a rate distortion– theoretic point of view, the superiority of a vector coder over a scalar one, is guaranteed (at least for asymptotic vector dimensions) when the source input for quantization is *memoryless* [69,73]. In particular, the minimum rate function (maximum compression factor), for a given distortion requirement, is realized for an independent identically distributed (i.i.d) source when the source is compressed using long vectors [57]. Independent simulations [74] have shown that the superiority of VQ over scalar quantization for memoryless Gaussian data is established at the three dimensional vector level when using a MSE fidelity constraint.

The in–built inter–sample correlation control of VQ, makes it an attractive and robust compression procedure for typically highly correlated projection domain data (cf. figs. 2.15–17); the robustness is clearly relevant for PDC due to the extra distortion constraints of the image reconstruction process.

A survey of some of the important and recent image based VQ applications is presented in the following section. The fundamental features of VQ along with its basic design procedure are outlined in section 4.3. The rest of the chapter concentrates on the development of a VQ processor for PDC. Some attention is given to varied approaches of vector formation (or block–sample selection) from given projected information. Enhancement of a straightforward VQ application within the domain by inter–vector memory control is discussed. The adaptivity of VQ, within the domain, based on the geometrical and/or energy distribution of the corresponding frequency structure, is considered. Alternative adaptation with a view to possibly address uniqueness problems of image–projection domain mappings, is also studied. Multi–stage vector quantization (MVQ) is used to reduce the required distortion computations in this latter adaptive approach.

As in the previous chapter, the experimentation in this chapter has been to serve a mode 1 usage of PDC. Thus, the VQ based procedures considered herein are initiated to encode the projection data subject to final fidelity levels of reconstructed imagery.

4.2 Survey of Image based VQ

Several investigations abound in the literature on the use of VQ for image encoding, however, most procedures that have emerged can be classified as spatial (image) or transform domain VQ systems. In the first case, vectors are typically formed from small blocks of image data in order to generate optimal vector quantizers while transform based techniques derive vectors from orthogonally transformed image information. In the succeeding sub–sections, some illuminating VQ applications in the respective spatial and transform domains are reviewed.

4.2.1 Spatial domain VQ

A very early example of VQ applied directly to images is found in [75]. Using vectors obtained from non–overlapping square cells of pixels, bit rates between 0.5 and 1.5 bits/pixel are realized. A block/staircase effect is noticeable at lower bit rates, mainly due to the inter–vector statistical dependence and consequent poor edge structure rendition. Adaptivity is introduced to substantially rectify this effect by a pre–classification of image vectors into edge (high intensity change) or shade (low intensity change) image vectors. A so called product code is used to concatenate codebooks, derived from each set of vectors.

Predictive Systems

More elaborate strategies of controlling inter–vector correlation have evolved in the form of predictive vector quantization (PVQ) which broadly operates in a similar fashion to its scalar counterpart by using a predictive filter to remove redundancy in data and then VQ to compress the residual redundancy. Hang and Woods [76] have recently studied 2–D PVQ of images by using tree codes to implement elaborate predictive search systems. The main feature of the systems is to enable the decoder to systematically generate quantized residuals which in turn drive a tree code to recursively select reconstruction outputs, derived from a reconstruction filter. The effective delayed decision operation of the systems (executed in sliding block and block tree formats, respectively) allows the use of memory of previous and future information about the region of support of the current data. A comparison of bit rates at 1.0 bit/pixel indicates superior performance over classical DPCM.

A similar procedure for memory incorporation into the VQ process is the utilization of Finite State VQ (FSVQ) which may be viewed as an alternative configuration of PVQ [77]. Basically, FSVQ uses a finite collection of memoryless vector quantizers, each with its own codebook; however, each successive source vector is quantized with a codebook determined by a state transition switch. In the application of FSVQ to image encoding [78], the activity of the state transition switch or function is controlled by a perceptual image based classifier which attempts to characterize the intensity correlation and the edge structure at vector boundaries. Improved results over memoryless VQ are obtained, although the storage required for the codebooks is substantially increased.

While the PVQ/FSVQ schemes attempt to track memory for more efficient quantization, the accompanying design complexity appears to be substantial. Moreover, the stability of such systems in noisy environments may be in question since the search procedures of predictive tree coding or the state conditioning of FSVQ would allow errors to propagate through the system (as is the case for scalar predictive systems).

Shape and Statistic based Systems

The other main approach to spatial domain VQ is to adapt the quantization to local conditions over the imagery. This may be done at the vector level or within blocks of data from which the vectors may be formed. The vector based adaptation has been articulated in such schemes as Mean/Shape VQ (M/S–VQ) and Gain–Shape VQ (G/S–VQ) in combined and separate applications. Both techniques are effectively motivated by the advantages of discriminating between differing aspects of information; specifically, M/S–VQ pre–processes source vectors by removal (subtraction) of their respective component means (background level) while G/S–VQ is implemented by normalizing the vectors with their sample standard deviations (i.e. the energy bias of the vector). The residual vectors, in both cases, are appropriately called 'shape' vectors. The mean and/or gain terms are scalar quantized. The shape vectors tend to be smaller in magnitude and therefore do not bias the vector quantizer design; this is because for a given k–dimensional vector space $\Re^k$, the pre–processing by mean subtraction and/or gain normalization enables the vectors to be clustered about the origin of the signal space $\Re^k$. This clustering permits a better representation (or partition) of $\Re^k$ by the quantization.

A recent application of M/S–VQ, discussed by Allot and Clarke [79], involves the use of a multi–stage encoder (which offers considerable storage and distortion computation reduction in VQ) to enhance quantizer adaptivity over different images of varied detail. Superior performance is achieved over a similar configuration of non–adaptive M/S–VQ. Lee and Lee [80] have also combined G/S–VQ with M/S–VQ and report good results at 0.75 bits/pixel.

Although, not being a strictly shape generation process (in the sense of M/S–VQ) a two component scheme is suggested by Wu and Constantinides [81] to present a generalized 'shape' image field for subsequent vector formation and quantizer design. Essentially, an image is segmented into two *additive* components— one representing perceptibly important detail and the other, the residual component, representing background texture. The first component is encoded by a distortionless scheme such as run–length coding and the second effectively belonging to a wide class of a zero–mean random fields is encoded using VQ. Reliable performance is obtained over images of varying detail.

Sub–block based adaptation is extensively studied by Goldberg et al [82]. The emphasis is to adjust the VQ procedure in accordance with the non–stationary nature of typical pictures by designing different (small–sized) vector quantizers for the different sub–images. Slightly superior performance is realized over non–adaptive VQ in the range 1.0–1.5 bits/pixel. This scheme is also applied to coloured imagery, with low bit rates obtained in the region of 2.3 bits/pixel.

4.2.2 Transform Domain based VQ

Transform domain based VQ is developed, in the main, for either the reduction of dimensionality of the vector space and/or the reduction of memory between vectors. An additional factor, is of course, the relative robustness to degradation of transformed data, as the inversion from transformed space (after quantization) enables local degradations to be evenly filtered out at the decoding stage.

An early transform domain based VQ procedure has been proposed by Nasrabadi and King [83]. An intra–frame scheme operates by first reducing the correlation along rows of a picture, by applying row–based sequency transformations and then exploiting inter– row dependency by VQ; the row–based decorrelation effectively reduces the memory between vectors. A similar technique for inter–frame coding has been developed, in which 2–D block sequency transforms are followed by the application of VQ in the temporal direction. Adaptive extensions to both schemes are discussed in [82], where the vector lengths are modified in accordance with inter–row correlation (for the intra–frame case) and inter–frame correlation (for the inter–frame case), respectively. The systems perform well in the range 0.5–2.0 bits/pixel.

Sun and Goldberg [85] report extensive simulation based on the development of novel adaptive VQ techniques for 3–D Hadamard transformed image data for inter–frame coding. The energy compaction of the transforms allow a reduction of dimensionality of vectors as vector elements are selected from a subset of coefficients of the 3–D transformed sub–blocks. Systematic vector quantizer or codebook change using a vector label replenishment strategy, a mean–shift algorithm and a selective codeword replenishment scheme are applied jointly and severally to maintain fairly constant distortion over a sequence of image frames with minimal overhead requirements. Impressive rates have been obtained, using large vector dimensions, in the region of 0.5 bits/pixel.

Zonal VQ Systems

A rather recent innovation of transform domain VQ is the use of zonal vector quantization (ZVQ) in a similar fashion to the classical zonal quantization [58, pg 673] where the transformed space is partitioned into zones on an energy spread basis; the subsequent quantization is varied from the high energy regions to low energy zones.

Ang and Durrani [86] describe such a scheme in which large sized (2–D) blocks of Cosine transformed image data are partitioned into zones of coefficients; the number of coefficients per zone specify the vector dimensions. A procedure is proposed for global bit assignment in which the total number of zones and hence zonal vector quantizers are systematically distributed over all transformed blocks in order to satisfy a given bit rate requirement. Optimal zonal vector quantizers, conditioned on vector dimensions and zonal bit assignments, are designed using the generalized Lloyd algorithm [70]. They report good performance at 0.5 bits/pixel and below.

Saito et al [87] have also developed a similar ZVQ system, however they focus on providing an analytical basis for the bit assignment. On block transformation of data and zonal or band partitioning, zonal vector quantizers are generated using a G/S–VQ configuration that is matched to a spherically symmetric model of the vector space. The model is used to derive closed form bit allocation relationships for the gain and shape components, respectively. Using discrete Cosine transformations (DCTs), they have achieved good results within the range 1.0–1.5 bit/pixel for coloured imagery. They also report better performance of the VQ based scheme over DCT–based scalar quantization.

It should be remarked that the transform domain VQ approaches are generally more desirable than the spatial domain schemes. The relatively simple facilities of fast and robust reduction of dimensionality of the vector space and removal of inter–vector memory are respectively favourable aspects of the transform approach. Moreover, the ability of transform domain VQ to distribute the degradations over the image plane rather than localize the errors, as spatial domain techniques do, is of importance.

4.3 VQ in a Projection Domain Environment

Having reviewed image based VQ schemes, we wish to consider the application of VQ to projection domain data, with a view of achieving high levels of the data compression, subject to acceptable quality of image reconstructions. We first discuss the main features of VQ with respect to its codebook design.

4.3.1 Main features of VQ

4.3.1.1 Definition and Design [69],[70]

Given a k–dimensional vector space $\Re^k$ (assuming a real Euclidean vector space) and a subspace C , $C \subset \Re^k$, with M disjoint partitions $C = [\,C_1 \,|\, C_2 \,|\, \cdots \;|\, C_M]$, a memoryless vector quantizer is a mapping Q of vectors from $\Re^k$ into a representative subspace C, that is

$$Q\colon \Re^k \to C \qquad C \subset \Re^k \tag{4.1}.$$

The mapping $Q(\mathbf{v})$ of vectors $\mathbf{v} \in \Re^k$ is preferably chosen to partition $\Re^k$ into a set of M minimum distortion regions $C_1, C_2, \ldots, C_M$. Therefore, for a given measure of *mapping* distortion $d\{\mathbf{v}, Q(\mathbf{v})\}$, an optimal vector quantizer is obtained when the mapping of (4.1) is such that the expected mapping distortion $\mathrm{E}[d\{\mathbf{v}, Q(\mathbf{v})\}]$ is a minimum for all possible mapping strategies.

A simple geometrical interpretation of (4.1) is shown in fig. 4.1 for $\Re^3$, where vectors (depicted as crosses) are mapped by Q into a number of representative partitions C_i, each defined around a corresponding representative vector $\mathbf{w}_i$.

In order to achieve the minimum distortion mapping, the vector quantizer must first select the best partition, given the set C of all partitions and then C must be modified accordingly, to yield the minimum distortion, given the mapping process. Based on the argument of Lloyd [88], for a squared error mapping distortion measure, the forward mapping or encoding can do no better than select the partition $C_i \subset C$ for vectors $\mathbf{v} \in \Re^k$ such that C_i, represented by $\mathbf{w}_i$, would yield the minimum distortion

$$d\{\mathbf{v}, Q(\mathbf{v})\} = \min_{\forall i} d\{\,\mathbf{v}, \mathbf{w}_i \mid \mathbf{w}_i \in C_i\,\} \tag{4.2}$$

which is a ***nearest neighbour*** mapping criterion. The second requirement of C being the minimum distortion partition of $\Re^k$, given the nearest neighbour mapping $Q(\mathbf{v})$, is realized by selecting the representative partition vectors $\mathbf{w}_i$ according to the rule:

$$\mathbf{w}_i = \mathrm{E}\{\mathbf{v} \mid Q(\mathbf{v})\colon \Re^k \to C_i\,\} \tag{4.3}$$

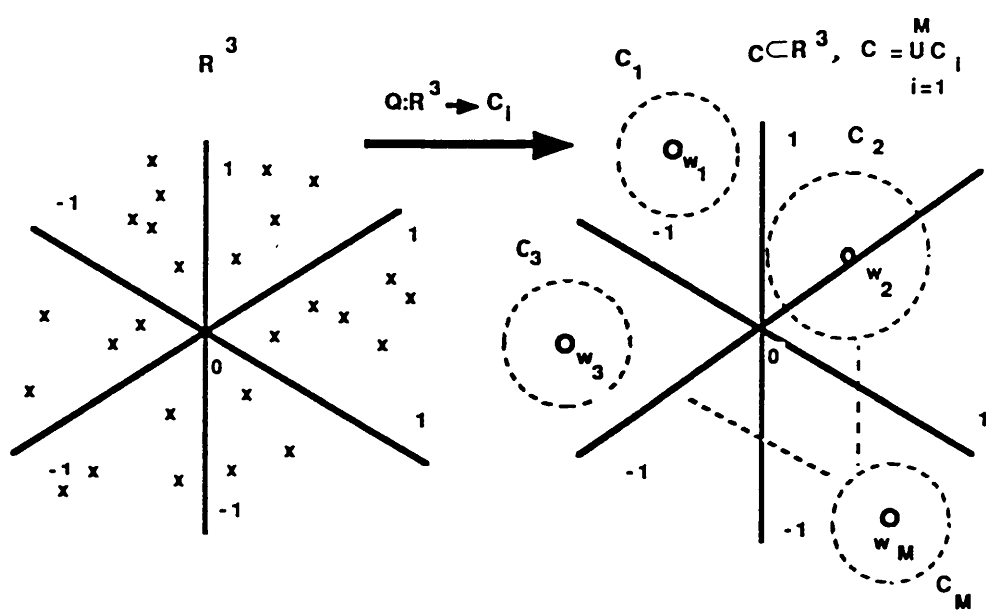

FIG. 4.1 VECTOR QUANTIZER MAPPING FROM R^3 INTO PARTITIONS C_i OF R^3

that is, the $\mathbf{w}_i$s are the generalized centroids of the corresponding partitions C_i.

The design process of the vector quantizer $Q(\mathbf{v})$, based on (4.2–3), is therefore a recursive one in which the encoder Q iteratively tracks the structure of the decoder C and the decoder the encoder's, until an acceptable level of expected mapping distortion is obtained. An algorithm for implementing this has been proposed by Linde et al [70]; the algorithm has been referred to as the generalized Lloyd algorithm or the LBG algorithm. The LBG approach is applicable to data with a known or unknown probability distribution. In both cases the aim is to control the average mapping distortion. Essentially, the algorithm measures the long term average distortion over a large number of source vectors in $\Re^k$ and iteratively reduces the distortion level for a given partition C (also known as the codebook).

The LBG procedure may be summarized in the following steps

1. Given an initial codebook $C(0)$ or representative subset of $\Re^k$, a distortion convergence parameter ϵ and a training sequence $\{\mathbf{v}\}$ of vectors, $\mathbf{v} \in \Re^k$, set initial average distortion $D_{-1} = \infty$.

At the m^{th} iteration

2. Having $C(m)$, effect the optimal mapping (according to (4.2)), $Q: \Re^k \rightarrow C(m)$ $= \left[C_1(m) \,|\, C_2(m) | \cdots | C_M(m) \right]$ and measure the average distortion D_m at the m^{th} iteration of the mapping.
3. If the difference between the distortion at the previous iteration and the current distortion is smaller than a specified fraction of the present distortion level, then we have the desired partition set or codebook $C(m)$, that is if $D_{m-1} - D_m \leq \epsilon D_m$, then stop iterations. Otherwise go to step 4.
4. Find the optimum reproduction codebook (using (4.3)) $C(m+1)$ based on $C(m)$. Go to step 2. for the $(m+1)^{th}$ iteration.

The initial problem is choosing the initial representative subspace $C(0) \subset \Re^k$, which may be improved upon in subsequent iterations. Several techniques have been suggested [69], however, they may be classified into two fundamental procedures. The first commences with a codebook of correct dimensions (M, k), which may be obtained by choosing vectors at random in $\Re^k$ [71], or vectors sufficiently distant (on an Euclidean basis) from one another [89]. The second basic procedure starts with codebooks of size (M_s, k_s) where $M_s \leq M$ and/or $k_s \leq k$. Two well known initialization methods that fall within this category are the product code structure and the splitting technique [69] respectively. The general approach of both schemes is to synthesize the desired M–level k–dimensional codebook from succesively optimized codebooks of smaller dimensions. We shall not describe these schemes here as they are found in several places in the literature.

It must be noted that the vector quantizer design procedure does not generally yield a globally optimum quantizer for a given convergence parameter ϵ. From detailed analysis and simulations, Gray and Karnin [74], by using a variety of initial codebooks and convergence parameters, have shown the existence of multiple local optima for memoryless Gaussian information in vector quantizers with definite geometrical shapes in $\Re^2$ and $\Re^3$ respectively. In theory, a search through the local optima would yield the best quantizer, however, this is clearly computationally expensive and the product code or splitting techniques of initialization do lead to reliable results.

Other Methods of VQ design

There has been some use of other schemes for vector quantizer generation. The k–means classification technique [71] operates on the principle of forming group patterns in multi–variate analysis such that each vector sample of a multi–dimensional distribution is represented by the mean (or centroid) of vectors within a group. It may be implemented by using the condition of (4.3) . This approach may be more appropriate for initializing the partition set or codebook before optimization by the LBG algorithm.

A novel technique described in [72] is the *Peano mapping* strategy. The object is to reduce the burden of the quantizer design when the training set $\{\mathbf{v}\}$ in $\Re^k$ is large. Essentially, a 'near–adjacency' preserving mapping of vectors is made from

$\Re^k$ to $\Re$ and classical Max quantization is implemented in $\Re$. The Max centroids are then used to generate the appropriate vector centroids (i.e. codewords) in $\Re^k$ through an inverse mapping. the LBG algorithm performs only slightly better than the Peano mapping strategy, according to [72].

4.3.1.2 Distortion Considerations

In order to yield to tractable analysis where possible, VQ theory [70,90] customarily assumes a generalized vector input weighted mapping–distortion. The general form is

$$d\{\mathbf{v}, Q(\mathbf{v})\} = (\mathbf{v} - Q(\mathbf{v}))^T \mathbf{W}_{\mathbf{v}} (\mathbf{v} - Q(\mathbf{v})) \tag{4.4}$$

where $\mathbf{W}_{\mathbf{v}}$ is an input dependent positive definite matrix. Some typical forms of $\mathbf{W}_{\mathbf{v}}$, for $\mathbf{v} \in \Re^k$, are $\mathbf{W}_{\mathbf{v}} = \mathrm{E}[\mathbf{v}\mathbf{v}^T]$ (i.e. is the auto–correlation matrix of input vectors; of prominent use in linear predictive coding of speech [90]), $\mathbf{W}_{\mathbf{v}} = \left[\mathrm{E}[\mathbf{v}\mathbf{v}^T]\right]^{-1}$ which results in the Mahalanobis distortion measure when used in (4.4) (this is widely applied in pattern classification problems [91]), and $\mathbf{W}_{\mathbf{v}} = \mathbf{I}$, the identity matrix which makes (4.4) equivalent to a squared error distortion criterion. In general, non–identity forms of $\mathbf{W}_{\mathbf{v}}$ have the advantage of emphasizing statistical [90] or perceptual [92] properties of vector data, when incorporated into the Lloyd algorithm. Expectedly, the complexity of the VQ design increases.

The expected distortion $\mathrm{E}[d\{\mathbf{v}, Q(\mathbf{v})\}]$, may be estimated analytically when the distribution of the input source is known. However, if it is only known that the data source is stationary and ergodic, then it is reasonable to compute the long term average distortion over a large number L of training vectors. In particular, in the limit of large L, the ensemble average distortion is equivalent to the expected distortion. That is

$$\lim_{L\to\infty} \frac{1}{L} \sum_{i=1}^{L} d\{\mathbf{v}_i, Q(\mathbf{v}_i)\} = \mathrm{E}[d\{\mathbf{v}, Q(\mathbf{v})\}] \tag{4.5}$$

where $\mathbf{v}_i$ is the i^{th} vector of a training sequence $\{\mathbf{v}\}$. Accordingly, the long term average mapping–distortion is used in the LBG algorithm as an estimate of the expected distortion. It has been noted that such a procedure is valid for non–ergodic and non–stationary sources (with or without asymptotic stationarity) [93].

4.3.1.3 Bit Rate Considerations

A vector quantizer $Q(\mathbf{v})$ is specified by the number M of partitions in C and the vector dimensions k. In general, an upper bound $R_k^M(Q(\mathbf{v}))$ of vector quantization bit rate is achieved from $Q(\mathbf{v})$; this is given as

$$R_k^M(Q(\mathbf{v})) = \log_2 M^{1/k} \quad \text{bits/sample} \qquad (4.6).$$

By defining a conditional probability $P(\mathbf{w}_i \mid \mathbf{v}, \quad \mathbf{v} \in C_i)$ on each partition, a probabilistic scheme of codebook addressing of vectors $\mathbf{w}_i \in C_i \subset C$ may be developed, through an entropy based codeword identification procedure, to achieve a lower bit rate than (4.6). Nevertheless, the rate estimation of (4.6) is normally assumed in the VQ design, for simplicity.

In practical transmission or storage systems, some overhead is required for informing the decoder about the structure of the partition or codebook C. Typically, the overhead is very small in comparison with the amount of data processed by vector quantization. The main aim of the work of this chapter is to find a set of reliable procedures for achieving good performance of projection domain based VQ and as such, we have not emphasized the overhead requirements in view of this primary objective.

4.3.1.4 Vector formation from Projection Data

Having a projection domain matrix $\mathbf{P} = [\,\mathbf{P}_1 \,|\, \mathbf{P}_2 \,|\, \cdots \,|\, \mathbf{P}_{M_\theta}\,]^T$ and a corresponding set $S_e\{\mathbf{P}\}$ of elements in $\mathbf{P}$ *, it is required to form vectors $\mathbf{v} = [v_1, v_2, \ldots, v_k]^T$, $\mathbf{v} \in \Re^k$, $v_i \in S_e\{\mathbf{P}\}$ to generate a vector quantizer $Q(\mathbf{v})$. This corresponds to the vector formation problem.

Several methods of vector formation have been utilized for VQ design. Many procedures in 2–D or 3–D image processing choose the vector samples $v_1, v_2, \ldots, v_k$

* The elements of $S_e\{\mathbf{P}\}$ are not necessarily ordered as they are in $\mathbf{P}$.

from square blocks within 2–D or cubic blocks within 3–D imaging [75,85]. This approach is mainly adopted to present vectors to the quantizer that emphasize correlation between data samples, vertically and horizontally (in 2–D images) and temporally (in 3–D images). Where it is known, apriori, that the correlation along one of the directions is limited or extensive, a rectangular–block (for 2–D data) or cuboid–block (for 3–D information) selection of samples may be effective; the block lengths in a given direction are chosen to de–emphasize or emphasize the correlation span in the data accordingly. These approaches are considered in [83,84,89] where orthogonal transformations are applied to reduce correlation in one or two dimensions of 2–D or 3–D image compression, respectively, and rectangular-block vector formation is used to exploit correlation in the final dimension.

Figs. 4.2a–b show schematic forms of vector formation from 2–D and 3–D blocks of data. Fig. 4.2c depicts the so called Schamming method [87] of vector formation which is mostly utilized in transform domain ZVQ; each zone has a vector of specific dimensions. The procedures illustrated in figs. 4.2a–b are also employed in transform domain VQ where transforms are either applied before vector formation (i.e. the implementation of an l–dimensional transform on an l–dimensional block) or after the selection (i.e. involving 1–D transformations of vector elements). Typically, a subset of the higher energy components is chosen to reduce the final dimensions of the vectors $\mathbf{v}$. The vector size is largely determined by the amount of compression desired, according to (4.6), the span of correlation in the information to be compressed and the inter–block or inter–vector memory.

The choice of vectors in the projection domain may also have a varied approach, given the high correlation obtainable within the domain. The empirical measures of auto–correlation within projections and between projections, respectively, for different types of imagery indicate that substantial correlation persists over short correlation spans. This may suggest that vectors should be chosen from the domain in such a way as to emphasize the inter–projection or intra–projection memory or both correlation profiles, simultaneously. These different types of vector selections

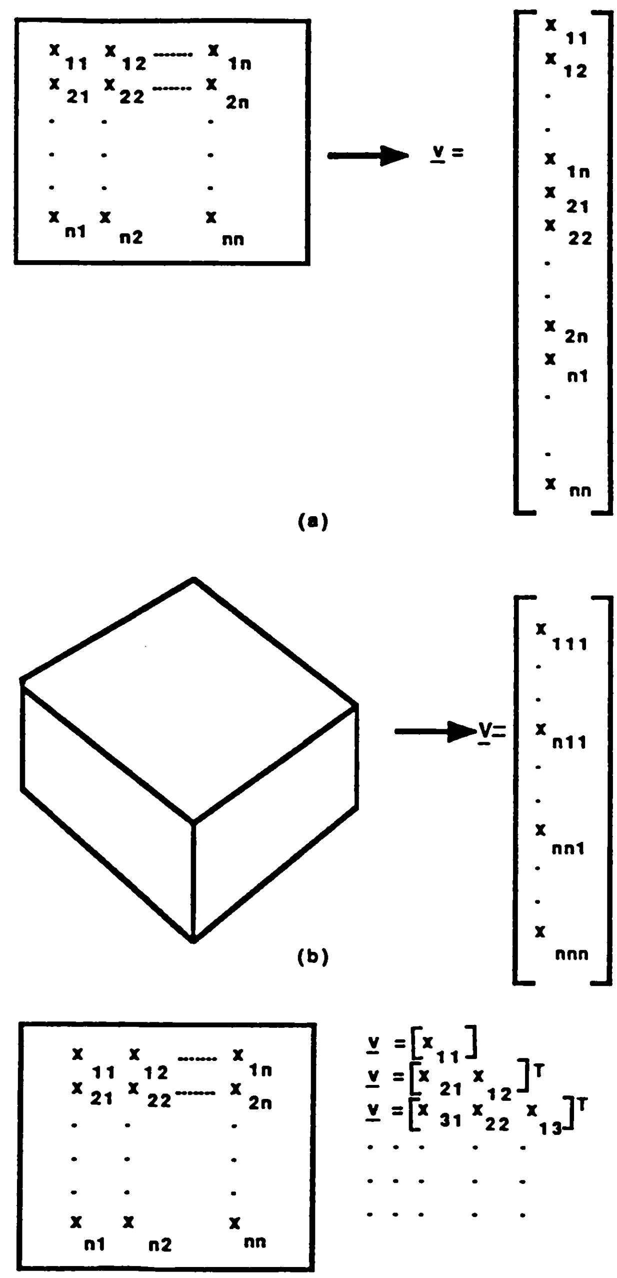

FIG. 4.2 Various types of vector formation (a) from 2-D blocks (b) from 3-D and (c) the Schamming method of vector selection.

and their possible implications with respect to PDC of image information are briefly discussed.

Inter–projection Based Vector Formation(VF1)

In this case, the selection of a vector $\mathbf{v}, \mathbf{v} \in \Re^k$ from a projection domain matrix $\mathbf{P}$ may be characterized by the general rule:

$$S_e\{\mathbf{v}\} \subset S_e\{\mathbf{O}_l\} = \bigcup_{i=a}^{b} S_e\{\mathbf{P}_i\} \tag{4.7}$$

where $S_e\{\mathbf{O}_l\} \subset S_e\{\mathbf{P}\}$ and $\bigcap_{l=1}^{n} S_e\{\mathbf{O}_l\} = \emptyset$. This axiom implies that the set $S_e\{\mathbf{v}\}$ of vector elements are chosen from a subset $S_e\{\mathbf{O}_l\}$ of projection data, that spans $(b-a+1)$ projections. Each subset $S_e\{\mathbf{O}_l\}$ is one of n non–overlapping subsets that may be derived from $\mathbf{P}$. Within these subsets, the components of a k–dimensional vector $\mathbf{v}$ correspond to a sequence of projection domain samples $\{P(i+k_2-1, j+k_3-1)\}$, in $\mathbf{P}$, for $\max(k_2, k_3) = k_2$ and $k_2 k_3 = k$; the condition $k_2 > k_3$ emphasizes the inter–projection correlation over intra–projection correlation. An extreme case of this is when $k_3 = 1$ and $k_2 = k$ such that $\mathbf{v}^T = [P(i,j), P(i+1,j), \ldots, P(i+k-1,j)]$. In this instance, the objective is to completely emphasize the inter–projection correlation; this vector formation protocol is graphically depicted in fig. 4.3.

Although this latter vector selection procedure may not be wholly acceptable if intra–projection redundancy is pronounced, it offers some predictability of how distortion will be manifested in reconstructed imagery. For an AR based projection domain function, an inter–projection based VQ approach is likely to produce angular artifacts in the image reconstructions.

Intra–projection Based Vector Formation (VF2)

To emphasize intra–projection correlation, we have a similar rule for vector selection; this may be specified as

$$S_e\{\mathbf{v}\} \subset S_e\{\mathbf{O}_l\} = \bigcup_{i=a}^{b} S_e\left\{\mathrm{col}[\mathbf{P}^T]_i\right\} \tag{4.8}$$

where $\mathrm{col}[\mathbf{P}^T]_i$ is the i^{th} column vector of $\mathbf{P}^T$ and $S_e\{\mathbf{O}_l\} \subset S_e\{\mathbf{P}^T\}$ and $\bigcap_{l=1}^{n} S_e\{\mathbf{O}_l\} = \emptyset$. Here, the subset $S_e\{\mathbf{O}_l\}$ spans $(b-a+1)$ radial positions and the k–dimensional vectors $\mathbf{v}$ are derived from the sample sequence $\{P(i+k_2-1, j+k_3-1)\}$, $\max(k_2, k_3) = k_3$. For $k_2 = 1$ (i.e full intra–projection based vector formation), the mode of vector formation may not be efficient if inter–projection correlation persists, however, its principal advantage lies in the flexibility of the associated vector codec. This is because the projections $\mathbf{P}_i$ may be encoded independently of other projections $\mathbf{P}_j$, $i \neq j$.

Square Block Vector Formation (VF3)

Clearly, square block selection of vector samples from $\mathbf{P}$ may be described by either the VF1 or VF2 axioms, with the additional constraints $k_2 = k_1 = k^{1/2}$. This might be a more reliable vector formation strategy, over small spans of projection samples, since inter–projection and intra–projection memory can both be substantial over small correlation lags.

As observed in the previous chapter, the square–block transform coding offers better results than the intra–projection or inter–projection coding approaches. However, the block size is a constraint for VQ. Given high projection domain correlation, the use of small block sizes in a memoryless VQ scheme may impair performance as a result of high inter–block correlation. Larger block based VQ would obviously increase the complexity of the VQ design and implementation. Some effects of VF3 are considered along with VF1 and VF2, respectively, in the following section.

4.3.2 Direct VQ in the Projection Domain (PDC–VQ)

Here, we present results of VQ applied directly to projected information (for convenience we call this approach PDC–VQ) of the MAN image function, using the different vector formation approaches, described. A convergence parameter of $\epsilon = 0.01$ is used in full searched vector quantizer design , based on the LBG algorithm. The squared error distortion measure is employed and the algorithm is seeded by the

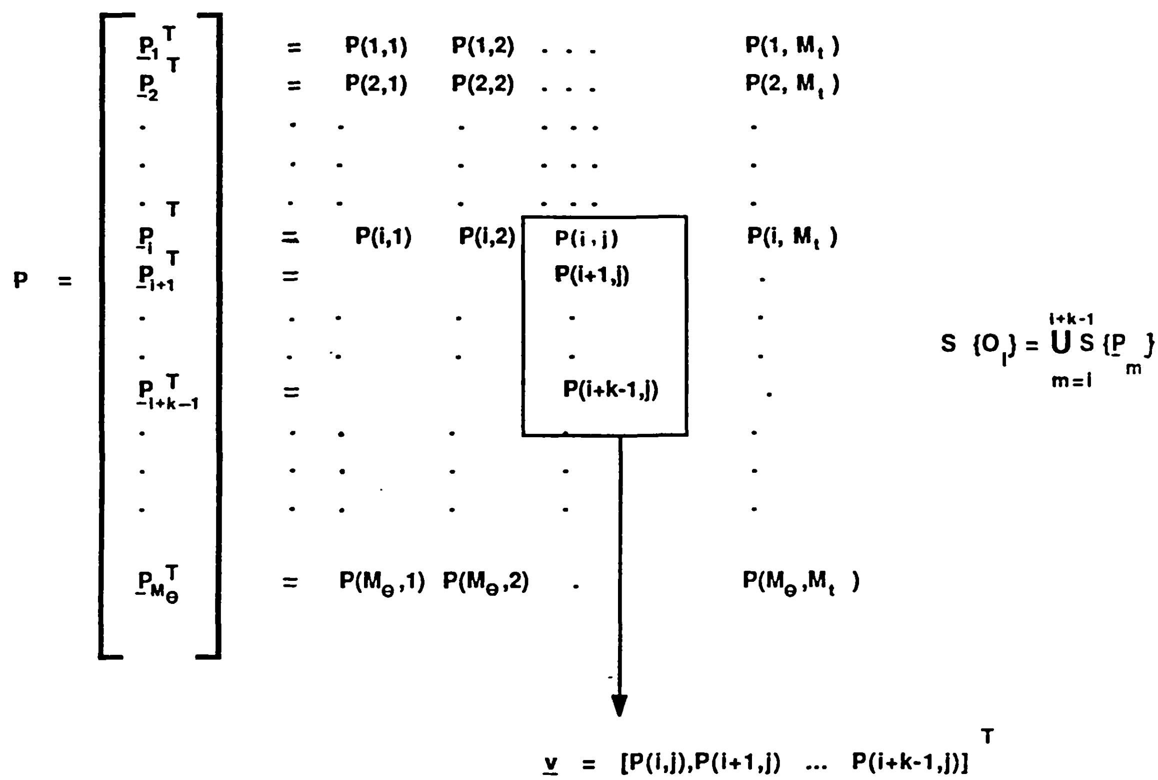

Fig. 4.3 Full inter-projection based vector formation VF1(k_3 = 1); full intra-projection based vector selection VF2 (k_3 = 1) is realized by taking vertical windows over samples of P .

successive vector splitting procedure. A block diagram of the VQ processor for PDC–VQ is shown in fig. 4.4.

The pictorial results are shown in figs 4.5a–c. Fig. 4.5a is the result from using a VF1 vector selection mode from non–overlapping blocks of 4×2 dimensions. A circular distortion effect is noticeable; this becomes more evident for the extreme case (VF1 ($k = 1$)) using blocks of 8×1 (fig. 4.5b) and 4×1 (fig. 4.5c). The bit rates are 1.125, 1.125 and 2.0 bits/ps respectively. While the strong circular cloudy effect is not evident in fig. 4.5d, using 2×4 blocks (i.e. VF2), a smearing effect manifests towards the picture centre . This also occurs in fig. 4.5e, for 1×4 blocks at 2.25 bits/ps. A square block formation (VF3) result of PDC–VQ is shown in fig. 4.5f at 2.0bits/ps for 2×2 blocks and appears to exhibit a rather speckled appearance.

The overall quality of the results of PDC–VQ is not very impressive, given the prevalent circular smearing and speckle effects observed in compressed imagery. While it may be difficult if not impossible to make subjective assessments of the effects of PDC–VQ on projection domain information, it is reasonable to assume that there is a degrading inter–block or inter–vector dependence, due to high correlation, in the VQ design process. In direct image space based VQ, this dependence may manifest itself as a 'block' effect in compressed imagery [75]. Of importance is the implicit assumption, by the LBG algorithm, of a *zero-order* memory vector training sequence $\{\mathbf{v}\}$. Therefore, there may be a loss of efficiency when the sequence exhibits considerable memory especially in view of the fact that the LBG algorithm seeks to choose a representative subset $\{\mathbf{w}_1, \mathbf{w}_2, \ldots, \mathbf{w}_M\}$, $\mathbf{w}_i \in \Re^k$ for the training sequence and intuitively, the more distant the members of the subset, the better the representation. Therefore, the PDC–VQ scheme may be enhanced by introducing some form of control for the inter–vector memory.

4.3.3 Enhanced VQ for PDC (PDC–HT–VQ/PDC–CT–VQ)

Predictive vector coding techniques may be appropriate for inter–vector memory control, however, the resulting system may be unacceptably complex due to the rather involved procedures used in current techniques [76,77,78]. A larger–block

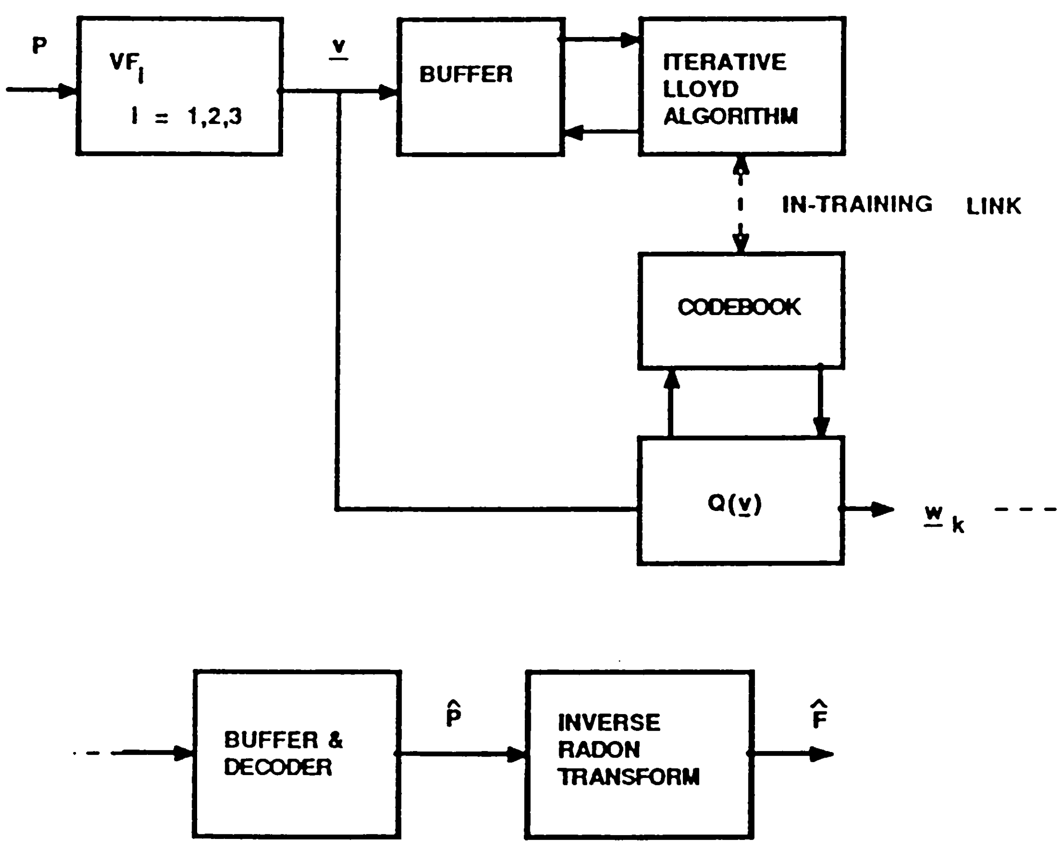

FIG. 4.4 PROCESSING FOR DIRECT VQ

Fig. 4.5a Direct VQ (VF1, 4 x 2 blocks)
1.125 bits/ps. (MAN)

Fig. 4.5b Direct VQ (VF1, 8 x 1 blocks)
1.125 bits/ps. (MAN)

Fig. 4.5c Direct VQ (VF1, 4 x 1 blocks)
2.0 bits/ps. (MAN)

Fig. 4.5d Direct VQ (VF2, 2 x 4 blocks)
1.125 bits/ps. (MAN)

Fig. 4.5e Direct VQ (VF2, 1 x 4 blocks)
2.25 bits/ps. (MAN)

Fig. 4.5f Direct VQ (VF3, 2 x 2 blocks)
2.0 bits/ps. (MAN)

vector formation approach for memory reduction would also increase the VQ complexity, although it may be facilitated by introducing orthogonal energy compacting data transforms and choosing subsets of the transformed coefficients for vector formation [85]. It is reasonable, however, to enable the enhanced vector quantizer to exploit the physical and theoretical relationships between projection domain information in $\mathbf{P}$ and a corresponding image domain matrix $\mathbf{F}$. It is recalled that the compression schemes of the preceding chapter were principally motivated by such $\mathbf{P} \leftrightarrow \mathbf{F}$ relationships.

In order to simultaneously reduce inter–vector memory and constrain the resulting vector quantizer $Q(\mathbf{v})$ to operate within the correspondence of $\mathbf{P}$ and $\mathbf{F}$, the following generalized structure for enhanced VQ is suggested.

Given $\mathbf{P} = [\,\mathbf{P}_1, |\,\mathbf{P}_2\,| \cdots |\,\mathbf{P}_{M_\theta}\,]^T$, implement the transformations

$$\mathbf{TP}_i, \qquad \mathbf{TT}^T = \mathbf{I}, \quad i = 1, 2, \ldots, M_\theta \tag{4.9}$$

to give a collection $\mathbf{Q}$ of vectors:

$$\mathbf{Q} = [\,\mathbf{TP}_1\,|\,\mathbf{TP}_2\,| \cdots |\,\mathbf{TP}_{M_\theta}\,]^T = \mathbf{PT}^T \qquad (4.10).$$

Then use the axiom VF1 ($k_3 = 1$):

$$S_e\{\mathbf{v}\} \subset S_e\{\mathbf{O}_l\} = \bigcup_{i=a}^{b} S_e\{\mathbf{TP}_i\} \tag{4.11}$$

where $S_e\{\mathbf{O}_l\} \subset S_e\{\mathbf{P}\}$ and $\bigcap_{l=1}^{n} S_e\{\mathbf{O}_l\} = \emptyset$ and $(b - a + 1) = k$, $\mathbf{v} \in \Re^k$, for subsequent vector formation and design.

In order to completely remove the memory between vectors formed from elements of $S_e\{\mathbf{O}_l\}$, according to (4.11), we effectively require transformed samples $Q(i, m_1)$ associated with $S_e\{\mathbf{TP}_i\}$ to obey

$$\mathrm{E}\{Q(i, m_1)Q(i, m_2)\} = \begin{cases} \sigma_{m_1}^2 & m_1 = m_2 \\ 0 & m_1 \neq m_2 \end{cases} \tag{4.12}$$

as a sufficient condition where $\sigma_{m_1}^2$ is the variance of $Q(i, m_1)$. Moreover, a satisfactory requirement on $\mathbf{T}$, for the preservation of the correspondence between $\mathbf{P}$ and $\mathbf{F}$, is

$$S_e\{\mathbf{TP}_i\} \subset S_e\{\mathbf{TFT}^T\} \qquad i = 1, 2, \ldots, M_\theta \tag{4.13}$$

which is simply an implication of the generalized projection theorem.

The condition of (4.12) may be realized when the eigen vectors of the covariance matrix $\mathrm{E}\left[\mathbf{P}_i\mathbf{P}_i^T\right]$ are equivalent to the rows of $\mathbf{T}$. That is, when $\mathbf{T}$ is a KLT matrix transformation. The constraint of (4.13) is only approximately achieved for discrete-space image and projection domain processing, for reasons already discussed in chapter two. For ease and speed of implementation, the KLT may be replaced by a robust (in the sense of a partial realization of (4.12)) frequency transformation which would in turn yield a frequency–slice interpretation of (4.13). In terms of data compression, additional gains evolve from the transformation of (4.11) when considerable projection energy is constrained within a small band of transformed data. The resulting vector quantizer may readily take advantage of such an energy distribution by replacing vectors corresponding to the low energy zones with zero vectors.

4.3.3.1 Simulation Details and Results

Fig 4.6 is a schematic of the generalized processor for enhanced vector quantization for PDC; it is similar in structure to the intra–projection compressor discussed in the previous chapter.

In the simulations, the vector quantization is accompanied with scalar coding of elements of a gain vector $\mathrm{diag}[\Sigma] = [\sigma_1, \sigma_2, \ldots, \sigma_{M_t}]^T$ (M_t remains the number of radial components of each projection) where the gain elements σ_i are computed over the elements of the vector $\mathrm{col}[\mathbf{PT}^T]_i$, as sample standard deviations. In general, each column vector is normalized by the corresponding gain elements, to produce a matrix of the form

$$\mathbf{PT}^T\Sigma = \left[\frac{\mathrm{col}[\mathbf{PT}^T]_1}{\sigma_1} \,\Big|\, \frac{\mathrm{col}[\mathbf{PT}^T]_2}{\sigma_2} \,\Big|\, \cdots \,\Big|\, \frac{\mathrm{col}[\mathbf{PT}^T]_{M_t}}{\sigma_{M_t}}\right] \tag{4.14a}$$

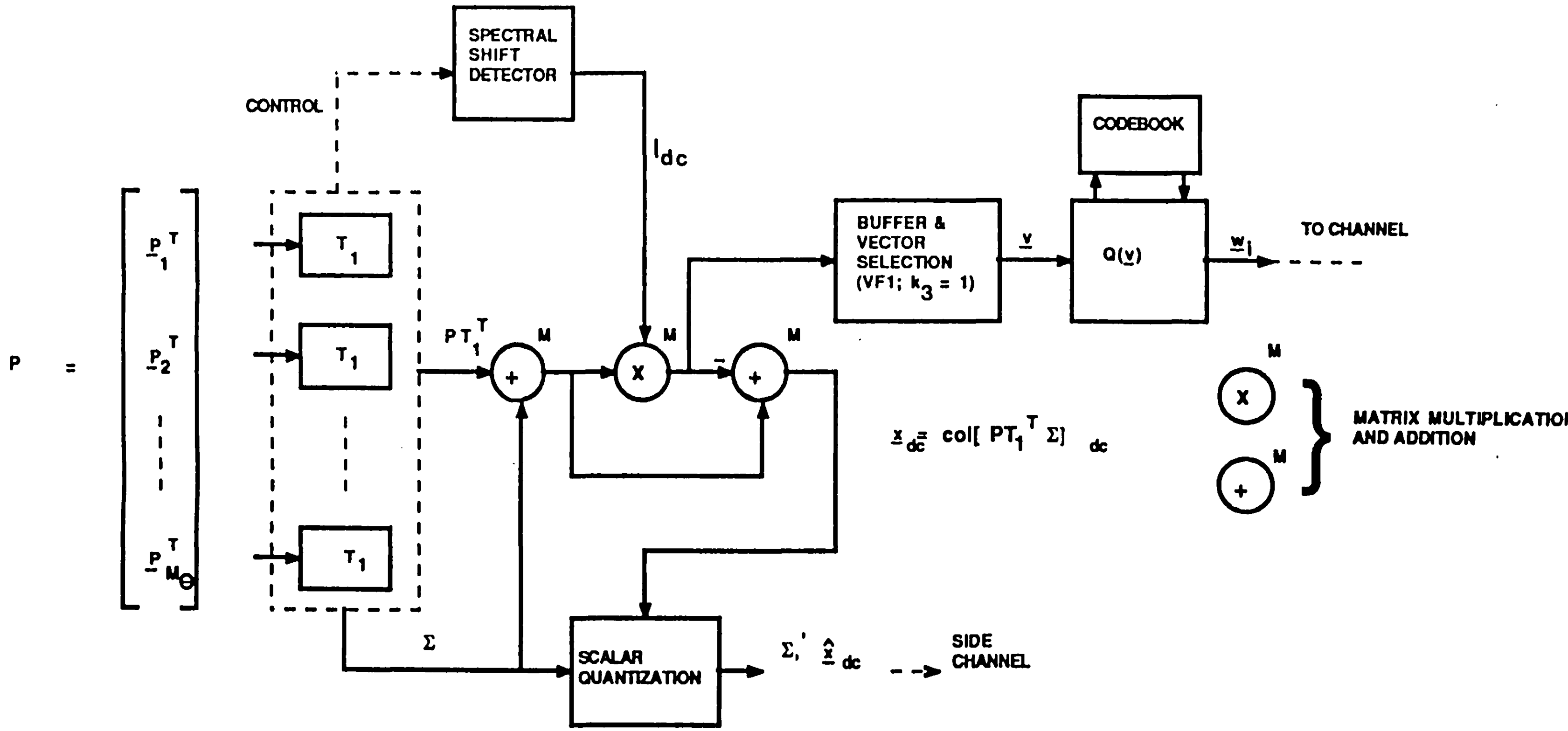

FIG. 4.6 ENHANCED VQ SCHEME FOR PDC.

and

$$\mathbf{\Sigma} = \begin{bmatrix} \sigma_1^{-1} & 0 & \dots & 0 \\ 0 & \sigma_2^{-1} & \dots & 0 \\ \vdots & \vdots & \ddots & \vdots \\ 0 & 0 & \dots & \sigma_{M_t}^{-1} \end{bmatrix} \qquad (4.14b).$$

The matrix format of (4.14a) enables the vector formation process VF1 ($k_3 = 1$) to window $k \times 1$ samples from a unit energy vector, in a similar fashion to G/S–VQ, where each vector $\mathbf{v} \in \Re^k$ is normalized by the standard deviation of its components to yield the shape vector. In applying VF1 ($k_3 = 1$) to (4.14), the vectors $\mathbf{v} \in \Re^k$ are sub–vectors of larger shape vectors $\text{col}[\mathbf{PT}^T]_i\sigma_i^{-1} \in \Re^{M_\theta}$, such that the shape is being extracted in M_θ–dimensional Euclidean space. This gain normalization enables the Lloyd algorithm to be un–biased to samples of high or low energy.

The set of d.c. elements obtainable over the vectors $\mathbf{TP}_i$, $i = 1, 2, \dots, M_\theta$ corresponds to one of the column vectors of $\mathbf{PT}^T$. According to the projection–slice theorem, the gain term σ_{dc} of this column vector $\text{col}[\mathbf{PT}^T]_{dc}$ should be zero, as the projections should, in theory, have identical mean values. Due to the approximate projection generation procedure, in practice there is some small variation in the d.c. coefficients. However, the mean value of these coefficients is representative of the d.c. column vector and it is therefore extracted from $\mathbf{PT}^T$ before the gain normalization. Therefore, the VF1 axiom is actually applied to the matrix

$$\mathbf{PT}^T\mathbf{\Sigma}\mathbf{I}_{dc} = \left[\frac{\text{col}[\mathbf{PT}^T]_1}{\sigma_1} \,|\, \frac{\text{col}[\mathbf{PT}^T]_2}{\sigma_2} \,|\, \cdots \,|\, \mathbf{0} \,|\, \cdots \,|\, \frac{\text{col}[\mathbf{PT}^T]_{M_t}}{\sigma_{M_t}} \right] \qquad (4.15a)$$

where $\mathbf{I}_{dc}$ is a singular matrix (of the same dimensions as $\mathbf{PT}^T$) whose diagonal $\text{diag}[\mathbf{I}_{dc}]$ is such that

$$\text{diag}[\mathbf{I}_{dc}] = [1, 1, \dots, 0, \dots, 1]^T \qquad (4.15b);$$

the off–diagonal values of $\mathbf{I}_{dc}$ are identically zero. The zero column vector $\mathbf{0}$ corresponds to the location of the d.c. vector $\text{col}[\mathbf{PT}^T]_{dc}$.

Pictorial results are shown in figs. 4.7a–f for enhanced VQ applied to projection data of the MAN image, for a distortion convergence parameter of $\epsilon = 0.01$. The Hadamard and Cosine transformations have been used, respectively, for the

Fig. 4.7a PDC - HT - VQ (VF1) 1.125 bits/ps.
(MAN)

Fig. 4.7b PDC - HT - VQ (VF1) 2.0 bits/ps.
(MAN)

Fig. 4.7c PDC - CT - VQ (VF1) 0.56 bits/ps.
(MAN)

Fig. 4.7d PDC - CT - VQ (VF1) 1.0 bits/ps.
(MAN)

Fig. 4.7e PDC - CT - VQ (VF1)1.125 bits/ps.
(MAN)

Fig. 4.7f PDC - CT - VQ (VF1) 2.0 bits/ps.
(MAN)

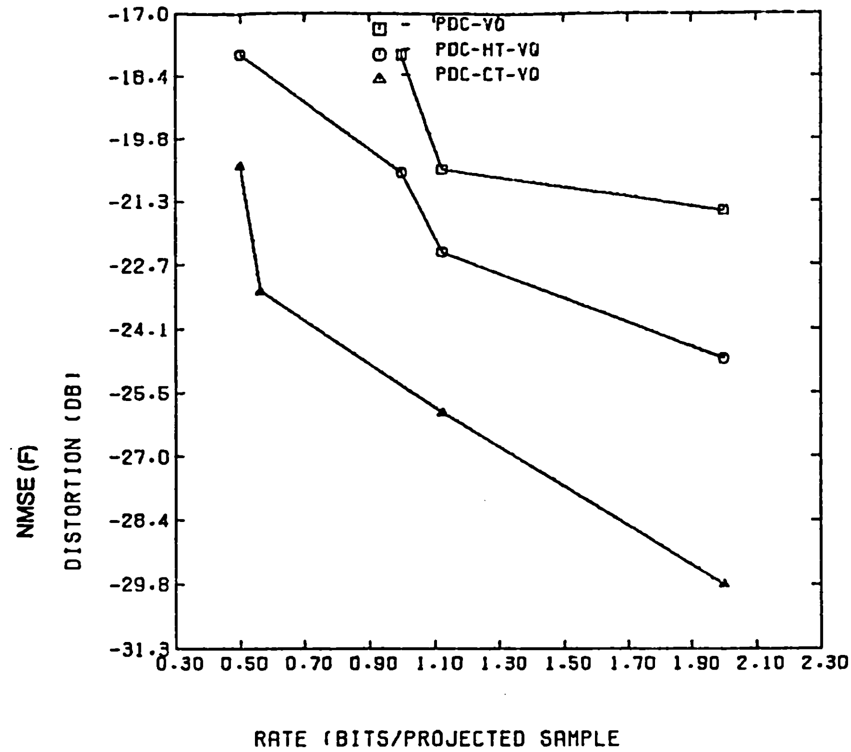

FIG. 4.8 COMPARATIVE PERFORMANCE MEASURES OF PDC-VQ, PDC-HT-VQ AND PDC-CT-VQ (VF1).

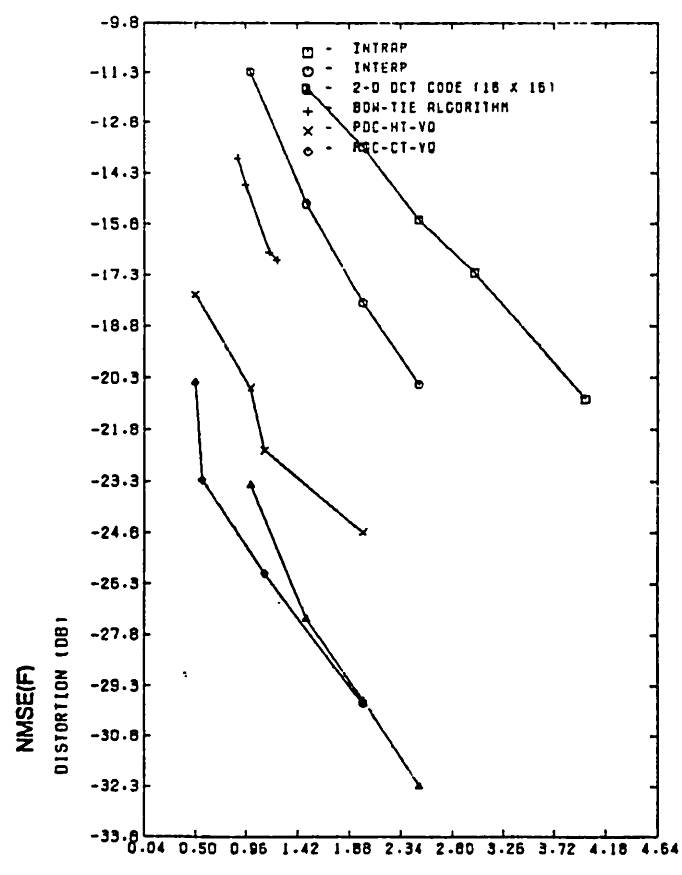

FIG. 4.9 COMPARATIVE PERFORMANCE MEASURES OF VQ BASED SCHEMES (FOR $\varepsilon = 0.01$) WITH FREQUENCY STRUCTURE BASED PDC SCHEMES.

enhanced processor implementation. The Hadamard based (PDC–HT–VQ) results (figs. 4.7a–b) are not quite impressive; this might be a reflection of the fact that the Hadamard transform (HT) is not a powerful decorrelator in the sense of (4.12). Moreover, its kernel is essentially a binary one and therefore does not readily offer a frequency–slice interpretation as required by (4.13). The Cosine transform based (PDC–CT–VQ) performance is clearly of superior quality as seen in figs. 4.7c–f; this is expected as its decorrelating potential is known to be close to that of the KLT and of course can satisfy a projection–slice constraint. While reliable image structure is maintained at bit rates of 1bit/ps and above, the quality deteriorates below these rates.

Some comparative objective performance measures of PDC– VQ, PDC–HT–VQ and PDC–CT–VQ, based on the VF1 vector selection rule, are presented in fig. 4.8. The improved performance, with successive inter–vector memory reduction, is largely evident.

Although the PDC–CT–VQ results may be considerably improved for stricter convergence values of ϵ, a performance comparison (fig. 4.9) of the VQ based schemes with the mode 1 algorithms of the previous chapter , show that the VQ strategy is a reliable approach.

4.3.4 Adaptive Enhanced VQ : A Zonal VQ Variation.

The frequency–slice partial equivalence between a transformed projection domain matrix $\mathbf{PT}^T$ and transformed image information $\mathbf{TFT}^T$ may readily offer an adaptive approach to VQ, applied to projection data. The adaptivity may be conditioned on the geometrical and/or energy distribution of frequency coefficients of $\mathbf{PT}^T$.

The radial distribution of frequency coefficients of projected information has been discussed in chapter two; the low frequency samples are more closely clustered together in the 2–D frequency plane than the higher frequency components. This may suggest that there is a stronger angular dependency or redundancy between low frequency samples; such considerations are discussed at length in [14], where so called redundancy ratios are computed for different AR projection–slice generation formats.

From an information theoretic viewpoint, longer vectors would be required to encode data where high memory prevails. This is observable from one of the *de facto* relationships utilized in the proof of Shannon's noiseless coding theorem for sources with memory [94,pg32]:

$$H_N(\mathbf{X}) = (N - M)H(\mathbf{X}) + \delta \tag{4.16a}$$

where $H_N(\mathbf{X})$ is the block entropy of a source $\mathbf{X} = \{x\}$ over a number of N symbols $x_i, x_{i+1}, \ldots, x_{i+N-1}$, with memory extending over M , $M < N$ such symbols. $H(\mathbf{X})$ is the entropy per symbol and δ is a positive constant. Clearly, for large M, N must be increased to allow $H_N(\mathbf{X})/N$ in

$$\frac{H_N(\mathbf{X})}{N} = \frac{N-M}{N}H(\mathbf{X}) + \frac{\delta}{N} \tag{4.16b}$$

to approach the lower limit of (noiseless) source coding $H(\mathbf{X})$.

While (4.16) offers an axiomatic argument for the use of longer vectors within low frequency regions of $\mathbf{PT}^T$, the high energy within the regions would constrain a vector quantizer $Q(\mathbf{v})$ to encode the low frequency regions at relatively higher bit rates than the relatively low–energy high–frequency regions or zones. Therefore, the codebooks required to satisfy both the geometrical and energy constraints would be exceedingly large. The relative codebook sizes over various regions of the frequency plane, are considered shortly. First, we describe a simple zonal–like vector quantizer scheme for adapting to the variations in geometrical structure and energy distribution in the frequency transformed projection domain.

Given a transformed projection domain matrix $\mathbf{PT}^T$, we partition it into a number of zones Z_i such that $\mathbf{PT}^T = [\,Z_1 \,|\, Z_2 \,|\, \cdots \,|\, Z_L\,]$ and different vector quantizers $Q_i(\mathbf{v})$, $i = 1, 2, \ldots, L$ are applied to corresponding zones Z_i. Geometrically, these zones are configured as concentric regions about an inner zone; in fig 4.10, the inner zone is assumed to be Z_1 for convenience. A composite bit rate R_C of vector coding may be realized, under the tenable assumption that the $Q_i(\mathbf{v})$s operate independently, as :

$$R_C = \sum_{i=1}^{L} \alpha_i \, R_{k_i}^{M_i}(Q_i(\mathbf{v})) \tag{4.17a}$$

and

$$\sum_{i=1}^{L} \alpha_i = 1 \tag{4.17b}$$

where $R_{k_i}^{M_i}(Q_i(\mathbf{v}))$ is the associated bit rate of quantizer $Q_i(\mathbf{v})$ and the α_is are proportional to the respective areas of the concentric zones Z_i. These zonal area–dependent parameters are chosen to emphasize or de–emphasize the respective zonal quantizers.

Ideally, the quantizer $Q_i(\mathbf{v})$ should be synthesized from the vectors whose components belong to the zone Z_i, however, this is rather computationally expensive and in demonstrating the performance of the adaptive zonal VQ scheme (based on the VF1 ($k_3 = 1$) vector formation procedure and gain normalization, discussed in the previous section), codebooks have been generated by using training vectors whose elements are obtainable from all zones. This approach also enables flexible switching between quantizers $Q_i(\mathbf{v})$ when applied to different zones Z_j.

Fig. 4.11 is a block diagram of the adaptive zonal vector quantizer. Fig. 4.12a is a relatively poor result of non–adaptive PDC–CT–VQ at 0.875bits/ps. Fig. 4.12b is obtained by using area–dependent parameters $\alpha_1 = \alpha_2 = 0.5$ quantizer bit rates $R_8^{512}(Q_1(\mathbf{v})) = 1.125$ and $R_{16}^{512}(Q_2(\mathbf{v})) = 0.5625$. Switching these quantizers around, for the same α_is, yields fig. 4.12c. A three zone result of $\alpha_1 = 0.2$, $\alpha_2 = 0.3$ and $\alpha_3 = 0.5$ with $R_4^{256}(Q_1(\mathbf{v})) = 2.0$ for Z_1 and $R_8^{512}(Q_1(\mathbf{v}))$ and $R_{16}^{512}(Q_2(\mathbf{v}))$ for Z_2 and Z_3, respectively, is shown in fig. 4.12d. The configuration used to produce fig. 4.12c is a geometrical based scheme, where the low frequency–slice zone components are encoded with longer vectors than the outer zone; the objective measure obtained is inferior to that of the energy based adaptation associated

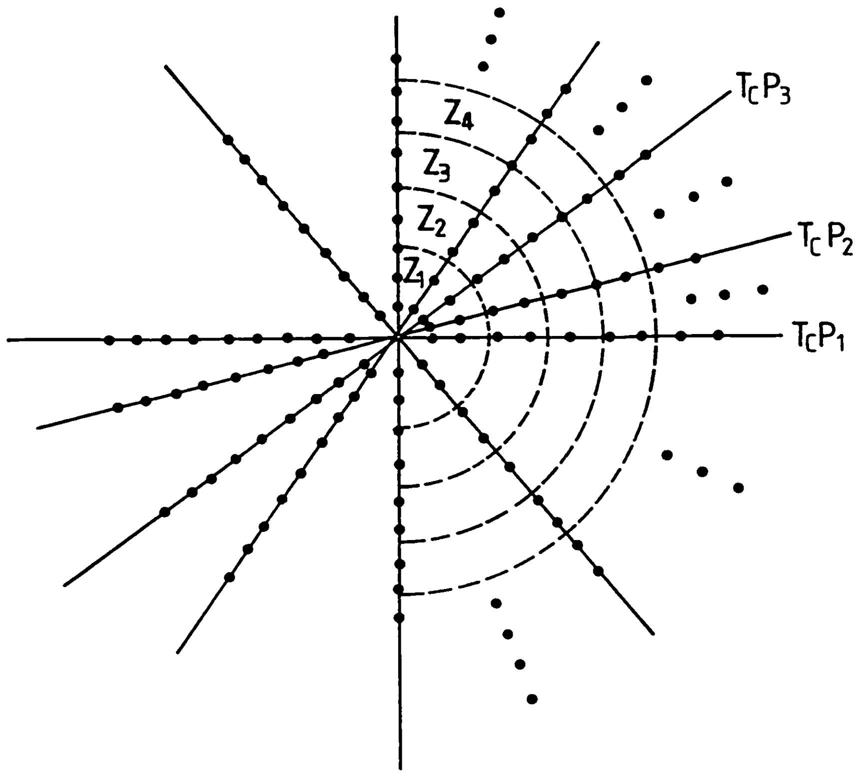

FIG. 4.10 GEOMETRICAL DISTRIBUTION OF FREQUENCY TRANSFORMED PROJECTION SAMPLES

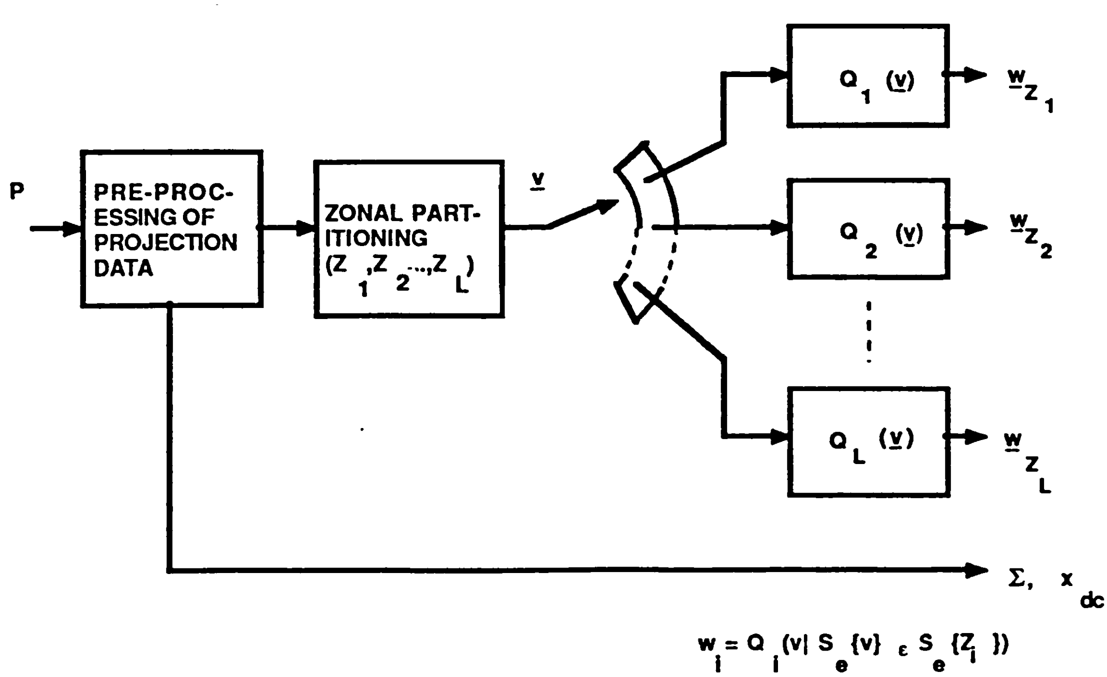

FIG. 4.11 ADAPTIVE ENHANCED VQ (FOR PDC): ZONAL APPROACH

with fig. 4.12b. The performance obtained from the three zone result indicates that this adaptive strategy is an attractive procedure for obtaining better quality below 1.0 bit/ps. However, we note that it would only be feasible when applied to large amounts of projection data so that the overhead incurred for transmitting or storing a greater number of codebooks (than in a non-adaptive procedure) would be small in comparison to the actual composite bit rate of vector quantization.

The relative quantizer (codebook) sizes over the zones for geometrical/and or energy based adaptation is briefly considered. Assuming the energy within the frequency plane of fig. 4.10 decreases outwardly from the d.c. region, then energy based adaptation between zones requires that the quantizer rate for an inner zone Z_a with respect to an outer zone Z_b, be such that

$$R_{k_a}^{M_a}(Q_a(\mathrm{v})) = \gamma R_{k_b}^{M_b}(Q_b(\mathrm{v})) \qquad (4.18a)$$

where $\gamma > 1$. The geometric proximity of frequency points within Z_a relative to Z_b provides the additional constraint:

$$k_a = \beta k_b, \qquad \beta > 1 \qquad (4.18b).$$

Satisfying (4.18a) and (4.18b), simultaneously, requires that (on using (4.6)):

$$M_a = M_b^{\gamma\beta} \qquad \gamma, \beta > 1 \qquad (4.18c).$$

The exponential increase in memory requirement for a zonal vector quantizer whose switching is conditioned on *both* energy and geometric based constraints, is implicit.

The constraints on M_a may be reduced by the use of more sophisticated codebook structures such as multi–stage VQ codebook configurations, however, the overall complexity of the zonal VQ scheme may become prohibitive. It appears that the best course of action is to employ only one zonal switching criterion, depending on the application. For projection data of relatively low correlation, the energy would be more evenly distributed between zones and the geometrical distribution of transformed projection samples would constrain the adaptation. Otherwise the energy

Fig. 4.12a Non-adaptive PDC-CT-VQ , 0.875bits/ps

Fig. 4.12b Adaptive PDC-CT-VQ $\alpha_1 = \alpha_2 = 0.5$, 0.84 bits/ps.

Fig. 4.12c Adaptive PDC-CT-VQ $\alpha_1 = \alpha_2 = 0.5$, 0.84 bits/ps

Fig. 4.12d Adaptive PDC-CT-VQ $\alpha_1 = 0.2$, $\alpha_2 = 0.3$, $\alpha_3 = 0.5$ (0.65 bits/ps)

based zonal VQ would be the feasible approach. In the next section we consider another adaptive approach that apparently would be more practicable.

4.3.5 Large Shape Adaptation based VQ for PDC

Having obtained a reliable procedure for the application of VQ to projection domain information $\mathbf{P}$, as suggested in section (4.3.3), it is instructive to study how the enhanced VQ approach adapts to projection domain information data $(\mathbf{P}^{(1)},\mathbf{P}^{(2)},\dots,\mathbf{P}^{(l)})$ that corresponds to different images $(\mathbf{F}^{(1)},\mathbf{F}^{(2)},\dots,\mathbf{F}^{(l)})$. This would not only imply enlarging the training set $\{\mathbf{v}\}$ for the design of optimal quantizers $Q(\mathbf{v})$ (as vector selection will be carried out over the different projection matrices), but would also require a preservation of the 'character' of a given projection domain matrix $\mathbf{P}^{(s)}$, in the course of vector quantization.

The latter constraint is explained by a uniqueness problem specified, in brief, as follows. Given two projection domain matrices $\mathbf{P}^{(m)}$, $\mathbf{P}^{(n)}$, each with a *finite* number M_θ of projections (and M_t samples per projection), that is, $\mathbf{P}^{(m)} = [\mathbf{P}_1^{(m)} \,|\, \mathbf{P}_2^{(m)} \,|\, \cdots \,|\, \mathbf{P}_{M_\theta}^{(m)}]^T$, $\mathbf{P}^{(n)} = [\mathbf{P}_1^{(n)} \,|\, \mathbf{P}_2^{(n)} \,|\, \cdots \,|\mathbf{P}_{M_\theta}^{(n)}]^T$, and if these matrices are derived on the same projection paths (orientations) from the respective images $\mathbf{F}^{(m)}$, $\mathbf{F}^{(n)}$, then it is possible that

$$\mathbf{P}_i^{(m)} = \mathbf{P}_i^{(n)}, \qquad i = 1,2,\dots,M_\theta \tag{4.19}$$

for $\mathbf{F}^{(m)} \neq \mathbf{F}^{(n)}$ [95]; this indicates that the same *finite* set of projections may be obtained from different images. A direct inference from (4.19) is that

$$\mathbf{T}\mathbf{P}_i^{(m)} = \mathbf{T}\mathbf{P}_i^{(n)}, \qquad i = 1,2,\dots,M_\theta \tag{4.20}$$

for $\mathbf{F}^{(m)} \neq \mathbf{F}^{(n)}$ and therefore the encoder $Q(\mathbf{v})$, constrained by the relations (4.9–11), would find it impossible to differentiate between the mappings $\mathbf{P}^{(m)} \leftrightarrow \mathbf{F}^{(m)}$, $\mathbf{P}^{(n)} \leftrightarrow \mathbf{F}^{(n)}$.

If (4.19) is only approximately valid or true for a number $M_o < M_\theta$ of available projections per projection matrix $\mathbf{P}^{(s)}$, then it is worthwhile presenting the matrix

$\mathbf{P}^{(s)}\mathbf{T}^T\mathbf{\Sigma}^{(s)}\mathbf{I}_{dc}$ to the VF1 vector selector for enhanced VQ processing of the data in $\mathbf{P}^{(s)}$. When the information in the associated gain matrix $\mathbf{\Sigma}^{(s)}$ is robustly encoded, the gain information about each vector $\text{col}[\mathbf{P}^{(s)}\mathbf{T}^T]_i \in \Re^{M_\theta}, i = 1, 2, \ldots, M_t$ is largely retained; this gain information effectively describes the 'character' of each $\mathbf{P}^{(s)}$. Additional information will further enhance the performance of the VQ adaptation over different projection domain matrices. In particular, at relatively small additional overhead, we may incorporate, into the VQ process, a mean vector statistic $\widehat{\mathbf{\Upsilon}}^{(s)} = [\widehat{\upsilon}_1^{(s)}, \widehat{\upsilon}_2^{(s)}, \ldots, \widehat{\upsilon}_{M_t}^{(s)}]^T = \mathbf{\Sigma}^{(s)}\mathbf{\Upsilon}^{(s)}$ where $\mathbf{\Upsilon}^{(s)}$ is the vector of sample means computed over the components of $\text{col}[\mathbf{P}^{(s)}\mathbf{T}^T]_i$, $i = 1, 2, \ldots, M_t$. Specifically, training vectors $\mathbf{v} \in \Re^k$ are chosen according to VF1$(k_3 = 1)$, from shape vectors

$$[\frac{\text{col}[\mathbf{P}^{(s)}\mathbf{T}^T]_i}{\sigma_i^{(s)}} - \tilde{\upsilon}_i^{(s)}\mathbf{e}] \in \Re^{M_\theta} \tag{4.21}$$

for $\mathbf{e} = [1, 1, \ldots, 1]^T$, $i = 1, 2, \ldots, M_t$ and $s = 1, 2, \ldots, L$. The resulting vector quantizer $Q(\mathbf{v})$ so derived from the sequence $\{\mathbf{v}\}$, operates in conjunction with a robust scalar quantizer that encodes the gain and mean information within the statistics $\mathbf{\Sigma}^{(s)}$ and $\widehat{\mathbf{\Upsilon}}^{(s)}$, respectively computed from $\mathbf{P}^{(s)}$.

Due to the fact that the shape information is derived in M_θ–dimensional space rather than k–dimensional space as implemented in [79], k being the dimension of each training vector $\mathbf{v}$, we call this approach a *large* shape adaptive VQ scheme for PDC. An advantage of this procedure, is that the shape information does not have to be extracted from *every* training vector $\mathbf{v}$, as suggested by shape based procedures in [87], in the course of VQ design. There may however be more initial delays in obtaining the information, since all the projections would be required before shape extraction in the approach outlined here. For mode 1 purposes, this may depend very much on the projection generation process, as state of the art medical based systems may generate projection information on a parallel basis [8] which may , in effect, reduce envisaged computational delays.

In general, the aim of the described shape adaptive VQ processor is to ensure as reliable a performance as possible when required to compress projection data obtained from several image functions and more so, given possible uniqueness problems that may evolve. The basic structure of this processor would very much resemble the non–adaptive enhanced VQ scheme of fig. 4.6 except that an additional matrix subtractor would be required to account for the mean statistic.

4.3.5.1 Simulation, Results and Discussion

The simulation of the large shape adaptive processor is carried out using projection information, derived from the MAN, BOY and BOX images. The corresponding profiles of vector statistics diag[$\Sigma^{(s)}$] and $\widehat{\Upsilon}^{(s)}$ are portrayed in figs. 4.13a and figs. 4.13b, respectively. They generally taper off with increased sequency. The uniform scalar quantization of the components, at 8bits/sample, of both of these vectors, at most, results in 0.12bits/ps; further reduction is possible through a suitable companding arrangement. Initially, the performance of the adaptive scheme is assessed for the case when members of the training sequence $\{\mathbf{v}\}$ are derived from all three projection sets, that is, the in–training (IT) performance is studied. A few results corresponding to the out–of–training (OT) approach are subsequently presented.

Figs. 4.14a–c are pictorial results from full–searched shape adaptive VQ (IT) at $R_4^{128}(Q(\mathbf{v})) = 1.75$ bits/ps with a convergence parameter of $\epsilon = 0.007$. Corresponding objective distortion results are found in table 4.1.

Multi–stage VQ (MVQ) incorporation

In order to achieve lower bit rates from the training sequence $\{\mathbf{v}\}$ of vectors, derived from over 48K samples of projected information, the computational effort in the codebook generation stage for full searched VQ has to be reduced (especially in a non–dedicated environment e.g. multi–user mainframe). A feasible approach is to use a multi–stage vector quantizer (MVQ); some benefits of MVQ have been mentioned earlier. Of importance, is its ability to simultaneously reduce computation, as in tree–searched VQ schemes [96], and storage requirements of full–search quantizers.

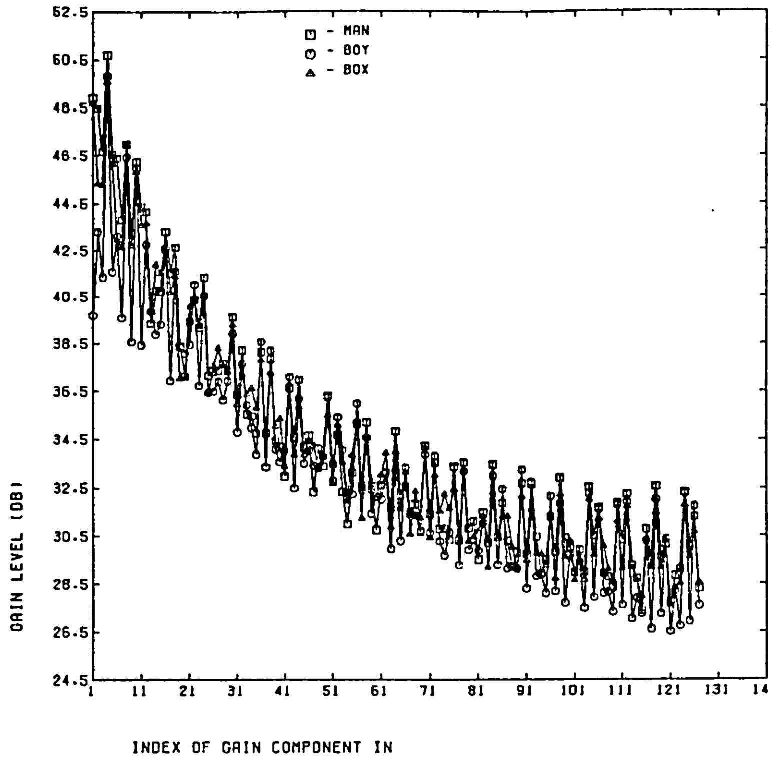

FIG. 4.13a PROFILE OF VECTOR STATISTIC $\Sigma^{(s)}$.

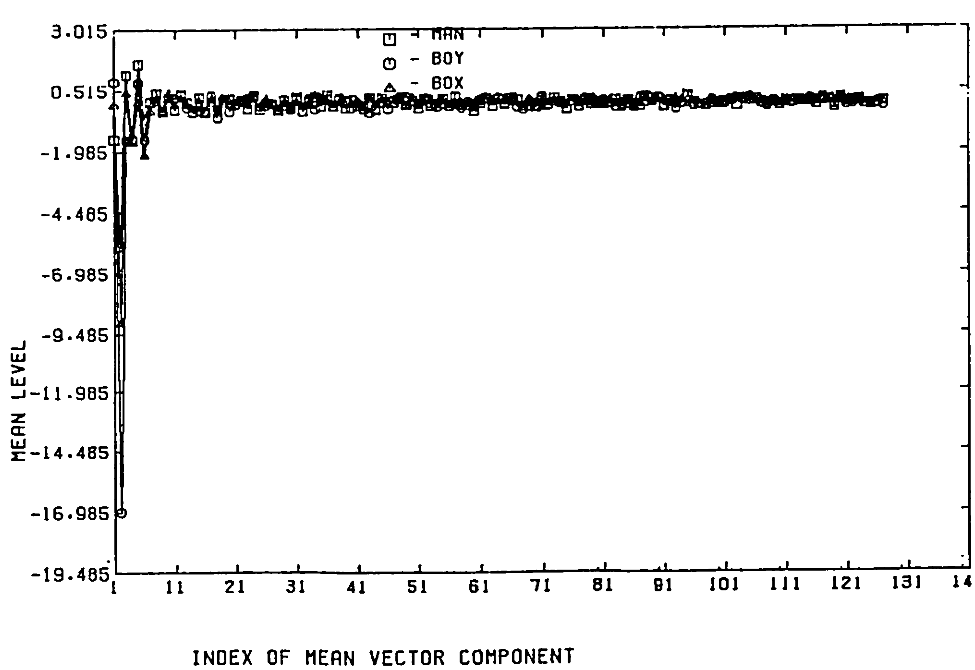

FIG. 4.13b PROFILE OF VECTOR STATISTIC $\hat{Y}^{(s)}$.

Fig. 4.14a Large Shape Adaptation (IT, 1.75 bits/ps).
(MAN)

Fig. 4.14b Large Shape Adaptation (IT, 1.75 bits/ps).
(BOY)

Fig. 4.14c Large Shape Adaptation (IT, 1.75 bits/ps).
(BOX)

Distortion 10^{-4}	MAN	BOY	BOX
NMSE(F)	17.714	74.026	40.503
NMSE(P)	7.875	4.778	8.209

Table 4.1 : Shape Adaptive (Enhanced) VQ Performance at 1.75 bit/ps

A J–stage Vector quantizer, illustrated in fig. 4.15, may be viewed as a J–layered tree–search vector quantizer with a codebook stored at each layer of the tree (instead of each node). The mapping sequence for a vector $\mathbf{v} \in \Re^k$ is specified by $Q(\mathbf{v}): \Re^k \rightarrow C^{(1)}, Q(\mathbf{e}_1): C^{(1)} \rightarrow C^{(2)} \ldots, Q(\mathbf{e}_{J-1}): C^{(J-1)} \rightarrow C^{(J)}$, where $C^{(m)}$ is the partition of $\Re^k$ at the m^{th} stage and $\mathbf{e}_m$ is the error vector generated at the $(m-1)^t h$ stage. The implicit product code structure yields a vector quantization bit rate of the form [69]:

$$R_{k'}^{M}(Q(\mathbf{v})) = \frac{1}{k'} \sum_{i=1}^{J} \log_2 M_i \tag{4.22}$$

for $k' = Jk$. Instead of the computation of $M = \prod_{i=1}^{J} M_i$ vector distortions , to achieve $\log_2 M$ *bits/vector* for full searched VQ, only $\sum_{i=1}^{J} M_i$ such distortions are required in MVQ for the *same vector rate*. However, the resulting VQ design is no longer optimal, in the sense of the complete search through a partition (codebook) of k–dimensional space $\Re^k$, as required by (4.2). Nevertheless, each partition $C^{(m)} = [\, C_1^{(m)} \,|\, C_2^{(m)} \,|\, \cdots \,|\, C_{M_m}^{(m)} \,]$ may be independently optimized according to the full searched LBG algorithm, for given partition dimensions (M_m, k).

Here, we use a two–staged configuration for enhancing the performance of the shape adaptive processor, in terms of achieving lower bit rates at acceptable distortion levels. We select a biased stage ratio of $M_1/M_2 = 16$. This biased arrangement permits a robust first stage quantization which produces a 'fine' error sequence $\{\mathbf{e}_1\}$ at the second stage. Although an unbiased two–staged structure, for which $M_1 = M_2 = M^{1/2}$, requires the least storage (hence, least number of distortion evaluations) for any type of two–staged configuration, it is known to produce the most distortion [79].

The image results of adaptive vector quantization, based on in–training two–staged VQ, over different projection domain data are presented in figs. 4.16a–i. Figs. 4.16a–f are results obtained for VQ without high frequency coefficient discarding and table 4.2 contains corresponding distortion measures NMSE(P) and NMSE(F) produced in the projection and image domains, respectively. Introducing

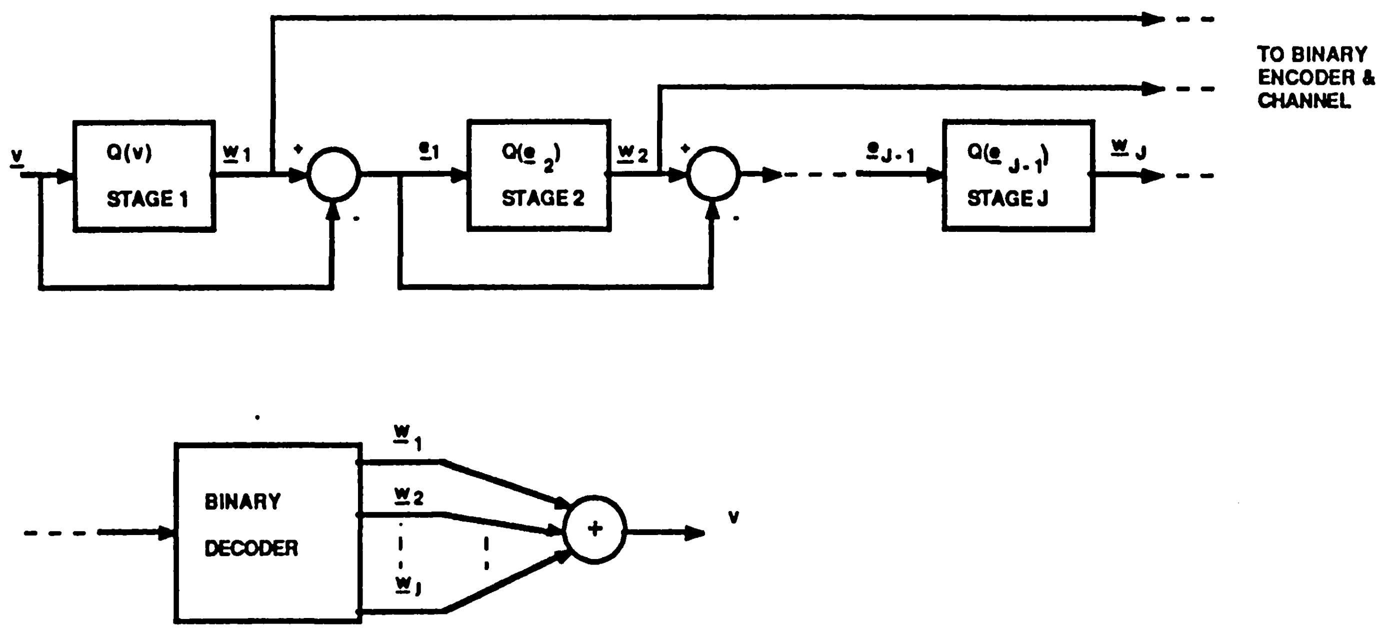

FIG. 4.15 A J-STAGE VECTOR QUANTIZER CONFIGURATION

Fig. 4.16a Large Shape Adaptation (IT, MVQ, MAN, 0.75 bits/ps)

Fig. 4.16b Large Shape Adaptation (IT, MVQ, BOY, 0.75 bits/ps).

Fig. 4.16c Large Shape Adaptation (IT, MVQ, BOX, 0.75 bits/ps).

Fig. 4.16d Large Shape Adaptation (IT, MVQ, MAN, 0.44 bits/ps).

Fig. 4.16e Large Shape Adaptation (IT, MVQ, BOY, 0.44 bits/ps).

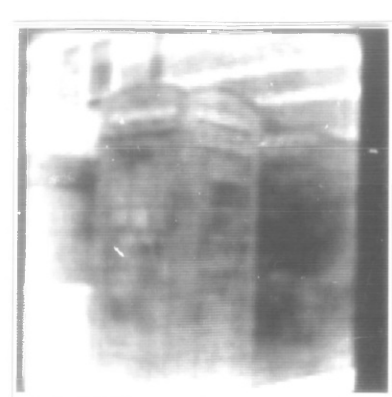

Fig. 4.16f Large Shape Adaptation (IT, MVQ, BOX, 0.44 bits/ps).

Fig. 4.16g Large Shape Adaptation (IT, MVQ, High Freq. Zero VQ, MAN, 0.47 bits/ps).

Fig. 4.16h Large Shape Adaptation (IT, MVQ, High Freq. Zero VQ, BOY, 0.47 bits/ps).

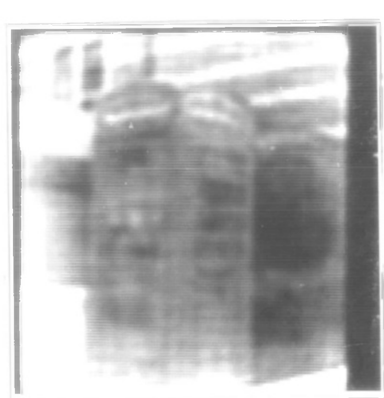

Fig. 4.16i Large Shape Adaptation (IT, MVQ, High Freq. Zero VQ, BOX, 0.47 bits/ps).

Two Stage VQ Paramters	Bit Rate bits/ps	Distortion 10^{-4}	MAN	BOY	BOX
$M_1 = 128$ $M_2 = 8$ $k = 4$	1.250	NMSE(F)	10.675	39.404	20.118
		NMSE(P)	6.420	3.495	6.677
$M_1 = 256$ $M_2 = 16$ $k = 8$	0.750	NMSE(F)	20.120	76.613	38.578
		NMSE(P)	7.134	4.313	7.524
$M_1 = 512$ $M_2 = 32$ $k = 16$	0.438	NMSE(F)	59.645	131.34	—
		NMSE(P)	8.052	4. 580	7.327

Table 4.2: Performance of Shape Adaptive VQ Scheme for Different Two Staged VQ Configurations.

Two Stage VQ Paramters	Bit Rate bits/ps	Distortion 10^{-4}	MAN	BOY	BOX
$M_1 = 128$ $M_2 = 8$ $k = 4$	0.78	NMSE(F)	26.778	129.990	54.000
		NMSE(P)	7.115	4.242	7.589
$M_1 = 256$ $M_2 = 16$ $k = 8$	0.47	NMSE(F)	35.086	16.291	69.464
		NMSE(P)	7.799	5.027	8.384

Table 4.3: Performance of Shape Adaptive VQ Scheme with Zero Vector Quantization of High Frequency Content of Projected Information

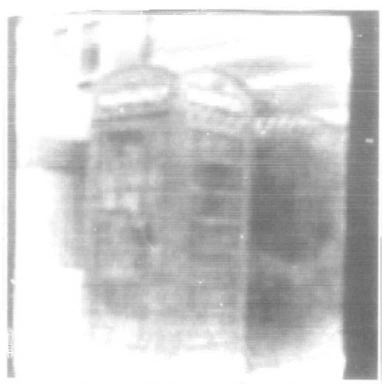

Fig. 4.17a Large Shape Adaptation (OT, MVQ, High Freq. ZeroVQ, BOY, 1.25 bits/ps).

Fig. 4.17b Large Shape Adaptation (OT, MVQ, High Freq. Zero VQ, BOX, 1.25 bits/ps).

Distortion $(10)^{-4}$	BOY	BOX
NMSE(F)	51.622	26.835
NMSE(P)	3.509	7.197

Table 4.4 Quantitative Results of Out–of–training Large Shape Adaptive VQ for PDC

zero–vectors at the receiver to replace high frequency components of the transformed, normalized and mean shifted projection spaces, does not appear to significantly increase the projection domain distortion (see table 4.3) but considerably increases the image domain objective distortion. This increase may account for the relative blur of detail, noticeable in the imagery of figs. 4.16g–i.

Out of training based adaptivity is introduced by obtaining training vectors (according to VF1) from projection domain matrices associated with the MAN and BOX images and applying the corresponding (two–staged) vector quantizer to projection domain information of the BOY image; this is also carried out for training vectors similarly derived from the MAN and BOY images with subsequent vector quantization of the BOX image. Pictorial results are shown in figs. 4.17a–b and NMSE distortion measures are presented in table 4.4. These results are of acceptable quality as those obtained from the in–training VQ approach. A comparison of tables 4.2 and 4.4 also show that the numerical distortion does not increase significantly as a result of out–of–training.

These results indicate that through shape–extraction, the adaptive vector quantizer treats the projection data, associated with different image functions, as belonging to the same homogeneous (statistically) information with the update of shape information (or projection domain 'character' information) being provided by the overhead of the respective gain and mean large vector statistics.

4.4 Summary

Having reviewed some recent developments of VQ of images, we have developed a reliable VQ approach for the compression of projection domain information under a mode 1 PDC framework. Although the effects of different vector samples are briefly studied with VQ applied *directly* to projection data, the main strategy has been to maintain correspondence between linear transformations of the projected information and the corresponding image domain. In adhering to such a guideline, substantial inter–vector memory, that would otherwise prevent efficient memoryless vector quantizer design, is reduced.

Adaptivity has been introduced within an enhanced VQ structure via two schemes. The first, a zonal vector quantization approach, is motivated by sample geometrical/energy distributions within the transformed projection information and the other attempts to preserve the uniqueness of projection–image mapping by shape adaptation over different projection data.

In general, bit rates in the range of 0.5–2.0 bits/ps (compression factors up to the order of 20, with respect to 10 bits/ps for representing original projection data) are realized through VQ based projection domain compression, with acceptable fidelity being retained in image reconstructions.

CHAPTER FIVE

SOME DEVELOPMENTS FOR MODE 2 PDC

5.1 Introduction

Although the compression algorithms considered in chapter three and the vector quantization approach of chapter four are, in principle, respectively applicable to either mode 1 or 2 processing, the results are more representative of tomographic compression (i.e. compression of projection data corresponding to unknown image information) than image compression (i.e compression of known image information). This is because the projection domain compressor must be able to work at a relatively high resolution in an image processing environment in order to compare favourably with other image coding schemes. In effect, more stringent conditions on the sampling of the Radon transform are required for mode 2 PDC. Of additional importance, is the need for fast projection generation and image reconstruction procedures, respectively.

In discussing how the basic principles of tomography may be applied to image data compression, Fraser et al [14] simulate an optical encoder by what may be considered to be an 'in–place' Fourier technique which produces adequate resolution with a reasonably fast turnaround of results. With the aid of their basic algorithm which is outlined in section 5.2, we investigate projection based block coding (PBBC) of image data and compare the performance with that of a conventional Fourier transform code, in section 5.3. An adaptive version of the PBBC scheme that is conditioned on the a.c. Fourier energy per block of transformed image data is also presented.

Section 5.4 discusses unique experimentation, of importance to mode 2 PDC, in particular, but with possible applications to mode 1 processing, for studying the effects of image reconstruction error as a function of image auto–correlation, the number of projections , used in the reconstruction, and the image size, jointly and severally. The images employed for the study have been modelled from 2–D Gauss–Markov statistics.

As discussed earlier, the reconstruction error limits the performance of mode 2 PDC systems. It is therefore purposeful to develop a mechanism for projection generation, subject to a fidelity criterion on the reconstruction error. On the basis of the experiments of section 5.4, a novel *projection allocation* algorithm emerges which systematically pre–determines, over an arbitrary number of images, the number of projections required to be generated from each image in order that the reconstruction error be minimized. This minimization is constrained by a pre–specified total number of projections to be acquired from all the images. The derivation of the algorithm, a discussion on its potential applications and various performance tests are respectively presented in section 5.5. Associated lower bounds of the reconstruction error are also considered.

5.2 'In–place' Fourier Simulation for PDC [14]

Fig. 5.1 is a representative block diagram of the hybrid optical image encoder proposed by Fraser et al. An image intensity profile is illuminated on an angular basis through a lens arrangement. The output of the illuminator is a projection of the image field and the lens optically produces a Fourier transform of the projection. The Fourier transform is accordingly quantized for transmission or storage. In principle, this scheme is similar to the intra–projection coder, discussed in chapter three. However, our main interest is in the method of computer simulation which has its roots in the projection–slice theorem and Fourier inversion, respectively discussed in chapter two. The associated steps of the simulation are outlined as follows:

1. Generate an $N \times N$ Fourier transform function $\mathcal{F}(u,v)$ of an image $F(i,j)$ of the same dimensions (note: only $(N/2+1) \times N$ coefficients are required, subsequently, due to the approximate half–plane redundancy of the Fourier transform).

2. Projection–Slice determination:

   a. For each component $\mathcal{F}(u,v)$, defined with respect to cartesian co-ordinates of the Fourier plane, determine the equivalent polar co-ordinate location i.e. $r = (u^2+v^2)^{1/2}$, $\theta = \tan^{-1} v/u$.

   b. For each of a desired number M_θ of projections at angles $\theta_k = k\pi/M_\theta$, $k = 0, 1, \ldots, M_\theta - 1$, check if the component $\mathcal{F}(u,v)$ is within the *circular vicinity* of a Fourier slice at θ_k (i.e a Fourier transform of a projection at θ_k) by using the condition:

$$r\,\mathrm{abs}(\theta - \theta_k) \leq 0.5 \tag{5.1}$$

   If the condition is obeyed then $\mathcal{F}(u,v)$ is considered to belong to the slice, otherwise $\mathcal{F}(u,v)$ is set to zero (note: in practice, we do not search through all the θ_k to check the circular distance criterion for the one projection angle; the check is made for a θ_k when $k = [\theta M_\theta \pi^{-1}]$, where $[\cdot]$ refers to the nearest integer of the argument).

3. Encoding/Quantization: If the complex Fourier coefficient $\mathcal{F}(u,v)$ belongs to a projection slice, then quantize its respective magnitude and phase components. The two components are uniformly quantized although the magnitude is companded before quantization.

4. Implement the inverse transform to obtain a compressed picture $\widehat{F}(i,j)$.

It is clear from the algorithm, that the projection domain is directly accessed from the Fourier space in a manner dictated by the projection–slice theorem. However, we do not actually move to a polar co-ordinate system from the cartesian samples but simply determine, through a *nearest neighbour* interpolation of (5.1), if samples may or may not belong to slices (projections) and act according to steps 2b, 3 and 4 of the algorithm. Hence, the name 'in–place'. Several pictures depicting the Fourier plane that results from the slicing operation (step 2) are found in [14]; they confirm the tomographic or slice effect of the simulation.

One advantage of this 'in-place' procedure is that the difficulties associated with the determination of appropriate sampling intervals in the radial parameter

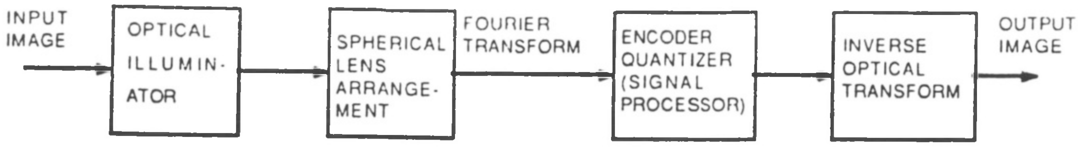

FIG. 5.1 OPTICAL SYSTEM FOR FOURIER BASED PDC.

Fig. 5.2 'Fourier based PDC' 1.5 bits/pixel.
(80 projections, MAN)

Fig. 5.3 'Fourier based PDC' 1.5 bits/pixel.
(80 projections, BOY)

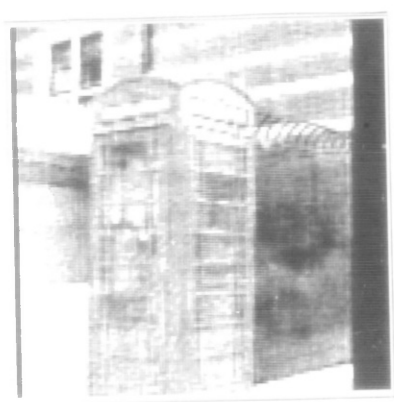

Fig. 5.4 'Fourier based PDC' 1.5 bits/pixel.
(80 projections, BOX)

are bypassed and therefore the resolution problems in that respect are controlled. In practice, this resolution may be achieved by optical processing, as described in [14]. The encoding functions may be implemented by a signal processing chip prior to an inverse optical arrangement for reconstruction.

Figs. 5.2–4 are results of coding, at 1.5bits/pixel, based on the 'in–place' approach. Each picture has resulted from the use of 80 projections or slices and the bit allocation process as described for the bow–tie algorithm of chapter three; this bit allocation procedure which is more adaptable to image statistics is preferable to the deterministic approach employed in [14].

5.3 Projection Based Block Coding of Images (PBBC)

5.3.1 Description and Implementation

Block coding of image data typically involves partitioning an image into sub–blocks and compressing them in a fully or partially independent manner [97,98]. With respect to projection based block coding (PBBC) of image data, projections are taken on each block of a partitioned image and encoded for onward transmission or storage. Working in smaller blocks effectively lowers the complexity of larger–block or whole–image based compression. Intuitively, the number of projections to be employed in a PBBC system must be commensurate with the image block dimensions. This premonition is empirically examined in the numerical experiments of section 5.4.

At this point, we present some results of PBBC of 128×128 images; each image is sub-divided into 16×16 blocks with 16 projections acquired per block. The projection information is encoded using the Fourier based procedure. Pictorial results of the PBBC schemes are shown in figs. 5.5–9 with associated bit rates. The 'block' effect, noticeable at lower bit rates, is indicative of the inter–block statistical dependency. This effect may be offset by various procedures such as processing larger blocks or employing recursive block coding techniques [97] to reduce the statistical inter–block correlation. The recursive techniques are designed to effect

Fig. 5.5 PBBC, 16 x16 blocks. (16 proj./block)
MAN, 2.0 bits/pixel

Fig. 5.6 PBBC, 16 x 16 blocks. (16 proj./block)
MAN, 1.44 bits/pixel

Fig. 5.7 PBBC, 16 x 16 blocks. (16 proj./block)
MAN, 1.0 bits/pixel

Fig. 5.8 PBBC, 16 x 16 blocks. (16 proj./block)
BOY, 2.0 bits/pixel

Fig. 5.9 PBBC, 16 x 16 blocks (16 proj./block)
BOY, 1.45 bits/pixel

Fig. 5.10 PBBC, 64 x 64 blocks (64 proj./block)
MAN, 2.0 bits/pixel

Fig. 5.11 PBBC, 64 x 64 blocks (64 proj./block)
BOY , 2.0 bits/pixel

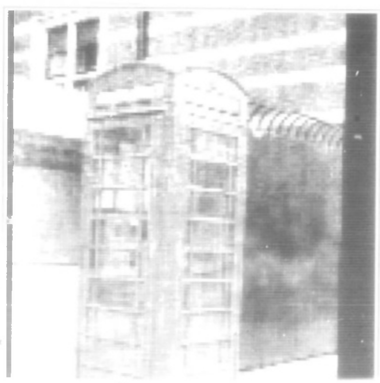

Fig. 5.12 PBBC, 64 x 64 blocks (64 proj./block)
BOX, 2.0 bits/pixel

Quantizer Rate	Final Bit Rate (bits/pixel)
B_Q	B'_Q
2.50	2.00
2.25	1.82
2.00	1.63
1.75	1.44
1.50	1.25
1.25	1.06
1.00	0.85

Table 5.1: Final bit rates B'_Q for encoding 16×16 image sub-blocks with 16 projections per block; each projection (or Fourier slice) is quantized at B_Q bits/pixel.

additional processing of image blocks as described in [97]. Some results that are representative of larger–block processing are shown in figs. 5.10–12 for final bit rates of $B'_Q = 2.0$ bits/pixel with 64×64 block processing and 64 projections generated per block. The results have a better appearance than those corresponding to the 16×16 block processing at the same rate.

5.3.2 Comparison of PBBC with 2–D Fourier Transform Coding

The Fourier based projection method clearly makes Fourier transform image block coding the closest conventional compression scheme to PBBC. Hence, comparisons between the methods are in order.

Table 5.1 is presented to reflect a basic advantage of the PBBC approach which is one of adequately representing an image area by a few projections and therefore potentially fewer bits than required by conventional codecs for a specified bit rate B_Q. The values in the left hand column correspond to the average number of bits B_Q allocated for quantization of Fourier transformed image blocks while those in the right hand column are the *final* bit rates B'_Q obtained by encoding slices of the Fourier transforms (i.e. projections of the image blocks) at an average bit rate of B_Q bits/pixel. On average $B'_Q = 0.85 B_Q$, however, from equation (2.57), this reduced bit allocation is generally achieved for a given number M_θ of projections, derived from $N_1 \times N_2$ image blocks, when

$$\frac{B'_Q}{B_Q} < \frac{M_\theta}{N_1 N_2} \qquad (5.2).$$

Therefore, the gain of reduced bit allocation must be weighed against additional distortion produced by the Fourier slicing or image projecting procedure (this distortion is of course manifested at the reconstruction stage).

By setting the average bit rate of a conventional Fourier transform code to the final bit rates, obtained by PBBC, the additional distortion that results from the slicing may be observed. Figs. 5.13–15 are graphical results of distortion rate curves that compare the Fourier transform code with PBBC, for the three images. The results indicate that the projection procedure or Fourier plane slicing can produce

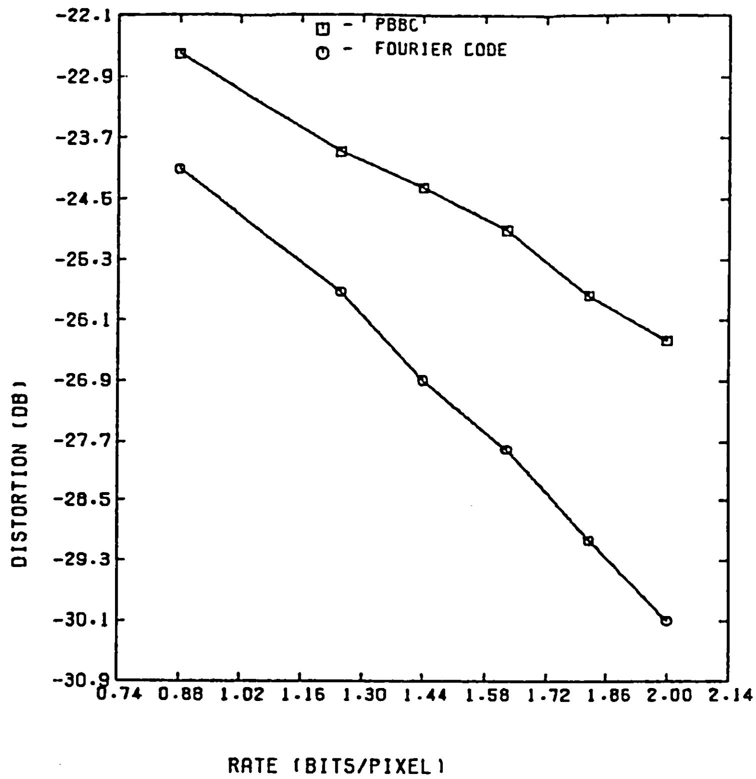

FIG. 5.13 DISTORTION - RATE COMPARISON OF PBBC WITH 2-D FOURIER TRANSFORM CODING (MAN).

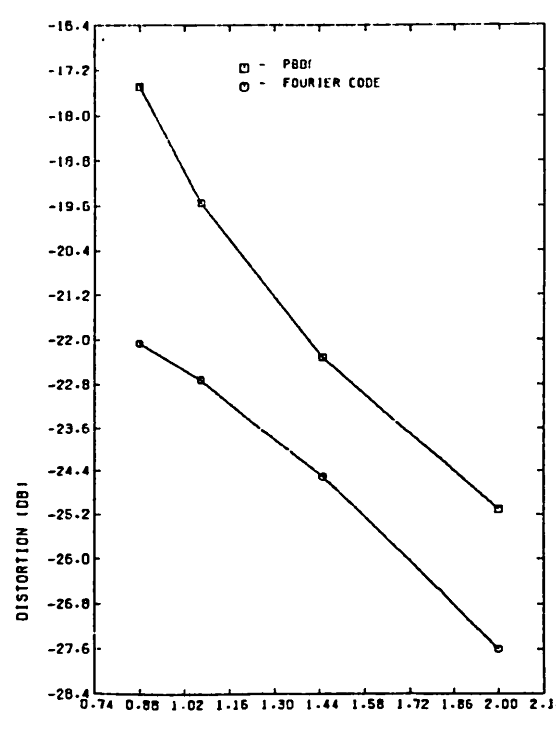

FIG. 5.14 DISTORTION - RATE COMPARISON OF PBBC WITH 2-D FOURIER TRANSFORM CODING (BOY).

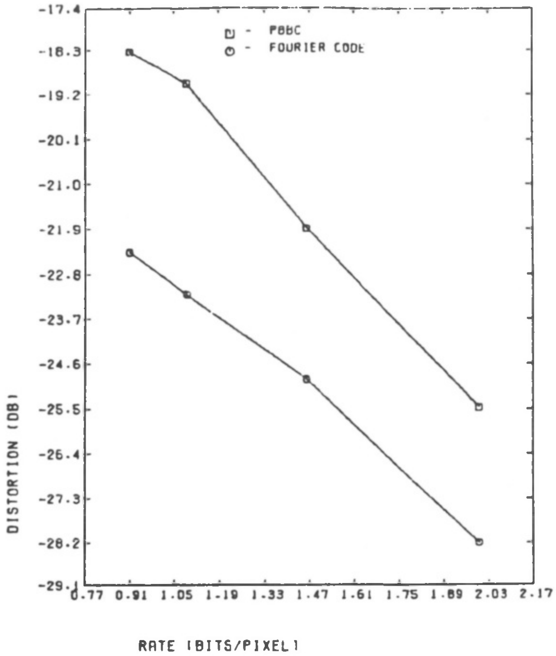

FIG. 5.15 DISTORTION - RATE COMPARISON OF PBBC WITH 2-D FOURIER TRANSFORM CODING (BOX).

Fig. 5.16 2 - D Fourier transform coding (16 x 16 blocks), MAN, 2.0 bits/pixel.

Fig. 5.17 2 - D Fourier transform coding (16 x 16 blocks), BOY, 2.0 bits/pixel.

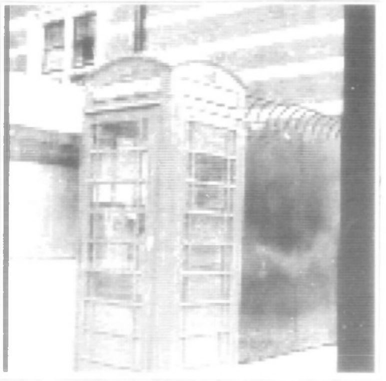

Fig. 5.18 2 - D Fourier transform coding (16 x 16 blocks), BOX, 2.0 bits/pixel.

up to 4dB more distortion than the Fourier transform code at the same bit rate. To a large extent, this is expected, as points that do not correspond to the slices in the Fourier space are effectively zeroed out , through the slicing process, both in the typical low magnitude high frequency region and the high magnitude low frequency region. On the other hand, the discarding of coefficients in the Fourier transform code is only controlled by the bit allocation process which systematically discriminates between low and high energy Fourier zones. Some pictorial results of the Fourier transform code, operating at 2.0 bits/pixel are found in figs. 5.16–18.

At the expense of increasing the ratio B'_Q/B_Q, this additional distortion may be reduced by employing more projections in the PBBC scheme. Perhaps the most significant advantage of a PBBC scheme or any mode 2 intra–projection procedure is its ability to decompose the 2–D transform code into a potentially small number of 1–D projection based schemes. Ultimately, a mode 2 procedure may be employed to the extent of its not introducing unacceptable *subjective* distortion in compressed imagery.

5.3.3 Adaptive PBBC

An adaptive PBBC approach may be considered in which the number of projections generated per image block is varied in accordance with the image block a.c. energy which is a measure of the image *activity* within the block [98]. A simple procedure is developed in which an energy threshold, corresponding to the averaged energy over all available sub–blocks in an image, is computed. When an image block is to be encoded using the PBBC algorithm, the block a.c. energy is estimated and compared with the pre–computed threshold. A higher number of projections are employed for coding a block whose energy exceeds this threshold, otherwise, fewer projections are involved.

This is implemented for 16×16 blocks of image data where 16 projections are used for blocks of high a.c. energy and 8 projections for low a.c. energy blocks. Some performance results of the adaptive scheme and their comparison with those of the

Image	Code Protocol	B'_Q (bits/pixel)	NMSE (10^{-3})	Average A.C. Energy (dB)
MAN	Adaptive	1.39	3.492	77.20
	Non-adaptive	2.00	2.301	
BOY	Adaptive	1.36	4.886	75.00
	Non-adaptive	2.00	3.054	
BOX	Adaptive	1.43	4.946	76.94
	Non-adaptive	2.00	2.817	

Table 5.2: Performance Results of Adaptive PBBC for $B_Q = 2.5$ bits/pixel.

Fig. 5.19 Adaptive PBBC (MAN) 1.39 bits/pixel.

Fig. 5.20 Adaptive PBBC (BOY) 1.36 bits/pixel.

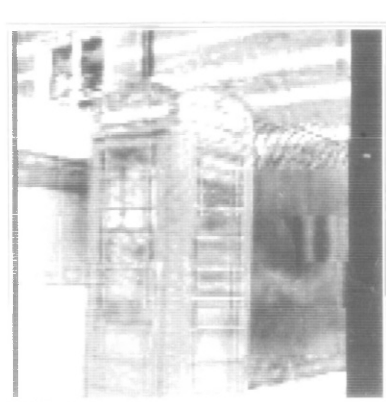

Fig. 5.21 Adaptive PBBC (BOX) 1.43 bits/pixel.

non–adaptive approach are tabulated in table 5.2. The results show that, on average, the distortion increases only by about 2dB by using fewer projections on blocks of low a.c. energy. However, up to 0.6 bits/pixel of reduced bit rates is realized through the adaptivity. Corresponding picture results are shown in figs. 5.19–21 and are of good quality compared to those output from the non–adaptive based PBBC at the same rate of quantization $B_Q = 2.0$ bits/ sample.

A more systematic means of determining the number of projections as a function of image activity is developed, in section 5.5, for images with Gauss–Markov statistics; the algorithm is linked to the experiments reported in the following section.

5.4 Relationships of Reconstruction Error with Image Correlation, Image Area and the Number of Projections: A Quantitative Study

5.4.1 Introduction

The performance of PDC is clearly constrained by the image reconstruction error which is in turn a function of the number of projections available for reconstruction. The problem of ascertaining an adequate number of projections for reconstruction has been highlighted in various places in the literature [7,26,99]. Typically, sampling theory is used to establish a relationship between the number of projections and the radial sampling along the projections. This requires knowledge of the radial bandwidth and the area of the region to be reconstructed. The number of projections are chosen to limit angular artifacts to the outer regions of the reconstruction area [26,99]. Peak to peak measurements of the error or artifacts generated from reconstructions of a unit point mass, as reported in [99], indicate that a greater number of projections are required to keep the artifacts without larger reconstruction regions for a specified radial sampling.

Image correlation, a possible measure of image smoothness (in the sense of the level of contrast change in image data), is vital for data compression purposes and more so for PDC based algorithms, as it is known that the sensitivity of pictures with respect to reconstruction errors is largely dependent on the smoothness of the picture [7]. The smoothness measure, used in the mathematical discussion of [7], is used to formulate continuity results, of the AR–RT (as mentioned in section 2.3.2 of chapter two), that guarantee stability of the inversion process. Small values of the parameter (less than a half) are representative of high contrast pictures with rapid intensity changes while large values (much greater than unity) correspond to smooth slowly varying image functions. Bates et al [45] also point out the reconstruction problem encountered in medical diagnostic practice when there exists intermittent bone and tissue structure of a rapidly changing density; this profile type often introduces streaking artifacts in the accompanying reconstructions.

In this section, we wish to study the error of reconstruction on a quantitative basis, using the fast 'in–place' Fourier based reconstruction scheme, as a function of the image correlation, number of projections and the image size on a joint and several basis.

5.4.2 Description and Results of Quantitative Experiments for Study

5.4.2.1 Random Picture Generation

As this study is being carried out in the context of PDC, which must be able to effect adequate compression of sample images from a random ensemble, the image to be reconstructed is fittingly modelled as a random one with associated correlation and area. Specifically, a random ensemble of images $\{\mathbf{F}_1, \mathbf{F}_2, \ldots, \mathbf{F}_N\}$ is generated under the assumption that each image has fully separable 2–D Gauss-Markov statistics with autocorrelation function:

$$R_F(k', l') = \sigma_F^2 \rho_1^{|k'|} \rho_2^{|l'|} \qquad \text{for} \qquad 0 \leq \rho_1, \rho_2 < 1 \tag{5.3}$$

where σ_F^2 is the variance of the discrete–space image function $F(i, j)$ and k' and l' are integer lags over which the auto–correlation function is estimated. Employing a causal minimum variance model [100], the l^{th} image field is generated by the white noise driven recursion

$$F_l(i+1,j+1) = \rho_1 F_l(i,j+1) + \rho_2 F_l(i+1,j) - \rho_1\rho_2 F_l(i,j) + W(i+1,j+1) \quad (5.4)$$

for $l = 1,2,\dots,N$ and where the statistics of the white noise sequence $\{W(i,j)\}$ are such that its auto-correlation function $R_W(m,n)$ is:

$$R_W(m,n) = \sigma_F^2(1-\rho_1^2)(1-\rho_2^2)\delta_{m,0}\delta_{n,0} \quad (5.5)$$

where

$$\delta_{m,0} = \begin{cases} 1 & m = 0 \\ 0 & m \neq 0. \end{cases}$$

The experiments generally proceed by varying the number of projections (or Fourier slices) used in reconstructions, for given image correlation $\rho_1 = \rho_2$ (equal correlation along the image rows and columns has been assumed for simplicity). The correlation values are varied in the range [0.0,0.99].

5.4.2.2 Reconstruction Error as a Function of Image Correlation and the Number of Projections.

This first experiment is designed to observe the NMSE of reconstruction of an image field of the same dimensions (128×128) and same mean (132.1) and standard deviation (59.4) of intensity values as those of the original MAN image.

Fig. 5.22 is a graphical representation of the results of experiment. The reconstruction error is seen to fall more significantly with the increased use of projections for medium to highly correlated ($\rho_1, \rho_2 = 0.6 - 0.9$) images than those of low correlation. The advantages of compressing and/or reconstructing smooth images with fewer projections than those with more rapid changes in contrast, are evident from the results.

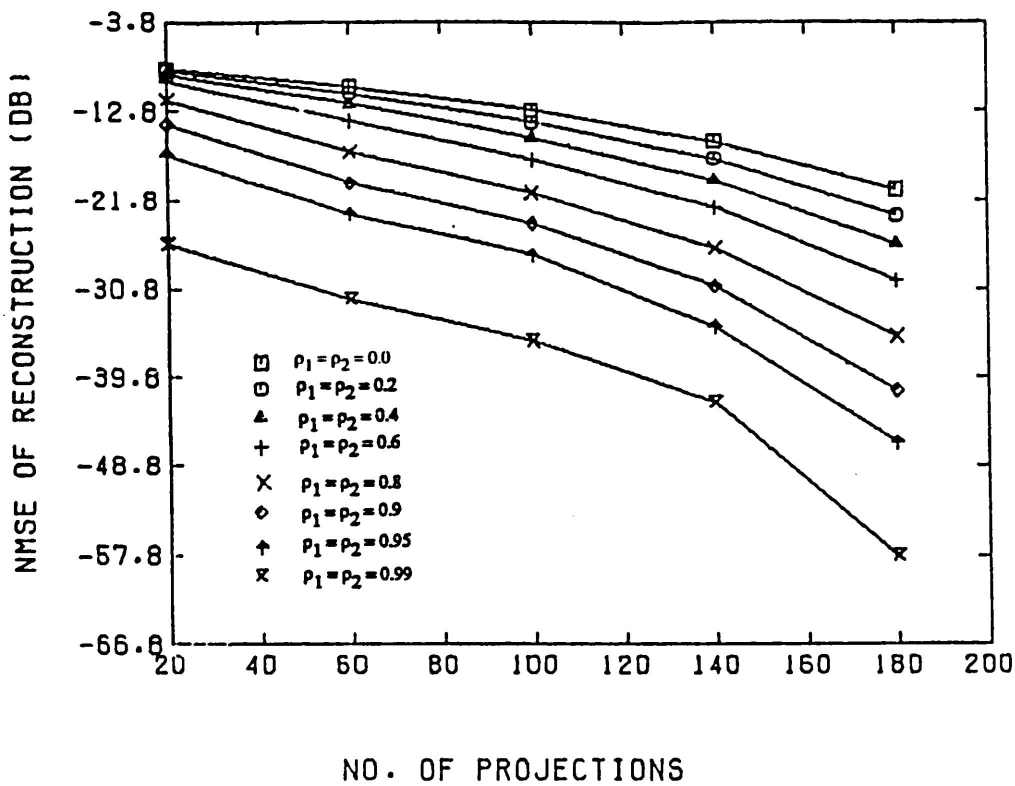

FIG. 5.22 RECONSTRUCTION DISTORTION AS A FUNCTION OF IMAGE CORRELATION AND THE NUMBER OF PROJECTIONS.

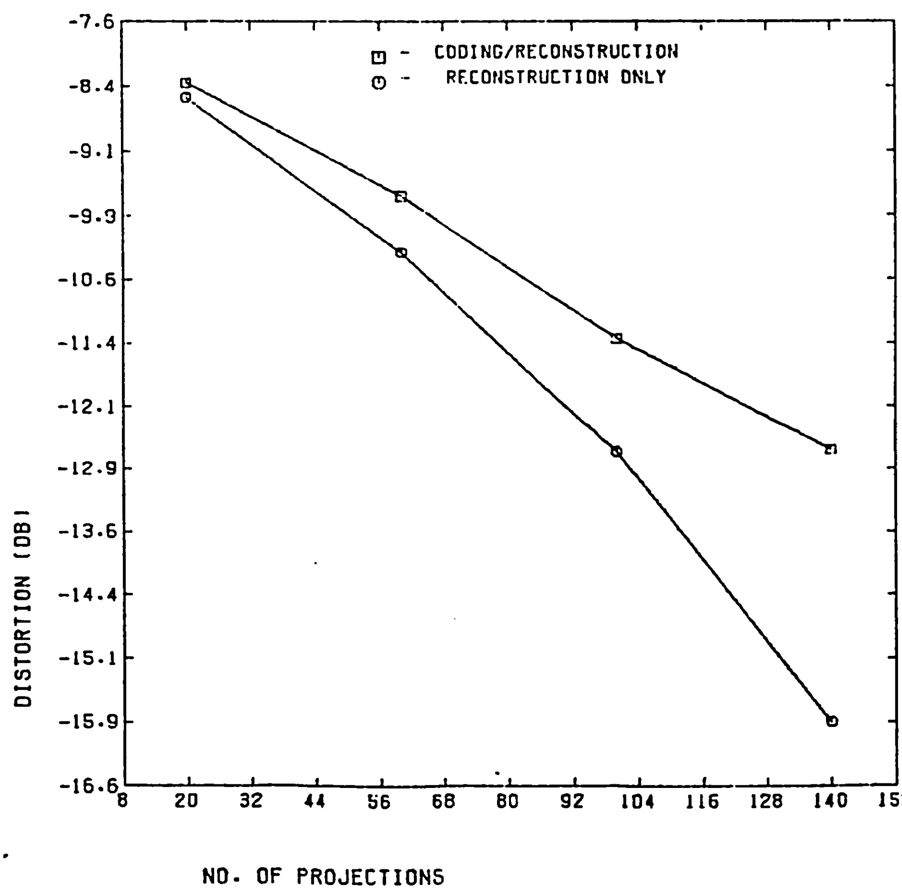

FIG. 5.23 COMPARISON OF COMBINED ERROR OF ENCODING AND RECONSTRUCTION WITH RECONSTRUCTION - ONLY DISTORTION ($\rho_1=\rho_2=0.0$).

5.4.2.3 Interaction of Reconstruction Error with Encoding Distortion

This experiment is carried out to observe the total distortion due to quantization and reconstruction, as a function of correlation and the number of projections available for reconstruction; the quantization rate is fixed at $B_Q = 2.0$ bits/pixel. The image size, mean and standard deviation are respectively the same as those employed in the previous sub–section.

Comparisons of the results of this combined error of encoding and reconstruction (as a function of the number of projections) with reconstruction–only distortion are shown for $\rho_1, \rho_2 = 0.0$, $\rho_1, \rho_2 = 0.6$ and $\rho_1, \rho_2 = 0.99$, respectively, in figs. 5.23–25. In general, the effect of encoding (quantization) distortion is more significant when the reconstruction error rapidly tapers off, as a consequence of the use of a higher number of projections for reconstruction. Smaller values of B_Q would certainly cause an elevation of the combined error curves above the ones obtained for uncoded projections, however, the reconstruction error may still dominate when few projections are utilized.

It is apparent that a trade–off is required between the number of projections and the average bit rate of encoding B_Q. It may however be more advantageous to exploit PDC based schemes by using as few projections as possible, at relatively high values of B_Q than more projections at low encoding rates. In fact, the main purpose of mode 2 PDC may be defeated by adopting the latter protocol, as a high number of projections implies a significantly larger amount of the Fourier plane samples are available in which case a straightforward Fourier transform code may be employed for compression.

Since the results of this second experiment indicate that distortion from reconstruction is the dominant element when a smaller number of projections are encoded at relatively medium to high average bit rates, a judicious choice of the number of projections as a function of the reconstruction distortion is of importance.

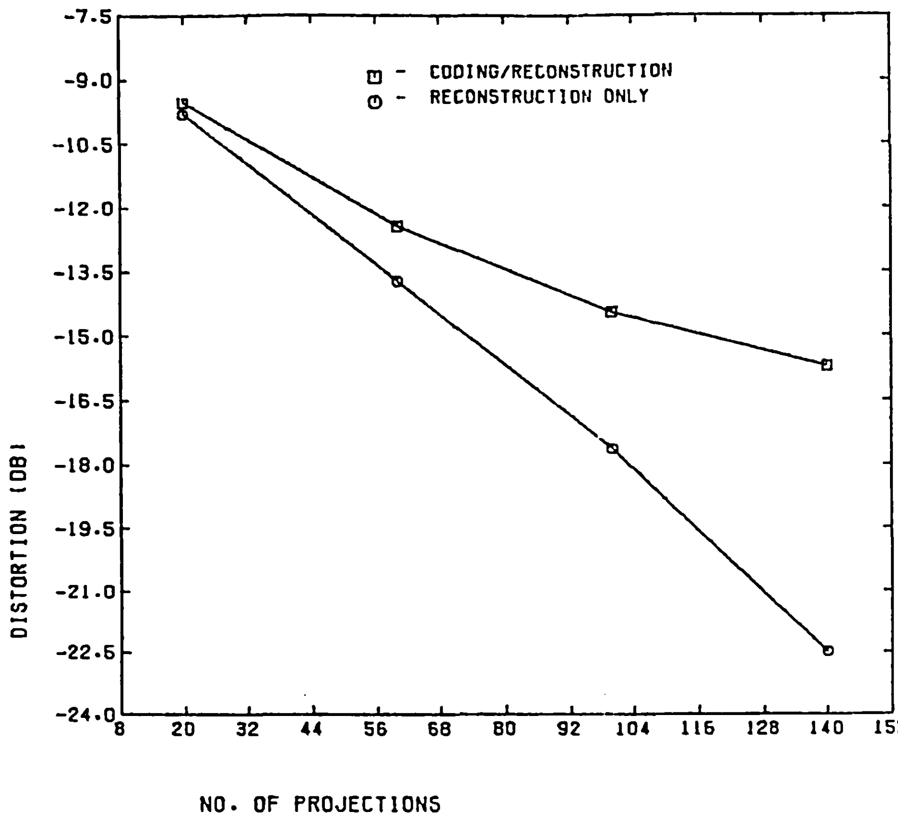

FIG. 5.24 COMPARISON OF COMBINED ERROR OF ENCODING AND RECONSTRUCTION WITH RECONSTRUCTION - ONLY DISTORTION ($\rho_1 = \rho_2 = 0.6$).

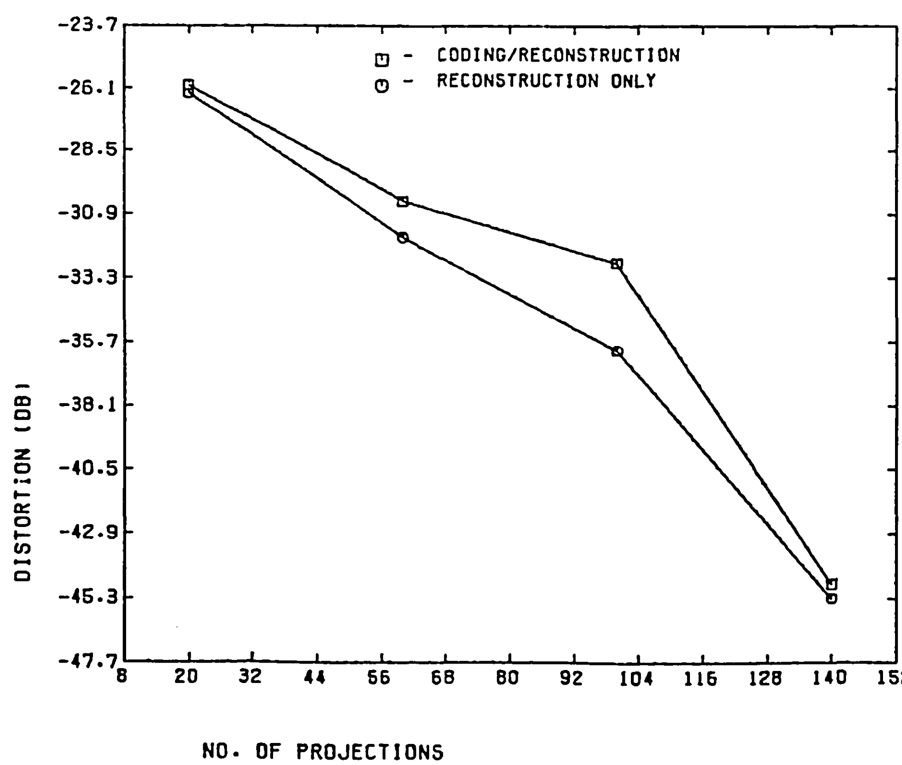

FIG 5.25 COMPARISON OF COMBINED ERROR OF ENCODING AND RECONSTRUCTION WITH RECONSTRUCTION - ONLY DISTORTION ($\rho_1 = \rho_2 = 0.99$).

5.4.2.4 Reconstruction Error as a Function of Image Correlation, Image Area and the Number of Projections

Here, the reconstruction error is observed for zero mean unit variance random image fields of 64×64 and 128×128 dimensions, respectively. The correlation is set to 0.2, 0.6 and 0.9 respectively. The results of the experimentation are presented in graphical form in figs. 5.26–28; each graph corresponds to the reconstruction error results for both image sizes for a given correlation value. Each distortion curve has the same trend, with respect to the number of projections, as those observed in fig. 5.22. The area of the image field clearly has a significant effect on the reconstruction error and more so at higher image correlation values, when the error associated with smaller image fields is considerably lower than that corresponding to larger image areas, for the same number of projections.

Table 5.3 shows the distortion results associated with 60 and 65 projections for 64×64 image fields and 120 and 130 projections for the 128×128 image fields. The area–dependent distortion values are apparently very close for a given correlation level. This indicates that there exists a definite relationship between the number of projections required to produce a certain distortion level and the corresponding image field size. It is worthwhile noting that the ratios of the respective diameters of circles that can just contain 64×64 and 128×128 images (each image pixel is assumed to have a length unit of 1) to 65 (projections) and 130 (projections) are exactly the same. Although the hypothesis has not been pursued to a definite conclusion here, it may be quite possible to determine the number of projections needed to satisfy a certain reconstruction distortion level for one image size and then from that number, simply estimate the number that would produce the same distortion for an image of a different size. This would of course require more investigation of the area–dependency of reconstruction distortion; this is not pursued further herein.

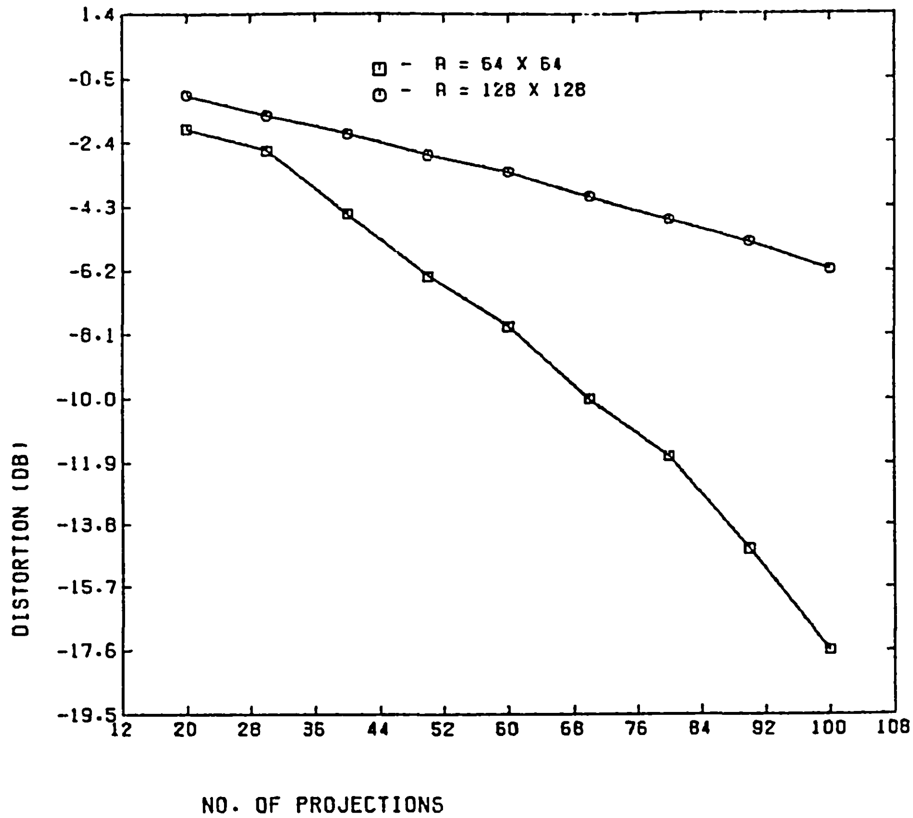

FIG. 5.26 RECONSTRUCTION ERROR AS A FUNCTION OF IMAGE CORRELATION, IMAGE AREA AND THE NUMBER OF PROJECTIONS ($\rho_1 = \rho_2 = 0.2$).

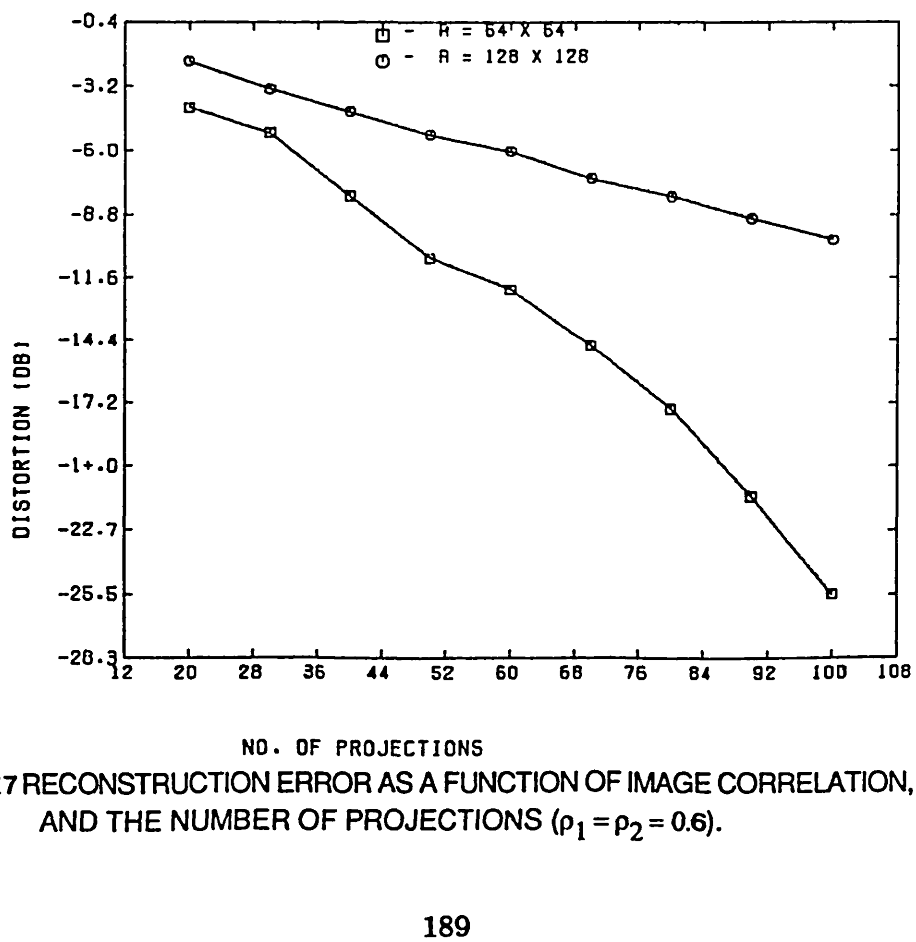

FIG. 5.27 RECONSTRUCTION ERROR AS A FUNCTION OF IMAGE CORRELATION, IMAGE AREA AND THE NUMBER OF PROJECTIONS ($\rho_1 = \rho_2 = 0.6$).

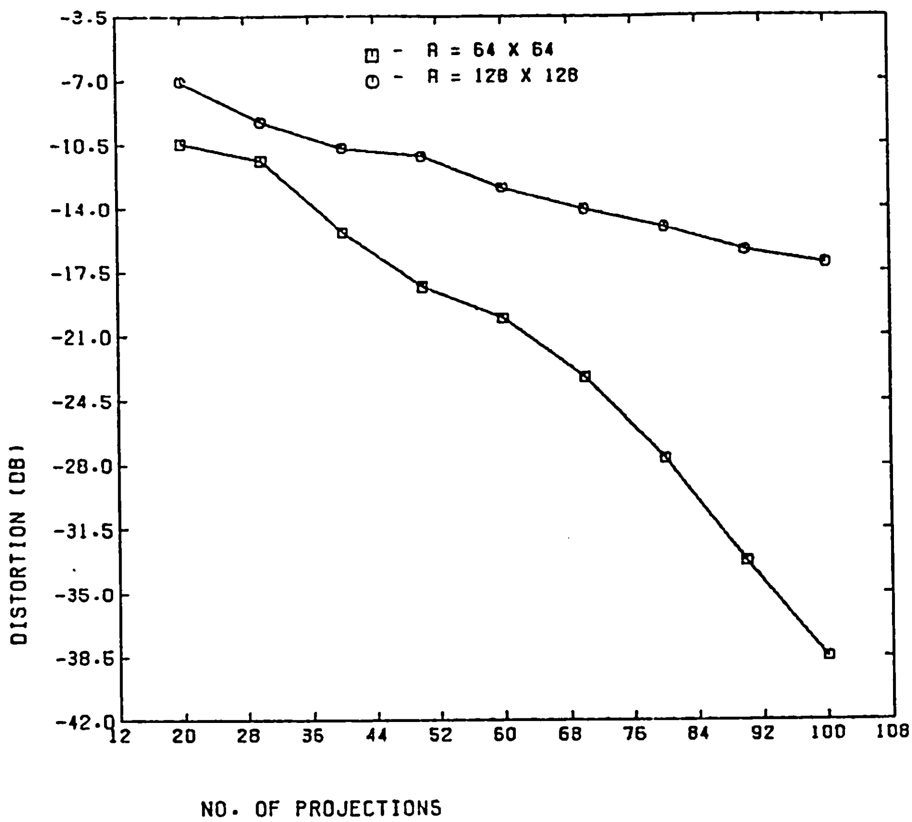

FIG. 5.28 RECONSTRUCTION ERROR AS A FUNCTION OF IMAGE CORRELATION, IMAGE AREA AND THE NUMBER OF PROJECTIONS ($\rho_1 = \rho_2 = 0.9$).

Image Area	Number of Projections	NMSE of Reconstruction (dB) for Specified Correlation Levels $\rho_1 = \rho_2 = 0.2$	$\rho_1 = \rho_2 = 0.6$	$\rho_1 = \rho_2 = 0.9$
64 × 64	60	−7.85	−12.06	−20.06
	65	−9.09	−13.64	−20.63
128 × 128	120	−7.75	−12.06	−19.91
	130	−8.71	−13.28	−21.44

Table 5.3: Approximately Equivalent Reconstruction Distortion Results Associated with Different Image Areas

5.5 A Projection Allocation Algorithm for Minimal Reconstruction Distortion

5.5.1 Introduction

The importance of determining the appropriate number of projections in mode 2 PDC systems has been discussed at length. In this section, we present an algorithm for the systematic computation of the number of projections to be generated from an image such that it is guaranteed that a minimal average reconstruction distortion is realized for a specified total number of projections, taken over an ensemble $\mathbb{E} = \{\mathbf{F}_1, \mathbf{F}_2, \ldots, \mathbf{F}_N\}$ of Gauss–Markov images.

We first describe a parametric formula for the dependence of reconstruction distortion on the number of projections and verify the formula through least squares fitting to the empirical results obtained from the experimentation of the previous section. A reconstruction error minimization problem, based on the parametric formula, is formulated and the derivation of the projection allocation algorithm follows. Various performance test results of the algorithm are also presented.

5.5.2 A Parametric Formula for Reconstruction Distortion as a Function of the Number of Projections

An inspection of the curves of results in section 5.4.2.4 indicate that the logarithmically transformed reconstruction error, for a given correlation level and image area, varies linearly with the number of projections over much of the range considered.

On the basis of the results, we propose a formula between the NMSE of reconstruction distortion D_i of the i^{th} sample image $\mathbf{F}_i$ and the associated number of projections M_{θ_i}; the formula is given as

$$D_i = K(\rho_1, \rho_2, A) \exp(-G(\rho_1, \rho_2, A) M_{\theta_i}) \tag{5.6}$$

where $K(\rho_1, \rho_2, A)$ and $G(\rho_1, \rho_2, A)$ are constants for a given set of image correlation coefficients ρ_1, ρ_2 and an image area A.

Image Area (A)	Range of the No. of Projections	Estimated Parameters	$\rho_1 = \rho_2 = 0.2$	$\rho_1 = \rho_2 = 0.6$	$\rho_1 = \rho_2 = 0.9$
64×64	10–80	$G(\rho_1, \rho_2, A)$	0.03621	0.04889	0.06027
		$K'(\rho_1, \rho_2, A)$	0.27477	0.02698	−1.12614
		Residue*	0.08145	0.06005	0.36032
128×128	20–130	$G(\rho_1, \rho_2, A)$	0.01599	0.02297	0.02768
		$K'(\rho_1, \rho_2, A)$	0.15129	−0.02368	−1.27604
		Residue*	0.02298	0.01530	0.08101

* (residue of fit)

Table 5.4: Values of parametric constants and associated residues obtained from the fit of parametric formula (equation 5.6) to empirical results of reconstruction distortion (as a function of the number of projections.)

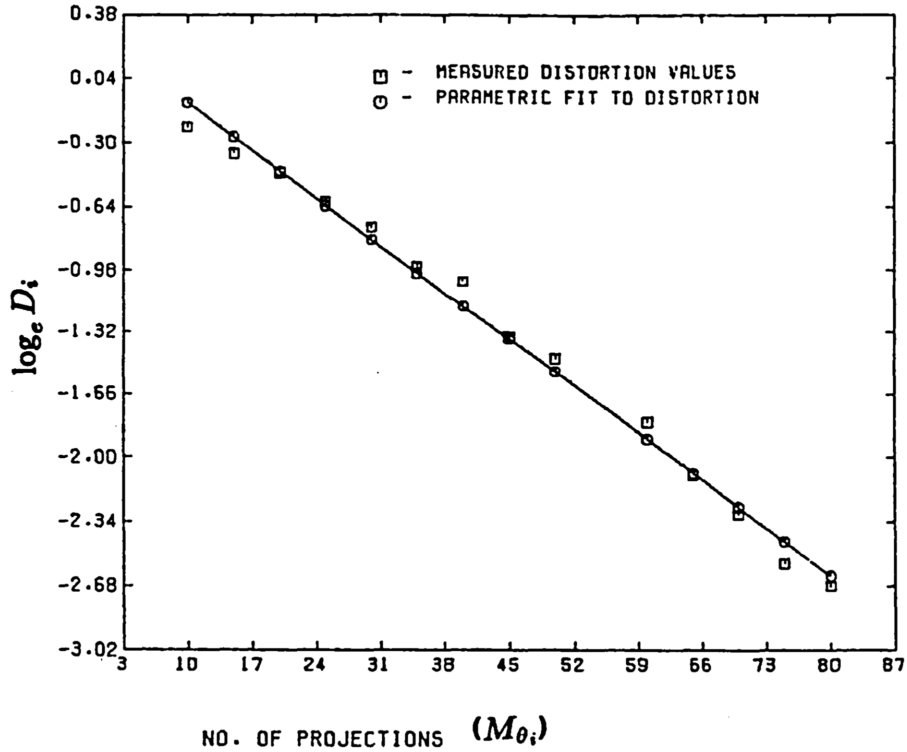

FIG. 5.29 FIT OF PARAMETRIC FORMULA (EQUATION 5.6) TO MEASURED RECONSTRUCTION DISTORTION VALUES FOR $\rho_1 = \rho_2 = 0.2$, A = 64 x 64.

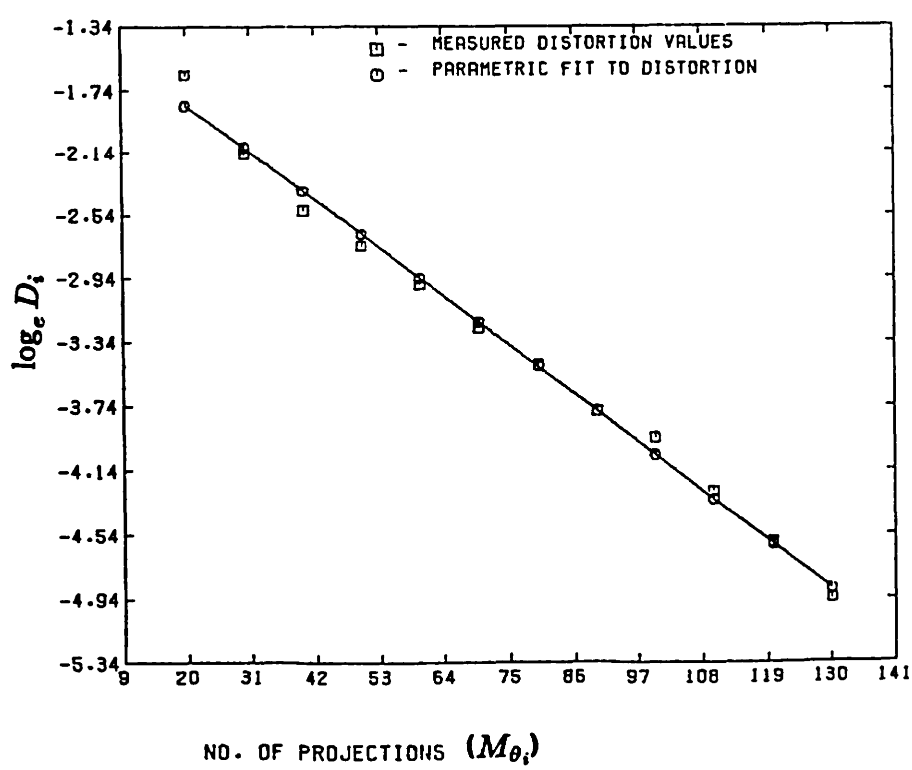

FIG. 5.30 FIT OF PARAMETRIC FORMULA TO MEASURED RECONSTRUCTION DISTORTION VALUES FOR $\rho_1 = \rho_2 = 0.9$, A = 128 x 128.

This formula may be verified, within a tolerance level, by a least squares fit of the equation

$$\log_e D_i = -G(\rho_1, \rho_2, A) M_{\theta_i} + K'(\rho_1, \rho_2, A) \tag{5.7a}$$

to the empirical results, where

$$K'(\rho_1, \rho_2, A) = \ln K(\rho_1, \rho_2, A) \tag{5.7b}$$

The results of the fit for the 64×64 and 128×128 images are found in table 5.4. Some associated plots of the fits as compared to the empirical data are shown for $\rho_1 = \rho_2 = 0.2$ for $A = 64 \times 64$ and $\rho_1 = \rho_2 = 0.9$ for $A = 128 \times 128$ in fig. 5.29 and fig. 5.30, respectively.

5.5.3 Statement of the Projection Allocation Problem

The projection allocation problem is one of specifying the number of projections (or Fourier plane slices) M_{θ_i} to be generated from an image $\mathbf{F}_i$, belonging to an ensemble $\mathbb{IE} = \{\mathbf{F}_1, \mathbf{F}_2, \ldots, \mathbf{F}_N\}$, in order to minimize an *average* reconstruction distortion D over the ensemble, where the mean squared error (MSE) of distortion is

$$D = \frac{1}{N} \sum_{i=1}^{N} \sigma_i^2 D_i \tag{5.8}$$

and σ_i^2 is the associated energy in $\mathbf{F}_i$ and D_i is as specified in (5.6). This minimization is subject to the constraint that only a finite *total* number of projections

$$M_\theta^{(N)} = \sum_{i=1}^{N} M_{\theta_i} \tag{5.9}$$

may be acquired from the image ensemble.

5.5.4 Potential Applications of Projection Allocation

It is clear that the problem of projection allocation is particularly relevant to mode 2 PDC systems where there is a direct access to the control of the projection generation which is an integral part of the mode 2 compressor, as discussed previously.

When the image ensemble $\mathbb{IE}$ is one of image sub–blocks rather than whole images, the solution to the projection allocation problem is directly applicable to PBBC. A time separation between image samples of the ensemble may enable a real–time application of projection allocation.

Where it is desirable to adapt the projection generation process in a tomographic environment, such as imaging different layers of the body (anatomical, astronomical, geological etc) of similar density (correlation) and area but with different levels of irradiation (energy) subject to equipment limitations (e.g. on the total number of detections of projected information), an efficient projection allocation procedure is of importance.

The parametric constants $K(\rho_1, \rho_2, A)$ and $G(\rho_1, \rho_2, A)$ of (5.6) suggest that the potential solution to the allocation problem will be only valid for a specific set of correlation and area parameters. This would obviously limit the versatility of the allocation algorithm as the correlation level specified by (ρ_1, ρ_2) may certainly differ from image to image within an ensemble of images even if they had the same area. This is true of either tomographic or image based systems. Although we have adhered to the use of the parametric constants in deriving the allocation formula in the following sub–section, we consider some relaxed forms of the constants that appear in the final algorithm when testing its performance in section 5.5.6.

5.5.5 Development of the Allocation Formula

Let $\Sigma = \{\sigma_1^2, \sigma_2^2 \ldots, \sigma_N^2\}$ be an image energy set corresponding to the ensemble $\mathbb{IE} = \{\mathbf{F}_1, \mathbf{F}_2, \ldots, \mathbf{F}_N\}$ of zero mean images $\mathbf{F}_i$ (i.e Σ would be a set of variances corresponding to non–zero mean images). Then from the problem statement in section 5.5.3, it is necessary that if the elements of Σ are ordered in the manner

$$\sigma_1^2 \geq \sigma_2^2 \cdots \geq \sigma_N^2 \tag{5.10a}$$

that we have the following respective orders on elements of a projection number set $M(\Theta) = \{M_{\theta_1}, M_{\theta_2}, \ldots, M_{\theta_N}\}$ and a corresponding reconstruction distortion set

$D(\Theta) = \{ D_1, D_2, \ldots, D_N \}$:

$$M_{\theta_1} \geq M_{\theta_2} \cdots \geq M_{\theta_N} \qquad (5.10b)$$

and

$$D_1 \leq D_2 \cdots \leq D_N \qquad (5.10c).$$

The respective orders of elements Σ and $M(\Theta)$ are principally related by the projection slice theorem, as the energy of an image can readily be measured from the Fourier transform which, in turn, implies that the more the number of Fourier slices (projections) available, the better represented is the image energy. The orders specified by (5.10a) and (5.10b) immediately follow from the empirical results of section 5.4, however, it must be noted that (5.10c) also depends very much on the stability of the reconstruction process.

Against the background of the aforementioned orders and the stated allocation problem, we wish to solve the following equation

$$\frac{\partial}{\partial M_{\theta_j}}\left(\frac{1}{N}\sum_{i=1}^{N}\sigma_i^2 K(\rho_1,\rho_2,A)\exp(-G(\rho_1,\rho_2,A)M_{\theta_i}) + \lambda\sum_{i=1}^{N} M_{\theta_i}\right) = 0 \qquad (5.11)$$

where λ is a Lagrange multiplier.

By carrying out the differentiation, it can be shown, after some simplification, that

$$\sigma_j^2 \exp(-G(\rho_1,\rho_2,A)M_{\theta_j}) = N\lambda(K(\rho_1,\rho_2,A)G(\rho_1,\rho_2,A))^{-1} \qquad (5.12)$$

The expression on the right hand side may be absorbed into a parametric constant $C(\rho_1,\rho_2,A)$; solving for M_{θ_j}, in terms of this constant, we obtain

$$M_{\theta_j} = \frac{1}{G(\rho_1,\rho_2,A)}\left[\ln\sigma_j^2 - \ln C(\rho_1,\rho_2,A)\right] \qquad (5.13).$$

On substituting equation (5.13) into the constraint of equation (5.9) and solving for $-\ln C(\rho_1,\rho_2,A)$, we realize

$$-\ln C(\rho_1,\rho_2,A) = \frac{1}{N}\left[M_\theta^{(N)}G(\rho_1,\rho_2,A) - \ln\prod_{i=1}^{N}\sigma_i^2\right] \qquad (5.14).$$

Using (5.14) in (5.13), we obtain a projection allocation formula, given as

$$M_{\theta_j} = \frac{M_\theta^{(N)}}{N} + \frac{1}{G(\rho_1,\rho_2,A)}\Big[\ln\sigma_j^2 - \frac{1}{N}\big(\ln\prod_{i=1}^{N}\sigma_i^2\big)\Big] \qquad (5.15).$$

5.5.6 Some Performance Tests of the Algorithm

Some tests of the algorithm are carried out to principally compare its performance with uniform allocation of projections which may well be the spontaneous approach to allocation over an ensemble of images. The effects of varying the parametric constant $G(\rho_1,\rho_2,A)$ for a given A, are also observed with the object of finding a representative value of the constant over different levels of image correlation (specified by (ρ_1,ρ_2)).

The steps for implementing the algorithm are first outlined below:

1. Given an energy set $\Sigma = \{\sigma_1^2,\sigma_2^2\ldots,\sigma_N^2\}$ associated with an image ensemble $\mathbf{IE} = \{\mathbf{F}_1,\mathbf{F}_2,\ldots,\mathbf{F}_N\}$ and a total number $M_\theta^{(N)}$ of projections that may be generated from the ensemble, use the allocation formula of (5.15) to compute respective elements of the set $M(\Theta) = \{M_{\theta_1},M_{\theta_2},\ldots,M_{\theta_N}\}$ *. Sum the M_{θ_j} to check if (5.9) is satisfied. If so stop, otherwise if the sum is less than $M_\theta^{(N)}$ go to 2 or if the sum is greater than $M_\theta^{(N)}$ go step 3.
2. Add 1 to the highest M_{θ_j} and check the sum. If (5.9) is satisfied stop, otherwise add 1 to the next highest M_{θ_j}; check the sum again. Continue this process over all elements of $M(\Theta)$ in descending order of values and repeat, if necessary, until (5.9) is satisfied, then stop.
3. Subtract 1 from the lowest non–zero M_{θ_j} and check the aggregate of the M_{θ_j} (5.9). If the constraint is satisfied stop, otherwise subtract 1 from the lowest but one M_{θ_j} and check the sum again. Continue the subtraction over all elements

* In practice, the M_{θ_j}, generated by the allocation formula, are non–integer values and have to be rounded off to the nearest integer. Moreover, the M_{θ_j} must be set according to $M_{\theta_j} = \max(M_{\theta_j},0)\forall j$, for obvious reasons.

of $M(\Theta)$ in ascending order of the M_{θ_j} and repeat, if required, until (5.9) is obeyed, then stop.

The images used in the test of the algorithm are generated as described in section 5.4.2.1. The size N of the image ensemble is 4 and the arbitrarily chosen energy set is $\Sigma = \{4.0, 12.25, 23.04, 7.29\}$ which corresponds to a *root mean square* (rms) value set $\Sigma^{1/2} = \{2.0, 3.5, 4.8, 2.7\}$. Due to numerical errors in the image generation there is some deviation in the rms values and the elements of $\Sigma^{1/2}$ measured over all the tests are such that $\Sigma^{1/2} = (1.97 \pm 0.03, 3.46 \pm 0.07, 4.58 \pm 0.20, 2.51 \pm 0.19)$.

Tables 5.5 and 5.6 are respective summaries of the test results for 64×64 and 128×128 images, respectively, at varied levels of smoothness or correlation. The first test, reported in table 5.5, is a direct application of the allocation formula with the parametric constant $G(\rho_1, \rho_2, A) = G(0.9, 0.9, A)$ exactly matched to the statistics of the images. All the images have homogeneous correlation $\rho_1 = \rho_2 = 0.9$ and area $A = 64 \times 64$. A reduction of 1dB of average reconstruction distortion D_a, as a result of systematic projection allocation, is achieved with respect to the distortion D_u associated with uniform allocation.

The sensitivity of the parametric fits over larger ranges of the number of projections is observed in the second test. In this case, the range of the fit is extended to include reconstruction performance up to 100 projections (the residue of the fit is about 2.6 compared to 0.36 for the 10–80 range of number of projections). The corresponding average MSE of reconstruction is still over 0.4dB below that associated with the uniform allocation procedure although it is about 0.7dB above the distortion D_a obtained from the better fit. Similar tests (3 and 4) are repeated for the lower correlation based parametric constant $G(0.2, 0.2, A)$ and the same trends are observed. Expectedly, the distortion levels increase relative to the results of tests 1 and 2 due to the extra sensitivity of reconstruction to images that exhibit rapid changes in contrast (i.e. low correlation images).

Test No.	$G(\rho_1,\rho_2,A)$	Projection allocation over four images; each with specified correlation (ρ_1,ρ_2) (1)	(2)	(3)	(4)	$(D_a)^*$ (dB)	$(D_u)^{**}$ (dB)
1.	$G(0.9,0.9,A)$ $= 0.60207$	37 (0.90,0.90)	56 (0.90,0.90)	65 (0.90,0.90)	42 (0.90,0.90)	−7.60	−6.41
2.	$G(0.9,0.9,A)$ $= 0.07150$	40 (0.90,0.90)	55 (0.90,0.90)	62 (0.90,0.90)	43 (0.90,0.90)	−6.89	"
3.	$G(0.2,0.2,A)$ $= 0.03621$	26 (0.20,0.20)	57 (0.20,0.20)	75 (0.20,0.20)	42 (0.20,0.20)	3.21	4.56
4.	$G(0.2,0.2,A)$ $= 0.04560$	31 (0.20,0.20)	55 (0.20,0.20)	70 (0.20,0.20)	44 (0.20,0.20)	3.44	"
5.	$\overline{G(\rho_1,\rho_2,A)}^{***}$ $= 0.04848$	33 (0.60,0.60)	57 (0.20,0.20)	66 (0.90,0.90)	44 (0.60,0.60)	0.12	0.63
6.	$G(0.9,0.9,A)$ $= 0.06027$	37 (0.60,0.60)	55 (0.20,0.20)	63 (0.90,0.90)	45 (0.60,0.60)	0.20	"
7.	$G(0.2,0.2,A)$ $= 0.03621$	28 (0.60,0.60)	59 (0.20,0.20)	71 (0.90,0.90)	42 (0.60,0.60)	0.34	"
8.	$\overline{G(\rho_1,\rho_2,A)}$	33 (0.15,0.25)	54 (0.95,0.85)	69 (0.80,0.35)	44 (0.45,0.75)	−0.51	0.11

* (Reconstruction distortion due to allocation algorithm)
** (Reconstruction distortion due to uniform allocation)
*** $\overline{G(\rho_1,\rho_2,A)} = \frac{1}{3}[G(0.2,0.2,A) + G(0.6,0.6,A) + G(0.9,0.9,A)]$

Table 5.5: Results of performance tests of the projection allocation algorithm and comparison with uniform allocation.
Further Specs. $M_\theta^{(N)} = 200$, $N = 4$, $A = 64^2$,
$\Sigma = \{1.97 \pm 0.03, 3.46 \pm 0.20, 4.58 \pm 0.20, 2.51 \pm 0.19\}$

The last four tests are designed to view the performance of the algorithm under more realistic conditions, where the correlation may vary between images. In the fifth test, the parameter $G(\rho_1, \rho_2, A)$ is a representative average of the low, medium and high correlation related values of the parametric constants. The derived value is close to $G(0.6, 0.6, A)$ (in table 5.4) which is appropriate for the choice of combination of the correlation values employed in test 5 (in which there are two medium correlated images). When the parametric constants are biased towards the low and high correlation levels (as in tests 6 and 7, respectively) the respective MSEs of reconstruction distortion are still below the corresponding results of uniform allocation. The last test shows the performance of the algorithm when the images each have different row and column one step correlations (i.e $\rho_1 \neq \rho_2$). For this case D_u is about 0.5dB above D_a.

It is noted that the respective projection allocations resulting from tests 1,2 and 6 differ, for the same $G(\rho_1, \rho_2, A)$, as a result of the deviation in rms values, mentioned earlier. This is also the case for tests 3,4 and 7 and tests 5 and 8, respectively. However, it is easily inferred from the tests that the allocation algorithm distributes the projections more evenly over images when $G(\rho_1, \rho_2, A)$ is based on a high correlation fit. In theory, an infinite value of $G(\rho_1, \rho_2, A)$ would cause a uniform allocation of projections. Therefore, uniform allocation may be considered to be is a sub–procedure of the general allocation formula.

Table 5.6 shows the performance of the algorithm for the assignment of 320 projections over four 128×128 images. The MSE of distortion (not measured in dB) produced by the reconstruction of each image is also included. In comparison to uniform allocation, the projection allocation distributes projections in such a way as to even out the image reconstruction distortion in each image. The equivalent decibel values of average distortion of D_a and D_u are 1.50dB and 2.56dB respectively.

In summary, it is worthwhile examining the statistics within an ensemble of images, as the algorithm does, before specifying the number of projections to be

Image No.	Rms Value of Image	Systematic Allocation	Uniform Allocation	D_a	D_u
1.	2.0	43	80	1.370	0.621
2.	3.5	91	80	1.453	1.902
3.	4.8	118	80	1.439	3.575
4.	2.7	68	80	1.394	1.131
Average Distortion				1.414	1.807

Table 5.6 : Performance tests and comparisons for $A = 128^2$.
Further specs.: $M_0^{(N)} = 320$, $N = 4$, $\rho_1 = \rho_2 = 0.6$ (for all images) and $G(\rho_1, \rho_2, A) = 0.04889$

generated from each image. While the algorithm is designed to minimize the reconstruction error, for a given parametric constant $G(\rho_1, \rho_2, A)$, over an ensemble of Gauss–Markov type images of the same correlation level (ρ_1, ρ_2) and for a specific A, it is observable from the performance tests that a representative average value of the constant may suffice for achieving low reconstruction distortion.

Although we have observed the performance of the algorithm for the Gaussian distributed images which are in effect maximum entropy images for specified second order statistics [57,pg. 109], it is not clear how it would operate on other types of images especially when the statistics are of a non–stationary nature as is typically the case. It is felt that the development of an algorithm for such image ensembles would largely depend on the stability of the reconstruction algorithm that would permit the orders of (5.10c) to be maintained.

Further studies of the dependence of the reconstruction error on image correlation and area are desirable for more image sizes. This may lead to the useful factorization of the parametric constant $G(\rho_1, \rho_2, A)$, in the manner

$$G(\rho_1, \rho_2, A) = G_1(\rho_1, \rho_2) G_2(A) \tag{5.16}$$,

which would certainly make the allocation procedure more flexible and amenable to varied applications.

5.6. A Lower Bound of Reconstruction Distortion

A lower bound of reconstruction from projected information of wide sense stationary (WSS) Gauss–Markov image fields (modelled on a causal minimum variance basis) with specified one step row and column correlation levels and image area, respectively, may readily be obtained by substituting (5.15) into (5.6) and the result in (5.8). The final result of the distortion bound is

$$D_L(\rho_1, \rho_2, A) = K(\rho_1, \rho_2, A) \exp\left(-G(\rho_1, \rho_2, A) \frac{M_\theta^{(N)}}{N}\right) \left(\prod_{k=1}^{N} \sigma_k^2\right)^{1/N} \tag{5.17}$$.

The graphical results of the experiments, in section 5.4, indicate that $K(\rho_1, \rho_2, A)$ controls the elevation of the reconstruction distortion, for given image areas. Therefore, a global bound $D_L(A)$ exists for a given area A such that

$$D_L(A) \leq D_L(\rho_1, \rho_2, A) \qquad (5.18).$$

In accordance with the experimental results, this bound may be approached, for a specified finite total number $M_\theta^{(N)}$ of projections, by taking the limit on $D_L(\rho_1, \rho_2, A)$ in the manner

$$D_L(A) = \lim_{\rho_1, \rho_2 \to 1.0} D_L(\rho_1, \rho_2, A) \qquad (5.19).$$

Of course $D_L(A)$ becomes independent of area when $\rho_1, \rho_2 = 1$, that is, when there is complete redundancy in the images. In practice, however, the reconstruction error is ultimately controlled by the total number of projections to be acquired for a given image ensemble.

5.7 Summary and Conclusions

Some useful procedures for the development of mode 2 PDC have been discussed. We have investigated the feasibility of projection based block coding (PBBC) of images in its non–adaptive and adaptive forms, respectively. PBBC performs satisfactorily in the range of 1.0–2.0 bits/pixel. Adaptive PBBC operates by varying the number of projections generated from each block in accordance with the measured activity in the block. For a given average bit rate of quantization, the adaptive PBBC produces a much reduced final bit rate than non–adaptive PBBC, at the expense of a relatively small increase in distortion.

Due to the slicing effect of the PBBC on the 2–D frequency plane of each block, it does not perform as well as its closest conventional counterpart, the 2–D Fourier transform block code. However, the principal advantage of PBBC is that it permits the 2–D Fourier approach to be implemented as a series of 1–D frequency code operations. A compromise is required between the number of such operations (equivalent to the number of projection generations) and the final bit rate.

In comparison to orthogonal transform image coding systems, mode 2 PDC is limited by the errors that accrue from image reconstruction from projected information. An extensive quantitative study has been conducted to examine the image reconstruction error, for separable Gauss–Markov image statistics, as a function of image correlation, image area and the number of projections. Image correlation, effectively a measure of smoothness of the image intensity contours, has a considerable influence on the reconstruction error. In general, much fewer projections are required for encoding and reconstructing highly correlated images, than is the case for images that exhibit rapid changes in intensity. Expectedly, the results indicate that fewer projections need be acquired from images of smaller areas than larger ones in order to satisfy a certain fidelity of reconstruction, at a given image correlation level.

As a useful and novel contribution for developing a mechanism for projection generation, subject to a fidelity criterion for reconstruction, a projection allocation algorithm has been derived. The algorithm systematically specifies the number of projections to be generated from an image in order to minimize the average reconstruction distortion over an ensemble of images, subject to a constraint on the overall number of projections. In several performance tests, the algorithm performed better than straightforward uniform allocation over an ensemble of Gauss–Markov images.

Associated lower bounds of the reconstruction distortion have also been derived for a specified total number of projections.

CHAPTER SIX

A RATE–DISTORTION THEORETIC ANALYSIS FOR PDC

6.1 Introduction

In the previous chapter, a major concern was to control the PDC system, by systematically choosing the projections in order to minimize the average distortion of reconstruction, over a number of pictures, for a given compression level. It is worthwhile investigating the effect of maximizing the compression (minimizing the information rate) of projected information, subject to the fidelity constraints of accumulated distortion that results from compression (encoding/quantization) and reconstruction.

This chapter concentrates on such an analysis for a generalized compressor in which the respective distortions produced by compression and inversion of the projection domain are both taken into account. The generalized PDC scheme is generally representative of mode 1 and 2 PDC. However, the analysis places more emphasis on mode 1 processing as the main approach (of the analysis) is to determine how to minimize the information rate of given projection domain data whilst acknowledging the intrinsic distortion subsequently produced by reconstruction.

Some fundamentals of rate–distortion theory are reviewed in section 6.2. The analysis commences with the modelling of the generalized compressor in section 6.3 with a clear mathematical statement of the main problem which is one of finding the minimum rate of storage or transmission of projected information for a given fidelity criterion. The fidelity constraint is a mean squared error one and is explicitly defined in section 6.4. Section 6.5 discusses the derivation of a rate distortion function which is effectively an upper bound for the minimum information rate for projection data with known second order statistics. The corresponding compression structure for achieving the function is also described. A modified rate–distortion function, based on the stochastic nature of a projection domain, obtained from a wide sense stationary (WSS) image field, is presented in section 6.6. This modified function leads to a simplified compression structure which corresponds to intra-projection compression as studied in chapter three. Furthermore, a variation of this modified bound which is suitable for tomographic applications where there is considerable uncertainty in generating projections, is described in section 6.7.

The rate–distortion function is empirically evaluated on a *rate–compression distortion* basis for the projected information of MAN, BOY and BOX images, respectively, and for equivalent first order Markov–type information, derived from the statistics of the projected functions. These theoretical results are compared with a practical intra–projection compression scheme in which the bit rate allocation is conditioned on the distortion, under three types of storage/transmission protocols. The respective performances of the bow–tie algorithm and 2–D transform coding of projection data are compared with a 2–D Markov based rate–distortion function. These evaluations and comparisons are found in sections 6.8 and 6.9 respectively.

Section 6.10 discusses a procedure for controlling the intrinsic inversion noise, based on classical mean square estimation. This procedure, in tandem with the minimal information rate PDC system, produces a joint optimization of the compression and reconstruction processes. The efficacy of this approach is tested for the case when the noise is assumed to be channel noise, in section 6.11.

6.2 Fundamentals of Rate–Distortion Theory

Fig 6.1 describes a basic data compression scheme applied to a space or time discrete stochastic vector sequence $\{\mathbf{f}\}$; the scheme subsequently generates a compressed sequence $\left\{\widehat{\mathbf{f}}\right\}$. If the *source* vectors $\{\mathbf{f}\}$ and *sink* $\left\{\widehat{\mathbf{f}}\right\}$ vectors belong to a J–dimensional vector space $\mathcal{V}^J$ then the average information rate (mutual information) $M_J(\mathbf{f},\widehat{\mathbf{f}})$ between the vectors, when the vector components are of continuous amplitude, is defined as [57,101]

$$M_J(\mathbf{f},\widehat{\mathbf{f}}) = \int\int_{\mathcal{V}^J} P(\mathbf{f})Q(\widehat{\mathbf{f}}/\mathbf{f}) \log \frac{Q(\widehat{\mathbf{f}}/\mathbf{f})}{Q(\widehat{\mathbf{f}})} \, d\mathbf{f} \, d\widehat{\mathbf{f}} \tag{6.1}$$

where $P(\mathbf{f})$ and $Q(\mathbf{f})$ are the apriori and aposteriori joint probability density functions (pdfs) of the input and output vector sequences, respectively and $Q(\widehat{\mathbf{f}}/\mathbf{f})$ is the conditional density function of the output sequence with the input sequence specified; this latter function characterizes the data compressor. The aposteriori joint pdf is

$$Q(\mathbf{f}) = \int_{\mathcal{V}^J} P(\mathbf{f}) Q(\widehat{\mathbf{f}}/\mathbf{f})\, d\mathbf{f} \qquad (6.2).$$

A J–block rate distortion function $R_J(D)$ may be defined for the source generator, where $R_J(D)$ is the normalized minimum information rate [57,101]. That is

$$R_J(D) = \frac{1}{J} \inf_{Q \in Q_D} M_J(\mathbf{f}, \widehat{\mathbf{f}}) \qquad (6.3)$$

where Q_D is a D–admissible set of conditional densities $Q(\widehat{\mathbf{f}}/\mathbf{f})$ such that all the densities satisfy

$$D \geq d(Q) = \int\int_{\mathcal{V}^J} \Theta(\mathbf{f}, \widehat{\mathbf{f}})\, d\mathbf{f}\, d\widehat{\mathbf{f}} \qquad (6.4).$$

The function $d(Q)$ represents the average distortion obtainable for a given conditional density $Q(\widehat{\mathbf{f}}/\mathbf{f})$ (i.e. a given compression scheme), subject to a fidelity criterion $\Theta(\mathbf{f}, \widehat{\mathbf{f}})$. The upper bound of $d(Q)$ is D.

The rate–distortion function $R(D)$ of the source is the limiting value of $R_J(D)$ and is defined as

$$R(D) = \lim_{J \to \infty} R_J(D) \qquad (6.5).$$

Generally, there is an increased transmission or storage requirement, for utilizing finite J–dimensional blocks (vectors) of data, which is

$$\Delta R = R_J(D) - R(D) \qquad (6.6)$$

and this effectively implies that $R(D)$ is achieved with no constraint on the complexity of the compressor [102].

The fidelity criterion $\Theta(\mathbf{f}, \widehat{\mathbf{f}})$ may take on varied forms. One of these is the squared error measure

$$\Theta(\mathbf{f}, \widehat{\mathbf{f}}) = \left|\left|\mathbf{f} - \widehat{\mathbf{f}}\right|\right|^2 \qquad (6.7a)$$

$$= (\mathbf{f} - \widehat{\mathbf{f}})^T (\mathbf{f} - \widehat{\mathbf{f}}) \qquad (6.7b).$$

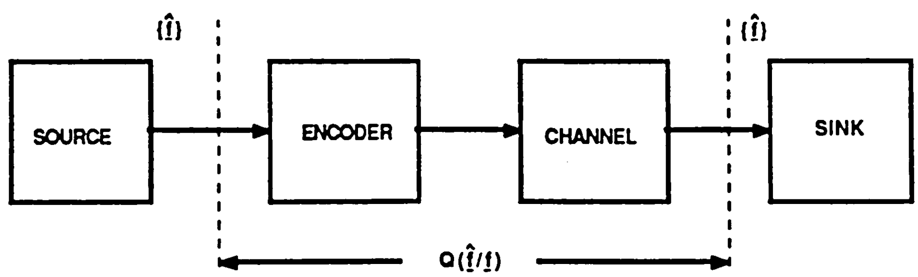

FIG. 6.1 BASIC DATA COMPRESSION SCHEME (SPECIFIED BY Q($\hat{f}$/f)).

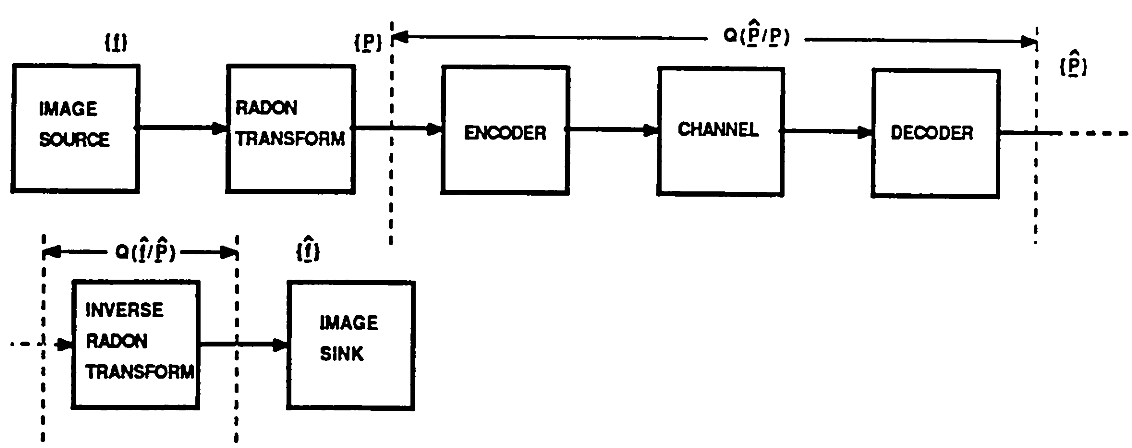

FIG. 6.2 GENERALIZED PDC SCHEME

This measure, in comparison to others, leads to mathematically tractable results of compression optimization (i.e constrained minimization of the information rate). Comprehensive discussions on other types of measures such as the absolute error, maximum distortion and frequency weighted distortion criteria appear in various places in the literature [101,103,104].

The major implication of the definition of $R_J(D)$ (hence $R(D)$) is that an optimal compression scheme is found by first narrowing down the range of compression schemes (i.e the conditional density functions $Q(\widehat{\mathbf{f}}/\mathbf{f})$ to the D–admissible set Q_D in which it is guaranteed that in selecting such a compression procedure, a specified average distortion D will not be exceeded. On locating this set, the $Q(\widehat{\mathbf{f}}/\mathbf{f})$ that satisfies (6.3) (i.e. minimizes the information rate between the compressor input $\mathbf{f}$ and output $\widehat{\mathbf{f}}$) is searched for.

When the discrete–time or space source information is considered to be statistically independent and identically distributed, the minimization is possible, analytically, for many types of distributions (e.g. Rayleigh, Gaussian, Laplacian etc) with respect to various fidelity constraints [57,103]. However, the optimization of sources with memory is traditionally implemented for information that is assumed to have Gaussian statistics [57,101]; the MSE is the predominant fidelity constraint in this case. Other combinations of distribution types and fidelity criteria do not yield analytical results, in general, and it is important to note that the rate–distortion function for a Gaussian source and MSE criterion serves as an upper bound on the possible performance for any source with specified second order statistics [103]. This bound is related to the entropy of a Gaussian source, which is also a maximum for all types of distributions [57,pg. 108]. Effectively, the solution for a Gaussian source does provide an idea of how well a non–Gaussian source can be compressed and is therefore most relevant.

6.3 The Generalized PDC Model

Fig. 6.2 is a schematic representation of a typical projection domain compressor. A typical realization $\mathbf{P}$ of the vector process $\{\mathbf{P}\}$ is generated by a DRT of an image vector $\mathbf{f}$. The decoder output $\widehat{\mathbf{P}}$ is the compressed version of $\mathbf{P}$ where the compression process is characterized by the conditional density function $Q(\widehat{\mathbf{P}}/\mathbf{P})$. A noisy inverse Radon transformation, specified by $Q(\widehat{\mathbf{f}}/\widehat{\mathbf{P}})$, generates a corresponding image $\widehat{\mathbf{f}}$ from $\widehat{\mathbf{P}}$. The representation of the inverse Radon transformation as a noisy one is designed to reflect the practical inexactedness of projection domain inversion.

Implicit in the model, is the assumption that the forward transformation to the projection domain is noiseless. From a theoretical point of view, the assumption is acceptable as the DRT may be generated under controlled synchronization through bandlimited interpolation, as discussed in chapter two for the AR–DRT and the SI–DRT in [23]. This would require that the elements, that constitute $\mathbf{f}$, to have been derived from band–limited sampling. Nevertheless, the reconstruction from projected information is the major problem rather than projection generation, practically and theoretically. Hence the emphasis in this model is on the distortion produced by reconstruction.

From the preceding section, it is known that a J–block rate– distortion function $R_J(D)$, associated with the compression of $\{\mathbf{P}\}$ or $\{\mathbf{f}\}$, may be obtained when $\mathbf{f}, \mathbf{P} \in \mathcal{V}^J$. If we let $J = N^2$, then the components of $\mathbf{f}$ and $\mathbf{P}$ may form the respective sequences $\{f(m,n); N_- \leq m, n \leq N_+\}$ and $\{P(m,n); N_- \leq m, n \leq N_+\}$, where $(N_+ - N_-) + 1 = N$. Ultimately, the function $R_J(D)$ is required and is obtained under the unconstrained complexity condition* of (6.5). Therefore, in order to achieve $R(D)$, $\mathbf{f}$ and $\mathbf{P}$ may each be considered to belong to an infinite dimensional vector space $\mathcal{V}^\infty$. The DRT is represented as a generalized linear matrix operation for the generation of $\mathbf{P}$ from $\mathbf{f}$ where $\mathbf{P}, \mathbf{f} \in \mathcal{V}^\infty, \mathbf{P} = \{P(k,l); -\infty \leq k, l \leq \infty\}, \mathbf{f} = \{f(m,n); -\infty \leq m, n \leq \infty\}$. This operation is written as

$$\mathbf{P} = \mathbf{R}_F \mathbf{f} \tag{6.8}$$

* Unconstrained complexity, here, refers to infinite delay processing.

where, in accordance with similar discrete formulations [27,39], $\mathbf{R}_F$ corresponds to a *projection matrix* *, $\mathbf{f}$ the image vector and $\mathbf{P}$ the measurement vector, respectively. The inexact inverse Radon transform of the compressed projection domain vector $\widehat{\mathbf{P}} \in \mathcal{V}^\infty$ is assumed to have the form

$$\widehat{\mathbf{f}} = R_I\widehat{\mathbf{P}} + \mathbf{r} \tag{6.9}$$

The transformation $\mathbf{R}_I\widehat{\mathbf{P}}$ is considered to be perturbed by an additive noise vector $\mathbf{r} \in \mathcal{V}^\infty$, $\mathbf{r} = \{r(m,n); -\infty \leq m,n \leq \infty\}$ that is regarded as independent of $\widehat{\mathbf{P}}$. The corresponding image vector $\widehat{\mathbf{f}}$ is the reconstruction from $\widehat{\mathbf{P}}$.

At this stage, it is pointed out that the sequences $\{f(m,n)\}$,$\{P(m,n)\}$, $\left\{\widehat{P}(m,n)\right\}$ and $\left\{\widehat{f}(m,n)\right\}$ are each considered to be wide sense stationary (WSS) and Gaussian. Therefore, the compression operation between the sequences $\{P(m,n)\}$ and $\left\{\widehat{P}(m,n)\right\}$ may also be expressed in linear form by employing a theorem, proved in [57,pg. 125], which permits any two *jointly stationary* ** Gaussian processes $\{\sigma(m,n)\}$, $\{\beta(m,n)\}$ to be written as:

$$\sigma(m,n) = \sum_{k=-\infty}^{\infty}\sum_{l=-\infty}^{\infty} \Gamma(k,l)\beta(m-k,n-l) + \gamma(m,n) \tag{6.10}$$

where $\Gamma(m,n)$ is a linear space invariant operator and $\gamma(m,n)$ is a realization of the WSS process $\{\gamma(m,n); -\infty \leq m,n \leq \infty\}$ that is independent of $\{\beta(m,n);$ $-\infty \leq m,n \leq \infty\}$. Therefore, the generalized PDC scheme is characterized by a third relation which qualifies the effects of the encoder–channel–decoder transformation $Q(\widehat{\mathbf{P}}/\mathbf{P})$; this is given as

$$\widehat{P}(m,n) = \sum_{k=-\infty}^{\infty}\sum_{l=-\infty}^{\infty} C(k,l)P(m-k,n-l) + t(m,n) \tag{6.11}$$

* This does not refer to a matrix of projections, as used in chapter three and four, but to the transformation that generates the projections

** Joint stationarity of the two Gaussian sequences exists when each sequence is stationary and their cross–correlation is stationary.

where $C(m,n)$ is an equivalent filtering operator that is symbolic of the compression process and $t(m,n)$ is a typical sample of the Gaussian sequence $\mathbf{t} = \{t(m,n)\}$ which is independent of $\mathbf{P}$.

6.3.1 Equivalent Compression Scheme

The model of fig. 6.2, described by equations (6.8–9) and 6.11, specify the two sources of distortion as compression distortion D_c and inversion or reconstruction distortion D_I. It is therefore appropriate to modify fig. 6.2 as shown in fig. 6.3. The (noiseless) DRT has been removed and an equivalent noisy transformation $Q(\widehat{\mathbf{P}}_v/\widehat{\mathbf{P}})$ has replaced the reconstruction transformation $Q(\mathbf{f}/\widehat{\mathbf{P}})$. The compressor specified by (6.11) remains intact. The output of $Q(\widehat{\mathbf{P}}_v/\widehat{\mathbf{P}})$ is $\widehat{\mathbf{P}}_\mathbf{v}$, a typical realization from the vector process $\left\{\widehat{\mathbf{P}}_v\right\}$. Specifically, we call $\widehat{\mathbf{P}}_v$ a *virtual* projection domain vector. This is for theoretical convenience as the model effectively limits the latent distortion due to reconstuction to the transformation that generates this virtual vector that, in turn, serves as an input into an 'ideal' inverse Radon transform; this ideal transformation does not produce distortion. This may be impracticable, however, the implication is that the inverse Radon transform has been decomposed into a two–staged processor as shown in fig. 6.4. From the viewpoint of the linear characterization of the generalized PDC model, it is mathematically valid.

Conceptually, the two–staged scheme may be viewed as one in which an inverse Radon transform frequency response $H_I(\omega_1,\omega_2)$* is windowed by another frequency response $H_N(\omega_1,\omega_2)$ that introduces distortion, such that the cascaded frequency response of the reconstructor is

$$\widehat{H}_I(\omega_1,\omega_2) = H_N(\omega_1,\omega_2)H_I(\omega_1,\omega_2) \qquad (6.12).$$

This generalized window structure is symbolic of the truncation effects of a typical inverse Radon transform in which the band–limiting of reconstruction filters may introduce blurring and artifacts in the reconstructed image domain. A means

* The frequency variables are associated with projection domain information

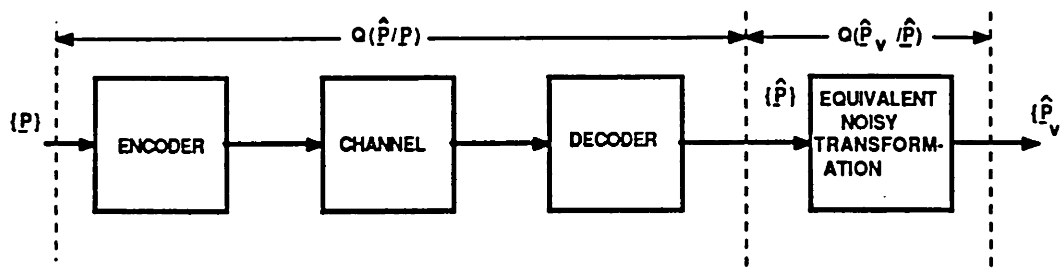

FIG. 6.3 EQUIVALENT COMPRESSION SCHEME.

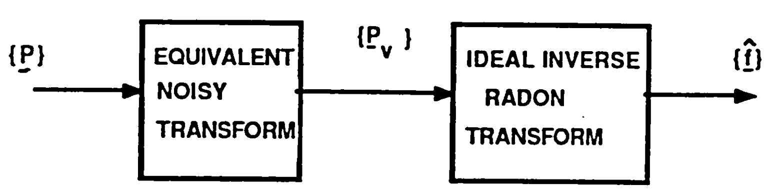

FIG. 6.4 CONCEPTUAL TWO STAGED PROCESSOR FOR RECONSTRUCTION.

of choosing $H_S(\omega_1, \omega_2)$, associated with a tenable form of the ideal Radon transform, in order to minimize the distortion of inexact reconstruction, is the subject of section 6.10.

All sequences involved in the equivalent model are projection domain ones (albeit $\left\{\widehat{\mathbf{P}}_v\right\}$ is a virtual one). Therefore, from the viewpoint of mode 2 PDC, the compression scheme between $\{\mathbf{f}\}$ and $\left\{\widehat{\mathbf{f}}\right\}$ is transformed (by the model) into an equivalent one between $\{\mathbf{P}\}$ and $\left\{\widehat{\mathbf{P}}_v\right\}$. For mode 1 processing, only $\{\mathbf{P}\}$ is available at the source point as $\{\mathbf{f}\}$ is not necessarily known.

By re–invoking the theorem that permitted the representation of equation (6.11), the transformation between the compressed vector $\widehat{\mathbf{P}}$ and the virtual vector $\widehat{\mathbf{P}}_v$ ($\widehat{\mathbf{P}}_v = \left\{\widehat{P}_v(m,n); -\infty \le m,n \le \infty\right\}$) may be expressed as

$$\widehat{P}_v(m,n) = \sum_{k=-\infty}^{\infty} \sum_{l=-\infty}^{\infty} S(k,l)\widehat{P}(m-k, n-l) + u(m,n) \tag{6.13}$$

where $\mathbf{u} = \{u(m,n); -\infty \le m,n \le \infty\}$ is an additive noise process, independent of $\left\{\widehat{P}(m,n)\right\}$ and $S(m,n)$ is the impulse response of what may be considered a blurring operation of the reconstruction process [38].

6.3.2 Problem Statement

Having characterized the generalized PDC model by the compression and reconstruction procedures by equations (6.11) and (6.13), respectively, the problem of representing the source information $\{P(m,n)\}$ by the minimum number of information units subject to a total distortion constraint is to be solved. We represent the total distortion D_T as the sum of the compression or encoding distortion D_C and reconstruction distortion D_I subject to the constraint

$$D_T = D_C + D_I \le D_{max} \tag{6.14}$$

where D_{max} is a specified maximum permissible distortion. This problem is a variational calculus one.

More precisely, for mutual information $M(P,\widehat{P})$ between $\{P(m,n)\}$ and $\left\{\widehat{P}(m,n)\right\}$, we wish to minimize the function

$$J(P,\widehat{P};\lambda) = M(P,\widehat{P}) + \lambda(D_C + D_I) \qquad (6.15),$$

where λ is a Lagrange multiplier, and obtain a rate–distortion function

$$R(D_T) = \inf_{Q(\widehat{P}/P)\in Q_{D_T}} M(P,\widehat{P}) \qquad (6.16)$$

and Q_{D_T} is the D_T–admissible set of conditional density functions or compressors that each produce a distortion level D_T that obeys the constraint of (6.14). We note that D_T is a MSE measure to be defined in the following section.

6.4 Fidelity Criterion

A typical realization of an error process $\mathbf{e} = \{e(m,n); -\infty \leq m,n \leq \infty\}$, between $\mathbf{P}$ and $\widehat{\mathbf{P}}_v$ (i.e between original and compressed and filtered projection information) may be specified as

$$\mathbf{e} = \mathbf{P} - \widehat{\mathbf{P}}_v \qquad (6.17)$$

For simplicity (and without loss of generality), the sequences $\{e(m,n)\}$, $\{P(m,n)\}$ and $\left\{\widehat{P}_v(m,n)\right\}$ are assumed to be zero mean processes. If there is no information about the transmitted or stored vector $\mathbf{P}$ at the retrieval or reception point, the information rate zeroes out and a maximum permissible distortion is realized. Moreover, if we assume the vector space $\mathcal{V}^\infty$ (on which the sequences are defined) is an infinite dimensional complex space, then the upper bound for the maximum distortion per sample may be deduced from

$$\mathrm{E}[\mathbf{e}\mathbf{e}^{*T}] = \mathrm{E}[\mathbf{P}\mathbf{P}^{*T}] \qquad (6.18)$$

where $\mathbf{e}^{*T}$ is the transposed complex conjugate of $\mathbf{e}$, $\mathbf{e} \in \mathcal{V}$, and $\mathrm{E}[\,.\,]$ is the usual ensemble average operator; the right hand side of (6.18) follows from (6.17) for the maximum distortion case. Equation (6.18) yields an infinite correlation matrix over the components of $\mathbf{e}$ (or $\mathbf{P}$). The limiting value of the average of the trace of this matrix is equal to the variance of the components within the infinitely dimensioned vectors, that is

$$\sigma_e^2 = \sigma_P^2 = \lim_{J\to\infty} \frac{1}{J}\mathrm{Tr}\{\mathrm{E}[\mathbf{e}\mathbf{e}^{*T}]\} \qquad (6.19).$$

The minimum MSE distortion D_{max} for no retrieval or reception (or maximum permissible distortion in storage or transmission) corresponds to the variance $\sigma_e^2 = \sigma_P^2$ of the source sequence which may be re–expressed in terms of the spectral density function (sdf) $\Phi_e(\omega_1, \omega_2)$ of the error function as

$$D_{max} = \sigma_P^2 = \left(\frac{1}{2\pi}\right)^2 \int_{-\pi}^{\pi}\int_{-\pi}^{\pi} \Phi_e(\omega_1,\omega_2)\, d\omega_1\, d\omega_2 \qquad (6.20).$$

The sdf is generally obtained by z-transformation of the corresponding lag dependent auto–correlation function $r_e(k,l)$, that is:

$$\Phi_e(\omega_1,\omega_2) = \sum_{k=-\infty}^{\infty}\sum_{l=-\infty}^{\infty} r_e(k,l)e^{-\jmath(k\omega_1+l\omega_2)} \qquad (6.21)$$

where it is apparent that $r_e(0,0) = \sigma_e^2$.

From the components of the respective stationary processes $\mathbf{e}$, $\mathbf{P}$ and $\widehat{\mathbf{P}}_v$ of (6.17), the error autocorrelation function may be expressed as

$$\begin{aligned} r_e(m,n;m',n') &= \mathrm{E}[e(m,n)e^*(m',n')] \\ &= \mathrm{E}[P(m,n)P^*(m',n')] - \mathrm{E}[P(m,n)\widehat{P}_v^*(m',n')] \\ &\quad - \mathrm{E}[\widehat{P}_v(m,n)P^*(m',n')] + \mathrm{E}[\widehat{P}_v(m,n)\widehat{P}_v^*(m',n') \qquad (6.22a). \end{aligned}$$

Stationarity permits

$$\begin{aligned} r_e(m-m',n-n') &= r_P(m-m',n-n') - r_{P\widehat{P}_v}(m-m',n-n') \\ &\quad - r_{P\widehat{P}_v}(-(m-m'),-(n-n')) + r_{\widehat{P}_v}(m-m',n-n') \end{aligned} \qquad (6.22b)$$

where the two central terms represent the stationary cross–correlation function between $\mathbf{P}$ and $\widehat{\mathbf{P}}_v$. Transforming (6.22b) as in equation (6.21) results in the expression

$$\Phi_e(\omega_1,\omega_2) = \Phi_P(\omega_1,\omega_2) - 2\mathrm{Re}[\Phi_{P\widehat{P}_v}(\omega_1,\omega_2)] + \Phi_{\widehat{P}_v}(\omega_1,\omega_2) \qquad (6.23).$$

Other spectral relations may be obtained from the linear operations of (6.11) and (6.13) respectively. From (6.11) we obtain the cross–correlation function

$$\begin{aligned} r_{P\widehat{P}_v}(m-m',n-n') &= \mathrm{E}[P(m,n)\widehat{P}_v^*(m',n')] \\ &= \mathrm{E}\big[P(m,n)\{\sum_{i=-\infty}^{\infty}\sum_{j=-\infty}^{\infty} S^*(m'-i,n'-j)\widehat{P}^*(i,j)+u^*(m',n')\}\big] \\ &= \sum_{k=-\infty}^{\infty}\sum_{l=-\infty}^{\infty} S^*(k,l)r_{P\widehat{P}}(m-m'+k,n-n'+l) \qquad (6.24). \end{aligned}$$

The corresponding sdf is

$$\Phi_{P\widehat{P}_v}(\omega_1,\omega_2) = S^*(\omega_1,\omega_2)\Phi_{P\widehat{P}}(\omega_1,\omega_2) \qquad (6.25).$$

Similarly, the following cross–correlation relationship is obtained from the compression operation of (6.11):

$$\begin{aligned} r_{P\widehat{P}}(m-m',n-n') &= \mathrm{E}[P(m,n)P^*(m',n')] \\ &= \sum_{k=-\infty}^{\infty}\sum_{l=-\infty}^{\infty} r_P(m-m'+k,n-n'+l)C^*(k,l)(6.26). \end{aligned}$$

Accordingly, the spectral form of (6.26) is

$$\Phi_{P\widehat{P}}(\omega_1,\omega_2) = C^*(\omega_1,\omega_2)\Phi_P(\omega_1,\omega_2) \qquad (6.27).$$

The auto–correlation of the compressed process is realized by using (6.11) in

$$r_{\widehat{P}}(m-m',n-n') = \mathrm{E}[\widehat{P}(m,n)\widehat{P}^*(m',n')]$$

which , on simplifying, yields

$$\begin{aligned} r_{\widehat{P}}(m-m',n-n') = \sum_{l=-\infty}^{\infty}\sum_{k=-\infty}^{\infty} & C(m-m'+k,n-n'+l)r_{P\widehat{P}}(k,l) \\ & + r_t(m-m',n-n') \qquad (6.28). \end{aligned}$$

Applying (6.28) in (6.21) gives

$$\Phi_{\widehat{P}}(\omega_1,\omega_2) = C(\omega_1,\omega_2)\Phi_{P\widehat{P}}(\omega_1,\omega_2) + \Phi_t(\omega_1,\omega_2) \qquad (6.29)$$

which may be re–written, on using (6.27), as

$$\Phi_{\widehat{P}}(\omega_1,\omega_2) = |C(\omega_1,\omega_2)|^2\,\Phi_P(\omega_1,\omega_2) + \Phi_t(\omega_1,\omega_2) \qquad (6.30).$$

Hence, the following spectral relations are obtained, on subjecting (6.13) to a similar analysis as carried out in (6.28–.30):

$$\Phi_{P\widehat{P}_v}(\omega_1,\omega_2) = S^*(\omega_1,\omega_2)\Phi_{\widehat{P}}(\omega_1,\omega_2) \qquad (6.31)$$

$$\Phi_{\widehat{P}_v}(\omega_1,\omega_2) = |S(\omega_1,\omega_2)|^2\,\Phi_{\widehat{P}}(\omega_1,\omega_2) + \Phi_u(\omega_1,\omega_2) \qquad (6.32)$$

and a complete expression is obtained for the error sdf by using (6.27) in (6.25) and substituting the result along with (6.32) in (6.23); the desired expression is

$$\begin{aligned}\Phi_e(\omega_1,\omega_2) = \Phi_P(\omega_1,\omega_2) - 2\mathrm{Re}\big\{S^*(\omega_1,\omega_2)C^*(\omega_1,\omega_2)\big\}\Phi_P(\omega_1,\omega_2)\\ + |S(\omega_1,\omega_2)|^2\,\Phi_{\widehat{P}}(\omega_1,\omega_2) + \Phi_u(\omega_1,\omega_2) \qquad (6.33).\end{aligned}$$

Therefore, the MSE fidelity criterion of the generalized PDC system is explicitly defined by using (6.33) in the integrand of equation (6.20).

6.5 An Upper Bound of the Rate Distortion Function for PDC

The fidelity criterion has been specified with respect to second order statistics (i.e the spectral density functions) of original $\{P(m,n)\}$ and encoded $\left\{\widehat{P}(m,n)\right\}$ data, subject to the total distortion constraint on D_T (cf. (6.14)). It is desirable that the corresponding information rate $M(P,\widehat{P})$ be represented in a similar manner. For this purpose, we use an approach of Pinsker [105,chapter 10] who defines the information rate between two joint stationary Gaussian processes in terms of the sdfs of the processes. This procedure along with its extension to our analysis is outlined in appendix III. On the basis of such considerations $M(P,\widehat{P})$ may be expressed as

$$M(P,\widehat{P}) = \frac{-1}{8\pi^2}\int_{-\pi}^{\pi}\int_{-\pi}^{\pi}\log\left[\frac{\Phi_P(\omega_1,\omega_2)\Phi_{\widehat{P}}(\omega_1,\omega_2) - \left|\Phi_{P\widehat{P}}(\omega_1,\omega_2)\right|^2}{\Phi_P(\omega_1,\omega_2)\Phi_{\widehat{P}}(\omega_1,\omega_2)}\right]d\omega_1 d\omega_2 \qquad (6.34).$$

With recourse to the problem statement (6.15), the ceiling of MSE distortion in (6.20), the spectral relation of (6.27), the fidelity criterion (6.33) and the information rate (6.34), it can be shown that the function to be minimized, for the derivation of the rate distortion function (6.16), is

$$J(\Phi_P(\omega_1,\omega_2),\Phi_{\widehat{P}}(\omega_1,\omega_2);\lambda') =$$

$$\frac{-1}{8\pi^2}\int_{-\pi}^{\pi}\int_{-\pi}^{\pi}\left\{\log\left[\frac{\Phi_P(\omega_1,\omega_2)\Phi_{\widehat{P}}(\omega_1,\omega_2)-|\,C(\omega_1,\omega_2)\,|^2\,\Phi_P(\omega_1,\omega_2)}{\Phi_{\widehat{P}}(\omega_1,\omega_2)}\right]\right.$$

$$-\lambda'\big(\,\Phi_P(\omega_1,\omega_2)-2\mathrm{Re}\big[S^*(\omega_1,\omega_2)C^*(\omega_1,\omega_2)\big]\,\Phi_P(\omega_1,\omega_2)+|S(\omega_1,\omega_2)|^2\,\Phi_{\widehat{P}}(\omega_1,\omega_2)$$

$$\left.+\Phi_u(\omega_1,\omega_2)\,\big)\right\}d\omega_1\,d\omega_2 \qquad (6.35)$$

where $\lambda' = 4\lambda$ (λ defined in (6.15)).

It is reasonable and practical to assume that the blurring operator $S(\omega_1,\omega_2)$ of the reconstruction process is given and therefore the unknowns of (6.35), for a given parameter λ' and input power $\Phi_P(\omega_1,\omega_2)$, are the phase reversed compression filter $C^*(\omega_1,\omega_2)$ and the power $\Phi_{\widehat{P}}(\omega_1,\omega_2)$ of the encoded sequence $\left\{\widehat{P}(m,n)\right\}$, respectively. A required non–negative definite constraint on $\Phi_{\widehat{P}}(\omega_1,\omega_2)$ is obtained from (6.27) and (6.30); the condition is

$$\Phi_t(\omega_1,\omega_2) = \Phi_{\widehat{P}}(\omega_1,\omega_2) - |\,C(\omega_1,\omega_2)\,|^2\,\Phi_P(\omega_1,\omega_2) \geq 0 \qquad (6.36)$$

and it ensures that the non–negative constraint also holds for the compression noise power $\Phi_t(\omega_1,\omega_2)$ and avoids the introduction of singularities in the information rate function of (6.34).

The stationary point of $J(\Phi_P(\omega_1,\omega_2),\Phi_{\widehat{P}}(\omega_1,\omega_2);\lambda')$ may be realized from partial first order derivatives (with respect to the various unknowns) of the integrand $\mathrm{IN}(\Phi_P(\omega_1,\omega_2),\Phi_{\widehat{P}}(\omega_1,\omega_2);\lambda')$ of (6.35); that is $C^*(\omega_1,\omega_2)$ and $\Phi_{\widehat{P}}(\omega_1,\omega_2)$ are evaluated when

$$\frac{\partial \mathrm{IN}(\,.\,;\lambda')}{\partial C^*(\omega_1,\omega_2)} = \frac{\partial \mathrm{IN}(\,.\,;\lambda')}{\partial \Phi_{\widehat{P}}(\omega_1,\omega_2)} = 0 \qquad (6.37).$$

It is more convenient to evaluate the complex differential by computing the separate derivatives of the real and imaginary parts of the complex independent variable. Therefore, for $C^*(\omega_1,\omega_2) = C_1(\omega_1,\omega_2) + jC_2(\omega_1,\omega_2)$, the following differential equations are to be solved:

$$\frac{\partial \mathrm{IN}(\cdot;\lambda')}{\partial C_1(\omega_1,\omega_2)} = \frac{\partial \mathrm{IN}(\cdot;\lambda')}{\partial C_2(\omega_1,\omega_2)} = \frac{\partial \mathrm{IN}(\cdot;\lambda')}{\partial \Phi_{\widehat{P}}(\omega_1,\omega_2)} = 0 \tag{6.38}$$

The respective derivatives are

$$-\frac{\partial \mathrm{IN}(\cdot;\lambda')}{\partial C_1(\omega_1,\omega_2)} = 2A(\omega_1,\omega_2)C_1(\omega_1,\omega_2)\Phi_P(\omega_1,\omega_2) - 2\lambda'\mathrm{Re}[S^*(\omega_1,\omega_2)]\Phi_P(\omega_1,\omega_2) = 0 \tag{6.39}$$

$$-\frac{\partial \mathrm{IN}(\cdot;\lambda')}{\partial C_2(\omega_1,\omega_2)} = 2A(\omega_1,\omega_2)C_2(\omega_1,\omega_2)\Phi_P(\omega_1,\omega_2) - 2\lambda'\mathrm{Im}[S^*(\omega_1,\omega_2)]\Phi_P(\omega_1,\omega_2) = 0 \tag{6.40}$$

$$-\frac{\partial \mathrm{IN}(\cdot;\lambda')}{\partial \Phi_{\widehat{P}}(\omega_1,\omega_2)} = A(\omega_1,\omega_2) - \left(\Phi_{\widehat{P}}(\omega_1,\omega_2)\right)^{-1} - \lambda' \,|\, S(\omega_1,\omega_2)|^2 = 0 \tag{6.41}$$

where

$$A(\omega_1,\omega_2) = \left(\Phi_{\widehat{P}}(\omega_1,\omega_2) - |\, C(\omega_1,\omega_2)\,|^2\, \Phi_P(\omega_1,\omega_2)\right)^{-1} \tag{6.42}$$

and Re $[\cdot]$ and Im $[\cdot]$ are real and imaginary operators respectively.

Solving for $C_1(\omega_1,\omega_2)$ and $C_2(\omega_1,\omega_2)$ in (6.39) and (6.40), respectively, and squaring and summing the results, yield

$$\begin{aligned} C_1^2(\omega_1,\omega_2) + C_2^2(\omega_1,\omega_2) &= |\, C(\omega_1,\omega_2)\,|^2 \\ &= \lambda'^2 \,|\, S(\omega_1,\omega_2)\,|^2 \left(A(\omega_1,\omega_2)\right)^{-2} \end{aligned} \tag{6.43}$$

From equations (6.41) and (6.42), it can be shown that

$$|C(\omega_1,\omega_2)|^2\, \Phi_P(\omega_1,\omega_2) = \lambda' \,|S(\omega_1,\omega_2)|^2\, \Phi_{\widehat{P}}(\omega_1,\omega_2) \left(1+\lambda' \,|S(\omega_1,\omega_2)|^2\, \Phi_{\widehat{P}}(\omega_1,\omega_2)\right)^{-1} \tag{6.44}$$

The application of (6.44) in (6.43) and considerable algebraic manipulation of the result give a closed form expression of $\Phi_{\widehat{P}}(\omega_1,\omega_2)$:

$$\Phi_{\widehat{P}}(\omega_1,\omega_2) = \frac{1}{|S(\omega_1,\omega_2)|^2}\left[\Phi_P(\omega_1,\omega_2) - (\lambda')^{-1}\right] \tag{6.45}$$

The non–negative definite constraint of (6.36) effectively requires that

$$\Phi_P(\omega_1, \omega_2) - (\lambda')^{-1} \geq 0 \tag{6.46}$$

and therefore, the general form of the compressed projection domain power is

$$\Phi_{\widehat{P}}(\omega_1, \omega_2) = \frac{\max(\Phi_P(\omega_1, \omega_2), \alpha)}{|S(\omega_1, \omega_2)|^2} \tag{6.47}$$

with $\alpha = \lambda'^{-1} = (4\lambda)^{-1}$.

To obtain the optimal compression filter $C^*(\omega_1, \omega_2)$ (where optimality refers to the minimization of (6.35), equation (6.45) is employed in (6.44); simplification of the result and the utilization of (6.46) provides the magnitude response $|C(\omega_1, \omega_2)|$ of $C^*(\omega_1, \omega_2)$:

$$|C(\omega_1, \omega_2)| = \frac{\max(\Phi_P(\omega_1, \omega_2), \alpha)}{|S(\omega_1, \omega_2)|^2 \, \Phi_P(\omega_1, \omega_2)} \tag{6.48}$$

where the parameter α has been defined previously. The phase information $\beta(\omega_1, \omega_2)$ of $C^*(\omega_1, \omega_2)$ is readily derived by dividing (6.40) by (6.39); this gives

$$\beta(\omega_1, \omega_2) = \angle C^*(\omega_1, \omega_2) = -\angle S^*(\omega_1, \omega_2) \tag{6.49a}$$

$$\beta(\omega_1, \omega_2) = -\angle C(\omega_1, \omega_2) = \angle S(\omega_1, \omega_2) \tag{6.49b}$$

Having obtained $C(\omega_1, \omega_2)$ and $\Phi_{\widehat{P}}(\omega_1, \omega_2)$, it is possible to find closed parametric forms (the parameter is α) of the rate distortion function and MSE distortion, respectively. The parametric rate distortion function $R(D_{T\alpha})$ is realized by joint application of (6.47) and (6.48) in (6.35); this result is

$$R(D_{T\alpha}) = \frac{1}{8\pi^2} \int_{-\pi}^{\pi} \int_{-\pi}^{\pi} \max\left(0, \log \frac{\Phi_P(\omega_1, \omega_2)}{\alpha}\right) d\omega_1 d\omega_2 \tag{6.50}$$

which corresponds to the familiar form of the rate– distortion function of a correlated Gaussian sequence, defined over a 2–D field [106]. The parametric MSE $D_{T\alpha}$

is arrived at by using equations (6.47–9) in the fidelity criterion of (6.33), under the integration of (6.20). The general form of $D_{T\alpha}$ is

$$D_{T\alpha} = \left(\frac{1}{2\pi}\right)^2 \int_{-\pi}^{\pi}\int_{-\pi}^{\pi} \min\left(\Phi_P(\omega_1,\omega_2),\alpha\right) d\omega_1\, d\omega_2 + \left(\frac{1}{2\pi}\right)^2 \int_{-\pi}^{\pi}\int_{-\pi}^{\pi} \Phi_u(\omega_1,\omega_2)\, d\omega_1\, d\omega_2 \tag{6.51}$$

where the first term is $D_{C\alpha}$, the parametric distortion due to the compression of the infinite–length projection vector $\mathbf{P} \in \mathcal{V}^\infty$ and the second term D_I is the latent MSE distortion due to reconstruction.

6.5.1 Discussion

The process $\mathbf{P} = \{P(m,n)\}$ has been assumed to be Gaussian and therefore the performance measure $R(D_{T\alpha})$ is an upper bound for the minimum information rate of transmission or storage of the infinite length vector $\mathbf{P}$ with a given power spectrum $\Phi_P(\omega_1,\omega_2)$. Nevertheless, it is emphasized that $R(D_{T\alpha})$ is obtained without constraints on complexity (i.e. infinite length sequence processing) and therefore is a lower bound to the performance obtainable for a practical finite length compression system with Gaussian statistics.

An optimal, though hypothetical, PDC structure for achieving (6.50) and (6.51) is depicted in fig. 6.5. The nerve centre of this processor is the compression filter $C^*(\omega_1,\omega_2)$ which gauges the power $\Phi_P(\omega_1,\omega_2)$ of projected information. Information about the blurring reconstruction stage filter $S^*(\omega_1,\omega_2)$ is fed to the compressor via a feedback path through the transmission or storage channel; this information effectively enables $C^*(\omega_1,\omega_2)$ to adjust itself according to (6.48) in a phase reversed manner, with respect to $S^*(\omega_1,\omega_2)$, of (6.49). The variable α may be considered to be a user specified 'tuning' parameter of the filter $C(\omega_1,\omega_2)$, which has the effect of determining the operational performance of the system.

The data independent reconstruction noise process $\{u(m,n)\}$ manifests itself as its additive average power in the MSE distortion D_T. Therefore, in principle, the compressor only needs to adjust its optimal rate $R(D_{T\alpha})$ of operation in such a

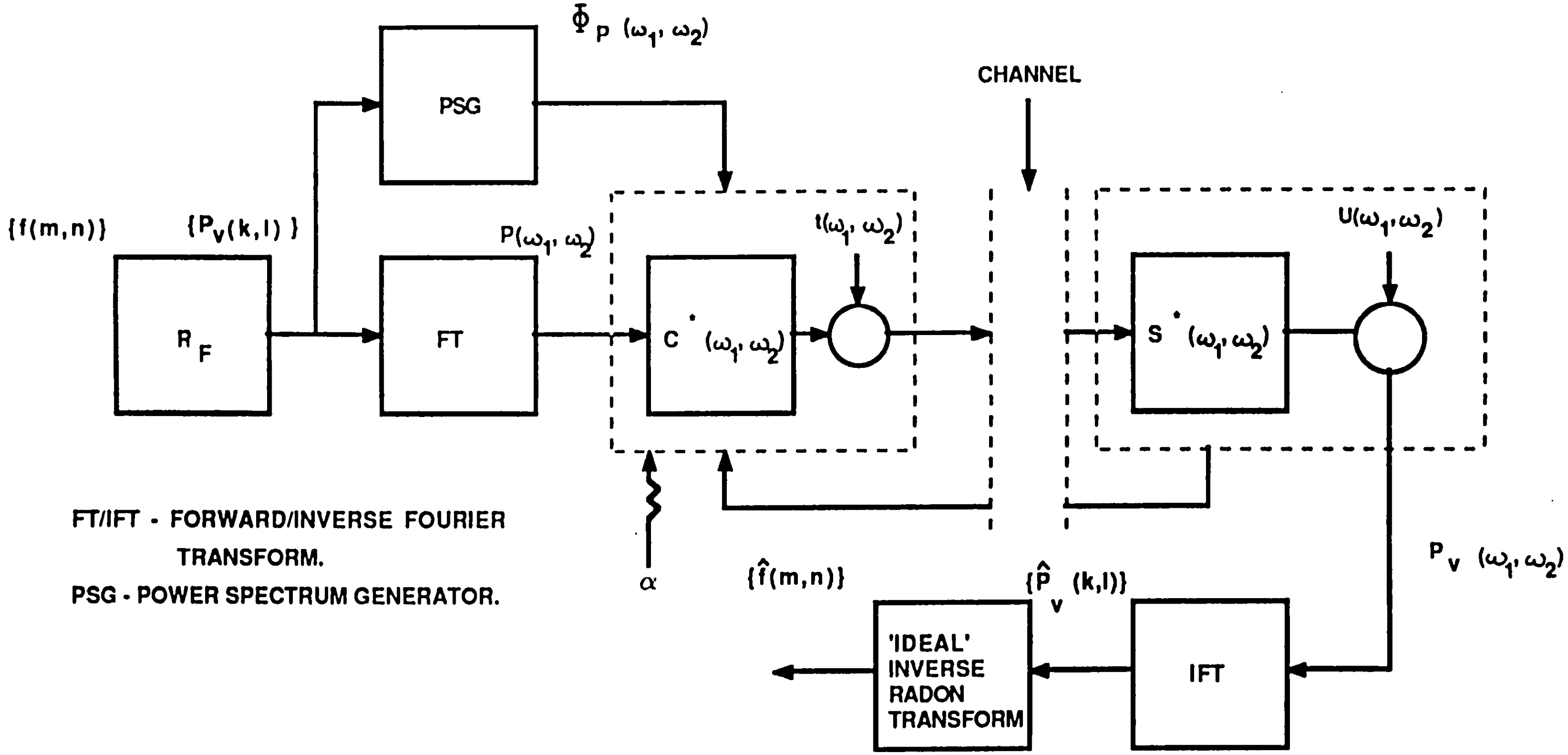

FIG. 6.5 HYPOTHETICAL OPTIMAL PROJECTION DOMAIN COMPRESSOR.

way as to balance $D_{C\alpha}$ against a given D_I in order for the total MSE of distortion to be within an acceptable limit. This in turn implies that D_I is specified by the tomographic application in which mode 1 PDC is being employed. Its presence, however, reflects the performance limitation of mode 2 PDC as compared to other procedures which on transforming image domain information prior to compression, only have to contend with $D_{C\alpha}$ in the MSE measure.

When the latent reconstruction noise is data dependent, as may be in physical tomographic based applications [6,50,99], the cross–correlated powers $\Phi_{Pu}(\omega_1, \omega_2)$ and $\Phi_{\widehat{P}u}(\omega_1, \omega_2)$ (respectively representative of the interactions of the noise and original projected information and the noise and compressed projected information) also contribute to the MSE. By not ignoring such correlation in the stochastic development of (6.3), it is found that the total (parametric) MSE is

$$D_{T\alpha} = \int_{-\pi}^{\pi}\int_{-\pi}^{\pi} (2\pi)^{-2} \{ \min(\Phi_P(\omega_1, \omega_2), \alpha) + 2\mathrm{Re}\big[\Phi_{Pu}(\omega_1, \omega_2) + S(\omega_1, \omega_2)\Phi_{\widehat{P}u}(\omega_1, \omega_2)\big] + \Phi_u(\omega_1, \omega_2) \} \, d\omega_1 \, d\omega_2 \tag{6.52}$$

by a similar algebraic analysis as used in this section. The corresponding rate–distortion function is identical to (6.50). The derivation of (6.52) assumes knowledge of the cross—correlation spectral densities $\Phi_{Pu}(\omega_1, \omega_2)$ and $\Phi_{\widehat{P}u}(\omega_1, \omega_2)$. This is reasonable as $\Phi_{Pu}(\omega_1, \omega_2)$ may be estimated before compression and $\Phi_{\widehat{P}u}(\omega_1, \omega_2)$ can be readily obtained from the relation

$$\Phi_{\widehat{P}u}(\omega_1, \omega_2) = C(\omega_1, \omega_2)\Phi_{Pu}(\omega_1, \omega_2) \tag{6.53}$$

when the compression and inversion latent noise processes $\{t(m, n)\}$ and $\{u(m, n)\}$ are independent. While the result of (6.52) has been presented for completeness, for simplicity, the solution of (6.51) is adhered to in subsequent considerations.

6.6 A Rate Distortion Bound for Intra–projection Compression

It may be argued that the results of section 6.5 are rather generalized and could well reflect the performance of any data compression scheme that produces inherent distortion at retrieval or reconstruction. Indeed, the generalized PDC scheme of fig. 6.2 may be considered to be a simpler configuration of the memory based communication link described in [57]. However, a structure more representative of PDC can be developed by incorporating the stochastic description of projected information into the rate distortion bound of (6.50–51).

The stochastic properties of projected information, acquired from wide sense stationary image fields, have been discussed in detail in chapter two. The prominent stochastic result for projections generated by the AR–Radon transform is that they are each stationary (in their radial parameters) and collectively uncorrelated. Therefore, if the spectral density function $\Phi_f(\omega_1', \omega_2')$ is associated with the image process $\{f(m,n)\}$ then the spectral density function $\Phi_P(\omega_1, \omega_2)$ of the corresponding projection process $\{P(m,n)\}$, according to the stochastic results, is such that

$$\Phi_P(\omega_1, \omega_2) = \Phi_P(\theta_i, \omega_2) = \frac{\Phi_f(\omega_1', \omega_2')}{|\,\omega_2\,|} \Big|_{\substack{\omega_1' = \omega_2 \cos\theta_i \\ \omega_2' = \omega_2 \sin\theta_i}} \tag{6.54}$$

where θ_i is the angle at which a projection is generated and ω_2 corresponds to the radial frequency.

We have earlier assumed that $\{f(m,n)\}$ has Gaussian statistics, therefore, according to the projection theorem for random fields, the corresponding projections are statistically independent and may, in turn, be compressed independently. Hence, associated angle–dependent filters $C^*(\theta_i, \omega_2)$ and $S^*(\theta_i, \omega_2)$ for the respective compression and reconstruction stages, may be defined in the context of equations (6.48–49) as

$$|\,C(\theta_i, \omega_2)\,| = \frac{\max[\,\Phi_P(\theta_i, \omega_2), \alpha\,]}{|\,S(\theta_i, \omega_2)\,|\;\Phi_P(\theta_i, \omega_2)} \tag{6.55}$$

and

$$\angle\, C^*(\theta_i, \omega_2) = -\angle\, S^*(\theta_i, \omega_2) \qquad (6.56).$$

The compression and reconstruction noise processes may also be characterized by angle–dependent sdfs $\Phi_t(\theta_i, \omega_2)$ and $\Phi_u(\theta_i, \omega_2)$.

In the light of these definitions and the results of (6.50–51), a rate–distortion bound and associated MSE of distortion corresponding to intra–projection compression may be respectively expressed as

$$R(D_{T\alpha}) = \frac{1}{M_\theta} \sum_{i=0}^{M_\theta - 1} \frac{1}{4\pi} \int_{-\pi}^{\pi} \max\big(0, \log \frac{\Phi_P(\theta_i, \omega_2)}{\alpha}\big)\, d\omega_2 \tag{6.57}$$

and

$$D_{T\alpha} = \frac{1}{M_\theta} \sum_{i=0}^{M_\theta - 1} \frac{1}{2\pi} \int_{-\pi}^{\pi} \big[\min\big(\Phi_P(\theta_i, \omega_2), \alpha\big) + \Phi_u(\theta_i, \omega_2)\big]\, d\omega_2 \tag{6.58}$$

where M_θ is the number of generated projections. These results reflect the independent processing of projections and state that the rate–distortion function and MSE of compression of projected information, generated from a WSS image field, are the respective averages of the rate distortion functions and MSEs associated with the compression of *each* projection.

Essentially, the structure for realizing the bound in (6.58) would correspond to the optimal intra–projection compressor for WSS images. Such a processor is shown in fig. 6.6 which depicts the fact that the power spectrum required by the angle–dependent compressor $C(\theta_i, \omega_2)$ may be obtained from the power spectrum of the image information; this is in accordance with the projection theorem for random fields. The buffering enables the storage of projections for future or from previous operations when their combined usage is required, however, the unconstrained complexity condition of deriving the compression bounds imply that there is no constraint on the buffer size. A practical approach is to eliminate the buffers in favour of parallel processing.

The possibility of using a specific α_i rather than a global α for tuning each angle–dependent compressor $C(\theta_i, \omega_2)$ is implicit in the compression scheme. This would clearly enable the fidelity of compression to be varied over the projections within a projection domain.

It is interesting to note that for projections generated by the slope–intercept Radon transform, the rate–distortion function would have the same form as equation

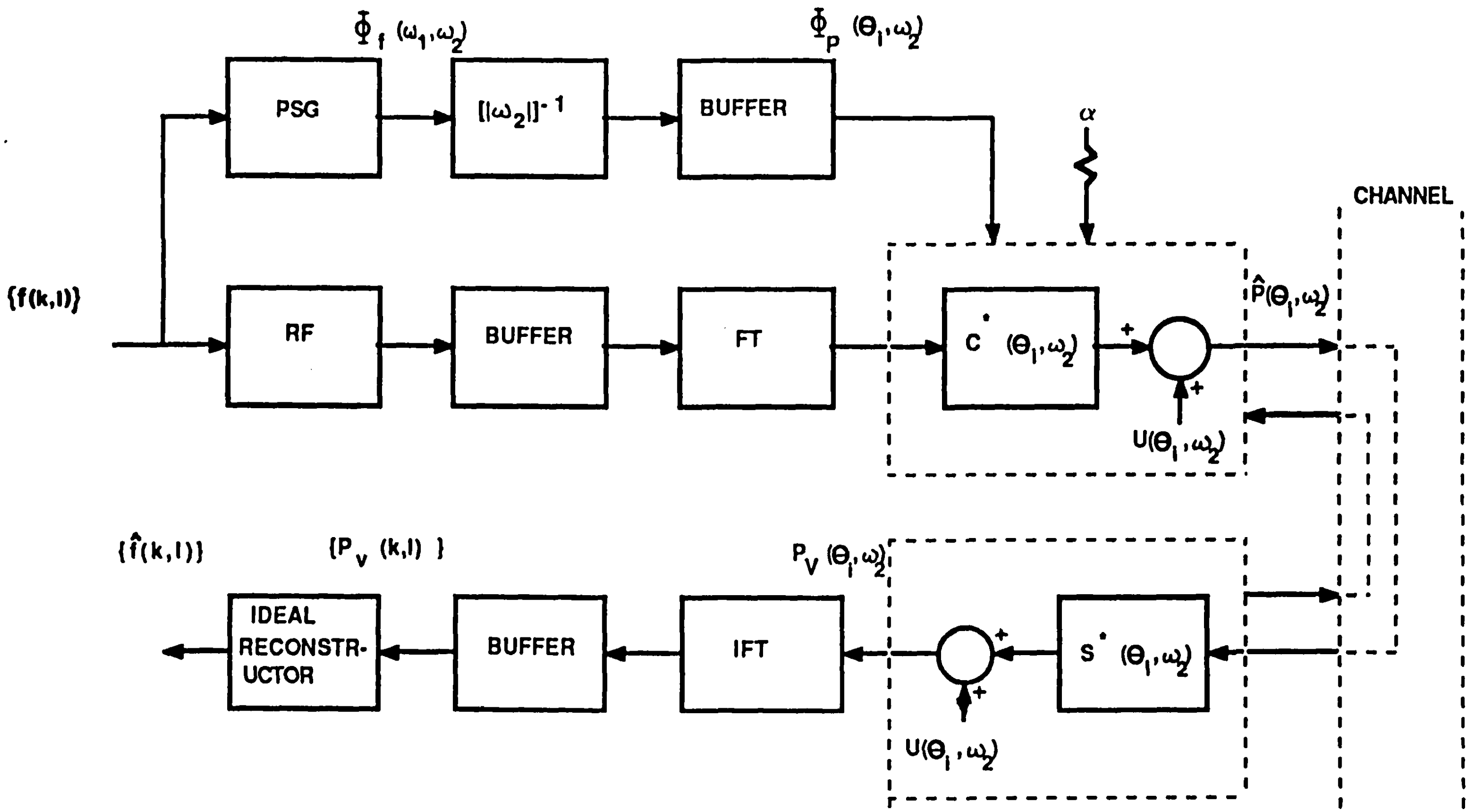

FIG. 6.6 HYPOTHETICAL OPTIMAL INTRA-PROJECTION COMPRESSOR.

(6.57) except that the angular parameter would be replaced by a discrete slope parameter and the frequency variable would correspond to intercept frequency.

In the next section, we comment on an intra–projection compression bound that is representative of a tomographic environment where there is considerable uncertainty in the projection generation process.

6.7 A Representative Compression Bound for Uncertain Projection Generation

An alternative interpretation of (6.57) and (6.58) is that the projection domain compressor partitions the source sample set $S_e\{\mathbf{P}\}$ of projected information into a number of disjoint subsets $S_e\{\mathbf{P}_0\}, S_e\{\mathbf{P}_1\}, \ldots, S_e\left\{\mathbf{P}_{M_\theta - 1}\right\}$ such that

$$S_e\{\mathbf{P}\} = \bigcup_{i=0}^{M_\theta - 1} S_e\{\mathbf{P}_i\} \tag{6.59}$$

and

$$\emptyset = \bigcap_{i=0}^{M_\theta - 1} S_e\{\mathbf{P}_i\} \tag{6.60}$$

where $\mathbf{P}_i$ is a projection generated at an angle θ_i and $\emptyset$ is the null set.

In the case where the subsets $S_e\{\mathbf{P}_i\}$ are not equiprobable and each are characterized by marginal probabilities $Z(S_e\{\mathbf{P}_i\})$ and where it is also necessary to separately identify each subset (assuming the projections are not being stored or transmitted in a sequential manner or have not been generated at equi–spaced angles), the representative intra–projection rate–distortion bound may be written as

$$R(D_{T\alpha}) = \sum_{i=0}^{M_\theta - 1} Z(S_e\{\mathbf{P}_i\}) R^i(D^i_{T\alpha}) - \sum_{i=0}^{M_\theta - 1} Z(S_e\{\mathbf{P}_i\}) \log Z(S_e\{\mathbf{P}_i\}) \tag{6.61}$$

and the associated parametric distortion is

$$D_{T\alpha} = \sum_{i=0}^{M_\theta - 1} Z(S_e\{\mathbf{P}_i\})\, D^i_{T\alpha} \tag{6.62}$$

where $R^i(D^i_{T\alpha})$ and $D^i_{T\alpha}$ are respectively identical to the summands of (6.57) and (6.58). The first term of (6.61) is the probability weighted rate–distortion function and the second is an entropy term that corresponds to the book keeping information, required for identifying each source subset $S_e\{\mathbf{P}_i\}$ (i.e. each projection).

The inclusion of the subset marginal probability weights in the bound of (6.61) implicitly takes into account the uncertainty problems encountered in projection generation in tomographic applications. It has been mentioned in chapter two, that internal structure of 3–D objects may prevent projection generation in some directions or within a sub–range of directions. The object of emission computed tomography (when the source of radiation is embedded in the body) is to determine the location and intensity of sources of emitted photons in the 3–D body. Due to attenuation within the medium and associated scatter of photon emission, there is considerable uncertainty in the detection (projection) process [107].

The book keeping data may not be necessary if convolution backprojection is to be employed as the reconstruction procedure, as the projections can be backprojected independently.

This approach of weighting the partitions of source information for the derivation of rate–distortion bounds is reported in [108], however, in that instance an iterative method had to be developed for optimal partitioning, based on the means and covariances of each partition. In our case, the partitions of the source space, naturally evolve as a result of the stochastic theorem for random fields which permits the projected information to be *directly* broken down into its component projections before compression.

For simplicity and because of our control of projection generation, we adhere to the rate–distortion results expressed in the previous section. These results are evaluated for projected information of typical imagery and compared with the performance of sub–optimal compression in the following section.

6.8 Evaluation of Bounds

6.8.1 Introduction

As mentioned in the introduction of the chapter, the emphasis of the rate–distortion treatment is on the structure of a mode 1 PDC system in which the distortion that results at the reconstruction stage is not under the direct control of the compressor (i.e. in terms of the choice of the number of projections to be generated, the radial and angular sampling etc). Therefore, in evaluating the bounds, we are more concerned with the bit rate of compression as a function of the compression distortion $D_{C\alpha}$, that is, the distortion produced before reconstruction. In section 6.10, we consider the control of distortion at the reconstruction stage when noise is introduced in the channel link of the compressor and reconstructor.

6.8.2 Comparisons of Intra–projection Compression Bounds based on Equivalent Markov and Sample Statistics

The equivalent Markov intra–projection or radial second order statistics and the true radial statistics have been compared in chapter two. Here, we estimate, for both sets of statistics, the power spectra $\Phi_P(\theta_i, \omega_2)$ over $M_\theta = 128$ projections by Fourier transformation of a smoothed version of the corresponding radial auto–correlation function of each available projection; the smoothing is carried out by applying a Hamming window on the auto–correlation before Fourier transformation. The integrals of (6.57) (at log to base 2) and of $D_{C\alpha}$ in (6.58) are computed from the power spectra by using an extrapolation to the limit procedure (otherwise known as Romberg–T integration) [109]. In general, the fidelity parameter α is varied within the interval

$$0 \leq \alpha \leq \inf_{\forall i} \{\text{ess sup}\, \Phi_P(\theta_i, \omega_2)\} \tag{6.63}$$

where 'ess sup' refers to the essential supremum of the function.

Comparisons of the theoretical rate–compression distortion functions (equation 6.57) are shown in figs. 6.7–6.9 for projection domain information of the MAN, BOY and BOX images, respectively (the MSE of compression distortion $D_{C\alpha}$ has been transformed to a decibel measure for convenience). Associated rate distortion curves of equivalent 2–D Markov statistics of the projected information have also been included for comparison. These 2–D processing based characteristics are not

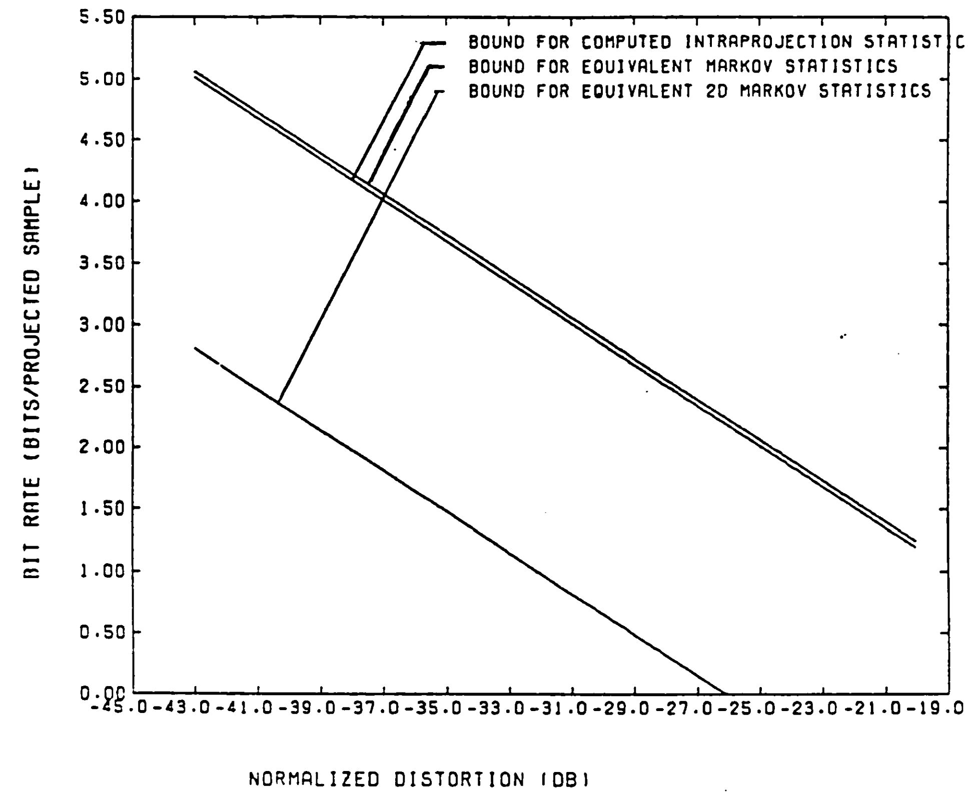

FIG. 6.7 THEORETICAL RATE - DISTORTION BOUNDS FOR PROJECTED 'MAN'.

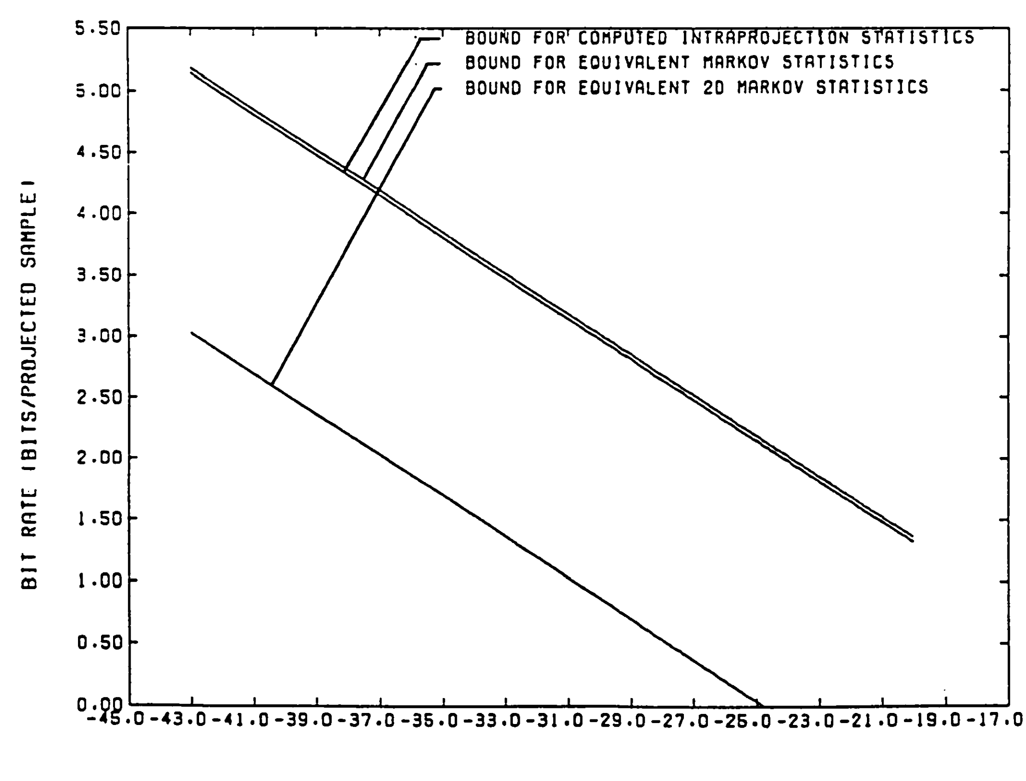

FIG. 6.8 THEORETICAL RATE - DISTORTION BOUNDS FOR PROJECTED 'BOY'.

computed using the 2–D power spectral density as suggested by equations (6.50–51) but by the well known formula [58, pg 192]

$$R(D_{C\alpha}) = \frac{1}{2}\log_2 \frac{(1-\rho_t^2)(1-\rho_\theta^2)}{D_{C\alpha}} \tag{6.64}$$

where ρ_t and ρ_θ are the respective intra–projection and inter–projection one–step correlation coefficients obtained from projection data. The results of figs. 6.7–6.9 have been produced by varying α over the range of $0.00005 \leq \alpha \leq 0.01$ for up to 151 points. This choice of interval ensures that $\alpha \approx D_{C\alpha}$ for most of the interval; some results that corroborate this condition are presented in table 6.1 for projection data of the MAN image. On the basis of these results, the plots of figs. 6.7–9 are actually characteristics of the information rate versus the fidelity parameter α.

It is clear from all the plots that the 1–D radial Markov based statistics are acceptable approximations to the corresponding true statistics as far as the determination of the minimum rates of compression are concerned. The differences are of the order of 0.04–0.05 bits/ps for the three types of projection data. The slightly higher value of the Markov based bound may be explained by the fact that there is some negative correlation in the actual (intra–projection) data, as observed in chapter two, and therefore the associated power spectra will always tend to be below that associated with the fully positively correlated equivalent Markov model. The advantages of 2–D compression (angle and radius based) are evident as the associated rate–distortion curves are, on average, about 2.0 bits/ps below the intra–projection based curves. Therefore, when there exists inter–projection correlation (which is the case in practice as infinitesimal integration lines cannot be realized although this possibility is implicitly assumed in the development of (6.57–8)) it is worthwhile exploiting in a compression procedure.

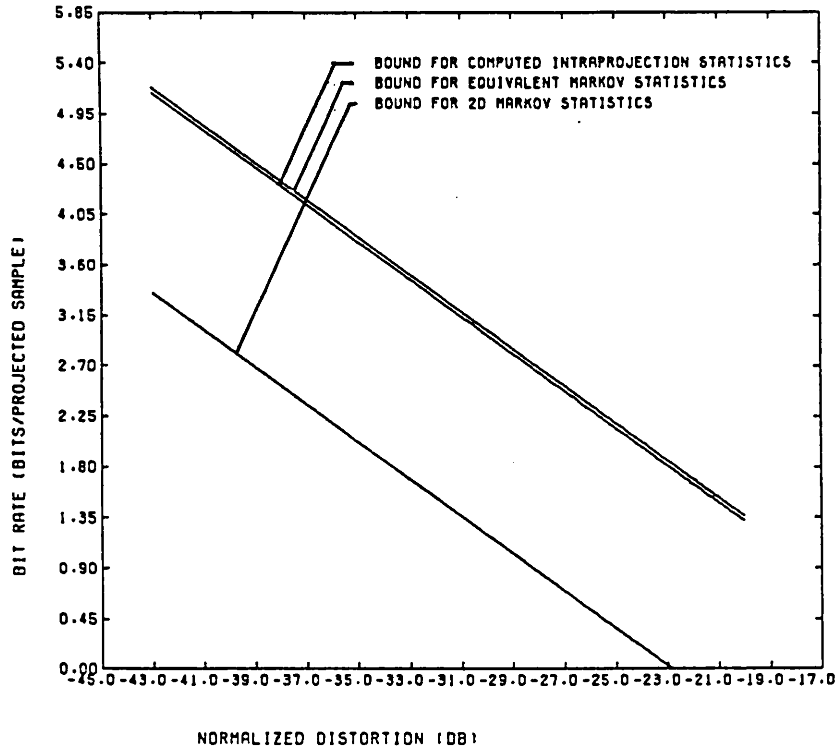

FIG. 6.9 THEORETICAL RATE - DISTORTION BOUNDS FOR PROJECTED 'BOX'.

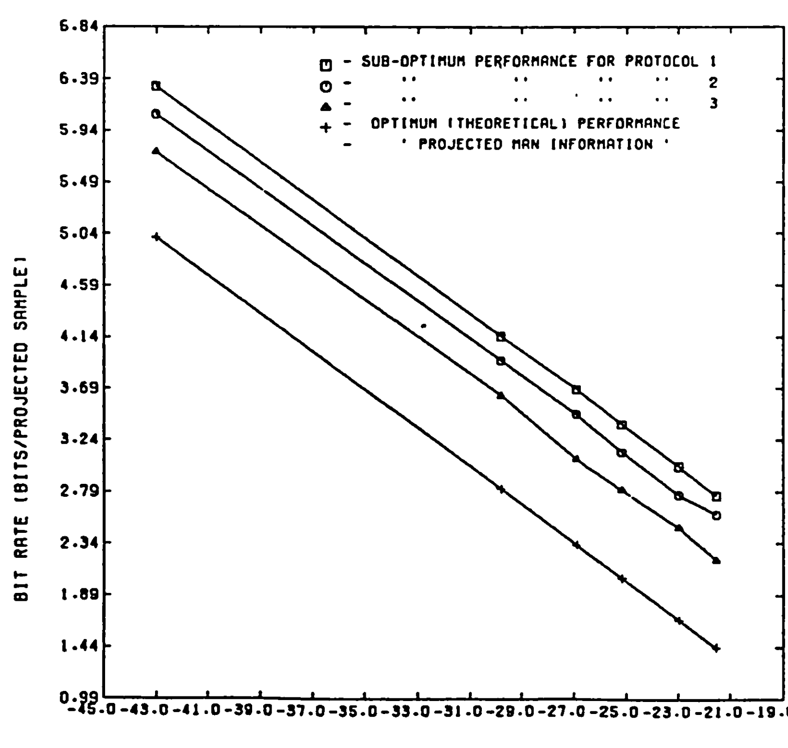

FIG. 6.10 PERFORMANCE COMPARISON OF SUB-OPTIMUM INTRA-PROJECTION COMPRESSION WITH OPTIMUM INTRA-PROJECTION COMPRESSION (MAN).

6.9 Comparison of Theoretical Bounds with the Performance of Sub–optimal Compressors

6.9.1 Sub-optimal Intra–projection Compression

The practical need for constraining the complexity of compression implies that the rate–distortion bound of (6.57) cannot be achieved in practice. A finite dimensionality constraint must be placed on the projection process $\mathbf{P} = \{P(m,n)\}$, $\mathbf{P} \in \mathcal{V}^J$, J being a finite integer. Another complexity constraint may arise from the practical processing of information with memory. It is well known [57] that if a 1–D Gaussian sequence of data $\mathbf{X} = \{x_k; 1 \leq k \leq J\}$ has a finite order memory, then the J–block rate–distortion function $R_J(D)$ of $\mathbf{X}$ may be achieved by first decorrelating $\mathbf{X}$ through a Karhunen Loéve transformation (KLT) that would yield a memoryless sequence $\mathbf{Y} = \{y_k; 1 \leq k \leq J\}$. Then a so called Shannon quantizer [1], operating at a rate

$$R_k = \begin{cases} 0.5 \log_2 \frac{\sigma_k^2}{D} & \sigma_k^2 \geq D \\ 0 & \sigma_k^2 < D \end{cases} \tag{6.65},$$

is used to encode each member y_k of the sequence where σ_k^2 is the variance of y_k and D is the average distortion constraint. The average value of R_k is equivalent to $R_J(D)$ i.e

$$R_J(D) = \frac{1}{J} \sum_{k=1}^{J} R_k \tag{6.66}$$

The KLT also minimizes the distortion in the reconstructed sequence [1,110] for a given compression level. However, its complexity of implementation necessitates the use of sub–optimal transformations that do not necessarily yield a statistically independent sequence $\mathbf{Y}$ and therefore the rate of (6.65) is rather pessimistic (as a result of transformed sample interdependence) and the associated encoder operates at a higher rate than required [57,pg 115].

The performance of a sub–optimal intra–projection compressor, relative to the bounds computed for the actual projection statistics, is assessed by employing the

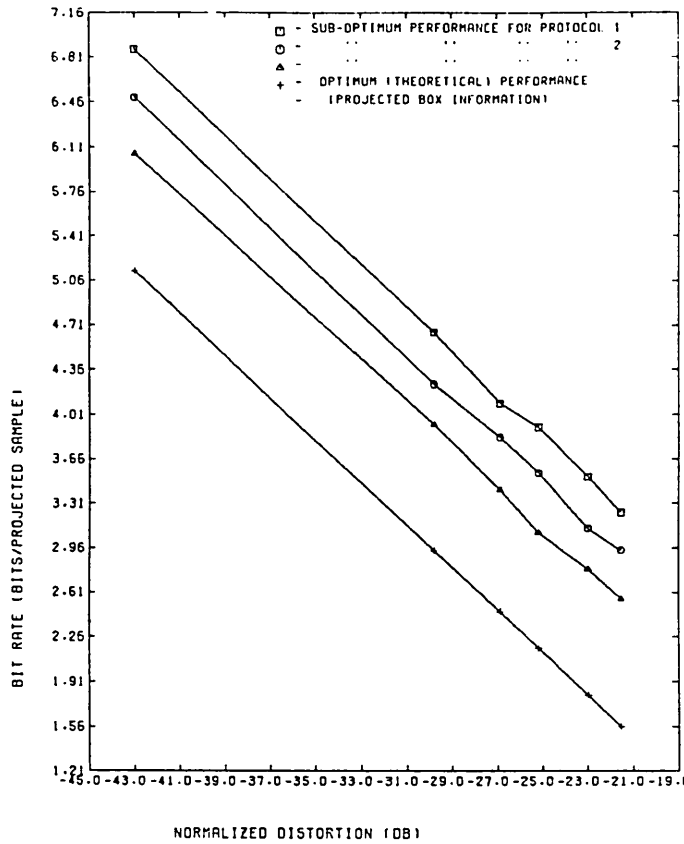

FIG. 6.11 PERFORMANCE COMPARISON OF SUB-OPTIMUM INTRA-PROJECTION COMPRESSION WITH OPTIMUM INTRA-PROJECTION COMPRESSION (BOY).

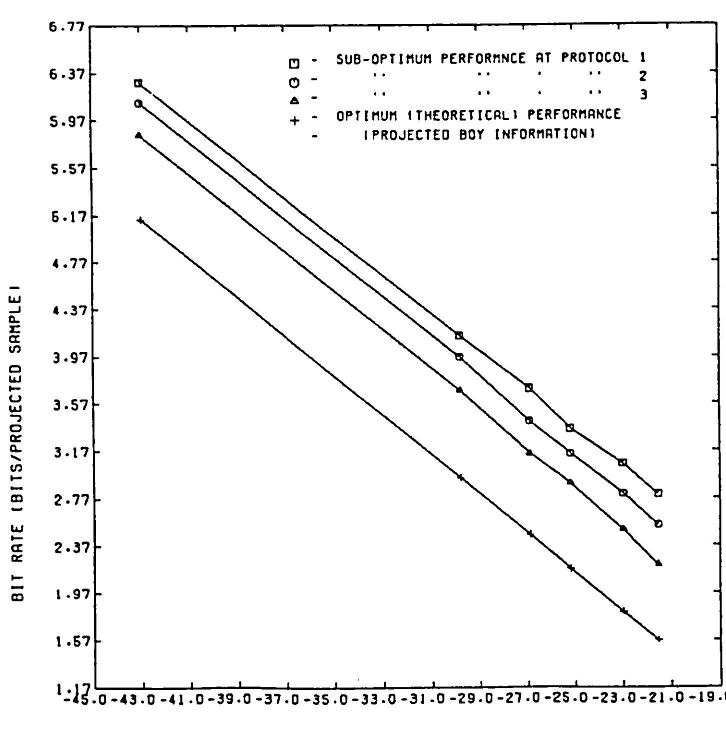

FIG. 6.12 PERFORMANCE COMPARISON OF SUB-OPTIMUM INTRA-PROJECTION COMPRESSION WITH OPTIMUM INTRA-PROJECTION COMPRESSION (BOX).

Cosine transform as the decorrelating transform of projections (in the manner discussed in chapter three), followed by the application of the Shannon quantizer for bit rate allocation in the J–block rate distortion function of (6.66). However, three different protocols for sub–optimal compression are employed by setting different levels of distortion D in (6.66), for a given normalized distortion α. These protocols, identified as PR1, PR2 and PR3 respectively, are specified by the following constraints:

$$\text{PR1} \qquad D = \alpha \min_{\forall i} \{\mathrm{Var}(\mathbf{P}_i)\} \tag{6.67}$$

$$\text{PR2} \qquad D = \alpha \overline{\mathrm{Var}(\mathbf{P})} \tag{6.68}$$

$$\text{PR3} \qquad D = \alpha \max_{\forall i} \{\mathrm{Var}(\mathbf{P}_i)\} \tag{6.69}$$

with α generally confined to the interval of (6.63) for angle–dependent power spectra $\Phi_P(\theta_i, \omega_2)$ associated with projections $\mathbf{P}_i$. The variable $\mathrm{Var}(\mathbf{P}_i)$ is the variance of samples of the i^{th} projection and $\overline{\mathrm{Var}(\mathbf{P})}$ is the average variance over all projections in $\mathbf{P}$. The stringency of these protocols, in respect of the amount of information that the sub–optimal compressor must transmit or store, reduces for a permitted fidelity level α, as we move from PR1 to PR3. The net effect is to move the rate distortion function characteristics of the sub–optimal compressor closer to the theoretical rate distortion, for a given α. This is observable from figs. 6.10–6.12 which show the relative performance of the sub–optimal compressor for MAN, BOY and BOX projected information respectively. The curves corresponding to MAN move from about 1.35 bits/ps to 0.80 bits/ps above the theoretical bounds, as we move from PR1 to PR3. The associated rate drops for the BOY and BOX images are about 1.3 to 0.75 bits/ps and 1.7bits/ps to 1.0 bits/ps respectively.

6.9.2 Sub–optimal 2–D Radial and Angular Compression

Employing similar considerations of the previous section on a 2–D basis, we present respective performance comparisons of 2–D block Cosine transform coding, the bow–tie algorithm based compression and full Fourier transform coding of projected

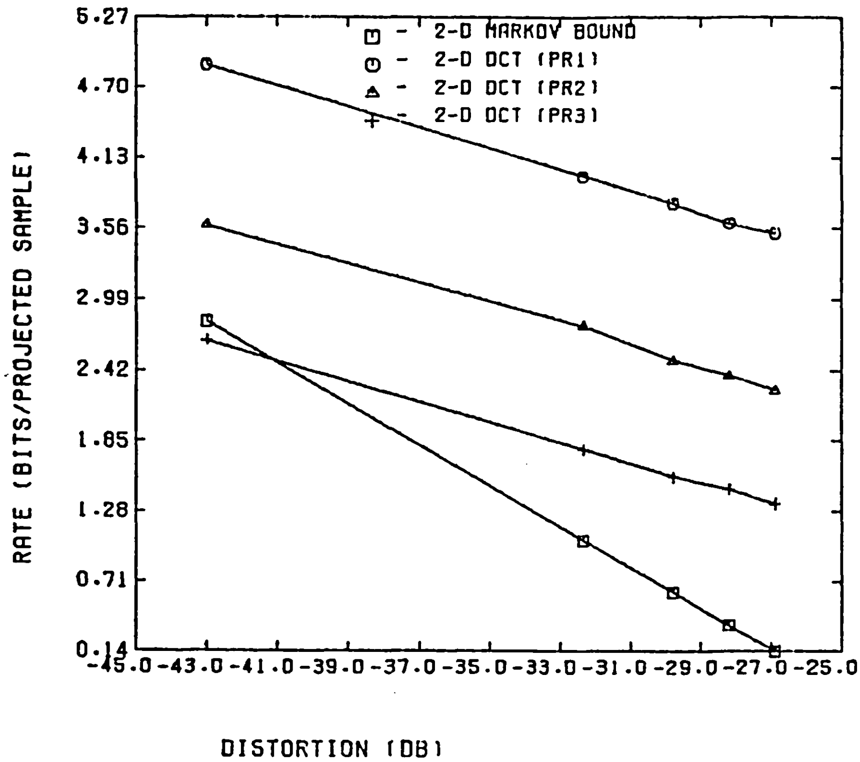

FIG. 6.13 PERFORMANCE COMPARISON OF 2-D DCT CODE WITH 2-D THEORETICAL BOUND.

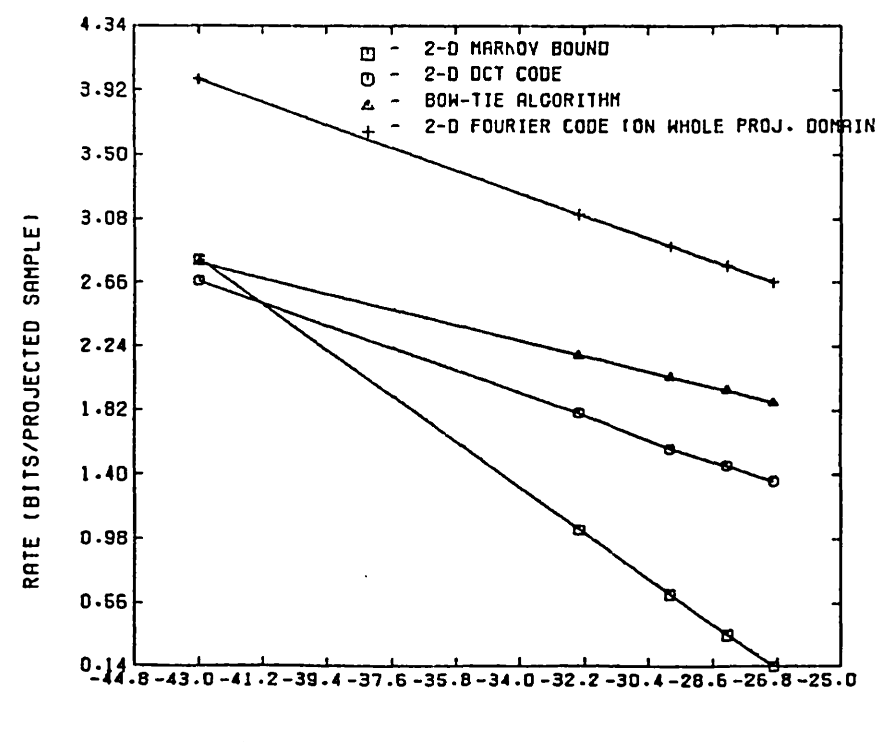

FIG. 6.14 PERFORMANCE COMPARISON OF 2-D AR SCHEMES WITH 2-D THEORETICAL BOUND.

information of the MAN image with the equivalent 2–D Markov based bound of (6.64). Fig. 6.13 shows plots of 2–D Cosine transform sub–optimal compression for 16×16 block coding, for various protocols, as compared to the Markov bound. The protocols are identical to the constraints of (6.67–69) except that the variance is computed over 2–D blocks rather than individual projections. It is noticeable that at very low distortion levels, the sub–optimal cosine transform compression system falls slightly below the Markov bound by 0.2 bits/ps. This may again be due to the fact that the Markov bound is rather pessimistic as it ignores the negative correlation in actual data and therefore registers a higher 2–D theoretical bound than it ought to, for given data. We have not numerically evaluated the 2–D bound associated with the true statistics of projected information because of the inherent complexity in such a procedure. Nevertheless, it is clear that as the normalized distortion α increases, the difference between the Markov bound and the practical performance results is considerably enhanced.

In fig. 6.14, Fourier transform coding (over the whole projection domain) is compared with the same procedure when systematic spectral shapening is employed in the bow–tie algorithm configuration of chapter three and with the Cosine transform code, for the same distortion level relative to the overall variance in the projection data. The advantages of the spectral shapening of the 2–D AR–Fourier spectrum are apparent from the results. However, the Cosine transform code outperforms the others (within 0.5 bits/ps) despite the smaller block sizes utilized. This may be an indication of the decorrelating and energy packing power of the Cosine transform.

6.10 Controlling Reconstruction Distortion

We are concerned about controlling the distortion D_I, associated with reconstruction stage transformations of equation (6.13). For this purpose, we may consider the virtual projection process $\left\{\widehat{P}_v(m,n)\right\}$ generated from (6.13) to be an observation sequence from which we wish to derive a best estimate sequence $\{\widehat{P}_E(m,n); -\infty \leq m,n \leq \infty\}$ of the compressed information $\left\{\widehat{P}(m,n)\right\}$, given the blurring transformation $S(\omega_1,\omega_2)$ and the spectral density function $\Phi_u(\omega_1,\omega_2)$ of the inversion noise process $\{u(m,n)\}$. Since we have assumed a MSE measure of D_I, the control problem becomes a classical mean squared estimation one in which we wish to minimize D_I. The solution to this problem is well known in optimum signal processing [111] and is derived from the optimal filtering of the process $\left\{\widehat{P}_v(m,n)\right\}$ in the manner:

$$\widehat{P}_E(m,n) = \sum_{k=-\infty}^{\infty} \sum_{l=-\infty}^{\infty} W(k,l)\, \widehat{P}_v(m-k, n-l) \tag{6.70}$$

where $W(m,n)$ is the impulse response of the infinite lag Wiener filter whose 2–D frequency response $W(\omega_1,\omega_2)$ is such that [111,pg 125]

$$W(\omega_1,\omega_2) = \Phi_{P\widehat{P}_v}(\omega_1,\omega_2) \left(\Phi_{\widehat{P}_v}(\omega_1,\omega_2)\right)^{-1} \tag{6.71}$$

According to equations (6.25) and (6.32), $W(\omega_1,\omega_2)$ may be written as

$$W(\omega_1,\omega_2) = \frac{S^*(\omega_1,\omega_2)\Phi_{\widehat{P}}(\omega_1,\omega_2)}{|S(\omega_1,\omega_2)|^2\, \Phi_{\widehat{P}}(\omega_1,\omega_2) + \Phi_u(\omega_1,\omega_2)} \tag{6.72}$$

From expressions (6.70–72) it can be shown (after deriving an expression for the auto–correlation function of $\{P_E(m,n)\}$ from (6.70) and further manipulation) that the spectral density function $\Phi_{P_E}(\omega_1,\omega_2)$ of the process $\{P_E(k,l)\}$ reduces to

$$\Phi_{P_E}(\omega_1,\omega_2) = |W(\omega_1,\omega_2)|^2\, |S(\omega_1,\omega_2)|^2\, \Phi_{\widehat{P}}(\omega_1,\omega_2) + |W(\omega_1,\omega_2)|^2\, \Phi_u(\omega_1,\omega_2) \tag{6.73}$$

Therefore, the minimal MSE of inversion D_{Imin} is

$$D_{Imin} = \left(\frac{1}{2\pi}\right)^2 \int_{-\pi}^{\pi}\int_{-\pi}^{\pi} |W(\omega_1,\omega_2)|^2\, \Phi_u(\omega_1,\omega_2)\, d\omega_1\, d\omega_2 \tag{6.74}$$

According to the conceptual reconstruction model characterized by equation (6.12), the frequency response of the reconstructor that would achieve D_{Imin} would be

$$\widehat{H}_I(\omega_1,\omega_2) = W(\omega_1,\omega_2) H_I(\omega_1,\omega_2) \tag{6.75}$$

where $H_I(\omega_1,\omega_2)$ is the ideal reconstruction filter response. This structure is more readily conceivable and practical, in the sense of explicitly defining $H_I(\omega_1,\omega_2)$, when we again invoke the stochastic results of chapter two for the AR–RT; the use of such results permits the 2–D sdfs and filters of (6.74) and (6.75) to be reduced to angle dependent 1–D radial frequency functions. Specifically an angle– dependent filter evolves, which is defined as

$$W(\theta_i,\omega_2) = \frac{S^*(\theta_i,\omega_2)\Phi_{\widehat{P}}(\theta_i,\omega_2)}{|S(\theta_i,\omega_2)|^2\,\Phi_{\widehat{P}}(\theta_i,\omega_2) + \Phi_u(\theta_i,\omega_2)} \tag{6.76}$$

where $S(\theta_i,\omega_2)$ has been mentioned in equations (6.55-56). Moreover, the minimum distortion D_{Imin}, when M_θ projections are available, becomes

$$D_{Imin} = \frac{1}{M_\theta}\sum_{i=0}^{M_\theta-1} |W(\theta_i,\omega_2)|^2\,\Phi_u(\theta_i,\omega_2)\,d\omega_2 \qquad (6.77).$$

In the context of convolution backprojection (CBP) (see chapter two), a radial–based ideal inverse reconstruction filter $H(\theta_i,\omega_2)$ is no other than the high frequency emphasis filter $H(\theta_i,\omega_2) = |\omega_2|$. On the basis of these definitions and observations, the optimal CBP algorithm (in a minimum MSE sense) for reconstructing the image process $\left\{\widehat{f}(m,n)\right\}$ may be written as

$$\begin{aligned}\widehat{f}(m,n) = \frac{\pi}{M}\sum_{i=0}^{M_\theta-1} I\bigg(\int_{-\pi}^{\pi} & W(\theta_i,\omega_2)\,|\omega_2|\,[S(\theta_i,\omega_2)\widehat{P}(\theta_i,\omega_2) \\ & + u(\theta_i,\omega_2)]e^{j\omega_2 l}d\omega_2\bigg)\end{aligned} \tag{6.78}$$

where it is apparent, from (6.13), that

$$\widehat{P}_v(\theta_i,\omega_2) = S(\theta_i,\omega_2)\widehat{P}(\theta_i,\omega_2) + u(\theta_i,\omega_2) \tag{6.79}$$

where $\widehat{P}(\theta_i,\omega_2)$and $u(\theta_i,\omega_2)$ are the radial frequency transforms of the compressed projection domain process $\left\{\widehat{P}(k,l)\right\}$ and noise process $\{u(k,l)\}$ respectively. Equation (6.78) depicts the fact that the optimal filtering of (6.70) is carried out on an angular basis in the radial Fourier domain , in cascade with the high frequency emphasis filter $|\omega_2|$. The variables k and l are integer indexes that respectively specify the angular position and the radial location of a projection sample. The operator $I(\cdot)$ is an interpolation operator whose function within the CBP procedure has been described in chapter two. It is noted that this result is, in principle, similar to an optimal reconstruction approach of Jain and Ansari [24], although the context and development of their results differ. In fig. 6.15, are shown the reconstruction procedures, that are characterized by equation (6.6), as they would feature at the reconstruction stage of the hypothetical intra-projection compressor of fig. 6.6.

The results of equations (6.57) and (6.78) suggest that a joint optimization procedure is possible in which the information rate of transmission or storage of projected data (subject to compression or encoding fidelity) and the associated reconstruction distortion may be simultaneously minimized. In practical terms, a finite number of projections, discretization in the radial parameter (for the AR–DRT), noise arising in the projection generation process and inappropriate filtering in the reconstruction process all severally and jointly contribute to inexact image reconstruction. However, thus far in this chapter, we have modelled the reconstruction distortion as a rather abstract intrinsic blurring and additive noise phenomenon (as in (6.13)) which either has an additive manifestation in the final distortion (cf. equations (6.51) and (6.57)) or a more complicated influence as in (6.52). While intuitively appealing answers have been provided by the analysis of this chapter on how to adapt the compressor to this intrinsic distortion and on how to control it through angle–dependent Wiener radial filtering, the relationship between the distortion and its listed contributing factors has not been established within this generalized PDC setup.

We have studied such a relationship of the reconstruction distortion with the number of projections, in chapter five; such a correspondence is clearly important to mode 2 PDC. In a mode 1 configuration, it might be reasonable and realistic to model the blurring and additive noise effects as being due to *channel* distortion since there may not be a control on the number of projections and other factors associated with reconstruction distortion (other than the optimized radial filtering)

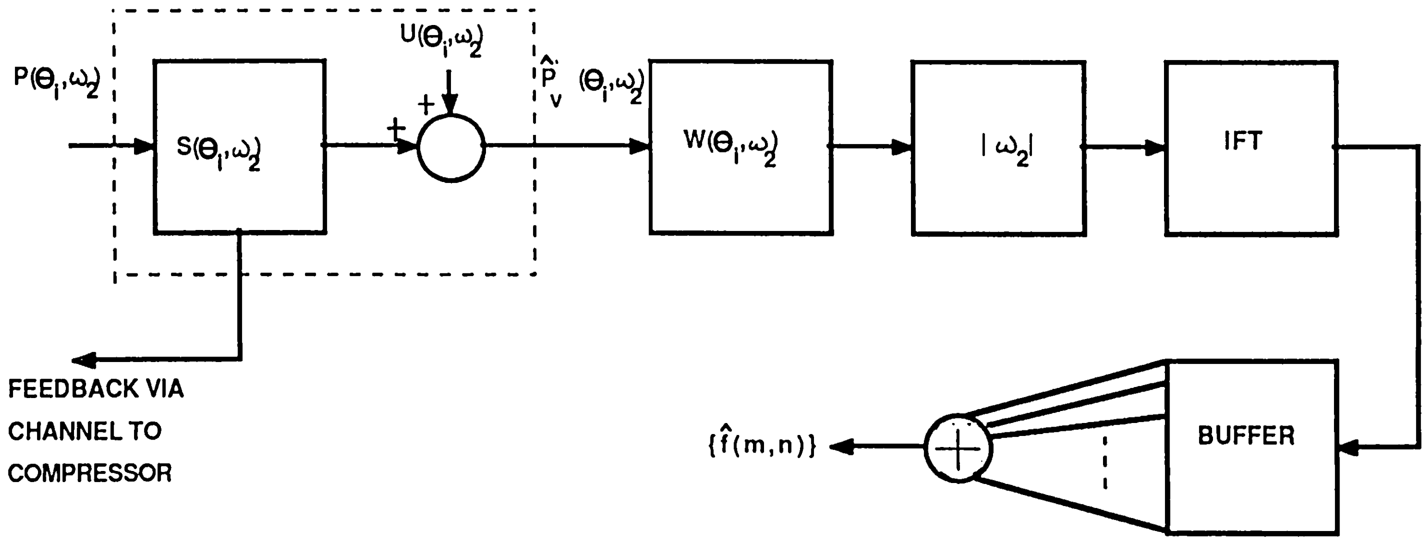

FIG. 6.15 MINIMUM MSE INVERSION FOR PDC.

and more so as channel noise is a relevant problem within any compression system. In effect, we may view the performance of optimal intra–projection compression in cascade with optimized radial filtering* through a very noisy channel link. That is, the reconstruction distortion is effectively dominated by channel distortion. We consider this in the following section.

6.11 Performance of Intra–projection Compression in the Presence of Channel Noise

Employing the sub–optimal intra–projection compression procedure described in section 6.9, we have applied additive white Gaussian noise (i.e $\Phi_u(\theta_i, \omega_2)$ is flat) of varying levels to compressed projections for two cases of CBP based image reconstruction. The first reconstruction procedure corresponds to radial filtering with $H_I(\theta_i, \omega_2) = |\omega_2|$ and the second is the cascaded response $H_I(\theta_i, \omega_2) = |\omega_2| W(\theta_i, \omega_2)$. The RAM–LAK filter (see table 2.1 in chapter two) has been used to approximate $|\omega_2|$ as the associated window function of the RAM–LAK filter is rectangular and therefore does not modify $|\omega_2|$ within an allowable proportion of the spectrum. For simplicity, the blurring filter $S(\theta_i, \omega_2)$ is assumed to have a flat frequency response equal to unity (i.e there is no blurring in the channel). Table 6.2 contains numerical results of distortion (NMSE) when compared to image reconstructions without compression or channel noise for the MAN and BOY images, respectively. The rms value η_c of the channel distortion is chosen such that

$$\eta_* \geq \eta_c \geq \eta_l \tag{6.80}$$

where

$$\eta_l = 0.01 \max_{\forall i} \left\{ (\mathrm{Var}(\mathbf{P}_i))^{1/2} \right\} \tag{6.81}$$

$$\eta_* = 0.1 \min_{\forall i} \left\{ (\mathrm{Var}(\mathbf{P}_i))^{1/2} \right\} \tag{6.82}$$

* Strictly, both procedures are sub–optimal since infinite delays, as theoretically required by the compressor and reconstructor, are not practically feasible.

α (10^{-4})	$D_{c\alpha}$ (10^{-4})
0.50	0.50
10.45	10.46
20.40	20.42
30.35	30.37
50.25	50.29

Table 6.1 : Some selected values of α vs $D_{c\alpha}$ for $0.00005 \leq \alpha \leq 0.01$ (for projected MAN data)

Image	Channel noise rms (η_c)	D_1† (10^{-3})	D_2†† (10^{-3})
MAN	71.0 (η_l)	6.715	6.672
	213.0 ($3\eta_l$)	21.617	19.214
	480.0 (η^*)	77.450	52.822
BOY	55.0 (η_l)	20.649	20.633
	165.0 ($3\eta_l$)	52.849	49.681
	387.0 (η^*)	167.264	130.252

†(Distortion with radial filter $|\omega_2|$)
††(Distortion with enhanced radial filter $|\omega_2| \; W(\theta_i, \omega_2)$)

Table 6.2 : NMSE(F) Distortion in image reconstructions from compressed projections in the presence of channel noise.

Fig. 6.16 INTRAP (2.1 bits/ps.), $n_c = 71$,
Reconstruction using RAM - LAK only.
(MAN).

Fig. 6.17 INTRAP (2.1 bits/ps.), $n_c = 71$,
Reconstruction using Minimum MSE filtering, (MAN).

Fig. 6.18 INTRAP (2.1 bits/ps.), $n_c = 55$,
Reconstruction using RAM - LAK only.
(BOY).

Fig. 6.19 INTRAP (2.1 bits/ps.), $n_c = 55$,
Reconstruction using Minimum MSE filtering, (BOY).

Fig. 6.20 INTRAP (2.1 bits/ps.), $n_c = 213$,
Reconstruction using RAM - LAK only.
(MAN).

Fig. 6.21 INTRAP (2.1 bits/ps.), $n_c = 213$,
Reconstruction using Minimum MSE filtering, (MAN).

Fig. 6.22 INTRAP (2.1 bits/ps.), $n_c = 165$,
Reconstruction using RAM - LAK only.
(BOY).

Fig. 6.23 INTRAP (2.1 bits/ps.), $n_c = 165$,
Reconstruction using Minimum MSE filtering, (BOY).

and $(\mathrm{Var}(\mathbf{P}_i))^{1/2}$ is the standard deviation corresponding to the projection $\mathbf{P}_i$. The objective results indicate that the Wiener filter is more effective at high channel distortions. Some pictorial results are shown in figs. 6.16–23.

In all cases, the bit rate of compression is 2.1 bits/ps which corresponds to a fidelity parameter of $\alpha = 0.0110$. The results do not indicate substantial visual differences between images reconstructed by radial filtering with the high frequency emphasis filter $|\omega_2|$ and those reconstructions based on the minimal MSE Wiener filtering, despite the lower objective distortion of the latter scheme.

6.12 Summary

A rate–distortion theoretic analysis of a generalized PDC system has been presented. Various rate distortion bounds of compression subject to fidelity constraints on the projection domain compression and image reconstruction have been derived. The emphasis has been placed on a simple bound, which as a result of stochastic results described in chapter two, reflects the potential of projections being processed in an uncorrelated manner. A variation of the bound, suitable for tomographic procedures in which there exists substantial uncertainty in the projection generation process, is also described.

The simple bound, derived under unconstrained complexity conditions, has been compared with the performance of intra–projection compression with the aid of Shannon quantization and various protocols for determining the appropriate fidelity criterion. Performance comparisons have also been made for 2–D compression (angular and radial) of projection data using the bow–tie algorithm and 2–D block coding, respectively, with equivalent 2–D Markov based compression bounds.

A means of controlling the intrinsic reconstruction distortion has been discussed with respect to intra–projection compression. This formulation effectively leads to a joint optimization of the compression and reconstruction processes, by simultaneously maximizing the compression level subject to the compression or encoding based distortion and minimizing the reconstruction distortion. The performance of intra–projection compression, within this jointly optimized, setup has been observed when reconstruction distortion is assumed to be dominated by channel noise.

CONCLUSIONS

This thesis has focused on the development of projection domain compression (PDC) of image information. The generalized concept of PDC has been established. Unique definitions of its two forms, namely, mode 1 and mode 2 PDC, have been presented.

Mode 1 PDC is configured to work in tomographic applications (medical imaging, radio astronomy, geophysical prospecting etc.), where image information is originally available in projected form. The mode 1 PDC systems offer the potential of efficient storage or transmission of projected information for retrieval or reception at image reconstruction sites. Various architectures for such applications have been outlined.

The mode 2 PDC systems operate as conventional image coders in the sense that, unlike mode 1 PDC, knowledge of the pictorial data is available at the input of such systems.

The main approach of the thesis has been to investigate and/or develop various theoretical structures that relate projection domain information to corresponding image domain data and where possible, develop various compression schemes that exploit such analytical correspondence. Accordingly, the examination of the stochastic properties and frequency domain properties of projection data has been a major direction of this research into PDC.

The opening theoretical discussion, however, has concerned the problem of inexact image reconstruction from projected information. This problem particularly limits the performance of mode 2 PDC in comparison to other digital image coding techniques that can ensure orthogonal mappings of the image data. Although we have shown in chapter two, through an entropy transformation analysis of discrete–space projection transformations, that this desirable orthogonality condition can be obtained in theory, no practical exact reconstruction procedures result. This observation is similar to the strictly theoretical conclusions of the one–projection theorems, proven for the angle–radius (AR) based projection mapping in [5] and in appendix I for the slope–intercept (SI) projection generation. These theorems claim that a discrete–space image array, sampled under band–limited conditions, may be exactly reconstructed from a single projection generated at a critical angle for the AR projection geometry or at a critical slope for the SI geometry.

Comprehensive independent proofs of the stochastic properties of projected information, that have been formally defined in [24] for the AR geometry, primarily reveal that projections derived from wide sense stationary (WSS) image information, are WSS in the radial parameter and jointly uncorrelated . Similar, but new results for SI–based projection data, formally presented in chapter two and fully proven in appendix II, show that the projections are whitened in the slope parameter but are WSS in the intercept variable. These interesting results are in effect a mathematical basis for intra–projection compression schemes, studied experimentally in chapter three and analytically in chapter six. It is noted, however, that the foregoing results are derived under the assumptions that the projections are generated by infinitesimally narrow line integrations which is impossible in practice. Thus, empirical evaluations of the auto–correlation of projection data, acquired from typical images (that are atypically WSS) using practical procedures, indicate that there is considerable inter–projection and intra–projection correlation in the data.

Chapter three has concentrated on studying compression procedures that can exploit such correlation in accordance with the frequency structure of the AR–based projected information, primarily for mode 1 PDC applications. Intra–projection compression is examined by implementing radial Cosine transformations of the projections before quantization. The basis of the Cosine transform approach is outlined in a discussion of a Cosine projection theorem which, in turn, is a special form of the generalized projection theorem that relates a 1–D operation on a projection to an equivalent 2–D operation on the corresponding image plane, along the orientation in which the projection is generated. Intra–projection compression is particularly sensitive to quantizer mismatch, as considerable circular artifacts are noticeable in the image reconstructions for uniform quantization of the Cosine transformed data at compression ratios of 3. Transmitting or storing fewer projections and employing finer uniform quantization on their respective frequency transforms lead to twice as much compression at acceptable fidelity in reconstructed imagery when missing projections are interpolated for at the reception or retrieval point before reconstruction. Appropriately matched distribution–dependent quantization, however, ensures higher compression ratios of the order of 10.

Inter–projection compression is studied by angle-based Cosine transformation of the projection information. Mismatched quantization in angular frequency coding produces more stable reconstructions than the radial frequency approach, however, some streaky effects in the reconstructions are still observable.

The 2–D AR frequency structure of projected information has been examined in some detail. The interesting structure is characterized by a bow–tie shaped band region. This band shape has led to the development of a so called bow–tie algorithm for exploiting both the intra–projection and inter–projection correlation for compression purposes. The algorithm relies on spectral shapening of the 2–D AR Fourier transform of projected information in accordance with the bow–tie structure; the shapening enables nearly a third of the coefficients to be systematically discarded. An elaborate encoding procedure of the remaining coefficients ensures that minimal additional distortion is produced in the projection domain. High compression ratios of the order of 8–13 of projection data may be achieved with relatively good image reconstructions.

The compression of projection information, using vector quantization (VQ), has been studied in chapter five. A main observation here is that the reduction of memory between vectors, derived from projection data, greatly enhances the performance of VQ based PDC. Specifically, memory reduction is incorporated by radial Cosine transformations of the projections before vector formation on an inter–projection (angular) basis. This procedure is reflective of one that exploits the analytical relationships between the projection and image domains. Two adaptive forms of this enhanced VQ strategy have been introduced. The first is a zonal VQ technique that vector quantizes different zones of the frequency transformed data according to the geometrical or energy distributions of the transformed samples. The second scheme is based on a gain shape adaptive multi–stage VQ approach that adapts to projection domain data, derived from different images. In general, VQ appears to be a robust and stable approach for PDC and compression ratios of up to 20 may be achieved with acceptable image reconstructions.

Chapter five introduces some important developments that are mostly relevant to mode 2 PDC. Using a Fourier based projection generation procedure, the performance of projection based block coding (PBBC) of images has been examined. The application of PBBC to 16×16 blocks of image data, with 16 projections generated per block, yields bit rates in the range 1.0–2.0 bit /pixel with reasonable image fidelity. The performance of PBBC is limited in comparison to block Fourier transform coding for a given bit rate, as a result of the inexact reconstruction problem. The difference in distortion, which can be up to 4dB, may be reduced by increasing the number of projections acquired from each image block and/or improving the interpolation procedure in the Fourier based reconstruction technique. An adaptive form of PBBC which varies the number of projections generated from each image block in accordance with the a.c. energy in the block is also studied. A saving of 0.6 bit/ pixel may be achieved over non–adaptive PBBC at the expense of a little increased distortion of at most 2dB.

The reconstruction problem has been revisited in this chapter in the form of estimating the error of reconstruction as a function of image auto–correlation, image area and the number of projections, respectively or jointly, when the image statistics are Gauss–Markov in nature. The reconstruction error is very sensitive to image correlation. The mean squared error (MSE) of reconstruction distortion for highly correlated image structure is significantly smaller, in comparison to the corresponding error for poorly correlated information, and for a given number of projections and image area. In addition, there is a strong correspondence between a specific level of reconstruction error and the ratio of the number of projections to the image area, for a given level of image auto–correlation.

These results have motivated the derivation of a projection allocation algorithm which systematically determines the required number of projections to be generated for compression purposes (in mode 2 applications), subject to a fidelity criterion of reconstruction. The algorithm has been designed to allocate projections in such a manner that the minimum average reconstruction error is achieved over an arbitrary number of images and for a specified total number of projections, image correlation and area. Several tests of the algorithm indicate that it is a reliable approach for Gauss–Markov image data. Gains of 1dB in reduced reconstruction distortion are obtained with respect to that produced by straightforward uniform allocation.

Although this algorithm is primarily developed for mode 2 PDC, it may be useful for tomographic applications for predetermining the accuracy of image reconstructions of internal structures as a function of the smoothness (equivalent to correlation) and area of the structures. A corresponding lower bound to the reconstruction error, for a given correlation level and image area, is also discussed.

The object of the rate distortion analysis of chapter six has been to determine the maximum amount of projection domain compression subject to the constraints of the MSE of distortion due to encoding and reconstruction, when the projection information is assumed to be generated from a WSS Gaussian image field. The analysis has been developed around a generalized PDC model which among other components features a compressor in tandem with a reconstructor, via a channel. Moreover, the analysis is more relevant for mode 1 PDC as no control on the choice of the number of projections is assumed. A main result is that in order to achieve the maximum compression of projected information, the compressor must take into account the latent reconstruction error. This is realized, in theory, by supplying information about the reconstruction transfer function to the compression function, via a feedback path.

The incorporation of the stochastic results of projected information into the analysis yields a rate distortion bound for intra–projection compression. The average difference between the respective evaluations of this bound for sample auto–correlation and first order Markov auto–correlation of projection data acquired from typical pictures is about 0.03 bits /projected sample. This indicates that Markov modelling of projected information is an appropriate procedure. By setting the normalized compression distortion to be a fraction of the maximum projection energy, the practical performance of intra–projection compression is on average 0.80 bits /projected sample above the theoretical bounds for typical projection data.

A variation of the intra–projection compression bound has been proposed. It is believed that this bound would be suitable for determining optimal compression performance for tomographic applications in which there is considerable uncertainty in the projection generation process. Such uncertainty may be characterized by the generation of largely hollow or truncated projections as a result of the projection illumination process being obscured by internal structure or high measurement noise preventing the effective detection of projections. To deal with such issues, this bound features a book–keeping term to track the projection generation process.

The rate distortion bound for the equivalent 2–D Markov statistics of projection data is over 1.5 bits / projected sample above the performance of the 2–D AR–based compression approaches of Cosine transform coding and the bow–tie algorithm, respectively.

Within the generalized PDC configuration, the control of the MSE of reconstruction distortion has been discussed. For a convolution backprojection reconstruction procedure, this problem requires an angle–dependent Wiener filter to be cascaded with an ideal radial based reconstruction filter in order to minimize the MSE of reconstruction. Consequently, an overall compression structure emerges which simultaneously enables a minimization of compression (subject to the compression fidelity level) and a minimization of the distortion in the reconstruction stage. The performance of a sub–optimal intra–projection structure (the optimal configuration assumes infinite lag processing i.e. unconstrained complexity) has been examined under the assumptions that the intrinsic distortion that occurs at reconstruction is predominantly due to channel distortion. The inclusion of the angle–dependent Wiener filtering has a significant effect on the objective values of reconstruction distortion.

Recommendations for further work

On the whole, PDC is a feasible approach in either mode 1 or mode 2 procedures. We have demonstrated its performance under low resolution mode 1 reconstruction procedures and in higher resolution mode 2 processing as required in the more conventional image coding schemes. There is however a considerable scope and need for its further development.

Future ventures with mode 1 PDC should concern the applications of algorithms developed in this study or suitably modified forms to actual tomographic data as a prelude to the development of custom–built compressors for inclusion in current tomographic systems. The huge amount of projection data, typically generated from such systems, may invariably require its (the data) decomposition into fields, in a manner akin to video processing, to allow some form of parallel processing. This may be a particularly suitable form for the bow–tie algorithm.

Future efforts for the development of intra–projection compression may include the use of another form of the generalized projection theorem, namely, the *projection moment theorem* [26]. This relates 1–D moments of the projections to 2–D moments of the image over the directions of projection. There is an implicit data compression effect in the use of moments as image information can be adequately described by a finite order expansion in terms of its moments [112]. The complexity of the image data determines the order of the expansion. It may be instructive, by virtue of the theorem, to compress projections by transmitting information about the respective sets of moments and synthesize the image at the receiver by generating the image moments from the projection moments.

Further work for the use of the 2–D bow–tie structure for compression purposes may be directed to the adoption of hexagonal sampling of projection data rather than rectangular sampling. The bow–tie structure is equivalent, to within a spectral shift, to a hexagonal band region. At least a saving of 13.4 percent mean sampling density may be achieved with hexagonal sampling over rectangular sampling for information that is band limited over a circular band region. The association of this reduced sampling representation with PDC would be of great benefit although it should be pointed out that some practical interfacing problems may arise in mode 1 applications, as state-of-the-art scanning systems almost exclusively process projection information on a rectangular sampling basis.

The mode 2 PDC systems would require hybrid optical/signal processors to effect fast and efficient projection generation and reconstruction, respectively. In particular, the projections may be acquired optically and the encoder implemented digitally before another optical based reconstruction procedure.

Although the projection allocation algorithm proposed here is certainly of considerable benefit to mode 2 PDC, more work is required to harmonize its performance with other types of image models and statistics other than the Gauss–Markov causal minimum variance structure considered in chapter five. Some effort is also needed to permit the correlation and area–dependent parametric constant of the algorithm to be factorized into *separate* correlation dependent and area dependent constants; this would certainly enhance the versatility of the algorithm.

The quantitative reconstruction error experiments (conducted in chapter five) may motivate, for future research of mode 2 PDC, a composite source coding approach in which the image signal may be segmented into spatially non–overlapping regions that have different correlation structure or possibly varied levels of psychovisual importance. The projection mapping of the whole image, on account of its linearity, may therefore be similarly decomposed into independent projection mappings of the constituent regions. The PDC based composite source code would therefore vary the number of projections with respect to the regions depending on their relative correlation or perceptual importance.

The *unification* of the encoding and reconstruction procedures, to permit reliable prediction of the performance of the mode 2 systems, remains an open problem.

Theoretical development of the respective stochastics and frequency properties of projection data generated, using other types of projection mapping geometries not considered in this thesis,would be quite illuminating. Some of these geometries include the divergent or fan beam geometry and the attenuated Radon transform geometry where the latter is employed in emission computed tomography.

An extension of PDC to 3–D image information processing where the third dimension may be temporal or spatial is in order.

It is hoped that the analytical work developed here and elsewhere for the SI–Radon transform, despite its similarity to the AR Radon transform, will motivate an investigation into its practical viability for PDC.

APPENDIX 1

THE ONE PROJECTION THEOREM FOR THE SLOPE-INTERCEPT RADON TRANSFORM

A one projection theorem for the angle–radius Radon transform (AR–RT) is presented in [5]. The main result is that a bandlimited sampled image function may be uniquely reconstructed from a single projection. A similar theorem is presented, here, for the slope–intercept Radon transform (SI–RT).

Theorem. *Let $u(x,t)$ be a bandlimited function of bandwidth $B = \max(B_1, B_2)$ and of finite order $M = \max(M_1, M_2)$, that is, the function may be exactly synthesized from a sequence $\{u(\frac{m\pi}{B}, \frac{n\pi}{B}); 0 \le m, n \le M-1\}$. Then $u(x,t)$ (or its sampled form) can be represented exactly by a single projection, derived from the SI–RT on a slope $q = \frac{\alpha}{\beta}$, if α and β are two positive integers that have no common factors and if $(m-m')\alpha + (n-n')\beta = 0$ if and only if $m = m'$ and $n = n'$ where m, m', n, n' are integers in the range $0 \le m, n, m', n' \le M-1$. Such a projection is said to be generated at a critical slope.*

Proof:

If $u(x,t)$ has been bandlimited to $B = \max(B_1, B_2)$ then from sampling theory the Fourier transform $U(\omega_x, \omega_t)$ of $u(x,t)$ may be expressed in terms of the sequence $\{u(\frac{m\pi}{B}, \frac{n\pi}{B}); 0 \le m, n \le M-1\}$ for $M = \max(M_1, M_2)$. Formally,

$$U(\omega_x, \omega_t) = \left(\frac{\pi}{B}\right)^2 \sum_{m=0}^{M-1} \sum_{n=0}^{M-1} u\left(\frac{m\pi}{B}, \frac{n\pi}{B}\right) \cdot \exp\left[-\jmath \frac{\pi}{B}(m\omega_x + n\omega_t)\right] W(\omega_x, \omega_t) \tag{A1.1}$$

where

$$W(\omega_x, \omega_t) = \begin{cases} 1 & \max(|\omega_x|, |\omega_t|) \le B \\ 0 & \text{otherwise.} \end{cases} \tag{A1.2}$$

From the projection slice theorem for the SI–RT [10], it is known that the 1–D Fourier transform $P(q,\omega)$ of a projection $P(q,\tau)$ of $u(x,t)$ is a slice of the two dimensional Fourier transform $U(\omega_x,\omega_t)$ along the line $\omega_x = q\omega$, $\omega_t = \omega$ where ω is the frequency associated with the intercept parameter τ of the SI–RT. Specifically,

$$P(q,\omega) = U(\omega_x,\omega_t)\Big|_{\substack{\omega_x = q\omega \\ \omega_t = \omega}} \tag{A1.3}$$

and when $q = \frac{\alpha}{\beta}$, (A1.3) may be fully expressed as

$$\begin{aligned} P(q,\omega) = \left(\frac{\pi}{B}\right)^2 \sum_{m=0}^{M-1}\sum_{n=0}^{M-1} u\left(\frac{m\pi}{B},\frac{n\pi}{B}\right) \\ \cdot \exp\left[\frac{-\jmath\pi\omega}{\beta B}(m\alpha+n\beta)\right]W(\omega) \end{aligned} \tag{A1.4}$$

where

$$W(\omega) = \begin{cases} 1 & |\,\omega\,| \le \frac{B|\,\beta\,|}{\max(|\,\alpha\,|,|\,\beta\,|)} \\ 0 & \text{otherwise.} \end{cases} \tag{A1.5}$$

For

$$|\,\omega\,| \le B_c = \frac{B\,|\,\beta\,|}{\max(|\,\alpha\,|,|\,\beta\,|)}$$

equation (A1.4) corresponds to the 1–D z transformation, of the form

$$H(z) = \sum_{k=N^-}^{N^+} h_k\, z^k \tag{A1.6a}$$

where

$$z = \exp\left[\frac{-\jmath\pi\omega}{\beta B}\right] \tag{A1.6b}$$

$$N^+ = \max(m\alpha + n\beta), \qquad 0 \le m,n \le M-1 \tag{A1.6c}$$

$$N^- = \min(m\alpha + n\beta), \qquad 0 \le m,n \le M-1 \tag{A1.6d}$$

These latter relations indicate that $H(z)$ is completely specified by a set $S_h = \{h_k; N^- \le k \le N^+\}$ of coefficients whose number of elements $\mathcal{N}(S_h)$ is at most

$$\mathcal{N}(S_h) = [(|\,\alpha\,| + |\,\beta\,|)(M-1)+1] \tag{A1.6e}$$

and the degree of $H(z)$ may therefore be set at $\mathcal{N}(S_h) - 1$. From (A1.4), it is clear that M^2 of the coefficients would correspond to the samples $\{u(m,n)\}$ of $u(x,t)$ for a constrained choice (according to the theorem statement) of α and β. It follows that for consistency, a maximum number of $\mathcal{N}(S_h) - M^2$ elements of S_h are identically zero, for the appropriate α and β.

When $P(q,\omega)$ corresponds to a projection $P(q,\tau)$ acquired at a critical slope q, then the elements of S_h including the M^2 samples $\{u(m,n)\}$ are uniquely evaluated from the correspondence:

$$h_k = \frac{1}{2\pi}\int_{-B_c}^{B_c} H(\omega)e^{\frac{k\omega}{\beta B}}\, d\omega \qquad N^- \leq k \leq N^+ \qquad (A1.7).$$

When the stated conditions on α and β are not satisfied, it follows that there exists at least a pair of integers m', n' within the range $0 \leq m', n' \leq M-1$ that satisfy

$$m\alpha + n\beta = m'\alpha + n'\beta$$

for $m \neq m'$ and/or $n \neq n'$ where $0 \leq m, n \leq M-1$.

With reference to (A1.4), this implies that at least one of the coefficients h_k of $H(z)$, obtained from (A1.7), be a sum of one or more of the function samples $\{u(m,n)\}$. Therefore, the sample sequence (and hence $u(x,t)$) cannot be uniquely determined from the set S_h whose number of identically zero elements increase, accordingly. This completes the proof.

Comments on the Size of the Coefficient Set S_h

It should be noted that there effectively exists an infinity of critical slopes that would enable reconstruction from a single projection, however, the theorem essentially stipulates that the minimum number $\mathcal{N}(S_h)$ should be M^2, since there are M^2 function samples $\{u(m,n)\}$, obtained under bandlimiting conditions, from the image function $u(x,t)$. However, there is no upper bound on the size of S_h. This is observable by choosing $\alpha = 1$, $\beta = 2M$ such that $q = 1/2M$ is a critical slope; according to (A1.6e), $\mathcal{N}(S_h)$ is equivalent to $2M^2 - M$. Nevertheless, $M^2 - M$ of these are identically zero. When $q = 1/M$, $\mathcal{N}(S_h) = M^2$. This corresponds to the minimum size of S_h and in effect the minimum length of $H(z)$ from which the function $u(x,t)$ can be uniquely reconstructed.

APPENDIX II

STOCHASTIC PROPERTIES OF THE SLOPE INTERCEPT RADON TRANSFORM

A2.1 Introduction

New results for stochastic characterization of the SI–RT have been formally defined in section 2.6.4 of chapter two. The proof of the properties are outlined here along with a proof of the slope–intercept projection theorem for random fields.

The SI–RT has been defined in equation (2.18) in chapter two. For convenience, we reiterate here that for a given function $f(x,t)$, its SI–RT is specified as

$$P(q,\tau) = \int\!\!\int_S f(x,t)\,\delta(xq - t + \tau)\,dx\,dt \tag{A2.1}$$

where S is the domain of $f(x,t)$ and $P(q,\tau)$ is a projection derived from the function on a slope q for an intercept location τ. Our foremost assumption is that $f(x,t)$ is a wide sense stationary (WSS) space–time or space–space random field. We first prove the cross–correlation and auto–correlation properties, respectively. For brevity, the definitions are only presented in mathematical form.

A2.2 Proof of Cross–correlation Property

The cross–correlation property $f(x,t)$ and $P(q,\tau)$ is

$$r_{fP}(x,t;q,\tau) = \mathrm{E}[f(x,t)P(q,\tau)] \tag{A2.2}$$

and from (A2.1)

$$= \int\!\!\int_S \mathrm{E}[f(x,t)f(r,s)]\,\delta(rq - s + \tau)\,dr\,ds$$

Under the stated conditions of $f(x,t)$ being WSS, we may write $r = \alpha + x$ and $s = \beta + t$, such that

$$r_{fP}(x,t;q,\tau) = \int\int_S r_f(\alpha,\beta)\,\delta(\alpha q - \beta + \tau + xq - t)\,d\alpha d\beta \qquad (A2.3)$$

where

$$r_f(\alpha,\beta) = \mathrm{E}[f(x,t)f(x+\alpha,t+\beta)] \qquad (A2.4).$$

Finally,

$$r_{fP}(x,t;q,\tau) = \widehat{\phi}(q, xq - t + \tau) \qquad (A2.5)$$

where $\widehat{\phi}(q, xq - t + \tau)$ is effectively the SI–RT of $r_f(\alpha,\beta)$ — the auto–correlation function of the image field $f(x,t)$. This completes the proof.

A2.3 Proof of Auto–correlation Property

The autocorrelation of $P(q,\tau)$ is

$$r_P(q_1,\tau_1;q_2,\tau_2) = \mathrm{E}[P(q_1,\tau_1)P(q_2,\tau_2)] \qquad (A2.6).$$

Using (A2.1) and (A2.5), it can be readily shown that

$$r_P(q_1,\tau_1;q_2,\tau_2) = \int\int_S \widehat{\phi}(q_2, xq_2 - t + \tau_2)\,\delta(xq_1 - t + \tau_1)\,dx\,dt \qquad (A2.7).$$

By definition, a Fourier transform relationship exists between a spectral density function $\widehat{\Phi}(q_2,\omega)$ and the cross–correlation $\widehat{\phi}(q_2, xq_2 - t + \tau_2)$, which is

$$\widehat{\phi}(q_2,s) = \frac{1}{2\pi}\int_{-\infty}^{\infty} \widehat{\Phi}(q_2,\omega)\,e^{\jmath\omega s}\,d\omega \qquad (A2.8).$$

Substitution of (A2.8) in (A2.7) and further manipulation yields

$$\begin{aligned} r_P(q_1,\tau_1;q_2,\tau_2) &= \frac{1}{2\pi}\int_{-\infty}^{\infty} \frac{\widehat{\Phi}(q_2,\omega)}{|\omega|} e^{\jmath\omega(\tau_2-\tau_1)}\,\delta(q_2 - q_1)\,d\omega \\ &= \psi(q_2, \tau_2 - \tau_1)\,\delta(q_2 - q_1) \qquad (A2.9) \end{aligned}$$

where the singularity identity used in the proof of the AR–RT auto–correlation property (see equation (2.43)) is also employed here. The proof is complete.

A2.4 Proof for the SI–RT Projection Theorem for Random Fields

The theorem has been stated in section 2.6.4 of chapter two. The proof is outlined below. The proven cross–correlation and auto–correlation properties are also employed in the proof.

Definition:

Two projection domain functions $\widetilde{P}(q,\tau)$ and $P(q,\tau)$ are obtained from a *modified* SI–RT and a standard SI–RT (as in equation(A2.1)), respectively. Their corresponding intercept based 1–D Fourier transforms $\widetilde{P}(q,\omega)$ and $P(q,\omega)$, have the following correspondence:

$$\widetilde{P}(q,\omega) = |\,\omega\,|^{1/2} P(q,\omega) \qquad (A2.10).$$

The following lemmas are employed

Lemma 1. *The modified SI–RT that produces $\widetilde{P}(q,\omega)$ is*

$$\widetilde{P}(q,\omega) = \int\!\!\int_S \widetilde{f}(x,t)\,\delta(xq - t + \tau)\,dx\,dy \qquad (A2.11)$$

where

$$\widetilde{f}(x,t) = \frac{1}{2\pi}\int_{-\infty}^{\infty}\int_{-\infty}^{\infty} |\,\omega_x\,|^{1/2}\,F(\omega_x,\omega_t)\,e^{\jmath(\omega_x x+\omega_t t)}\,d\omega_x\,d\omega_t \quad (A2.12)$$

for $\omega_x = q\omega_t$, and

$$F(\omega_x,\omega_t) = \int\!\!\int_S f(x,t)\,e^{-\jmath(\omega_x x+\omega_t t)}\,d\omega_x\,d\omega_t \qquad (A2.13).$$

This lemma follows from the projection slice theorem for the SI–RT (see equation (A1.3)) and the definition of (A2.10) which may be rewritten as:

$$\widetilde{F}(\omega_x,\omega_t) = |\,\omega_t\,|^{1/2}\,F(\omega_x,\omega_t)\,\Big|_{\substack{\omega_x=q\omega\\ \omega_t=\omega}} \qquad (A2.14)$$

Lemma 2. *If $\widetilde{f}(x,t)$ and $f(x,t)$ are WSS fields whose second order statistics are described by spectral density functions $\widetilde{\Phi}_{\widetilde{f}}(\omega_x,\omega_t)$ and $\Phi_f(\omega_x,\omega_t)$, respectively, then*

$$\widetilde{\Phi}_{\widetilde{f}}(\omega_x,\omega_t) = |\,\omega_t\,|\,\Phi_f(\omega_x,\omega_t)\,\Big|_{\substack{\omega_x=q\omega\\ \omega_t=\omega}} \qquad (A2.15)$$

This follows directly from lemma 1 (equations (A2.10) and (A2.14)) since the spectral density functions of the fields $\widetilde{f}(x,t)$ and $f(x,t)$ are directly proportional to the squared forms of their amplitude spectra $\left|\widetilde{F}(\omega_x,\omega_t)\right|^2$ and $|F(\omega_1,\omega_2)|^2$, respectively [113,pg. 220].

In continuing with the proof, the cross-correlation $r_{fP}(x,t;q,\tau)$ is first determined, where

$$r_{\widetilde{f}\widetilde{P}}(x,t;q,\tau) = \mathrm{E}[\widetilde{f}(x,t)\widetilde{P}(q,\tau)] \tag{A2.16}$$

which may be found to be of the form

$$= \gamma(q, xq - t + \tau) \tag{A2.17}$$

on following a similar analysis of section A2.2 for the modified SI–RT (equation (A2.11)), where $\gamma(\cdot)$ is equivalent to the Radon transform of the 2–D auto-correlation function

$$r_{\widetilde{f}}(\alpha,\beta) = \mathrm{E}[\widetilde{f}(x,t)\widetilde{f}(x+\alpha,t+\beta)] \tag{A2.18}$$

which, in turn, implies that

$$\gamma(q,s) = \frac{1}{2\pi}\int_{-\infty}^{\infty} |\,\omega\,|\;\Phi_f(q\omega,\omega)\,e^{\jmath\omega s}\,d\omega \tag{A2.19}$$

according to lemma 2.

The auto-correlation function of $\widetilde{P}(q,\tau)$ is obtained as follows

$$\begin{aligned} r_{\widetilde{P}}(q_1\tau_1;q_2\tau_2) &= \mathrm{E}[\widetilde{P}(q_1,\tau_1)\widetilde{P}(q_2,\tau_2)] && (A2.20)\\ &= \int\!\!\int_S \mathrm{E}[\widetilde{f}(x,t)\widetilde{P}(q_2,\tau_2)]\,\delta(xq_1 - t + \tau_1)\,dx\,dy && (A2.21)\end{aligned}$$

and from equations (A2.16), (A2.17) and (A2.19), it is clear that

$$r_{\widetilde{P}}(q_1\tau_1;q_2,\tau_2) = \int\!\!\int_S \Big[\frac{1}{2\pi}\int_{-\infty}^{\infty} |\,\omega\,|\,\Phi_f(q_2\omega,\omega)\,e^{\jmath\omega(xq_2-t+\tau_2)}\,d\omega\Big] \cdot \delta(xq_1 - t + \tau_1)\,dx\,dt \qquad (A2.22).$$

An interchange of integrals and the use of the singularity indentity mentioned in setcion 2.5.2 yields

$$r_{\widetilde{P}}(q_1\tau_1; q_2, \tau_2) = \frac{1}{2\pi}\int_{-\infty}^{\infty} \Phi_f(q_2\omega, \omega)\, e^{\jmath\omega(\tau_1-\tau_2)}\, \delta(q_2 - q_1)\, d\omega \qquad (A2.23)$$

$$= \varsigma(q_2, \tau_2 - \tau_1)\, \delta(q_2 - q_1) \qquad (A2.24).$$

The 2–D Fourier transform of (A2.24), with respect to $\tau_2 - \tau_1$ and $q_2 - q_1$, yields the spectral density function $\widetilde{\Phi}(q_2, \omega)$ such that

$$\widetilde{\Phi}(q_2, \omega) = \Phi_f(\omega_x, \omega_t)\Big|_{\substack{\omega_x = q_2\omega \\ \omega_t = \omega}} \qquad (A2.25)$$

The final constraint of the theorem

$$\Phi(q, \omega) = \frac{\widetilde{\Phi}(q, \omega)}{|\omega|} \qquad (A2.26)$$

is easily verified by observing the fact that the Fourier transform $\widehat{\Phi}(q_2, \omega)$ of the cross–correlation function $\widehat{\phi}(q_2, xq_2 - t + \tau_2)$ (see equation (A2.5)) is by definition (of the projection slice theorem for the SI–RT) equivalent to a slice of $\Phi_f(\omega_x, \omega_t)$ on the line $\omega_x = q\omega_t$. It follows, therefore, that

$$\widehat{\Phi}(q_2, \omega) = \widetilde{\Phi}(q_2, \omega) \qquad (A2.27).$$

Furthermore, by comparing the spectral form of (A2.9) (i.e. the power spectrum of $P(q_2, \tau)$) with (A2.27), equation (A2.26) immediately follows. The proof of the theorem is complete.

Corollary. *The corollary of this proof is that the SI–RT is a whitening transformation in its slope parameter.*

APPENDIX III

INFORMATION RATE OF GAUSSIAN RANDOM VARIABLES

Here, we wish to briefly outline the background of equation (6.34) which specifies the information rate between Gaussian sequences $\mathbf{P} = \{ P(m,n) \}$ and $\widehat{\mathbf{P}} = \left\{ \hat{P}(m,n) \right\}$.

Pinsker [105] considers an n–dimensional random variable $\mathbf{\Lambda}$ to be an ensemble of n *distinct* functions or processes, each with a *discrete* parameter τ; that is $\mathbf{\Lambda} = (\lambda_1(\tau), \lambda_2(\tau), \ldots, \lambda_n(\tau))$. If $\mathbf{\Lambda}$ is a typical realization from a WSS Gaussian vector sequence $\{ \mathbf{\Lambda} \}$ and $\mathbf{\Upsilon}$ is a realization from another WSS Gaussian sequence $\{ \mathbf{\Upsilon} \}$ (where $\mathbf{\Upsilon} = (\upsilon_1(\tau), \upsilon_2(\tau), \ldots, \upsilon_n(\tau))$) then the mutual information rate between the jointly Gaussian sequences is given as

$$M(\mathbf{\Lambda}, \mathbf{\Upsilon}) = -\frac{1}{2\pi} \int_0^{\pi} \log \frac{det \left\| \Phi_{\lambda_j \upsilon_k}(\omega) \right\|}{det \left\| \Phi_{\lambda_j \lambda_k}(\omega) \right\| \, det \left\| \Phi_{\upsilon_j \upsilon_k}(\omega) \right\|} \, d\omega \qquad (A3.1)$$

for $j, k = 1, 2, \ldots, n$ and where $det \left\| \Phi_{\lambda_j \upsilon_k}(\omega) \right\|$, $det \left\| \Phi_{\lambda_j \lambda_k}(\omega) \right\|$ and $det \left\| \Phi_{\upsilon_j \upsilon_k}(\omega) \right\|$ are the respective matrices of the cross–correlation spectral density functions (sdfs) of component realizations of the n–dimensional random variables.

For the case when $n = 1$, $\mathbf{\Lambda}$ and $\mathbf{\Upsilon}$ are respective ensembles of 1–D variables $\{ \lambda(\tau) \}$ and $\{ \upsilon(\tau) \}$ and the information rate between them reduces to [105]

$$M(\lambda, \upsilon) = -\frac{1}{2\pi} \int_0^{\pi} \log \left(\frac{\Phi_\lambda(\omega)\Phi_\upsilon(\omega) - |\, \Phi_{\lambda\upsilon}(\omega)\, |^2}{\Phi_\lambda(\omega)\Phi_\upsilon(\omega)} \right) d\omega \qquad (A3.2).$$

We note that the joint sdf $\Phi_{\lambda_j \lambda_j}(\omega)$ of the j^{th} component process $\{ \lambda_j(\tau) \}$ of the n–dimensional random variable $\mathbf{\Lambda}$ may be obtained from the Fourier transformation of a corresponding auto–correlation function $r_{\lambda_j}(\tau - \tau')$ i.e.

$$\Phi_{\lambda_j \lambda_j}(\omega) = \Phi_{\lambda_j}(\omega) = \sum_{k=-\infty}^{\infty} r_{\lambda_j}(k)\, e^{-\jmath k \omega} \qquad (A3.3)$$

for $k = \tau - \tau'$.

Therefore, in the light of these definitions and parameterizations, the J–dimensional projection domain vector $\mathbf{P}$ may be regarded as an ensemble of 1–D random variables $P(m,n)$ (each dependent on two discrete parameters m,n) that belong to the *same* process or field $\{P(m,n)\}$. Hence, the average mutual information rate between such a vector $\mathbf{P}$ and compressed vector $\widehat{\mathbf{P}} = \left\{ \widehat{P}(m,n) \right\}$ may be expressed as

$$M(P,\widehat{P}) = -\left(\frac{1}{2\pi}\right)^2 \int_0^\pi \int_0^\pi \log\left[\frac{\Phi_P(\omega_1,\omega_2)\Phi_{\widehat{P}}(\omega_1,\omega_2) - \left|\Phi_{P\widehat{P}}(\omega_1,\omega_2)\right|^2}{\Phi_P(\omega_1,\omega_2)\Phi_{\widehat{P}}(\omega_1,\omega_2)}\right] d\omega_1\, d\omega_2 \tag{A3.4}$$

APPENDIX IV

RELATIONSHIP BETWEEN THE SI–RT AND AR–RT

We wish to illustrate the relationship between the SI–RT and the AR–RT. We are concerned with the formal representation of the projection mapping in equation (1.7) and how it relates to the SI–RT. We consider fig. (A4.1) which depicts an x_1–x_2 co–ordinate system in $\Re^2$ relative to a system t_1–t_2. The angle α is effectively the angle of the slope from which a projection is to be generated. The intercept of a line of integration along t_1 is τ. It is clear from the geometry that

$$x_2 = qx_1 + \tau \qquad (A4.1)$$

where $q = \tan\alpha$. Therefore, we may write the co–ordinates of t_1–t_2 in terms of x_1–x_2 as

$$\begin{bmatrix} t_1 \\ t_2 \end{bmatrix} = \begin{bmatrix} \cos\alpha & \sin\alpha \\ -\sin\alpha & \cos\alpha \end{bmatrix} \begin{bmatrix} x_1 \\ x_2 \end{bmatrix} \qquad (A4.2)$$

that is,

$$\hat{\mathbf{t}} = A\mathbf{x} \qquad (A4.3)$$

and where $t_2 = \tau\cos\alpha$. It is apparent that

$$\mathbf{x} = A^T\hat{\mathbf{t}} \qquad (A4.4).$$

Therefore, a projection $P(t_1;t_2)$ may be generated from a function $f(\mathbf{x})$, defined on x_1–x_2 within a region $\mathcal{V}$, in the manner

$$P(t_1;t_2) = \int_{\mathcal{V}} f(A^T\hat{\mathbf{t}})\,dt_1 \qquad (A4.5).$$

However, the projection $P(t_1;t_2)$ is one that corresponds to the AR–RT for an angle α. Nevertheless, the line t_2 on which $P(t_1;t_2)$ is defined is also an orthogonal projection of the intercept parameter of the SI–RT. It follows, in general, that an

AR–RT may be acquired from the SI–RT (the angle of the AR–RT would correspond to the angle of the desired slope of the SI–RT) by projecting the hyperplane (N-dimensional intercept), on which the SI–RT is defined, on to a hyperplane (i.e the radial parameter of the AR–RT) whose location is determined by the slope parameter of the SI–RT.

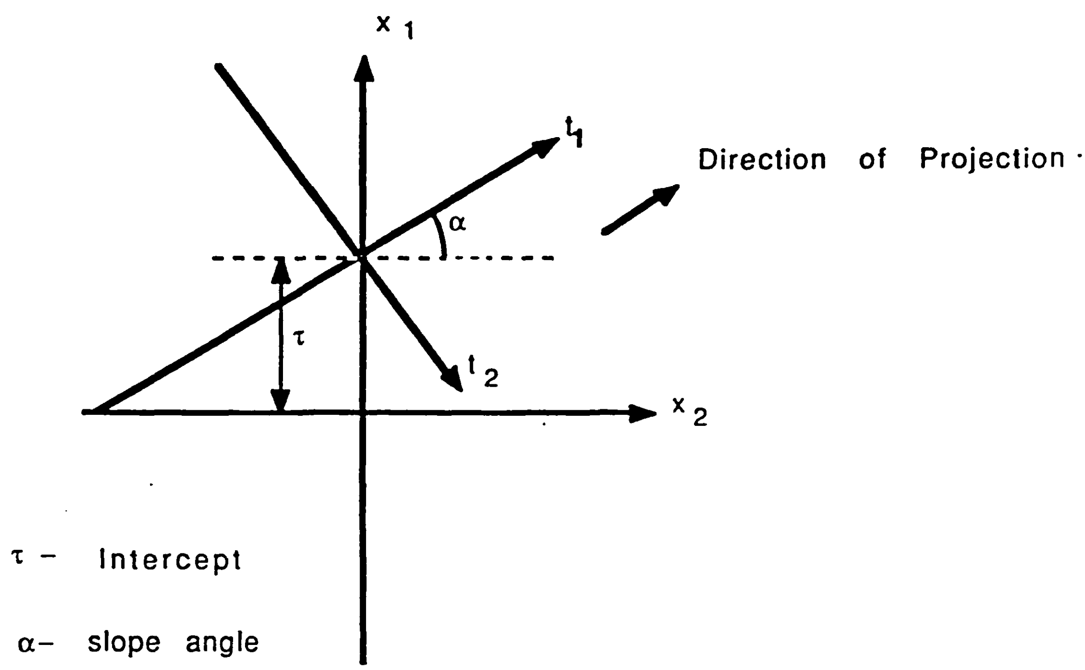

FIG. A4.1 GENERALIZED PROJECTION MAPPING FORMAT.

REFERENCES

1. A. K. Jain, "Image Data Compression. A Review", Proc. IEEE, vol. 69, No. 3, 1981, pp. 349–387.
2. R. W. Stafford, "Digital Television—Bandwidth Reduction and Communication Aspects", John Wiley, 1980.
3. A. Duerinckx, S. J. Dwyer III and J. M. S. Prewitt, "Digital Picture Archiving and Communication Systems in Medicine", Computer, vol. 16, No. 8, pp. 14–18.
4. A. Habibi, "Hybrid Coding of Pictorial Data", IEEE Trans. on Comm., vol. COM–25, No. 11, 1974, pp.1275–1284.
5. R. M. Mersereau and A. V. Oppenheim, "Digital Reconstruction of Multidimensional Signals from their Projections", Proc. IEEE, vol. 62, No. 10, 1974, pp. 1319–1338.
6. A. Rosenfeld and A. C. Kak, "Digital Picture Processing ", vol. 1,2nd Edition, Academic Press, 1982.
7. A. K. Lewis and F. Natterer, "Mathematical Problems of Computerized Tomography", Proc. IEEE, vol. 71, No. 3, March 1983, pp. 379–389.
8. E. H. Wood, J. H. Kinsey, R. A. Robb, B. K. Gilbert, L. D. Harris and E. L. Ritman, "Applications of High Temporal Resolution to Physiology and Medicine", Topics in Applied Physics , vol. 32, Springer Verlag 1979, Image Reconstruction from Projections: Implementation and Applications, edited by G. T. Herman, pp. 247–279.
9. R. N. Bracewell, "Image Reconstruction in Radio Astronomy", Topics in Applied Physics,vol. 32, Springer Verlag 1979, Image Reconstruction from Projections: Implementation and Applications, edited by G. T. Herman, pp. 81–104.
10. E. A. Robinson, "Spectral Approach to Geophysical Inversion by Lorentz, Fourier and Radon Transforms", Proc. IEEE, vol. 70, No. 9, 1986, pp. 1039–1054.

11. M. Bramanti and A. Tonazinni, "On the Resolution Properties of a Particular Tomographic Technique for Industrial Testing using Ultrasounds or Microwaves", Proc. CESTA, Dixieme Colloque Sur le Traitement du Signal et ses Applications, Nice, May 1985, pp. 735.
12. M. D. Altschuler, "Reconstruction of the Global-Scale Three-Dimensional Solar Corona", Topics in Applied Physics,vol. 32, Springer Verlag 1979, Image Reconstruction from Projections: Implementation and Applications, edited by G. T. Herman, pp. 105–143.
13. S. Y. Kung, "VLSI Array Processors", IEEE ASSP Magazine, 1985, pp. 4–22.
14. D. Fraser, B. R. Hunt and J. C. Su, "Principles of Tomography in Image Data Compression", Optical Engineering, vol. 24, No. 2, 1985, pp. 298–306.
15. J. R. Jain and A. K. Jain, "Interframe Adaptive Data Compression Techniques for Images", Signal and Image Processing Laboratory Report, Dept. of Electrical and Computer Engineering, Univ. CA, Davis, August 1979.
16. O. Ibikunle and R. A. King, "Image Data Compression in the Projection Domain", Proc. Dixieme Colloque Sur le Traitement du Signal et ses Applications, Nice , May 1985, pp. 841–846.
17. R. M. Mersereau: Computing in Biological Medicine 6, 1976, pp. 247.
18. O. Ibikunle, C. Y. Shin, N. M. Nasarabadi and R. A. King, "Numerical Recognition Using the Radon Transform and Relaxation Matching" , Proc. IERE Conf. in Digital Processing of Signals in Communications, Loughborough, April 1985, pp. 339–344.
19. N. M. Nasarabadi, O. Ibikunle and R. A. King, "A New Line Detection Technique in Noisy Images", 10^{th} International Conference in Satellite Remote Sensing, Reading, 1984, pp. 237–246.
20. C. Y. Shin, "Motion Analysis in the Projection Domain", M. Sc. Thesis, Imperial College of Science and Technology, London, Sept., 1984.

21. P. O. Ogunbona and R. A. King, "A Motion Estimation Scheme Using Projections of Frame, Element and Line Differences", Dixieme Colloque sur le Traitement du Signal et ses Applications, Nice, France, May 1985.
22. G. T. Herman, "Image Reconstruction From Projections: The Fundamentals of Computerized Tomography", New York Academic Press, 1980.
23. D. J. Scheibner and T. W. Parks, "Slowness Aliasing in the Discrete Radon Transform: A Multirate System Approach to Beam forming", IEEE Trans. Acoustics, Speech and Signal Processing, vol. ASSP 32, No. 6, 1984, pp. 1160–1163.
24. A. K. Jain and S. Ansari, "Radon Transform Theory for Random Fields and Optimum Image Reconstruction from Noisy Projections", ICASSP 84, pp. 12A.71–12A.74.
25. S. W. Rowland, "Computer Implementation of Image Reconstruction Formulas", Topics in Applied Physics, vol. 32, Springer Verlag, 1979, Image Reconstruction from Projections: Implementation and Applications, edited by G. T. Herman, pp. 1–79.
26. R. M. Lewitt, "Reconstruction Algorithms: Transform Methods ", Proc. IEEE, vol. 71, Nos. 3, 1983, pp. 390–408.
27. Y. Censor, "Finite Series Expansion Reconstruction Methods", Proc. IEEE, vol. 71, No. 3, pp. 409–419.
28. D. Slepian "On Bandwidth", Proc. IEEE, vol. 64, No. 3, 1976, pp. 292–300.
29. L. A. Shepp and B. F. Logan, "The Fourier Reconstruction of a Head Section", IEEE Trans. Nucl. Sci., vol. NS–21, 1974, pp. 21–43.
30. R. N. Bracewell and A. C. Riddle, "Inversion of Fan-beam Scans in Radio Astronomy", Astrophysics Journ., vol. 150, 1967, pp. 427–434.
31. G. N. Ramachandran and A. V. Lakshminarayanan, "Three Dimensional Reconstruction From Radiography and Electron Micrographs: Application of Fourier Transforms", Proc. Nat. Acad. Sci., U.S.A., vol.68, 1970, pp.2236–2240.

32. D. A. Chesler and S. J. Riederer, "Ripple Suppression during Reconstruction in Transverse Tomography", Physics Medical Biology 20, 4, 1975, pp. 632–636.
33. P. J. Davis. "Interpolation and Approximation", Dove Publications, Inc., New York, 1975.
34. X. Zhuang, K. B. Yu and R. M. Haralick, "A New Approach to the Solution of the Maximum Entropy Image Reconstruction Problem ", ICASSP 1984, pp. 12A8.1 –12A8.4.
35. J. G. Sanderson, "Reconstruction of Full Pin Bundles by a Maximum Entropy Method ", IEEE Trans. in Nuclear Science, vol. NS–26, No. 2, 1979, pp. 2685–2686.
36. A. J. Rockmore and A. Macovski, "A Maximum Likelihood Approach to Emission Image Reconstruction from Projections", IEEE Trans. on Nuclear Science, vol. NS–23, 1976, pp. 1428–1432.
37. A. J. Rockmore and A. Macovski, "A Maximum Likelihood Approach to Transmission Image Reconstruction from projections", IEEE Trans. on Nuclear Science, vol. NS–24, 1977, pp. 1929–1935.
38. M. E. Davidson and F. A. Grünbaum, "Tomographic Reconstruction with Arbitrary Directions", Communications on Pure and Applied Mathematics, vol. 34, 1981, pp. 77–120.
39. S. Wood and M. Morf, "A Fast Implementation of a Minimum Variance Estimator for Computerized Tomography Image Reconstruction", IEEE Trans. in Biomedical Engineering, vol. BME–28, No. 2, 1981, pp.56–68.
40. A. Lent and H. Tuy, "An Iterative Method for the Extrapolation of Band–limited Functions", Journal of Mathematical Analysis and Applications, vol. 83, 1981, pp.554–565.
41. Y. Koyonagi, T. Saito and Y. Hoshiko, "Image Reconstruction from Band–limited Data by Spectrum Extrapolation", Systems, Computers, Controls vol. 13, No. 5, 1982, pp. 18–26.

42. M. I. Sezan and H. Stark, "Tomographic Image Reconstruction from Incomplete Data using Convex Projections and Direct Fourier Inversion", Premier Colloque Image, Traitement Synthese, Technologie et ses Applications, 1985, pp.295–300.
43. R. M. Lewitt and R. H. T. Bates, "Image Reconstruction from Projections : III : Projection Completion Methods (Theory)", Optik 50, No. 3, 1978, pp. 189–204.
44. R. M. Lewitt and R. H. T. Bates, "Image Reconstruction from Projections : IV Projection Completion Methods (Computational Examples)", Optik 50, No. 4, 1978, pp. 269–278.
45. R. H. T. Bates, K. L. Garden and T. M. Peters, "Overview of Computerized Tomography with Emphasis on Future Development", Proc. IEEE, vol. 71, No. 3, 1983, pp. 356–372.
46. T. Inouye, "Image Reconstruction with Limited Angle Projection Data", vol. NS-26, No. 2, 1979,pp. 2666–2669.
47. H. C. Andrews, "Entropy Considerations in the Frequency Domain", Proc. IEEE (letters), vol. 46, 1968, pp. 113–114.
48. F. M. Reza, "An Introduction to Information Theory", McGraw Hill, 1961.
49. C. E. Shannon and W. Weaver, "The Mathematical Theory of Communication", University of Illinois Press, 1949.
50. A. Mackovski, "Physical Problems of Computerized Tomography", Proc. IEEE, vol. 71, No. 3, 1983, pp. 373–378.
51. D. J. Rossi and A. S. Willsky, "Reconstruction from Projections Based on Detection and Estimation of Objects—Parts I and II : Performance Analysis and Robustness Analysis", IEEE Trans. ASSP, vol. ASSP 32, No. 4,1984,pp. 886–906.
52. F. G. Stremmler, "Introduction to Communication Systems ", Addison–Welsley, 1977.
53. W. K. Pratt, J. Kane and H. C Andrews, "Hadamard Transform Coding", Proc. IEEE, vol. 57, No. 1, pp. 58–68.

54. K. R. Rao, M. A. Narasimhan and K. Revaluri, "Image Data Processing by Hadamard–Haar Transforms", IEEE Trans. Computers C–24, 1975, pp. 886–896.

55. W. K. Pratt, W. H. Chen and L. R. Welch, "Slant Transform Image Coding", IEEE Trans. COM–22, 8, 1974, pp. 1075–1093.

56. L. R. Rabiner and B. Gold, "Theory and Applications of Digital Signal Processing" Prentice–Hall, Englewood Cliffs, New Jersey 1975.

57. T. Berger, "Rate Distortion Theory : A Mathematical Basis for Data Compression", Englewood Cliffs, NJ, Prentice Hall, 1971.

58. W. K. Pratt, "Digital Image Processing", John Wiley and Sons, 1978.

59. Y. Luke, "Mathematical Functions and their Applications", Academic Press, New York, 1975, Chapter 11.

60. N. Ahmed, T. Natarajan and K. R. Rao, "Discrete Cosine Transform", IEEE Trans. on Computers (Correspondence), C–23 1974, pp. 90–93.

61. P. A. Wintz and A. J Kurtenbach "Waveform Error Control in PCM telemetry", IEEE Trans. Info. Theory, vol. IT–14, 1968, pp. 650–661.

62. R. S. Acharya, R. A. Robb and H. Weschsler, "An Image Reconstruction Algorithm for Time Varying X–Ray Projection Image Sequences", Proc. ICASSP, 1984, vol. 1, pp. 12A.4.1–12A.4.4.

63. J. Max, "Quantizing for Minimum Distortion", IRE Trans. Information Theory, vol. IT–6, 1960, pp. 7–12.

64. R. C. Reininger and J. D. Gibson, "Distributions of the Two–Dimensional DCT Coefficients for Images", IEEE Trans. on Communications, vol. COM–31, No. 6, 1983, pp. 835–839.

65. E. Kreyszig, "Advanced Engineering Mathematics", 4th Edition, John Wiley, 1979.

66. P. A. Rattey and A. G. Lindgren, "Sampling the 2–D Radon Transform", IEEE, vol. ASSP–29, No. 5, 1981, pp. 994–1002.

67. A. G. Lindgren and P. A. Rattey, "Tomographic Reconstruction from a Limited Number of Projections", Proc. CESTA, May 1985, pp. 301–311.

68. R. M. Mersereau, "The Processing of Hexagonally Sampled Two–Dimensional Signals", Proc. IEEE, vol. 67, No. 6,1979, pp. 930–949.

69. R. M. Gray "Vector Quantization", IEEE ASSP Magazine, April 1984, pp. 4–29.

70. Y. Linde, A. Buzo and R. M. Gray, "An Algorithm for Vector Quantizer Design", IEEE Trans. Comm., COM–28, 1980, pp. 84– 95.

71. J. MacQueen, "Some Methods for Classification and Analysis of Multivariate Distributions", Proc 5^{th} Berkeley Symposium on Math. Stat. and Prob., vol. 1, 1967, pp. 281–297.

72. F. Oliveri, G. Conte and M. Guglielmo, "A Technique using a One Dimensional Vector Quantization of Images", ICASSP 86, Tokyo, pp. 149–152.

73. A. Gersho, "Quantization", IEEE Communications Society Magazine, 1977, vol. 15, No. 5, pp. 20–29.

74. R. M. Gray and E. D. Karnin, "Multiple Local Optima in Vector Quantizers", IEEE Trans. on Information Theory, IT–28, 1982, pp. 256–261.

75. A. Gersho and B. Ramamurthi, "Image Coding Using Vector Quantization", Proc. IEEE ICASSP, 1982, pp. 428–431.

76. H. M. Hang and J. Woods, "Predictive Vector Quantization of Images", IEEE Trans. Comm., COM–33, No.11, Nov. 1985, pp. 1208–1219.

77. A.Haoui and D. G.Mersserschmitt, "Predictive Vector Quantization", ICASSP 1984, pp. 10.10.1–10.10.4 .

78. R. Aravind and A. Gersho, "Low–Rate Image Coding with Finite State Vector Quantization", Proc. ICASSP–86,pp. 137–140.

79. D. Allot and R. J. Clarke, "Adaptive Multi–Stage Mean Shape Vector Quantization of Images", IEE Colloquium on Vector Quantization, Nov. 1985, Digest No. 1985/92, pp. 4/11–4/15.

80. H. J. Lee and D. T. L. Lee, "A Gain–Shape Vector Quantizer for Image Coding", ICASSP 86, Tokyo, pp. 141–144.

81. J. Wu and A. G. Constantinides, "Composite Source Vector Quantization", IEE Colloquium on Vector Quantization, Nov. 1985, Digest No. 1985/92, pp. 3/11–3/15.

82. M. Goldberg, R. Boucher and S. Shlien, "Image Compression using Adaptive Vector Quantization", IEEE Trans. Comm., vol. COM–34, No. 2, 1986, pp. 180–187.

83. N. M. Nasarabadi and R. A. King, "A New Image Coding Technique using Transform Vector Quantization", IEEE ICASSP, California, 1984, pp. 19-21.

84. O. Ibikunle, N. M. Nasarabadi and R. A. King, "Design of a Codec for Video Conferencing", Proc. GRETSI/CESTA, May 1984, vol. 1, pp. 251–255.

85. H. F. Sun and M. Goldberg, "Adaptive Vector Quantization for Image Sequence Coding", IEEE ICASSP, vol. 1, 1985, pp.10.1.1–10.1.4.

86. Y. H. Ang and T. S. Durrani, "Adaptive Transform Vector Quantization", IEE Colloquium on Vector Quantization, Nov. 1985, Digest, No. 5/11–5/14.

87. T. Saito, H. Takeo, K. Aizawa, H. Harashima and H. Miyakawa, "Adaptive Discrete Cosine Transform Image Coding using Gain/Shape Vector Quantization", ICASSP Tokyo 86, pp. 4.1.1–4.1.4.

88. S. P. Lloyd,"Least Squares Quantization in PCM", IEEE Trans. on Information Theory, vol. IT-28, No. 2, 1982, pp. 129–137.

89. O. Ibikunle, "A Study of a Vector Quantization Technique for Transform Image Coding", M. Sc. Thesis, Imperial College of Science and Technology, 1983.

90. H. Abut, R. M. Gray and G. Rebolledo, "Vector Quantization of Speech and Speech–Like Waveforms", IEEE ASSP–30, 1982, pp. 423–435.

91. G. J. A. Hartigan, "Clustering Algorithms", John Wiley, N.Y., pp. 16,63,68 , 1973.

92. M. Hooper, "Two Component Coding using VQ", MSc Thesis, Imperial College of Science and Technology, 1986.

93. R. M. Gray and J. C. Kieffer, "Asymptotically Mean Stationary Measures", The Annals of Probability, 1980, vol. 8, No. 5, pp. 962–973.

94. N. Abramson, "Information Theory and Coding", New York McGraw Hill, 1963.

95. B. F. Logan and L. A. Shepp, "Optimum Reconstruction of a Function from its Projections", Duke Mathematical Journal, 1975, pp. 645–659.

96. B. H. Juang and A. H. Gray, "Multiple Stage Vector Quantization for Speech Coding", IEEE ICASSP, 1982, pp. 597–600.

97. A. K. Jain and P. M. Farelle "Recursive Block Coding: A New Approach to Transform Coding", IEEE Trans. on Comm., vol. COM–34, 1986, pp. 161–179.

98. W. H. Chen and C. H. Smith, "Adaptive Coding of Monochrome and Colour Images", IEEE Trans. on Comm. Tech., vol. COM–25, 1977, pp. 1285–1292.

99. G. Schwierz, W. Haner, K. Wiesent, "Sampling and Discretization Problems in X–Ray CT", Mathematical Aspects of Computerized Tomography, Proc., Oberwolfach, 1980, Springer–Verlag, pp. 292–309.

100. A. K. Jain, "Advances in Mathematical Models for Image Processing", Proc. IEEE, vol. 69, No. 5, 1981, pp. 502–528.

101. L. D. Davisson "Rate Distortion Theory and Application" Proc. IEEE, vol. 60, No. 7, 1972, pp. 800–808.

102. D. J. Sakrisson and V. R. Algazi, "Comparison of Line–by– Line and Two Dimensional Encoding of Random Images", IEEE Trans. on Info. Theory, vol. IT–17, No. 4, pp. 386–398.

103. A. J. Viterbi and J. K. Omura, "Principles of Digital Communications and Encoding", McGraw Hill, Kogakuska, 1979.

104. L. D. Davisson, "The Theoretical Analysis of Data Compression Systems", Proc. IEEE, vol. 56, No. 2, 1968, pp. 176–187.

105. M. S. Pinsker, "Information and Information Stability of Random Variables and Processes" Izd Akad Nauk SSSR Moscow, 1960, (Trans. Holden–Day San Francisco, 1964).

106. J. F. Hayes, A. Habibi and P. A. Wintz, "Rate Distortion Function for a Gaussian Source Model of Images", IEEE Trans. Info. Theory (Corresp.), July 1970, pp. 507–509.

107. T. F. Budinger, G. T. Gullberg and R. H. Huesman, "Emission Computed Tomography", Topics in Applied Physics, vol. 32, Springer Verlag, 1979, Image Reconstruction from Projections: Implementation and Applications, edited by G. T. Herman, pp. 147–246.

108. M. Tasto and P. A. Wintz, "A Bound on the Rate Distortion Function and Application to Images", Proc. IEEE Trans. on Info. Theory, vol. IT–18, No. 1,1972, pp. 150–159.

109. C. F. Gerald, "Applied Numerical Analysis", Addison Wesley, 1970.

110. J. J. Y. Huang and P. M. Schultheiss, "Block Quantization of Correlated Gaussian Random Variables", IEEE Trans. on Comm. Systems, CS–11, 1963, pp. 289–296.

111. S. J. Orfandis, "Optimum Signal Processing: An Introduction ", McMillan, 1985.

112. M. R. Teague, "Image Analysis via the General Theory of Moments", J. Opt. Soc. America, vol. 70, No. 8, 1980, pp. 920–930.

113. A. Papoulis, "Probability, Random Variables and Stochastic Processes", 2^{nd} Edition, Mcgraw–Hill, Singapore 1984.